Optical Computing for Adaptive Signal Processing and Associative Memories

Thesis by
John Hyunchul Hong

In Partial Fulfillment of the Requirements
for the Degree of
Doctor of Philosophy

California Institute of Technology
Pasadena, California

1987

Submitted May 25, 1987

Acknowledgements

I would like to thank my advisor, Professor Demetri Psaltis, for investing so much of his time and effort in me during my studies at Caltech. I appreciate especially his creativity and optimism, some of which hopefully has rubbed off on me. His technical insights have proven to be invaluable during the course of my research, and the constant encouragement and friendship that he has extended to me have made my stay at Caltech an enjoyable experience.

I am deeply indebted also to Dr. Eungi Paek, now at Bell Communications Research, for all of the help he has extended to me. The fifth chapter of my thesis is the result of a collaborative effort between Drs. Psaltis, Paek, and myself. I would like to also thank my colleagues in our research group. Among them, I would like to especially thank Jeffrey Yu, Fai Mok, Scott Hudson, Kelvin Wagner, Cheol Hoon Park, and Ken Hsu who have made valuable contributions to my work. Parts of the third chapter of this thesis are the results of collaborations between myself and Mr. Yu and Mr. Hudson. I would like to thank Professors Hyuk Lee and Santosh Venkatesh as well as Dr. Michael Haney for many helpful discussions. I am grateful for the administrative help that I received from Mrs. Helen Carrier and Mrs. Odessa Myles. I also gratefully acknowledge that my fourth year at Caltech was financially supported in part by a fellowship grant from the Program in Advanced Technologies at Caltech. I would like to also thank that small group of

people from the Wednesday Bible study group who have made my stay at Caltech a spiritually enriching time.

Constant encouragement has come from my family and more recently, from Christine, my joy. I would not have considered pursuing graduate studies if it weren't for the encouragement that I received from my brother and sisters. Words fail to describe the selfless love and prayerful devotion that my father and mother have given me, and it is to them that I dedicate this thesis.

"you shall know the truth

and the truth shall set you free."

John 8:32

"For God so loved the world

that He gave His only begotten Son,

that whoever believes in Him

should not perish, but have

everlasting life."

John 3:16

Abstract

Optical techniques for performing two computing tasks are investigated. First, acousto-optical systems that implement adaptive filtering structures are presented for operation in environments that are not well characterized *a priori* or are time-varying. Theoretical analyses along with experimental confirmations are given to identify the important system parameters that affect the performance. Extensions of the systems to the multidimensional domain of phased array signal processing are discussed as well as novel implementations that use photorefractive crystals as time-integrating elements.

Also investigated are various associative memory models. An acousto-optic implementation of the so-called Hopfield model is presented. The system's storage capacity and attraction radius are characterized experimentally and are shown to agree with computer simulations. Secondly, an upper bound is derived for the storage capacity of holographic associative memories that use planar holograms. It is shown that if the space bandwidth product of the hologram is N_2, then the holographic memory can store at most N_2/N_3 associations, where N_3 is the number of pixels in each output item. Finally, associative memories whose performance is invariant with respect to shifts in the input pattern position are considered. It is shown that nonlinear interconnections are required to achieve shift invariant operation, and optical implementations are discussed.

Table of Contents

Acknowledgements iii

Abstract vi

1. Introduction 1

References 6

2. Adaptive Filtering Systems 9

2.1 Adaptive Systems 9

2.2 Learning Machines and Adaptive Filters 12

2.3 Adaptive Estimation and Detection 20

References 29

3. Optical Adaptive Systems 31

3.1 Space Integrating Adaptive Filters 31

3.1.1 *space integrating convolver and correlator* 31

3.1.2 *description of implementation* 44

3.1.3 *performance and experimental results* 52

3.2 Space-Time Integrating Adaptive Filter 64

3.2.1 *time integrating correlator* 64

3.2.2 *time integration using a photorefractive crystal* 73

3.2.3 *space-time integrating optical processor* 82

References 89

4. Extension to 2-Dimensional Signal Processing 90

4.1 Narrowband Processors in Broadband Environments 90

4.2 Optimum Broadband Systems 90
4.3 Direction Cancellation of a Single Broadband Interference 101
4.4 Adaptive Array Processor 104
4.5 Optical Implementation 108
4.6 Adaptive Array Processor with Variable Look Direction 117
References 125

5. Associative Memory Models 126
5.1 Introduction 126
5.2 Linearly Interconnected Memories 129
5.2.1 *the Hopfield model* 129
5.2.2 *the spectral scheme* 135
5.3 An Acoustooptic Implementation of the Hopfield Model 138
5.3.1 *optical linear transformations* 138
5.3.2 *acoustooptic system description* 143
5.3.3 *experimental results* 144
5.3.4 *modifications for stability: relaxational operation* 152
References 160

6. Storage Capacity of Holographic Memories 161
6.1 Introduction 161
6.2 Degrees of Freedom Considerations 163
6.3 Holographic Associative Memories 166
6.3.1 *capacity derived from SNR considerations* 166
6.3.2 *an example* 172
6.4 Conclusion 173
References 175

7. Shift Invariant Associative Memories 177

7.1 Introduction....177

7.2 Shift Invariance and Linear Memories....180

7.3 Optical Systems with Linear Memories....183

7.4 Optical Memory with Distributed Nonlinearities....185

7.4.1 *nonlinear correlation plane*....185

7.4.2 *shift invariant optical memory*....188

7.5 2-D Shift Invariance for 1-D Data....193

References....198

8. Conclusions 200

8.1 Summary of the Thesis....200

8.2 Directions for Future Research....201

Appendix A: Effects of System Noise on the Passive Processor 203

Appendix B: Optimum Broadband Processors 207

Chapter 1. Introduction

In an effort to aid the understanding of how the brain processes information, various neural network models have been developed. Though very much simplified from reality, such models possess certain key features found in biological nervous systems such as relatively simple computing units coupled with extensive interconnections among the numerous units that comprise the system. The first such model was that of McCulloch and Pitts[1] in which each computing unit, the so-called "formal neuron," was, in essence, a threshold gate whose output is either "1" or "0" depending on a comparison made between the sum of its inputs and a threshold value. As shown schematically in Fig.1.1, the network is built up by interconnecting the neurons using real valued connection strengths, and communication with the external world is possible through pre-specified input and output lines.

Clearly, such systems are distinctly different from digital computers in the way information is stored and processed. Neural nets implement a massively parallel and distributed form of computation and information storage, whereas conventional computers rely on sequential computation and localized storage of information. While not nearly as versatile in terms of programmability as digital computers, many algorithms for training the networks to perform specific tasks exist for applications such as pattern recognition[2,3,4,5,6], associative memory[7-14], and the approximate solution of certain complex problems[15-17]. Most of these training

methods are supervised in that a sample set of inputs with known desired outputs are used to teach the desired behavior.

One particular network called the *Adaline* [4] employs a simple algorithm for learning, based on a gradient descent procedure to minimize a certain cost function. Originally intended for application in pattern recognition, the learning algorithm was used with success to solve problems in adaptive signal processing where dynamically updatable filters are required, which can be adjusted automatically to optimize certain criteria based on currently available data and past history. These filters generally have the same linear structure as the model of Fig. 1.1 without the output threshold unit, resulting in a linear form. In the case of processing one-dimensional temporal signals, the inputs x_1, x_2, ,..., x_N are time samples of the signal derived by using a tapped delay line. Here, the filter learns certain statistical properties of the encountered signals, and based on this, discriminates between useful and unwanted signals. Such filters are useful in situations wherever *a priori* information is insufficient to design and construct optimal systems.

Another area where neural modeling proves to be useful is associative memories. In contrast with conventional computer memories such as RAM or ROM where data is stored and retrieved from locations labelled with prescribed addresses, associative memories store pairs of data in relation to one another so that an item is retrieved by probing the memory with its associated datum. In addition to this lack of structure in the addressing, associative memories are usually required to exhibit some form

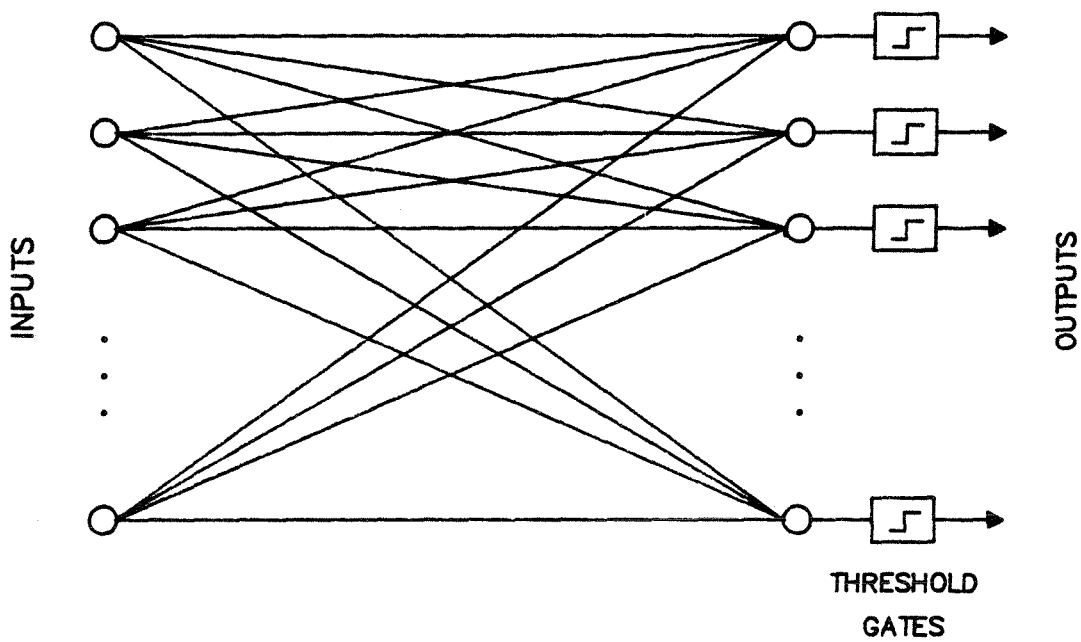

Fig. 1.1 Model of a Neural Network

of error correction to allow the recognition of addressing data that contain small errors. Specific models have been forwarded to implement such memory systems with neural networks [7,14,18], each offering varying degrees of storage capacity, robustness, and programmability. Because neural networks store information solely in the interconnections between the neurons, storage is not localized as it is in conventional memories, and as a result, the neural memories possess certain soft-fail robustness properties.

The fact that neural systems store data in the interconnections is an impetus for exploring optical implementations where holographic techniques may be used to provide the necessary connections between the "neurons." The motivation for using optics lies in the size of globally connected networks that can be implemented. Also, the emphasis in neural models is on the analog interconnections and not on the individual computing elements that are simple, and this fits well with optical technology, where the required holographic techniques are quite mature.

This thesis is an investigation into the implementation of neural modeling ideas in the domain of optics where, specifically, two problems are addressed. The first is the problem of adaptive processing, where a system is required to adapt to varying or unknown environments. Here, the learning aspects that are required will be discussed. Several optical approaches to the problems of adaptive filtration of temporal signals [19,20,21] as well as the processing of multidimensional spatio-temporal

signals [22,23] are presented. The generalization of these ideas to the more unstructured problem of associative memories is then discussed. In particular, capacities of holographic memories [24] as well as invariance issues [25] are explored. In so doing, several optical architectures for implementing such memories are presented.

References for Chapter 1

[1] W. S. McCulloch and W. H. Pitts, "A logical calculus of the ideas immanent in nervous activity," *Bulletin of Math. Biophysics*, **5**, 115 (1943).

[2] R. A. Fisher, "The use of multiple measurements in taxonomic problems," *Ann. Eugenics*, **7**, Part II, 179 (1936).

[3] K. S. Fu, *Sequential Methods in Pattern Recognition and Machine Learning*, Academic Press, New York, 1968.

[4] B. Widrow and M. E. Hoff, "Adaptive switching circuits," *1960 IRE WESCON Conv. Record*, **4**, 96 (Aug. 1960).

[5] F. Rosenblatt, *Principles of Neurodynamics: Perceptrons and the theory of brain mechanisms*, Spartan Books, Washington, D. C., 1962.

[6] Y. C. Ho and R. L. Kashyap, "An algorithm for linear inequalities and its applications," *IEEE Trans. Elec. Comp.*, **EC-14**, 683 (Oct. 1965).

[7] J. J. Hopfield, "Neural networks and physical systems with emergent collective computational abilities," *Proc. Natl. Acad. Sci. U.S.A.*, **79**, 2554 (1982).

[8] K. Nakano, "Associatron - a model of associative memory," *IEEE Trans. Sys. Man, and Cybernetics*, **SMC-2**, no.3, 380 (July 1972).

[9] W. A. Little, "The existence of persistent states in the brain," *Math. Biosci.*, **19**, 101 (1974).

[10] H. C. Longuet-Higgins, "The non-local storage of temporal information," *Proc. Roy. Soc. B*, **171**, 327 (1968).

[11] L. N. Cooper, "A possible organization of animal memory and learning," *Proc. Nobel Symposium on Collective Properties of Physical Systems*, **24**, 252 (1973).

[12] G. Palm, "On associative memory," *Biol. Cybern.*, **36**, 19 (1980).

[13] G. E. Hinton and J. A. Anderson, *Parallel Models of Associative Memory*, Lawrence Erlbaum Assoc., Hillsdale, New Jersey, 1981.

[14] T. Kohonen, *Self-Organization and Associative Memory*, Springer-Verlag, Berlin, Germany, 1984.

[15] J. J. Hopfield and D. W. Tank, "Neural computations of decision optimization problems," *Biol. Cybern.*, **52**, 141 (1985).

[16] J. J. Hopfield and D. W. Tank, "Collective computation with continuous variables," in *Disordered Systems and Biological Organization*, E. Bienstock, F. Fogelman, and G. Weisbuch, Eds., Springer-Verlag, Berlin, Germany, (1985).

[17] J. J. Hopfield and D. W. Tank, "Simple neural optimization networks: an a/d converter, signal decision circuit, and a linear programming circuit," *IEEE Trans. Circuits and Systems*, **CAS-33**, no.5, 533 (May 1986).

[18] S. Venkatesh and D. Psaltis, "Linear and logarithmic capacities in associative neural networks," *submitted for publication IEEE Trans. Info. Theory*, , ().

[19] D. Psaltis and J. Hong, "Adaptive acousto-optic filter," *Applied Optics*, **23**, no.19, (Oct. 1, 1984).

[20] J. Hong and D. Psaltis, "Acousto-optic signal processing," *SPIE Proceedings*, **551-20**, Arlington, VA (April 1985).

[21] D. Psaltis, J. Yu, and J. Hong, "Bias-free time-integrating correlator using a photorefractive crystal," *Applied Optics*, **24**, 3860 (Nov. 15, 1985).

[22] D. Psaltis and J. Hong, "Adpative acousto-optic signal processing," *SPIE Proceedings*, **519-09**, Cambridge, MA (October 1984).

[23] J. Hong, J. Yu, S. Hudson, and D. Psaltis, "Photorefractive crystals as adaptive elements in acousto-optic filters," *SPIE Proceedings*, **789-39**, Orlando, FL (May 1987).

[24] J. Hong and D. Psaltis, "Storage capacity of holographic associative memory," *Optics Letters*, **11**, 812 (Dec. 1986).

[25] D. Psaltis and J. Hong, "Shift invariant associative memory," *Optical Engineering*, **26**, no. 1, 10 (Jan. 1987).

Chapter 2. Adaptive Filtering Systems

2.1 Adaptive Systems

The design of optimum systems, in the classical sense, requires *a priori* some knowledge of the signals to be encountered. As a result, such systems perform poorly when the appropriate characteristics of the input signals are not known *a priori* sufficiently well or are time-varying. An adaptive processor has the ability to self-optimize by continually monitoring its performance and updating its parameters. Adaptive techniques have been applied to both the spatial and temporal filtering domains. Specifically, adaptive techniques have been applied to antenna array processing by Appelbaum[1], Widrow *et al.*[2], and others [3,4]. Applications to time domain problems include Lucky's work on data redundancy removal [5], Sondhi's adaptive echo canceller[6], Widrow's work on adaptive noise suppression [7], Morgan and Craig's adaptive linear predictor [8], and more [9,10].

In the work on time domain problems cited above, the adaptive filtering scheme is based on the orthogonality principle [11]. The basic idea behind the algorithm is to control a variable filter so as to minimize the correlation between the input signal and the residual signal, which is the difference between the input signal and the filter output. A particular implementation of this scheme, shown in Fig. 2.1, uses the transversal filter architecture, which consists of a tapped delay line, variable

filter weights, and a summer that produces a weighted sum of delayed versions of the input signal as its output.

The linearity and parallel nature of the transversal filter arrangement, commonly called the correlation cancellation loop (CCL) system, make an optical implementation possible. The advantages of optical processors in terms of bandwidth and the large effective number of taps make such an implementation attractive. For example, acousto-optic devices (AODs), which can serve as optically tapped delay lines, are superior in terms of bandwidth to charge coupled device (CCD) implemented delay lines that are currently used in analog adaptive filters [12,13]. Several adaptive optical filter implementations have been previously proposed. Psaltis *et al.* [14,15] proposed the use of an iterative electro-optic processor for adaptive spatial filtering of phased array antenna signals. Rhodes [16] described a system using acousto-optic and electro-optic modulators in a time-integrating architecture to implement the CCL algorithm in the time domain, and VanderLugt [17] described an optical processor which is a frequency domain implementation of the CCL algorithm. Lee *et al.* [18] have devised an adaptive filter that suppresses narrowband interference from wideband signals using an acousto-optic spectrum analyzer with an array of electro-optic modulators in the spatial frequency plane that can adaptively excise strong narrowband components of the signal spectrum.

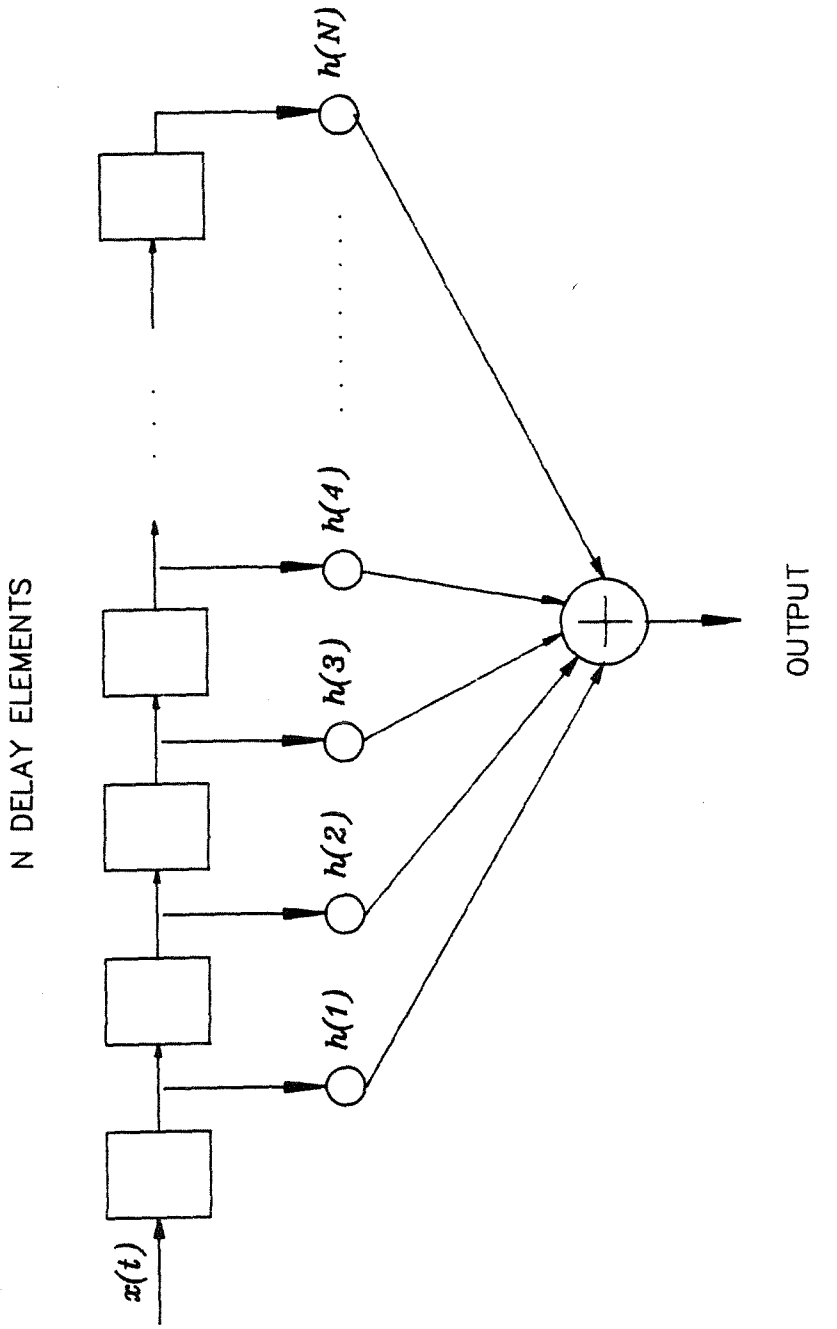

Fig. 2.1 Linear Transversal Filter

2.2 Learning Machines and Adaptive Filters

Adaptive filtering can be viewed as a pattern recognition problem in which certain waveforms are automatically classified as useful signals and others as noise to be rejected. Linear time-invariant filters can be synthesized using a transversal structure as shown in Fig. 2.1 in which the input waveform feeds a tapped delay line whose tap weights are given by the desired impulse response function. An adaptive filter with this structure constantly updates its tap weights based on how well the system performed with respect to some criterion function. Recognition machines that use the linear discriminant function (LDF) to classify patterns use basically the same structure as the adaptive filter. Shown in Fig. 2.2 is a general linear machine that uses LDFs to classify patterns into two groups, where each pattern is represented by an N dimensional vector $\underline{x}_m$. The input bits are linearly weighted with the vector $\underline{w}$ and compared to the bias value θ. Based on this comparison, the input pattern is assigned to one of two classes represented by the binary outputs $+1$ and -1. The choice of the weights depends on the patterns that the machine will encounter and also on the particular label assignments. The appropriate weights can be generated by using an algorithm that teaches the machine by repeatedly showing the input pattern and the associated label (± 1) as the desired output response. In particular, the *Perceptron* [19], which operates on inequality constraints and requires threshold decisions during the training phase and the *Adaline* [20], which

is an algorithm based on related constraints have received much attention several decades ago.

The *Perceptron* updates its weights only when the machine makes a mistake in classifying a particular pattern. The change made to the weight vector is proportional to the pattern that resulted in the error, and under certain conditions, the algorithm can be shown to converge to give the weight vector that correctly dichotomizes a given set of patterns if such a solution exists [19]. The *Adaline*, on the other hand, makes changes which are proportional to the size of the error for every training pattern it receives. If the training patterns are repeatedly presented to the machine along with their associated labels, then the magnitude of the changes decreases with time, and the weight values settle to constant values. If the weight solution exists, then the converged weight vector is the solution.

To discuss adaptive filtering from the viewpoint of learning in recognition machines, it is useful to examine the *Adaline* rule in more detail. Let the $N+1$ dimensional vector $\underline{a}(k)$ represent the weight vector at the k_{th} iteration. The weight vector has been augmented to $N+1$ dimensions to include the bias term $a_{N+1}(k) = \theta$, which is to be learned also. To dichotomize the set of M $(N+1)$ dimensional vectors $\{\underline{x}_m\}_{m=1}^{M}$ where the m_{th} vector has the label c_m, the following infinite sequence of training patterns and labels can be used: $(\underline{x}_1, c_1), (\underline{x}_2, c_2), \ldots, (\underline{x}_M, c_M), (\underline{x}_1, c_1), \ldots$. Let $\underline{y}(k)$ be an $N+1$ dimensional vector whose first N elements are equal to the corresponding bits of the k_{th} pattern of the infinite training sequence, and the last

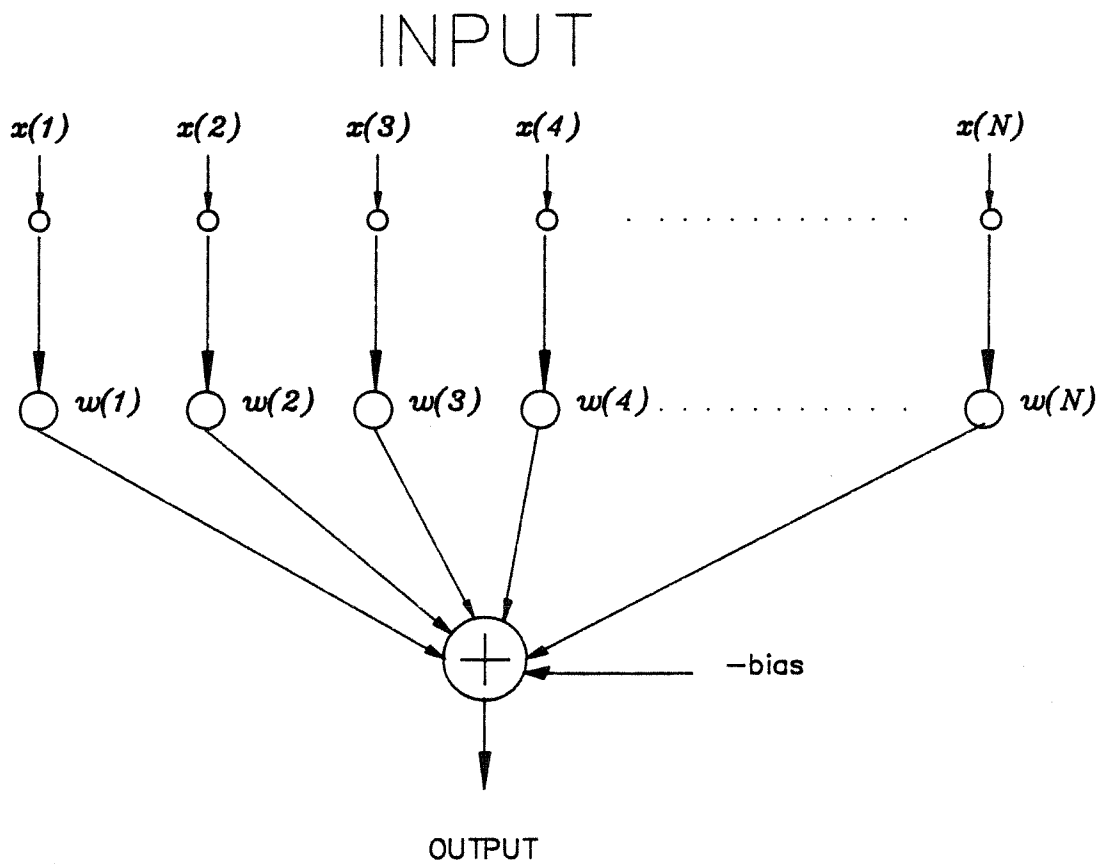

Fig. 2.2 Linear Discriminant Machine

bit $y_{N+1}(k)$ is equal to 1 to supply a constant input for the bias weight. Also, let $b(k)$ be the label of the pattern presented at the k_th iteration. With this, the weight update rule is defined by the recursive equation

$$\underline{a}(k+1) = \underline{a}(k) + \rho\big[b(k) - \underline{a}^t(k)\underline{y}(k)\big]\underline{y}(k), \tag{2.1}$$

which is convergent for sufficiently small ρ. This algorithm changes the weights by following an approximately steepest descent path on the mean-squared error surface (defined on the $N+1$ dimensional weight space) given by

$$\epsilon = (1/M)\sum_{m=1}^{M}\big(c_m - \underline{a}^t\underline{y}(m)\big)^2. \tag{2.2}$$

As long as the finite set of training patterns is linearly separable (i.e., they can be dichotomized by a linear machine), the *Adaline* will learn to correctly classify the samples, driving the error term given by $b(k) - \underline{a}^t(k)\underline{y}(k)$ to zero. As an example, we consider the following simple example. We wish to dichotomize the set of numbers $\{3, 17, 41, 10, 18, 46\}$ into sets of even and odd numbers by training a machine with the 6 bit binary representations of the numbers. An obvious way to dichotomize the numbers is to consider only the least significant bit (LSB), since the LSB of even numbers will be "0" while for odd numbers, it will be "1," but we use this example to train the machine to dichotomize the data by rote memory, where we have assigned the label "+1" to even numbers and "−1" to odd numbers.

Number	Binary Representation
3	0 0 0 0 1 1
17	0 1 0 0 0 1
41	1 0 1 0 0 1
10	0 0 1 0 1 0
18	0 1 0 0 1 0
46	1 0 1 1 1 0

a)

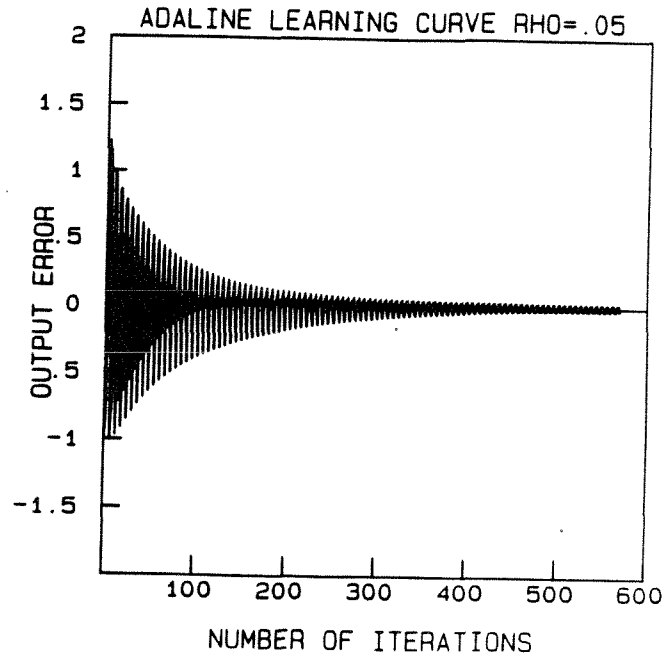

b)

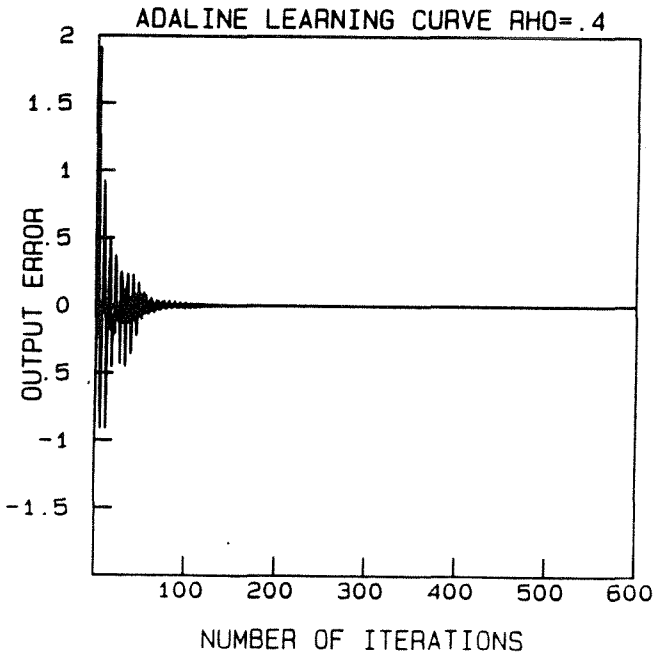

c)

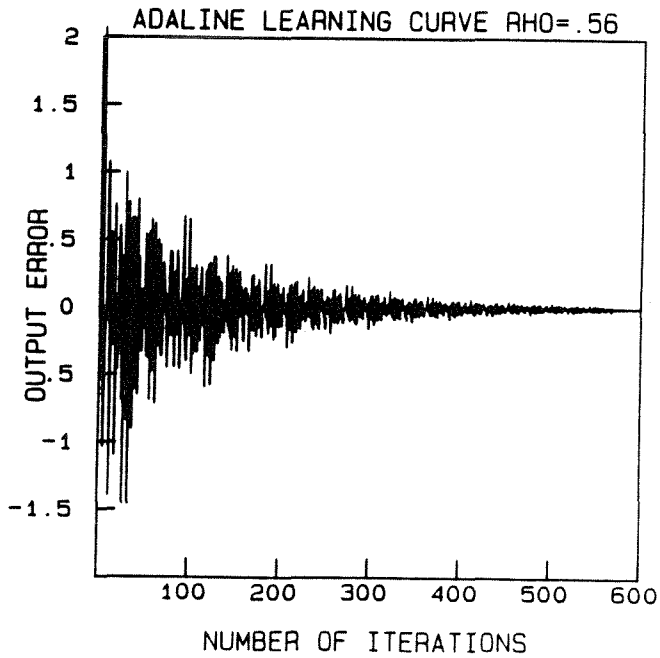

d)

Fig. 2.3 Classification Using the Adaline Rule a)training set representation b)error curve for ρ=.05 c)error curve for ρ=.4 d)error curve for ρ=.56

Fig. 2.3 gives the binary representations of the numbers (the training set) as well as a plot showing the decrease in the output error with increasing iterations when the training sequence {(3,-1), (17,-1), (41,-1), (10,+1), (18,+1), (46,+1), (3,-1), (17,-1), ...} is used for three values of the acceleration parameter, ρ. Values of ρ greater than .6 resulted in diverging weights. For this example, the machine was able to match exactly the desired binary outputs. The algorithm will converge even for training sets that are not linearly separable, and the resulting weight values will only approximately dichotomize the set.

A linear predictor [21] is a filter whose output estimates the future value of the input signal by a linear combination of the past values that it encountered. For optimal design in the sense of mean-squared error, the second-order statistics of the signal must be known beforehand. Specifically, if $x(k)$ represents the input time series at time k, then the output $\hat{x}(k)$ is given by

$$\hat{x}(k) = \sum_{j=1}^{N} h_k x(k-j). \tag{2.3}$$

An adaptive version of such a filter does not need *a priori* knowledge of the signal statistics and can be directly implemented using the learning algorithm illustrated above by using a tapped delay line to generate the training samples and using the present input value $x(k)$ as the "labels."

A system diagram of the predictor is shown in Fig. 2.4 for N taps, where the unnecessary threshold gate and the bias weight θ have been excluded. The weight

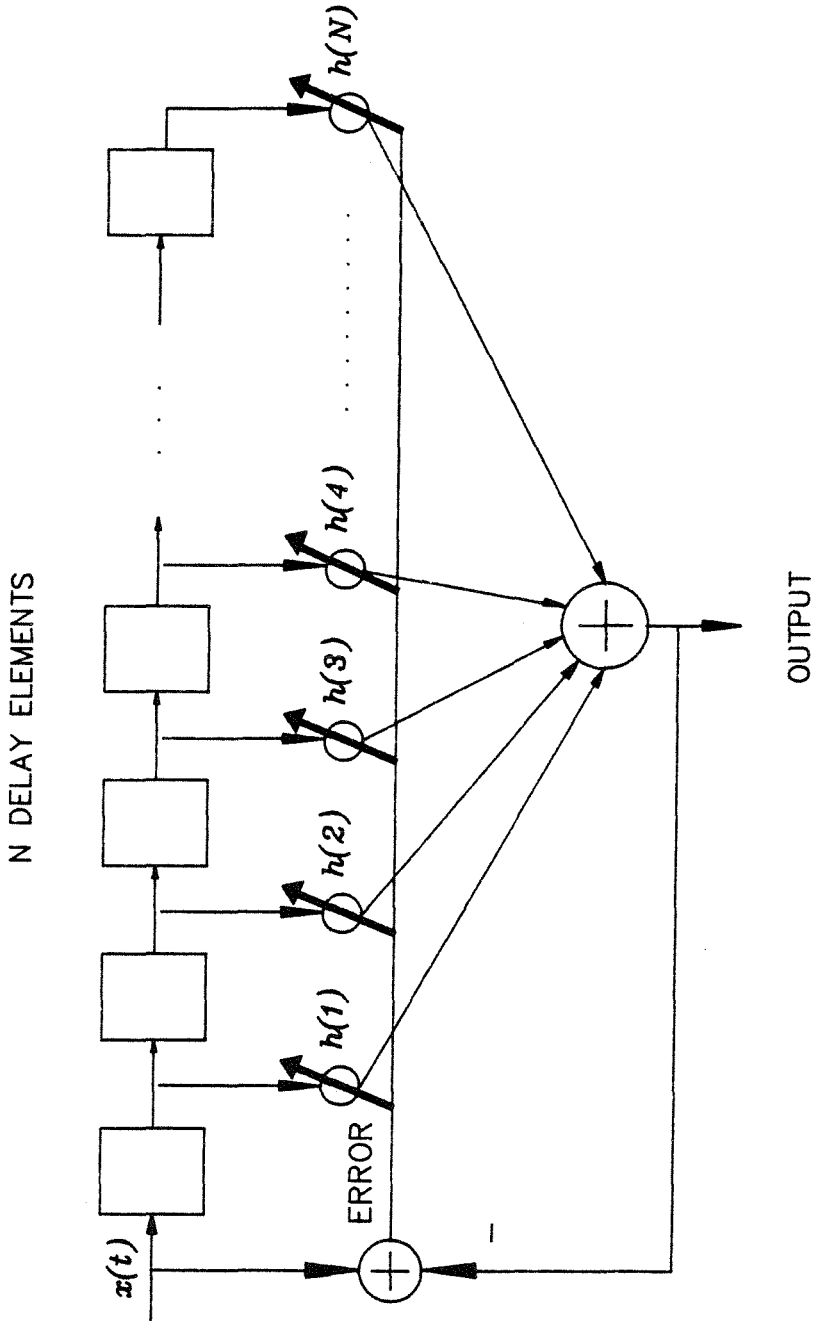

Fig. 2.4 Adaptive Linear Predictor

update rule, written for the j_{th} component, is given by

$$\begin{aligned} h_j(k+1) &= h_j(k) + \rho\big[x(k) - \hat{x}(k)\big]x(k-j), \\ \hat{x}(k) &= \sum_{j=1}^{N} h_j(k)x(k-j). \end{aligned} \tag{2.4}$$

As the *Adaline* algorithm minimized the mean-squared error of the classification of patterns, this adaptive predictor approximately minimizes the mean-squared error of the prediction. If we assume that the input time series $x(k)$ was obtained from a random process, then the predictor minimizes the cost

$$\epsilon = E\left[\left(x(k) - \hat{x}(k)\right)^2\right], \tag{2.5}$$

where $E[.]$ represents the statistical ensemeble averaging operation. If the signals are deterministic, then the predictor still minimizes the mean squared error where the average is now over a period of time rather than over ensembles. The predictor discriminates between two types of signals present in the input. The samples derived from signals with narrowband spectra are highly correlated, while random-like broadband signals result in samples that are poorly correlated; extremes are sinusoids and white noise. The adaptive predictor adapts quickly to the regular structure of the narrowband signals and produces good estimation for these signals, while the broadband signals, with their lack of regularity, result in poor estimation. If a signal contains both broadband and narrowband components in which the amplitudes of narrowband components are dominant, the output of the predictor will consist mainly of enhanced versions of the narrowband components. In contrast,

the error signal contains broadband components which are enhanced in comparison with the narrowband portions.

This effect is seen in the plots of Fig. 2.5, in which are shown the estimate and the error signals produced by an adaptive predictor in response to an input that consists of the sum of a large amplitude sinusoid and a smaller amplitude pseudo-random signal. The simulation used the prediction algorithm derived above for $N = 64$. While the presence of the sinusoid in the input obscures the broadband component, the predictor adapts to the situation to enhance the broadband component in its error signal. This example, along with the heuristic description of the adaptive predictor, illustrates the usefulness of learning algorithms for signal processing.

2.3 Adaptive Estimation and Detection

The extraction of information from a signal corrupted by additive noise requires *a priori* knowledge of the properties of the desired signal and the noise. If the necessary information is known, the optimum linear filters can be designed to satisfy the specified performance criteria. In the present investigation, we will be interested mainly in two performance criteria: the mean-squared error and the output signal-to-noise ratio (SNR). If some received signal $x(t)$ consists of the desired signal $s(t)$ contaminated by additive noise $n(t)$, then the mean-squared error is given by

$$\epsilon = E\left[|L\{x(t)\} - s(t)|^2\right], \tag{2.6}$$

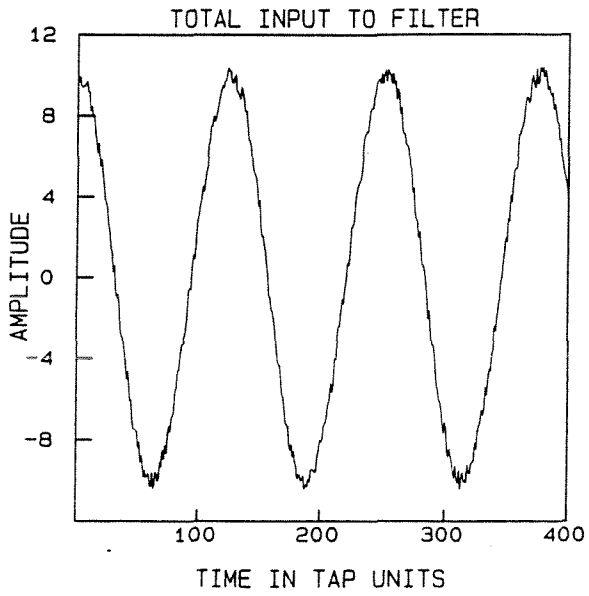

a)

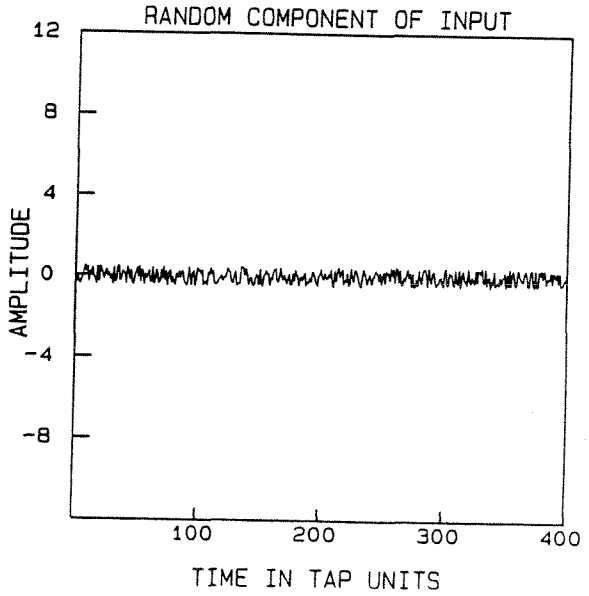

b)

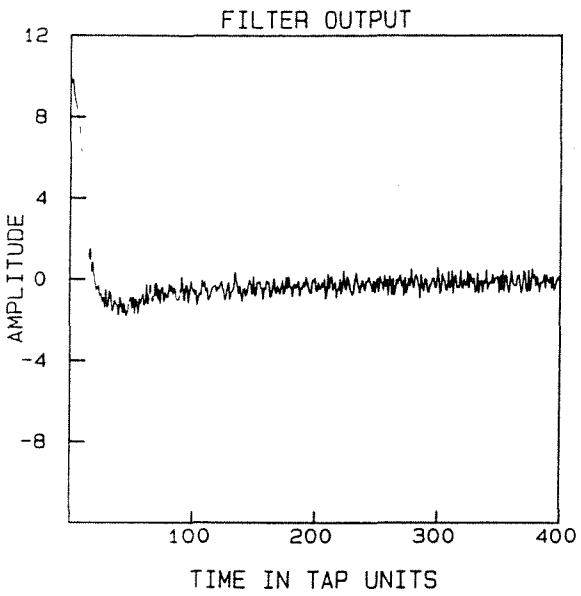

c)

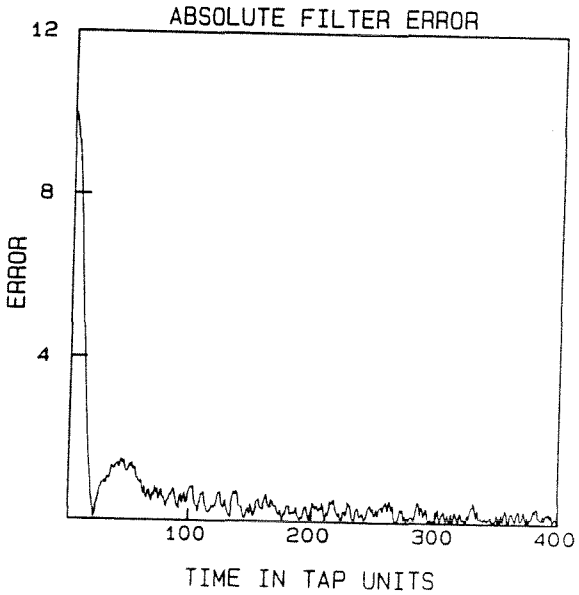

d)

Fig. 2.5 Operation of the Adaptive Linear Predictor a)total input to filter consisting of a broadband pseudorandom code and a sinusoid b)random component of input c)filter output d)absolute filter error

where $L\{x(t)\}$ is the output of the filter that operates on the received signal $x(t)$ and the signal and noise are assumed to derive from random processes over which $E[.]$ is the expectation operation. The output SNR, on the other hand is given by the ratio

$$SNR_{out} = \frac{\left|\left[L_s\{x(t)\}\right]\right|^2}{E\left[L_n^2\{x(t)\}\right] - E^2\left[L_n\{x(t)\}\right]}, \tag{2.7}$$

where $L_s\{x(t)\}$ and $L_n\{x(t)\}$ are the signal and noise components of the filter output. When considering only linear filters, the Wiener filter provides the minimum mean-squared error estimate of a signal in the presence of additive noise, but it requires that the autocorrelations as well as the cross-correlation of the signal and the noise be known in advance. The filter that maximizes the output SNR is the matched filter which requires prior knowledge of the autocorrelation of the noise and also the desired signal waveform.

When the necessary correlation functions are not known *a priori*, they must be estimated from the past history of the signal and the limited and qualititative information that is available. We assume that the available information is as follows. The signal and noise are uncorrelated, and the signal is broadband, as in spread spectrum systems. We model the wideband signal as bandlimited white noise, so that $S_s(f)$, the spectral density of the wideband signal $s(t)$, is equal to $S_0 rect\left[(f - f_0)/\delta f\right]$, where f_0 is the center frequency of the signal and δf is its

bandwidth. The function $rect[x]$ is defined by

$$rect[x] = \begin{cases} 1, & \text{if } |x| \leq .5; \\ 0, & \text{otherwise.} \end{cases}$$

The spectral density of the interference $n(t)$ is unknown, and it is adaptively estimated.

Shown in Fig.2.6a is a system diagram of the passive processor, which will be shown to adaptively perform an operation that approximates the Wiener filter under the conditions stated in the above paragraph. The two necessary operations in the implementation of this filter are convolution and correlation. The convolver serves as the variable filter that is controlled by the correlator, which estimates the correlation of the interference. The output of the correlator will be dominated by the autocorrelation of the narrowband interference component, since the broadband signal components present in the output correlate very poorly with the delayed version of the signal present in the input. The correlation output in which the broadband components have been suppressed is convolved with a delayed version of the input, resulting in a feedback signal that consists of an enhanced narrowband interference and a suppressed broadband signal component. The order of the operations of correlation and convolution can be switched as shown in Fig. 2.6b using the commutative property of convolutions. This change of order will be useful later, when the optical implementations are considered.

To show that the system converges approximately to the Wiener result under closed loop conditions, a mathematical model of the system is now given. The

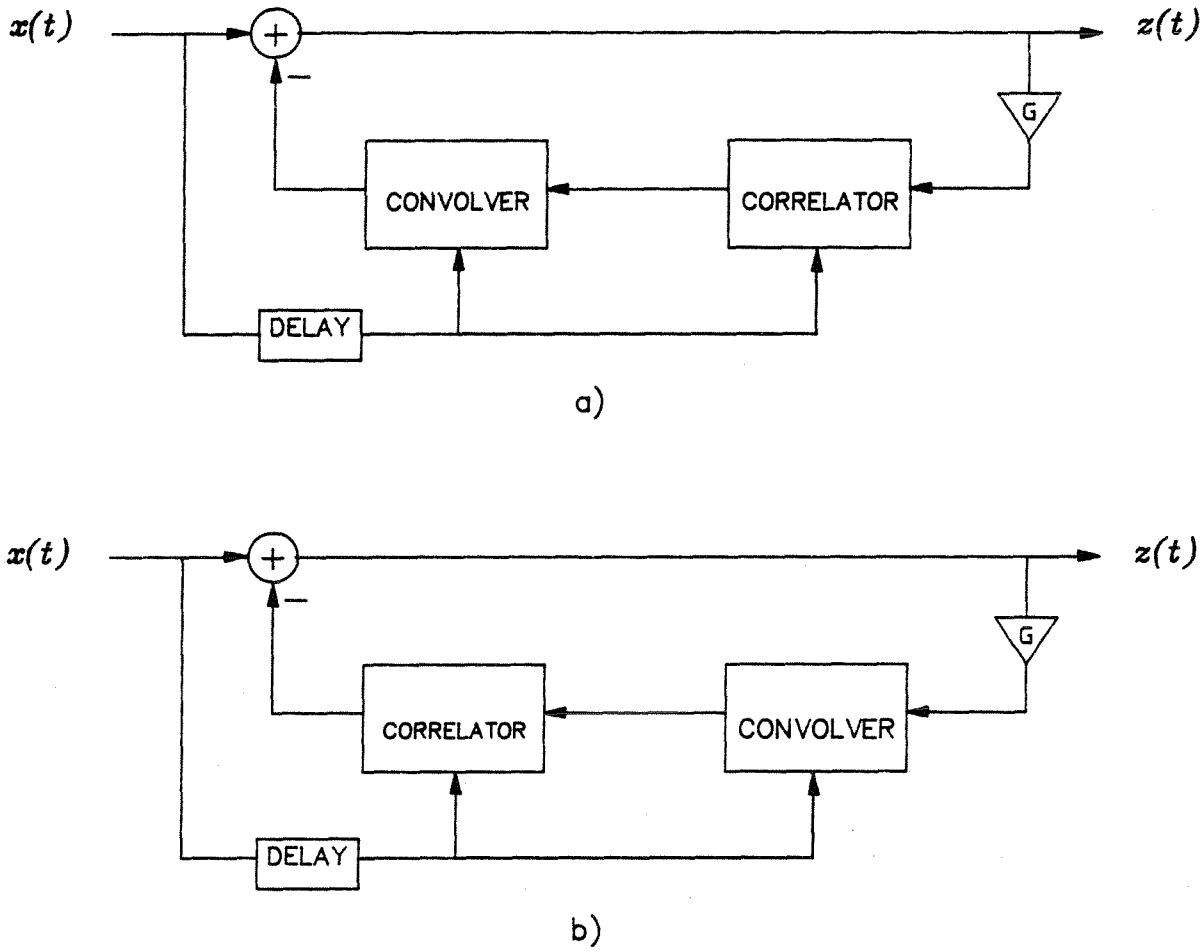

Fig. 2.6 a,b Two Versions of the Passive Processor

operation of the convolver and correlator blocks are described by the following input-output relations:

$$\begin{aligned} u(t) &= \int_{-\infty}^{\infty} i_1(t-\tau) i_2(\tau) d\tau, \\ w(t) &= \int_{-\infty}^{\infty} i_1(t+\tau) i_2^*(\tau) d\tau, \end{aligned} \tag{2.8}$$

where $i_1(t)$ and $i_2(t)$ are the inputs to the blocks. Using Eqs. 2.8, we find the relationship between the input and output signals, $x(t)$ and $z(t)$ respectively, of the passive processor of Fig. 2.6b to be

$$\begin{aligned} z(t) &= x(t) - G \int \int_{-\infty}^{\infty} z(\tau) x^*(\alpha - \sigma) x(t + \alpha - \tau - \sigma) d\alpha d\tau \\ &= x(t) - G \int \int_{-\infty}^{\infty} z(\tau) [s^*(\alpha - \sigma) + n^*(\alpha - \sigma)] \\ &\qquad [s(t + \alpha - \tau - \sigma) + n(t + \alpha - \tau - \sigma)] d\alpha d\tau, \end{aligned} \tag{2.9}$$

where σ is a time delay, and G is a feedback gain constant. Low input SNR along with the assumption of the uncorrelatedness between the signal $s(t)$ and the noise $n(t)$ results in the reduction of Eq. 2.9 into

$$z(t) \approx x(t) - G \int \int_{-\infty}^{\infty} z(\tau) n^*(\alpha - \sigma) n(t + \alpha - \tau - \sigma) d\alpha d\tau. \tag{2.10}$$

Fourier transformation of the above equation yields the approximate frequency domain description:

$$Z(f) \approx X(f) - GZ(f)|N(f)|^2, \tag{2.11}$$

where $Z(f)$ and $X(f)$ are the Fourier transforms of $z(t)$ and $x(t)$, respectively, and $|N(f)|^2$ is the power spectrum of a sample realization of $n(t)$. Solving for the output

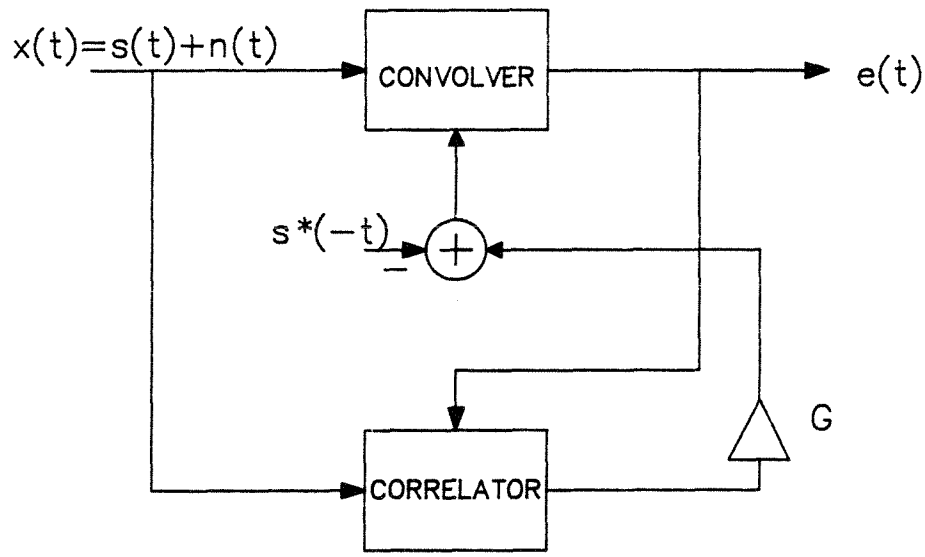

Fig. 2.7 Active Processor

$Z(f)$ gives

$$\begin{aligned} Z(f) &\approx \frac{X(f)}{1+G|N(f)|^2} \\ &= \frac{1/G}{1/G+|N(f)|^2}X(f). \end{aligned} \tag{2.12}$$

The input signal to the convolver and the correlator in Fig. 2.6a is delayed by the same amount, and therefore the interference components present in the output of the convolver-correlator combination $\hat{x}(t)$ become independent of the delay. This is an important result, since it assures that the feedback signal $\hat{x}(t)$ is in phase with the input signal, a condition required for proper nulling. With $G = 1/S_0$ and identifying $|N(f)|^2$ as the estimate of $S_n(f)$, the spectral density of $n(t)$, Eq. 2.12 describes the output of the well-known Wiener filter [22].

We now show that the active processor designed for signal detection, shown in Fig. 2.7, adaptively performs matched filtering. The filter is now varied not for estimation but to maximize the signal-to-noise ratio appearing at the output. If the input noise consisted entirely of white noise, then the optimal linear filtering procedure would be to correlate the total input against the reference signal that is to be detected in the input. If the signal is present in the input, then the output would be a sharply peaked pulse whose position in time indicates the arrival time of the signal relative to the position of the reference in time. If, however, the noise is not white and its statistics are not known, then we must resort to the adaptive techniques to be discussed to enhance the processing gain.

The exact input-output relationship that describes the system shown in Fig. 2.7 is given by

$$\begin{aligned} e(t) = &\int_{-\infty}^{\infty} x(t-\tau)s^*(-\tau)d\tau \\ &- G\int\int_{-\infty}^{\infty} x(t-\tau)x^*(\alpha)e(\tau+\alpha)d\alpha d\tau, \end{aligned} \tag{2.13}$$

where $e(t)$ is the output signal of the active processor. The assumption of low inpt SNR along with the conditions stated previously allows the following approximate form of Eq. 2.13:

$$\begin{aligned} e(t) \approx &\int_{-\infty}^{\infty} x(t-\tau)s^*(-\tau)d\tau \\ &- G\int\int_{-\infty}^{\infty} n(t-\tau)n^*(\alpha)e(\tau+\alpha)d\alpha d\tau. \end{aligned} \tag{2.14}$$

The Fourier transform of the output signal $e(t)$ is readily found to be

$$\begin{aligned} E(f) &\approx \frac{X(f)S^*(f)}{1+G|N(f)|^2} \\ &\approx \frac{X(f)S^*(f)}{G|N(f)|^2}, \end{aligned} \tag{2.15}$$

where $E(f)$ is the Fourier transform of $e(t)$, and the last result is valid if the feedback gain G is made sufficiently large. If the input SNR is high, it is evident from the equations that the system will equalize the spectrum of the total input signal while simultaneously performing a correlation with the reference signal, $s(t)$.

Identifying $|N(f)|^2$ as the power spectrum of the noise, Eq. 2.15 is the matched filter result [22]. Thus, from Eqs. 2.12 and 2.15, both active and passive processors share the common property of suppressing strong narrowband components that are present in the input signal. This property, commonly called *line cancellation*, is suitable in environments where sinusoidal jammers are present for either estimation or detection of broadband spread spectrum signals.

References for Chapter 2

[1] A. P. Appelbaum, "Adaptive arrays," *IEEE Trans. Antennas. Prop.*, **AP-24**, p.585 (1976).

[2] B. Widrow, P. E. Mantey, L. J. Griffiths, and B. B. Goode, "Adaptive antenna systems," *Proc.IEEE*, **55**, 2143 (1976).

[3] K. K. Scott, "Transversal filter techniques for adaptive array applications," *Proc.IEE*, **130**, Parts F+H, 29 (Feb. 1983).

[4] R. Riegler and R. Compton, Jr., "An adaptive array for interference rejection," *Proc.IEEE*, **61**, 748 (1973).

[5] R. W. Lucky, "Adaptive redundancy removal in data transmission," *Bell Syst. Tech. J.*, **47**, 549 (1968).

[6] M. M. Sondhi, "An adaptive echo canceller," *Bell Syst. Tech. J.*, **46**, 497 (1967).

[7] B. Widrow, *et al.*, "Adaptive noise cancelling: principles and applications," *Proc. IEEE*, **63**, 1692 (1975).

[8] D. R. Morgan and S. E. Craig, "Real time adaptive linear prediction using the least mean square gradient algorithm," *IEEE Trans. Acoust., Speech, Sig. Process.*, **ASSP-24**, 494 (1976).

[9] J. E. Bowers, G. S. Kino, D. Behar, and H. Olaisen, "Adaptive deconvolution using SAW storage correlators," *IEEE Trans. Microwave Theory Tech.*, **MTT-29**, 491 (1981).

[10] L. J. Griffiths, "Rapid measurement of instantaneous frequency," *IEEE Trans. Acoust., Speech, Signal Process.*, **ASSP-23**, 209 (1975).

[11] A. Papoulis, *Probability, Random Variables, Stochastic Processes*, McGraw-Hill, New York, 1965.

[12] M. White, I. A. Mack, G. M. Borsuk, D. R. Lampe, and F. J. Kub, "CCD adaptive discrete analog signal processing," *IEEE J. Solid State Circuits*, **SC-14**, 132 (1979).

[13] C. F. N. Cowan, J. W. Arthur, J. Mavor, and P. B. Denyer, "CCD based adaptive filters: realization and analysis," *IEEE Trans. Acoust., Speech, Signal Process.*, **ASSP-29**, 220 (1981).

[14] D. Psaltis *et al.*, "Iterative color-multiplexed electro-optical processor," *Opt. Lett*, **4**, 348 (1979).

[15] D. Psaltis *et al.*, "Iterative optical processor for adaptive phase array radar applications," *Proc. Soc. Photo-Opt. Instrum. Eng.*, **180**, 114 (1979).

[16] J. F. Rhodes, "Adaptive filter with a time-domain implementation using correlation cancellation loops," *Appl. Opt.*, **22**, 282 (1983).

[17] A. VanderLugt, "Adaptive optical processor," *Appl. Opt.*, **21**, 4005 (1982).

[18] J. N. Lee, N. J. Berg, and P. S. Brody, "High speed adaptive filtering and reconstruction of broadband signals using acousto-optic techniques," *Proc. Ultrasonics Symposium*, , 488 (1980).

[19] Rosenblatt, F., *Principles of Neurodynamics: Perceptrons and the theory of brain mechanisms*, Spartan Books, Washington D. C., 1962.

[20] B. Widrow and S. D. Stearns, *Adaptive Signals Processing*, Prentice-Hall Inc., Englewood Cliffs, N. J., 1985.

[21] J. Makhoul, "Linear prediction: a tutorial review," *Proc. IEEE*, **63**, no.4, 561 (April 1975).

[22] W. Davenport and W. Root, *Introduction to the Theory of Random Signals and Noise*, McGraw-Hill, New York, 1967.

Chapter 3. Optical Adaptive Systems

3.1 Space Integrating Adaptive Filters

3.1.1 Space integrating convolver and correlator

The two adaptive filters described in the previous section are both implemented with a convolver and a correlator. There are several ways to implement an optical correlator/convolver. In selecting an implementation that is best suited for this application, we must consider the following requirements: a)The optical filters should be capable of processing broadband signals (1 GHz bandwidth) to be applicable to spread spectrum systems. This requirement suggests an acousto-optic implementation. b)The impulse response of the convolver and the correlator must be dynamically controllable. The impulse response of the correlator, in particular, is also a broadband signal. c)The two filters must be compatible with one another; the impulse response of the convolver is determined by the output of the correlator, and the output of the convolver is one of the inputs to the correlator. d)We must select architectures that have the highest linear dynamic range possible. Adaptive filters are typically used to process signals with very low SNRs; this implies that they must have sufficiently high dynamic range to place very deep nulls at the frequencies where the interference occurs in order to suppress it effectively. Space integrating convolvers that use AODs are attractive for such applications because coherent architectures exist where the input as well as the output can be a broadband signal.

The acousto-optic space-integrating convolver, consisting of two AODs with counter propagating signals, an integrating lens, and a single high speed detector, is well suited for this application in that its two inputs and the output are broadband electrical signals, and a very high dynamic range is possible. One potential difficulty in using this implementation is that the output of the convolver is time-compressed by a factor of two, and thus it cannnot be directly correlated with the input signal as required for adaptive filtering. A second problem is that correlation cannot be readily performed with this architecture; one of the input signals must be time-reversed before it is applied to the convolver in order to compute correlations with such a system. These two problems combine to provide a solution in this case. We will show that a space-integrating correlator can be implemented with two AODs with signals propagating in the same direction if one of the inputs to the correlator is time-compressed by a factor of two. The output of the space-integrating convolver can thus be used as one of the inputs to such a correlator.

Before exploring the AO implementations further, a basic description of the AODs to be used is now given [1]. Shown in Fig. 3.1 is a typical AOD that consists of an acousto-optic crystal, a transducer that couples electrical energy into acoustic waves in the crystal, and an impedance-matching network to properly tailor the input electrical impedance to external signal sources. When a radio

frequency signal is applied to the device, the transducer launches an acoustic wave across the crystal, and the periodic local compression and expansion caused

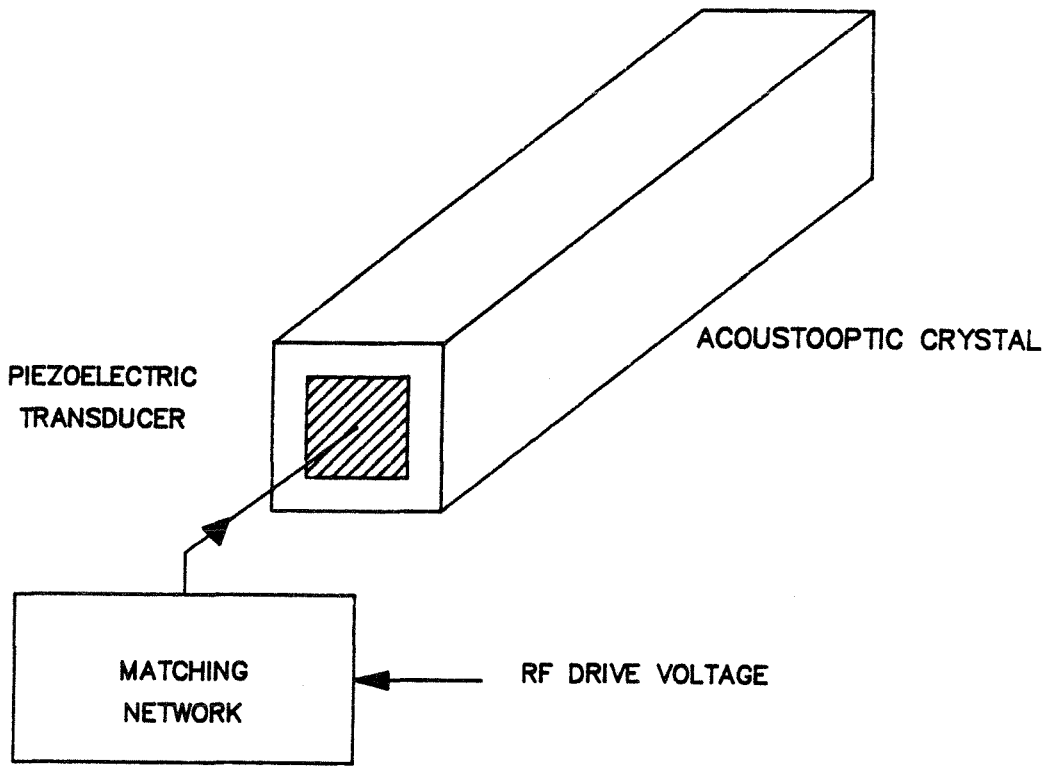

Fig. 3.1 Typical Acousto-optic Device

by the propagating wave induce a travelling optical index grating to appear in the crystal via the photoelastic effect. Usually, an acoustic absorber is placed at the end of the device so that reflections are suppressed and only the forward travelling wave is present in the crystal.

A collimated beam of light that illuminates the crystal perpendicular to the propagation direction of the acoustic beam is diffracted by the moving index grating into various orders. If the crystal is sufficiently thick, then the AOD can be rotated slightly to match the input optical beam to the desired diffracted order. The optical frequency of the diffracted orders are Doppler-shifted up for the $(+1)$ order and down for the (-1) order by f_0, the radio frequency of the electrical input to the device. For analytical modeling of the device, let $s(t) = a(t)cos\big(2\pi f_0 t + \phi(t)\big)$ represent the electrical signal applied to the AOD. The signal can be represented by its complex envelope $\mathrm{a}(t) = a(t)exp[j\phi(t)]$ from which the real signal is recovered by $s(t) = Re\big[\mathrm{a}(t)exp(j2\pi f_0 t)\big]$. The applied electrical signal induces a strain field whose amplitude is proportional to

$$s(t - x/v - T/2)rect[x/W] = \frac{1}{2}\{\mathrm{a}(t - x/v - T/2)exp[j2\pi f_0(t - x/v - T/2)] + \mathrm{a}^*(t - x/v - T/2)exp[-j2\pi f_0(t - x/v - T/2)]rect[x/W]\}, \tag{3.1}$$

where v is the speed of sound in the crystal, W is the width of the crystal, $T = W/v$ the time it takes an acoustic disturbance to propagate the entire length of the crystal, and $x = 0$ at the center of the cell. As shown in Fig. 3.2, the crystal is

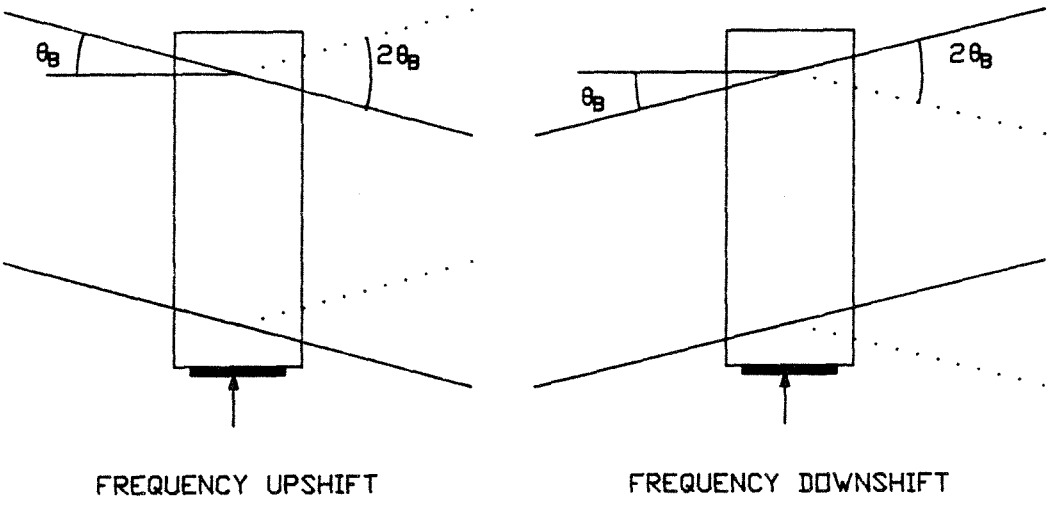

Fig. 3.2 Acousto-optic Diffraction Geometries

illuminated by a collimated coherent light beam incident at the Bragg angle θ_B given by

$$sin(\theta_B) = \lambda f_0/2v, \tag{3.2}$$

where λ is the wavelength of the light in the crystal. This geometry results in a diffracted beam whose amplitude is proportional to the first term of Eq. 3.1, where the Doppler frequency shift is positive.

If the AOD is slightly rotated so that the light is incident at an angle $-\theta_B$, then the diffracted beam is due to the second term of Eq. 3.1 with a negative Doppler shift.

We now consider the space-integrating AO convolver shown in Fig. 3.3. The

first AOD is rotated so that a portion of the incoming light is diffracted into the (-1) order. For weak modulation, the optical field at the exit plane of AOD1 is given by [1]

$$\begin{aligned} A_1(x,t) \propto & \{exp(-j2\pi sin\theta_B x/\lambda) + j(m/2)\mathrm{a}_1^*(t - x/v - T/2) \\ & exp[-j2\pi f_0(t - x/v - T/2)]exp(-j2\pi sin\theta_B x/\lambda)\}rect(x/W) \\ \propto & [exp(-j2\pi sin\theta_B x/\lambda) + j(m/2)\mathrm{a}_1^*(t - x/v - T/2) \\ & exp(-j2\pi f_0 t)exp(j2\pi sin\theta_B x/\lambda)]rect(x/W), \end{aligned} \tag{3.3}$$

where m is a constant, x is along the direction of the acoustic wave propagation, and W is the aperture size of the AOD. Note that the Bragg condition, Eq. 3.2, was used to derive the last line of Eq. 3.3.

The first term on the right-hand side of Eq. 3.3 corresponds to the DC or undiffracted light, which is unmodulated to first order. The second term corresponds to the (-1) diffracted order, which is modulated by $\mathrm{a}_1^*(t - x/v - T/2)$, Doppler-shifted by $-f_0$, and deflected by an angle $2\theta_B$. The amplitude distribution $A_1(x,t)$ is then imaged onto the second AOD by lenses L1 and L2; the imaging reverses the spatial cooordinate x. The second AOD is positioned at the Bragg angle with respect to the DC component from AOD1, and therefore a portion of it is diffracted at an angle $2\theta_B$ by AOD2. The major portion of the diffracted beam from AOD1 passes through AOD2 unaffected, since it is not Bragg-matched, and it propagates in the same direction as the beam diffracted by AOD2. The remaining components of the light at the exit of AOD2 are angularly separated from these two components

and, therefore, can be blocked at the focal plane of lens L3. The two components of interests are given by

$$A_2(x,t) \propto \big[\mathbf{a}_2(t - x/v - T/2)exp(-j2\pi sin\theta_B x/\lambda)exp(j2\pi f_0 t) + \mathbf{a}_1^*(t + x/v - T/2)exp(-j2\pi sin\theta_B x/\lambda)exp(-j2\pi f_0 t)\big] rect(x/W). \tag{3.4}$$

The first term on the right-hand side is the (+1) diffracted order term from AOD2, which is modulated by $\mathbf{a}_2(t - x/v - T/v)$, Doppler-shifted by f_0, and deflected from the DC beam by $2\theta_B$; this beam is collinear with the (-1) diffracted beam from AOD1 (i.e., the second term in Eq. 3.4). The light amplitude at the back focal plane of lens L3 is the Fourier transform of $A_2(x,t)$. A detector with an active area sufficiently large to integrate the entire transform is placed at the Fourier plane, and the resulting photocurrent is

$$\begin{aligned} I_1(t) &\propto \int_{-\infty}^{\infty} \Big| \int_{-T/2}^{T/2} [\mathbf{a}_1(t + \tau - T/2)exp(j2\pi f_0 t) \\ &\qquad + \mathbf{a}_2^*(t - \tau - T/2)exp(-j2\pi f_0 t)]exp[-jk\tau)d\tau\Big|^2 dk \\ &\propto \int_{-T/2}^{T/2} |\mathbf{a}_1(t + \tau - T/2)|^2 d\tau + \int_{-T/2}^{T/2} |\mathbf{a}_2(t - \tau - T/2)|^2 d\tau \\ &\qquad + 2Re\Big\{exp(j4\pi f_0 t) \int_{-T/2}^{T/2} \mathbf{a}_1(t + \tau - T/2)\mathbf{a}_2(t - \tau - T/2)d\tau\Big\}, \end{aligned} \tag{3.5}$$

where $\tau = x/v$, $k = \frac{2\pi}{\lambda F} v x'$, F is the focal length of the Fourier transform lens, and x' is the spatial variable on the detector plane.

The first two terms on the right side are low frequency components which are removed by electronically high pass filtering the output signal. The third term is

the desired operation, which is the convolution of $\mathbf{a}_1(t)$ and $\mathbf{a}_2(t)$. The convolution is compressed in time by a factor of two and translated to twice the original carrier frequency. Notice that in both passive and active processors, the time-compressed output of the convolver is one of the inputs to the correlator. Thus, the correlator must be designed to accept a time-compressed signal in one of its input ports.

Shown in Fig. 3.4 is a photograph of the laboratory set up of the space integrating convolver just described. The two AODs used employ flint glass as the acousto-optic medium and operate at 70 MHz center frequency with 50 MHz bandwidth. Each AOD is 3.9 cm wide, and the total access time is approximately $T = 10\ \mu secs$ [2].

The light is detected by an avalanche photodiode whose bandwidth exceeds 100 MHz. The input signals modulate the center frequency of the convolver, which is chosen to be 45 MHz, since its output appears on a carrier of twice the frequency and must be within the bandwidth of the AOD in the correlator. Fig. 3.5a is an oscilloscope trace of the input carrier (top) and the output carrier from the detector (bottom). The convolver was tested by using a square wave modulation (biphase) at $f_s = 1$ MHz as the input to both AODs; Fig. 3.5b shows the square wave in the upper trace and the actual rf signal that drives the AODs in the lower trace. The expected triangle modulated output, having taken the time compression property into account, is shown in Fig. 3.5c.

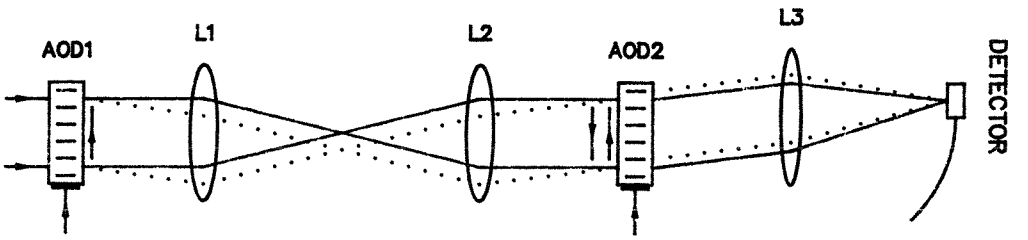

Fig. 3.3 Acousto-optic Space Integrating Convolver

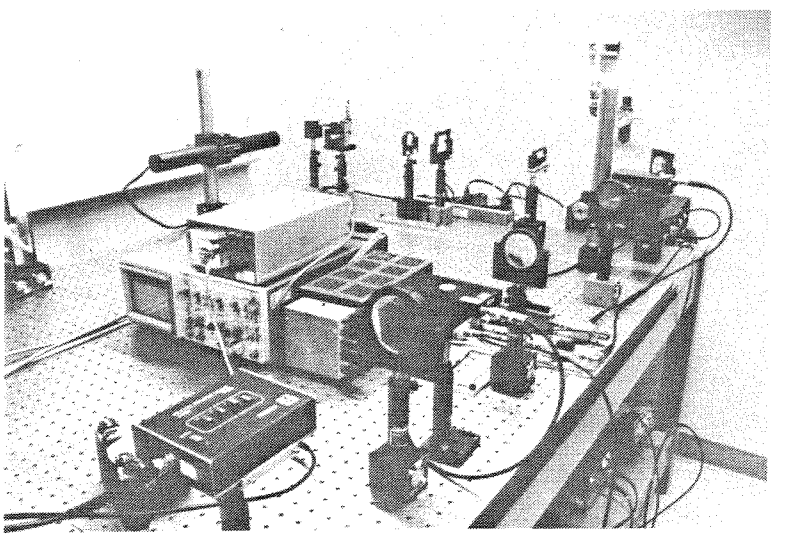

Fig. 3.4 Laboratory Setup of Convolver

In contrast to convolution, which requires an inversion of a coordinate, correlation requires that one of the input signals be in motion with respect to the other with no coordinate inversion. Referring to Fig. 3.6, the correlator consists of two identical AODs with counter-propagating acoustic signals; f_0 and $2f_0$ are the carrier frequencies of the signals driving AOD3 and AOD4, respectively. The imaging system reverses the spatial coordinate of the signal in AOD3, so that the two signals are copropagating at AOD4. The imaging system has a 2:1 demagnification ratio, so that the velocity of the image of the light that is diffracted by AOD3 is half that of the acoustic signal in AOD4. Thus the signals in the AODs continuously translate with respect to each other. The undiffracted beam from AOD3 is incident at the Bragg angle of AOD4 corresponding to its $2f_0$ center frequency. The demagnification by a factor of 2 increases the angular separation between the diffracted and undiffracted beams from AOD3 at the plane of AOD4. Therefore, the two diffracted beams from AOD3 and AOD4 are parallel to one another when they enter lens L6. L6 forms the Fourier transform of the light exiting AOD4, and a photodetector spatially integrates the entire spectrum.

Through a development similar to that illustrated for the convolver, we find that the photocurrent from the detector in Fig. 3.6 is

$$I_2(t) \propto \int_{-T/4}^{T/4} |\mathrm{a}_1(t+2\tau-T/2)|^2 d\tau + \int_{-T/4}^{T/4} |\mathrm{a}_2(t+\tau-T/4)|^2 d\tau + 2Re\Big\{exp(j2\pi f_0 t) \int_{-T/4}^{T/4} \mathrm{a}_1^*(t+2\tau-T/2)\mathrm{a}_2(t+\tau-T/4)d\tau\Big\}. \tag{3.6}$$

The limits of integration of the correlator are half those of the convolver. This implies that the apertures of the AODs used in the correlator must be twice as long as those in the convolver to obtain equal integration limits. Unilluminated portions of the AODs in the correlator and the convolver can be used for introducing delays. The third term is the desired operation, which resembles a correlation translated to the carrier frequency f_0. If $\mathbf{a}_2(t) = \mathbf{a}_3(2t)$, the correlation term of Eq. 3.6 becomes

$$corr = 2Re\big[exp(j2\pi f_0 t) \int_{t-T}^{t} \mathbf{a}_1^*(\alpha)\mathbf{a}_3(t+\alpha+T/4)d\alpha\big], \tag{3.7}$$

which is a finite aperture correlation of the signals $\mathbf{a}_1(t)$ and $\mathbf{a}_3(t)$ placed on the carrier frequency f_0.

Shown in Fig. 3.7 is a photograph of the laboratory setup of the space-integrating correlator just described. The AODs are identical to those used for the convolver implementation, as is the detector. The three-lens telescope is adjusted to yield a demagnifying factor of two in imaging the first AOD onto the second. To test this system, two carrier frequencies are necessary, since the second AOD must be driven at twice the frequency of the first. Fig. 3.8 shows the correlation between a periodic frequency chirped signal and an unmodulated carrier. The frequency of the signal in the first AOD is swept from 43 MHz to 49 MHz in an interval of 100 msecs, and the interval is repeated every 300 msecs; the second AOD is driven by an unmodulated sinusoid at 90 MHz. The output trace shows the expected correlation result at the difference carrier frequency of 45 MHz.

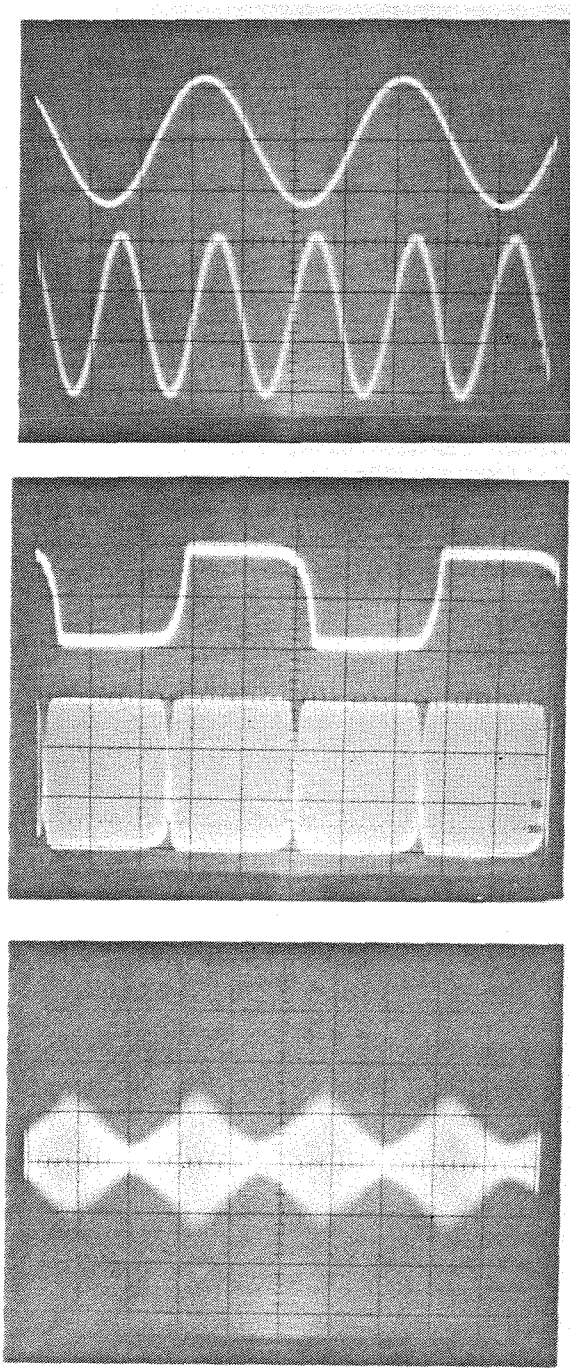

Fig. 3.5 Space-Integrating Convolution Results **a**)45 MHz input carrier (upper trace) and 90 MHz output carrier (lower trace)(5 nsec/div); **b**)1 MHz square wave (upper) and actual rf input to AODs (lower) (200 nsec/div); **c**)convolution output (100 nsec/div)

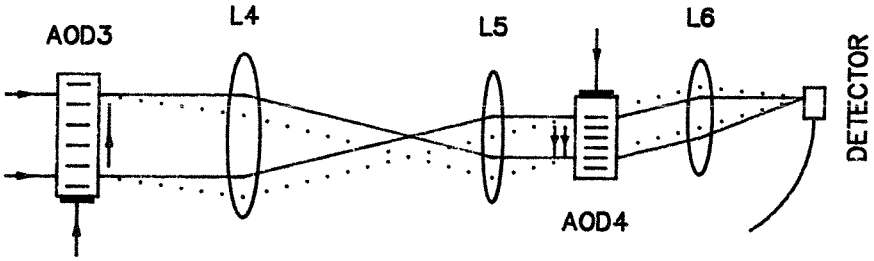

Fig. 3.6 Acousto-optic Space-Integrating Correlator

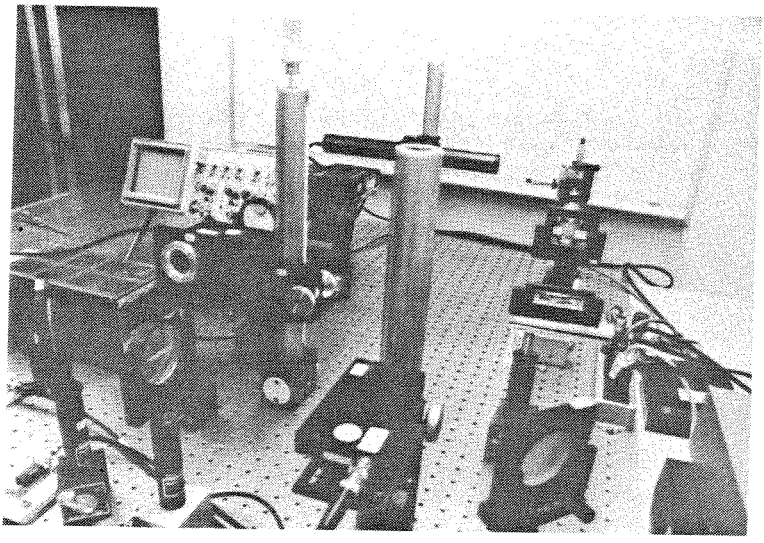

Fig. 3.7 Laboratory Setup of Correlator

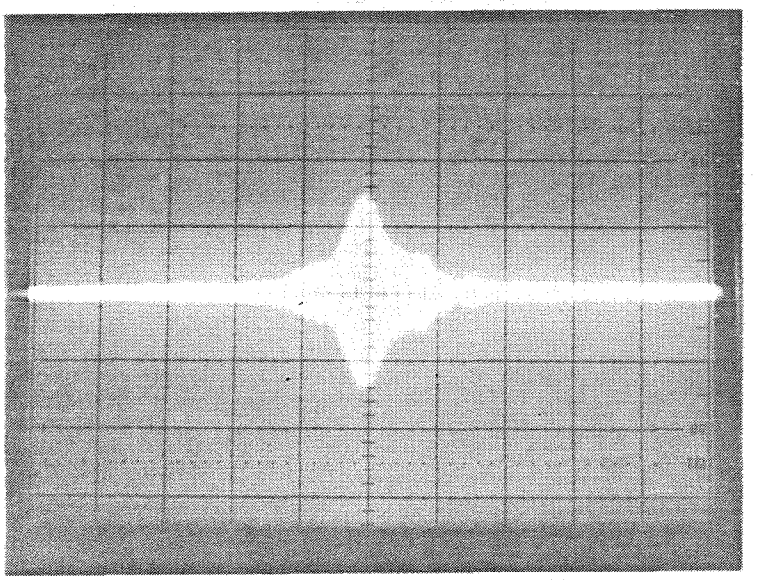

Fig. 3.8 Correlation of Frequency Chirped Signal and a Sinusoid: Bandwidth of chirp is 6 MHz centered at 46 MHz and 100 msecs. long. Sinusoid in second AOD has f_0=90 MHz.

3.1.2 Description of implementation

The outputs of the space-integrating convolver and correlator without the carrier terms are, from Eqs. 2.5 and 2.6,

$$\begin{aligned} \textit{convolution} : u(t) &= \frac{c_1}{T}\int_{-T/2}^{T/2} \mathbf{a}_1(t+\tau-T/2)\mathbf{a}_2(t-\tau-T/2)d\tau \\ \textit{correlation} : w(t) &= \frac{2c_2}{T}\int_{-T/4}^{T/4} \mathbf{a}_1^*(t+2\tau-T/2)\mathbf{a}_2(t+\tau-T/4)d\tau, \end{aligned} \tag{3.8}$$

where the signals $\mathbf{a}_1(t)$ and $\mathbf{a}_2(t)$ are the complex envelopes of the actual voltages that drive the AODs, and $u(t)$ and $w(t)$ are the voltages that appear at the outputs of the photodetectors. The constants c_1 and c_2 depend on the laser power, AOD diffraction efficiencies, and the quantum efficiencies of the detectors. Note that

from the instant that the two signals are applied to the convolver, a delay of $T/2$ is effected until an output appears. The correlator likewise has a delay of $T/4$ before an output appears after the application of its input signals. These delays must be carefully controlled to avoid phase dispersion within the system, as the following arguments demonstrate. If the passive processor of Fig. 2.6 is implemented with the above equations, the system output can be described by

$$\begin{aligned} z(t) =& x(t) - \frac{2Gc_1c_2}{T^2}\int_{-T/4}^{T/4}\int_{-T/2}^{T/2} x^*(t+2\beta-T/2) \\ & x(t+\tau-3T/4+\beta)z(t-\tau-3T/4+\beta)d\tau d\beta, \end{aligned} \tag{3.9}$$

where $x(t)$ is the complex envelope of the input to the system. For a monochromatic input $x(t) = Aexp(j2\pi f't)$, the output response can be shown to be

$$z(t) = \frac{x(t)}{1 + Gc_1c_2exp[-j2\pi f'T/2]}, \tag{3.10}$$

The dispersive phase factor in the denominator depends upon the frequency of the input signal. Because of the delays in the convolver and correlator, this will lead to instabilities that preclude the possibility for nulling of the input jammer.

The delays cannot be eliminated entirely from the convolver but they are controllable by simply translating the AODs in the directions of the acoustic propagation in the devices. Indeed, we can minimize the effects of the delays by adopting the modified convolver and correlator blocks shown in Fig. 3.9, whose AODs have been translated effect the delay modifications. The modified convolver and correlator are

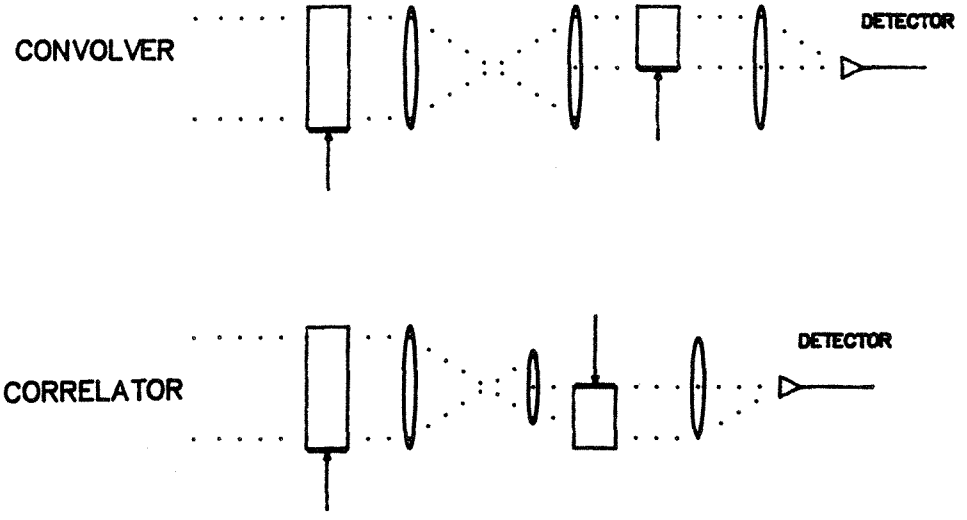

Fig. 3.9 Delay Modified Convolver and Correlator

described respectively by the equations:

$$\begin{aligned} convolution : u(t) &= \frac{2c_1}{T}\int_0^{T/2} \mathrm{a}_1(t+\tau-T/2)\mathrm{a}_2(t-\tau)d\tau \\ correlation : w(t) &= \frac{4c_2}{T}\int_{-T/4}^{0} \mathrm{a}_1^*(t+2\tau-T/2)\mathrm{a}_2(t+\tau)d\tau, \end{aligned} \tag{3.11}$$

where the apertures of the convolver and correlator have been halved to accommodate the delay changes.

A schematic diagram of the optical passive processor using these convolution and correlation blocks is shown in Fig. 3.10. Through the use of a beam splitter, both the convolver and the correlator have been incorporated into one system requiring only one light source and three AODs. The correlator and the convolver share the AOD, which is driven by the system input signal $x(t)$. The input signal,

translated in frequency by f_0, is applied to AOD1 and the summing node before entering AOD2. The convolution is performed by the lower leg of the processor and the correlation by the upper leg. As shown in the previous section, the optical convolver takes its two inputs, each at the carrier frequency f_0, and gives their convolution as its output compressed in time by a factor of two and shifted in frequency by $2f_0$. This output is amplified and used to drive AOD3 of the correlator. Recalling that, to achieve a proper correlation, one of the correlator inputs must be time-compressed by a factor of two and translated to $2f_0$, we see that its ouptut is free of time-scaling problems. This signal is then subtracted from the input signal to form the system output $z(t)$, which is fed back to the convolver via AOD2.

With Eqs. 2.11, the input-output equation of the passive processor is

$$z(t) = x(t) - \frac{8Gc_1c_2}{T^2} \int_{-T/4}^{0} \int_{0}^{T/2} x^*(t+2\beta-T/2)x(t+\beta+\tau-T/2)z(t+\beta-\tau)d\tau d\beta, \tag{3.12}$$

which for low input SNR conditions can be approximated by

$$z(t) = x(t) - \frac{8Gc_1c_2}{T^2} \int_{-T/4}^{0} \int_{0}^{T/2} n^*(t+2\beta-T/2)n(t+\beta+\tau-T/2)z(t+\beta-\tau)d\tau d\beta. \tag{3.13}$$

An approximate solution to the above equation can be derived by the use of Fourier transforms. Using the Fourier integral representations

$$x(t) = \int_{-\infty}^{\infty} X(f)exp(j2\pi ft)df,$$

$$n(t) = \int_{-\infty}^{\infty} N(f)exp(j2\pi ft)df,$$

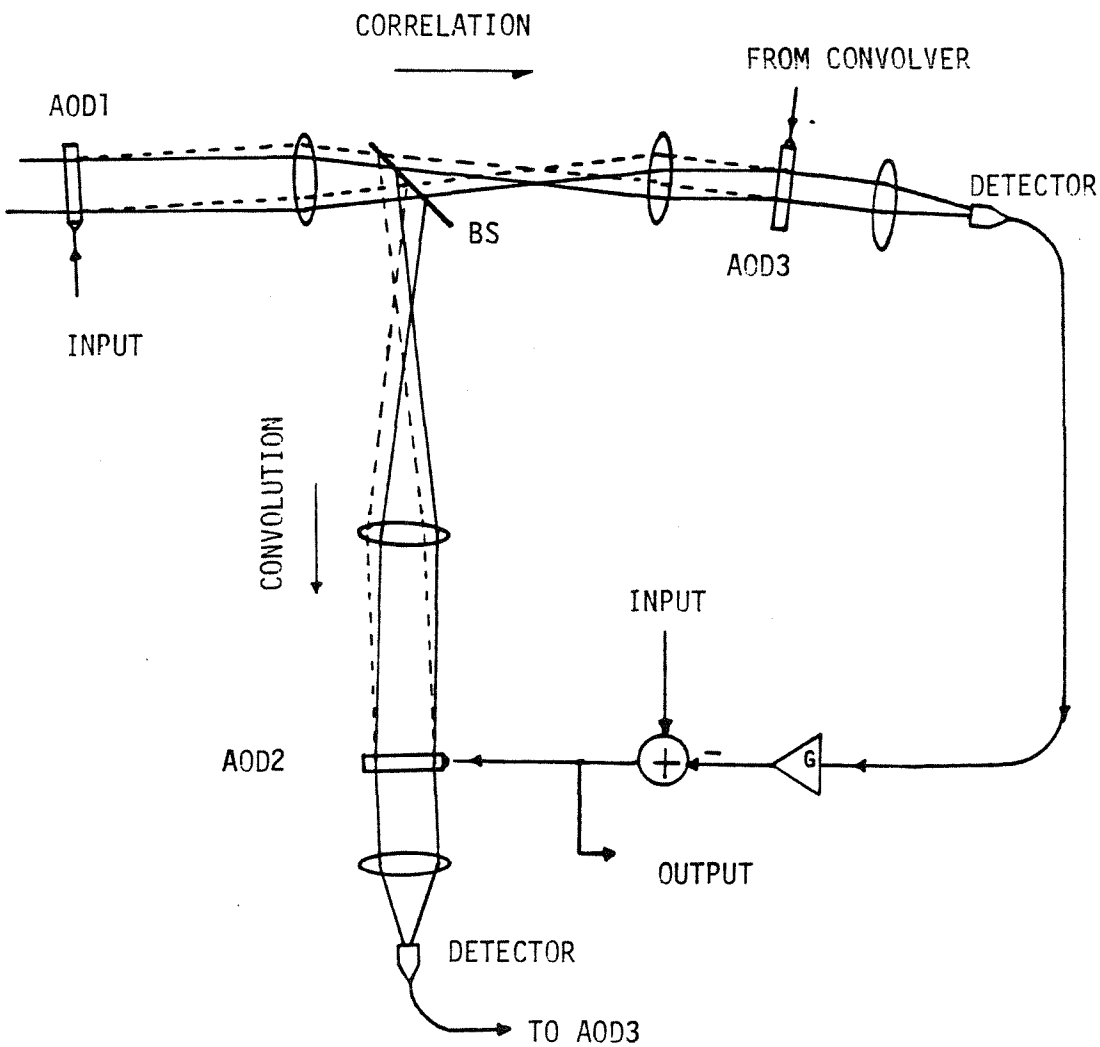

Fig. 3.10 Optical Passive Processor

the Fourier transform of Eq. 3.27 can be shown to be

$$Z(f) = X(f) - Gc_1c_2 \int \int_{-\infty}^{\infty} N^*(f_1)N(f_2)Z(f + f_1 - f_2)$$
$$exp[-j\pi(f - f_1)T/4]exp[-j\pi(f + f_1 - 2f_2)T/2] \quad (3.14)$$
$$sinc[(f - f_1)T/4]sinc[(f + f_1 - 2f_2)T/2]df_1df_2.$$

The double integral can be approximated by a single integral, since it is appreciably large only near the region $f_1 = f_2$, so that

$$Z(f) \approx \frac{X(f)}{1 + Gc_1c_2 \int_{-\infty}^{\infty} |N(f_1)|^2 K(f - f_1)df_1}, \quad (3.15)$$
$$K(f) \equiv exp[-j3\pi fT/4]sinc[fT/4]sinc[fT/2].$$

Except for the convolution with the $sinc(.)$ functions with the phase factors, the above result is similar to the optimum Wiener result discussed in 2.3. The particular form of the smoothing kernel derives from the fact that the system is causal and can view only present and past data, and information is accumulated through finite sized windows. The same smoothed spectral estimate can be obtained by taking the Fourier transform of the product of the autocorrelation function of $x(t)$ and the causal window shown in Fig. 3.11.

The optically implemented active processor is shown schematically in Fig. 3.12 and differs from the passive system only in its electrical interconnections. Here the output of the system is a time-compressed signal since it is taken at the output of the convolver; this presents no problems since the output signal is a correlation peak, and we are interested in signal detection rather than estimation. As in the passive case, the convolver output drives AOD3 of the correlator.

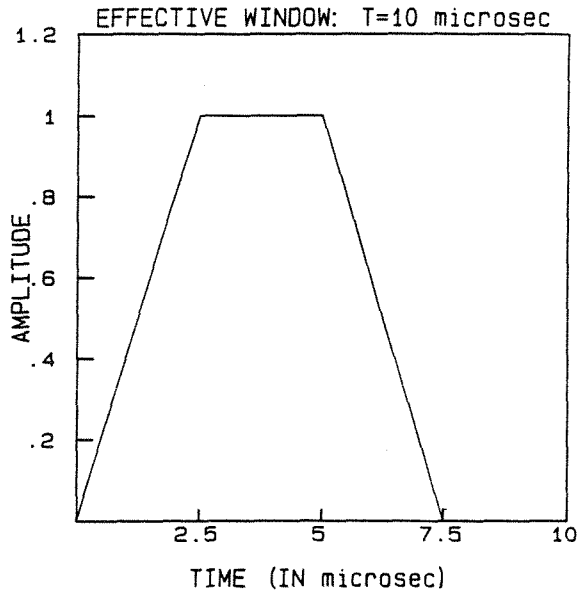

Fig. 3.11 Effective Windowing Function

The correlator output is then subtracted from the time-reversed reference signal (the matched filter impulse response) to form the input to AOD2 of the convolver; note that even though the output is time-compressed, the time scaling is compatible for all the signals within the system. To see this more precisely, we examine the input-output equation for the active system. Using Eqs. 3.11, we obtain

$$e(t) \approx \frac{2c_1}{T}\int_0^{T/2} x(t+\tau-T/2)s^*(\tau-t)d\tau$$
$$-\frac{8Gc_1c_2}{T^2}\int_0^{T/2}\int_{-T/4}^{0} n(t+\tau-T/2)n^*(t-\tau+2\beta-T/2)e(t-\tau+\beta)d\beta. \tag{3.16}$$

Here we have already used the approximation appropriate for low input SNR, and $S(f)$ is the Fourier transform of the signal that is to be detected. Fourier transformation along with the integration approximation used for the passive system leads

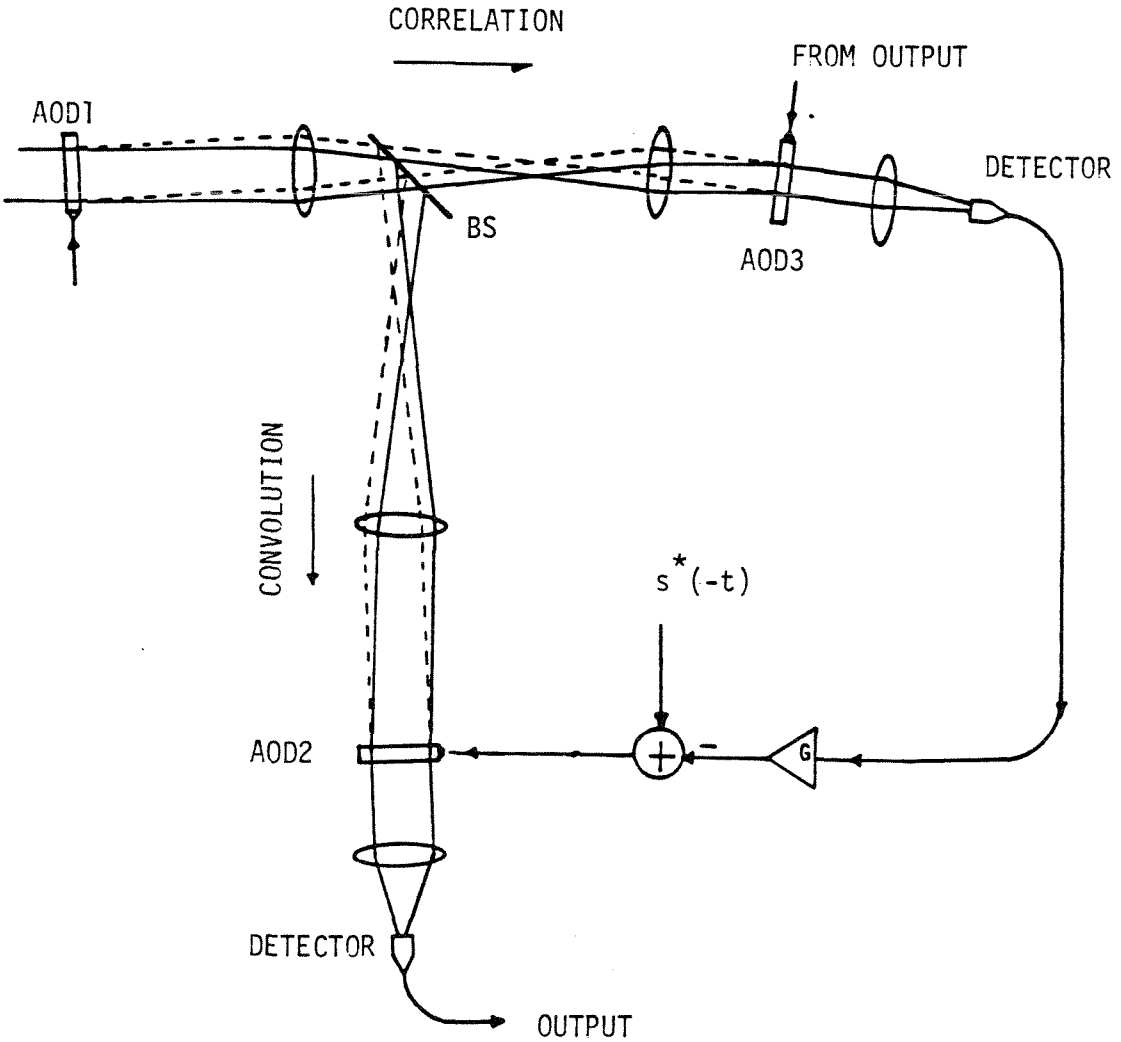

Fig. 3.12 Optical Active Processor

to the following equation for the output:

$$E(f) \approx \frac{c_1 exp(-j\pi fT) \int_{-\infty}^{\infty} X(f_1) S^*(f - f_1) sinc[(f - 2f_1)T/2] df_1}{1 + Gc_1c_2 \int_{-\infty}^{\infty} |N(f_1)|^2 K(f - f_1) df_1}, \qquad (3.17)$$

where $E(f)$ is the Fourier transform of the output signal and $K(f)$ is the smoothing function described in Eq. 3.15. Aside from the appearance of the sinc functions that arise due to the finite apertures of the AODs, time compression of the convolver, and the causality of the system, the above equation is quite similar to Eq. 2.15, the matched filter result.

3.1.3 Performance and experimental results

It is important to theoretically characterize the performance limits of the adaptive system in terms of parameters such as the AOD aperture size and detector noise to aid optimization of the system performance. In this section, three issues are discussed with regard to the passive processor: 1) the resolution with which the processor discriminates against jammers, 2) transients due to the delays in the system, 3) null depth (the level of jammer suppression) limitations due to detector noise.

The resolution of the system is characterized entirely by the size of the AOD apertures, for they determine the length of the signal sample at any one time. The effective window through which the processor forms an estimate of the jammer spectrum is not rectangular but trapezoidal as shown in Fig. 3.11. The Fourier transform of this window function (also called "apodizing function"), shown in Fig.

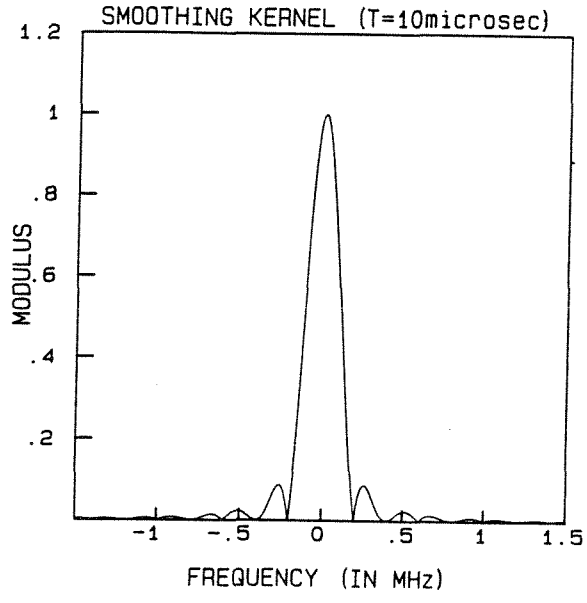

Fig. 3.13 Spectrum Smoothing Kernel: Fourier transform of effective window function

3.13, determines the frequency resolution of the system, and the sidelobe structure is due entirely to the finite apertures of the system. For AODs whose time delay is T, the minimum resolvable frequency increment is approximately $2/T$. For the flint glass AODs, the frequency increment is approximately 200 KHz.

A serious performance limitation arises from the time delays that exist in the AODs. To quantify this limitation, consider a purely monochromatic input $x(t) = Aexp(j2\pi f_0 t)$. Using Eq. 3.12, the response of the passive processor can be calculated exactly. The Fourier transform of the response is given by

$$Z(f) = \frac{X(f)}{1 + Gc_1c_2A^2exp[-j3\pi(f-f_0)T/4]sinc[(f-f_0)T/4]sinc[(f-f_0)T/2]}. \tag{3.18}$$

The phase factor present in the denominator is due to the delays accumulated through the convolver and correlator. The consequence of this phase factor is that the denominator is not guaranteed to be positive for large values of the feedback gain. If the gain is sufficiently large to allow the denominator to vanish for some f, then the system will become unstable. As G is increased, the first unstable point that the system encounters is when $3(f - f_0)T/4 = \pm 1$. The critical gain at this point is given by

$$G_c c_1 c_2 A^2 = [sinc(1/3)sinc(2/3)]^{-1} = \frac{8\pi^2}{27}, \approx 2.924 \quad , \tag{3.19}$$

where G_c is the critical value of the feedback gain. The factor by which the jammer is suppressed at this critical point is

$$K = \frac{1}{1 + 8\pi^2/27} \approx .255 = -11.875dB. \tag{3.20}$$

This value of maximum suppression is verified by computer simulations of the processor response to a step input. For the simulations, the input amplitude was fixed at $A = 1$, and the system was discretized, the convolver and correlator are implemented with tapped delay lines with 40 and 20 taps, respectively. Fig. 3.14 shows the envelope of the processor response to a unit step jammer input, for $Gc_1c_2 = 1$, $Gc_1c_2 = 2$, and $Gc_1c_2 = 2.9$, which is near the unstable point. The initial constant portion of the response is due to the delays incurred before the correlator is able to form the feedback signal. Indeed, the third plot shows an oscillatory behavior, indicating marginal stability.

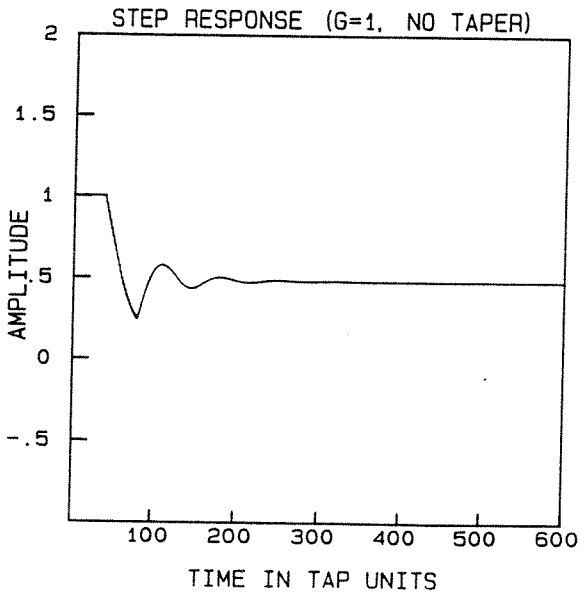

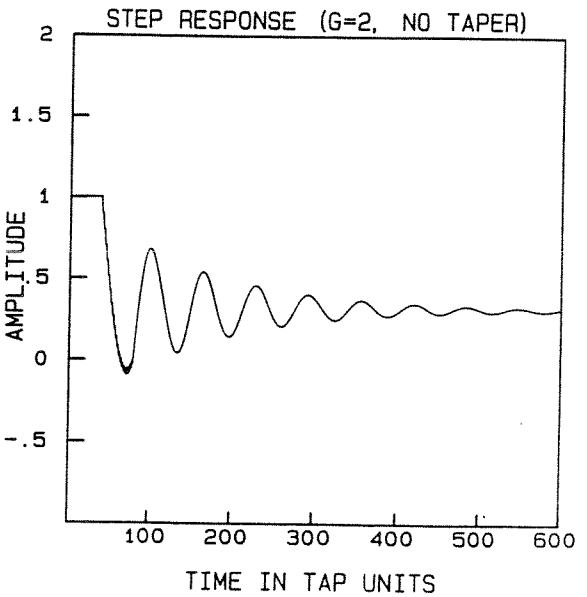

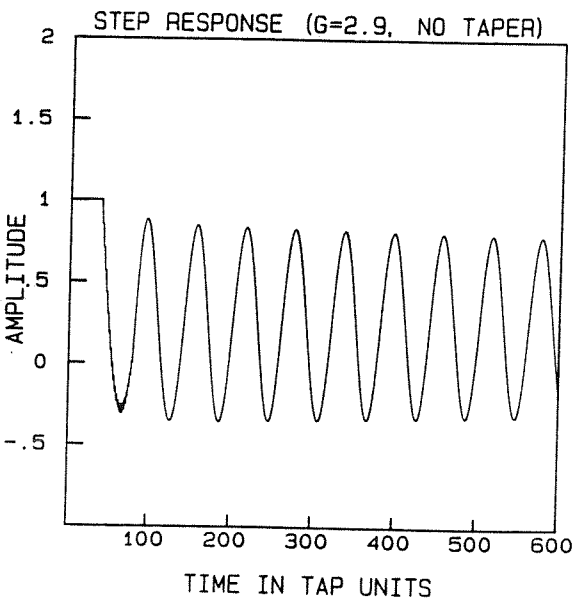

Fig. 3.14 Step Response of Passive Processor: a)Gc_1c_2=1, b)Gc_1c_2=2, c)Gc_1c_2=2.9

The low critical gain stems from the rather large sidelobes of the $sinc(.)$ functions coupled with the delay terms. At the cost of loss in resolution, the sidelobes can be reduced by apodizing the AOD windows, resulting in systems that can tolerate higher feedback gains while remaining stable. As a simple example, the improvements in suppression due to a linear tapering function are considered. Suppose a linearly tapered function is used to weight the aperture of AOD1 in the passive processor shown in Fig. 3.10 such that the most recent sample in the AOD is weighted maximally and the last sample in the AOD has zero weight. Then the system equation must be changed to

$$z(t) = x(t) - \frac{8Gc_1c_2}{T^2}\int_{-T/4}^{0}\int_{0}^{T/2} x^*(t+2\beta-T/2)x(t+\beta+\tau-T/2)z(t+\beta-\tau) \\ (1-\frac{2\tau}{T})(1+\frac{4\beta}{T})d\tau d\beta. \tag{3.21}$$

The effective window function by which the system accumulates data is trapezoidal for nonapodized AODs, as shown in Fig. 3.11. The linear weighting of the AOD aperture results in a smoother effective windowing function and consequently smaller sidelobes in its frequency response. The effectiveness of this technique is borne out by computer simulations of the step response, which are shown in Figs. 3.15a,b,c. Convergence is still rapid. Here, the suppression is improved to better than 25 dB.

The space-integrating passive processor was implemented using the flint glass AODs described previously. Shown in Fig. 3.16 is a photograph of the laboratory

setup. As in the schematic diagram, the first AOD is shared by the convolver and the correlator. Under open loop conditions, the dispersive phase delays were eliminated by carefully translating the AODs so that the feedback signal was in phase with the input signal even when the input was swept in frequency. Because of the peculiar time-compressing nature of the convolver, the useful bandwidth of the system was limited to approximately 5 MHz, much less than the AOD bandwidths.

Shown in Fig. 3.17 is a scope trace of the input sinusoid and the feedback sinusoid produced by the system at a particular frequency. The feedback phase remained locked to that of the input even when the input frequency was changed. The time delay of the step response is shown in Fig. 3.18 in which the top trace is the step sinusoid input (f_0=45 MHz) and the bottom is the delayed response of the system. The time delay is about 7.6 $\mu secs.$, which can be accounted for by the following arguments. A portion of the glass of about .7 cm in length adjacent to the transducer in each AOD was unpolished and inaccessible to the incoming light. This corresponds to a fixed time delay of about 1.8 $\mu secs.$ in each AOD. Although the total access time for each AOD was T=10 $\mu secs.$, only about 5 $\mu secs.$ of it were used. With reference to Fig. 3.9, the acoustic signals must propagate for $T/4$ before interacting to yield an output in the convolver, and $T/2$ for the correlator, so that the total time delay between the step input and response should be $3T/4$ if the AODs were ideal without inaccessible portions. To this we add the fixed delays due to the unpolished portions of the glass to predict the total delay to be

$2 \times 1.8 + .75 \times 5 = 7.35$ $\mu secs.$, where we used T =5 $\mu secs.$ This leaves a positive delay of 250 nsecs. as a discrepancy between the observed value and the predicted value, an error attributable to measurement error for the unpolished glass length and electrical delays in the system.

The maximum closed loop suppression of the single frequency input was approximately $6dB$. Shown in Figs. 3.19a,b,c are scope traces of the input jammer pulse (top trace) and the response (bottom). The first result was obtained for feedback gain below the critical value. The second picture was obtained for the gain set near the critical value and shows stable suppression of about $5.5dB$. The third picture shows the unstable operation of the system showing an output oscillation with an approximately 15 $\mu sec.$ period. Without the linear apodizing functions, the maximum suppression for this system is better than $-11dB$. The difference between this value and the observed value is due mainly to the extra time delays that arise from the inaccessible portions of the AODs. If we include an extra time delay of $\Delta = \alpha T$ in the system model, then the output response described by Eq. 3.18 must be changed to include an extra phase term $exp[-j2\pi(f - f_0)\alpha T]$ in the complex exponential term of the denominator. The total exponential phase term $exp[-j\pi(f - f_0)(.75 + 2\alpha)T]$ becomes -1 when $(.75 + 2\alpha)(f - f_0)T = \pm 1$. At this point, the gain that will drive the system to oscillations is given by

$$Gc_1c_2 = [sinc(\frac{1}{4(.75 + 2\alpha)})sinc(\frac{1}{2(.75 + 2\alpha)})]^{-1}, \qquad (3.22)$$

whose value for T =7.5 $\mu secs.$, and αT =2.6 $\mu secs.$ (the experimentally observed value) is $Gc_1c_2 \approx 1.01$. The maximum possible suppression of the jammer is therefore $K \approx -6dB$, which agrees well with the experimentally achieved value.

If apodizing techniques are used to enhance the jammer suppression capability, the noise produced by the detectors and amplifiers will become the dominant null-depth limiting factor. In order to better understand this limitation, the deterioration in the cancellation of one jammer, $x(t) = Aexp(j2\pi f_0 t)$, due to the system noise contributed by the detectors and amplifiers, is now studied. The system model depicting the noise sources is shown in Fig. 3.20, where $n_1(t)$ is the noise from the feedback amplifier, while $n_2(t)$ and $n_3(t)$ correspond to those arising from the photodetectors in the convolver and correlator, respectively. The noise processes are assumed to be independent, stationary, complex Gaussian processes [3], each with variance σ^2. Since the input is a single frequency jammer, the convolver and correlator behave as narrow-bandpass filters centered at that frequency. If the space bandwidth products of the convolver and correlator are larger than the feedback gain, the contribution of the noise sources $n_1(t)$, $n_2(t)$, filtered by the convolver and correlator, is negligible compared to $n_3(t)$, which is added directly onto the feedback signal $\hat{x}(t)$. These heuristic arguments are verified in Appendix A where the role played by $n_3(t)$ is shown to be dominant. The portions of noise that are fed back are suppressed by the correlator and convolver and can be neglected to first order. Thus, only the noise due to $n_3(t)$ appears directly at the output. We expect

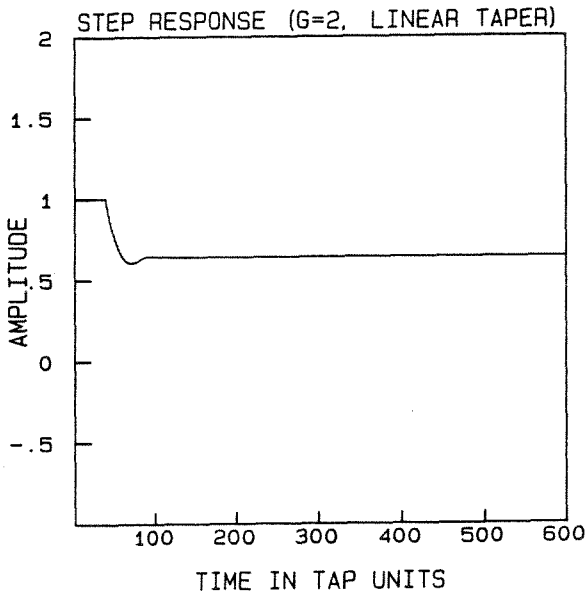

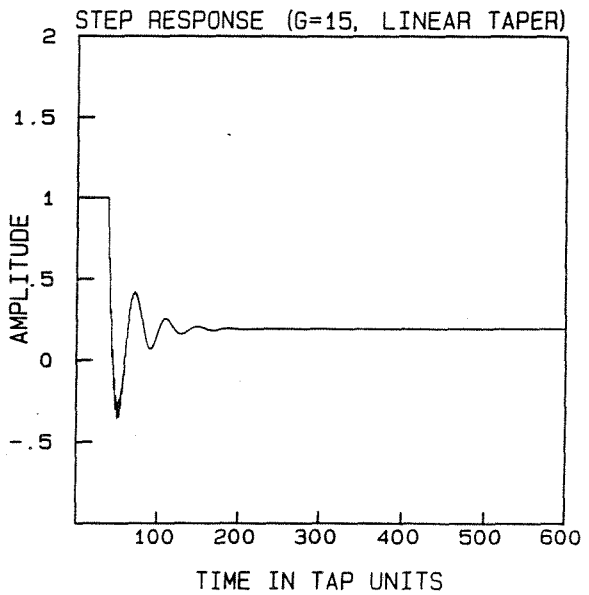

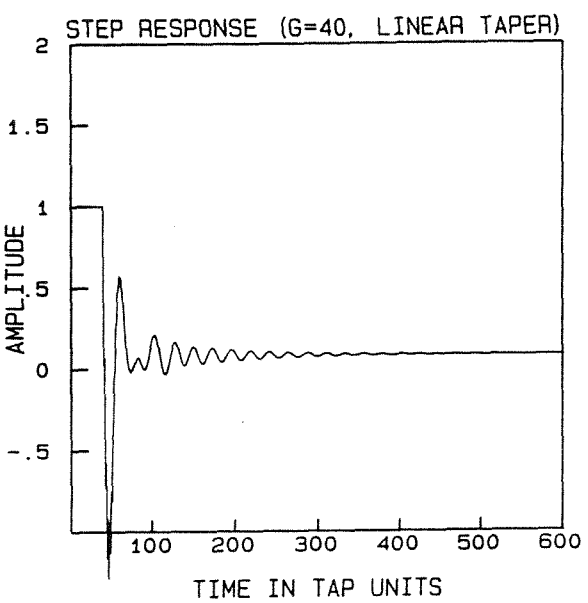

Fig. 3.15 Step Response of Passive Processor with Linearly Apodized AODs: a)Gc_1c_2=2, b)Gc_1c_2=15, c)Gc_1c_2=40

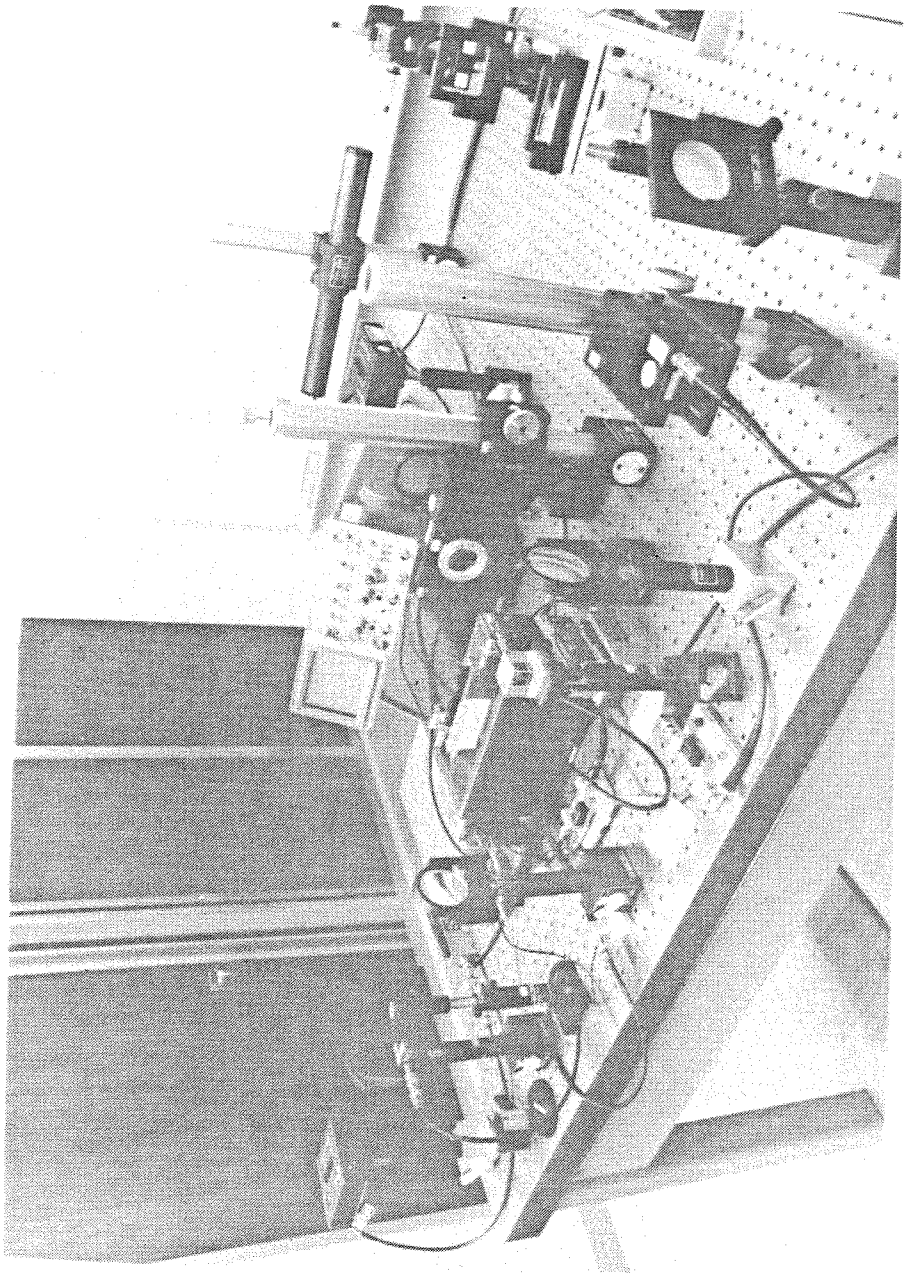

Fig. 3.16 Photograph of Laboratory Setup: Passive Processor

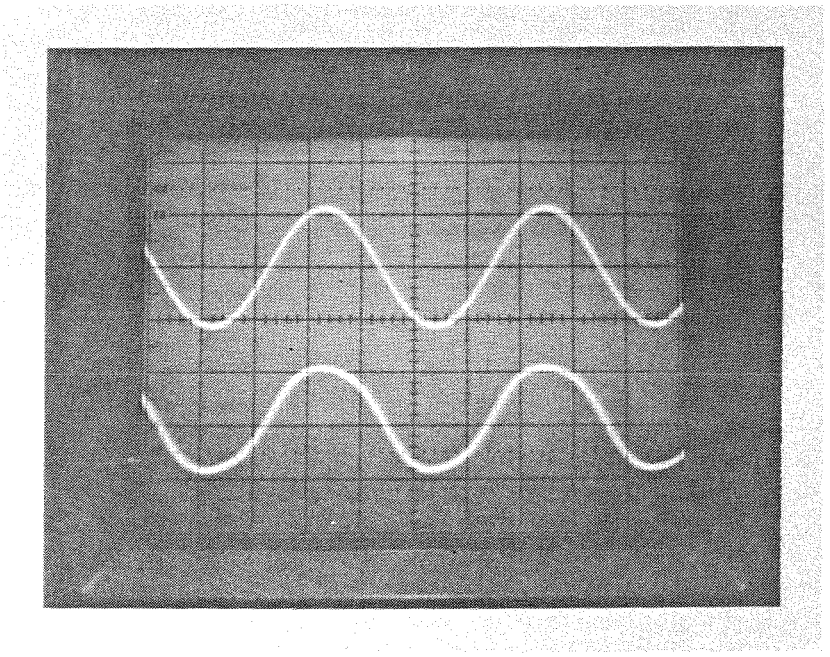

Fig. 3.17 Input Carrier and Feedback Carrier at f_0=45 MHz

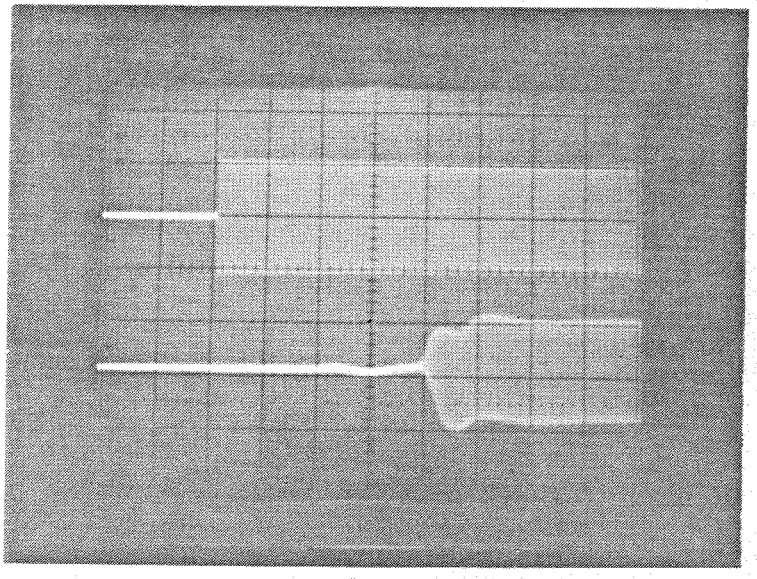

Fig. 3.18 Feedback Signal Response to Input Step (carrier at f_0=45 MHz)

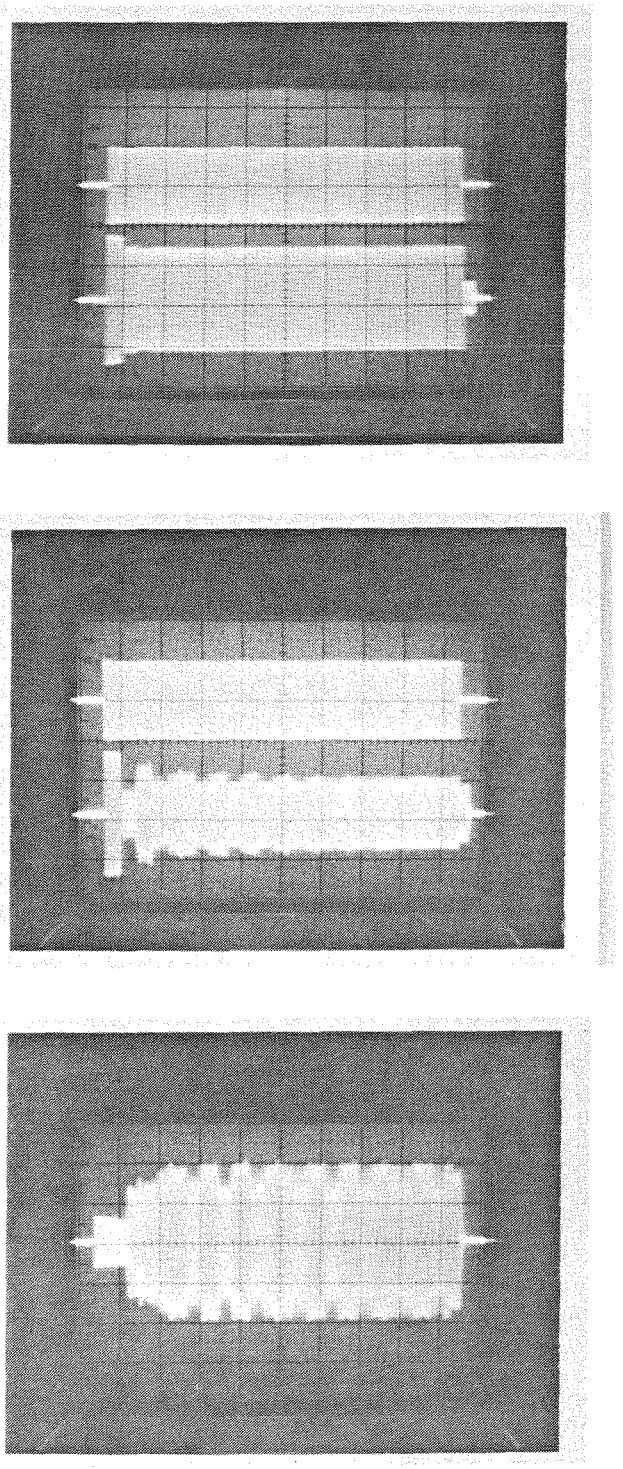

Fig. 3.19 Response of Space-Integrating Passive Processor a)overdamped, b)critically damped, c)unstable

that the performance limit set by the system noise would not be reached unless the jammer amplitude were suppressed to σ, the noise level.

3.2 Space-Time-Integrating Adaptive Filter

3.2.1 Time-integrating correlator

Although large bandwidths are possible, AODs have time apertures typically limited to less than 100 $\mu secs.$, determined by the size of the cell and the acoustic velocity. This creates a basic limitation for space-integrating correlators since the integration time is equal to the time apertures of the AODs. Time-integration is an alternative technique whereby this restriction is removed [4]. Whereas the space-integrating correlator produces an output with time as the shift variable, a time-integrating correlator produces its output as a function of space. The basic idea is illustrated by the diagrams on Figs. 3.21a and 3.21b, which show the principles of operation for both space-integration and time-integration. The AODs are represented by the tapped delay lines. As illustrated, the space-integrating convolver integrates the products of the samples in the delay line so that the maximum number of samples in the convolution sum is equal to the number of taps in each delay line. As pointed out in Section 3.1.1, this convolver is used as a correlator by feeding one of the tapped delay lines with a time reversed signal. In contrast, the time-integrating correlator of Fig. 3.21b produces the output correlation as an N-dimensional vector, where N is the number of taps in each delay line, and

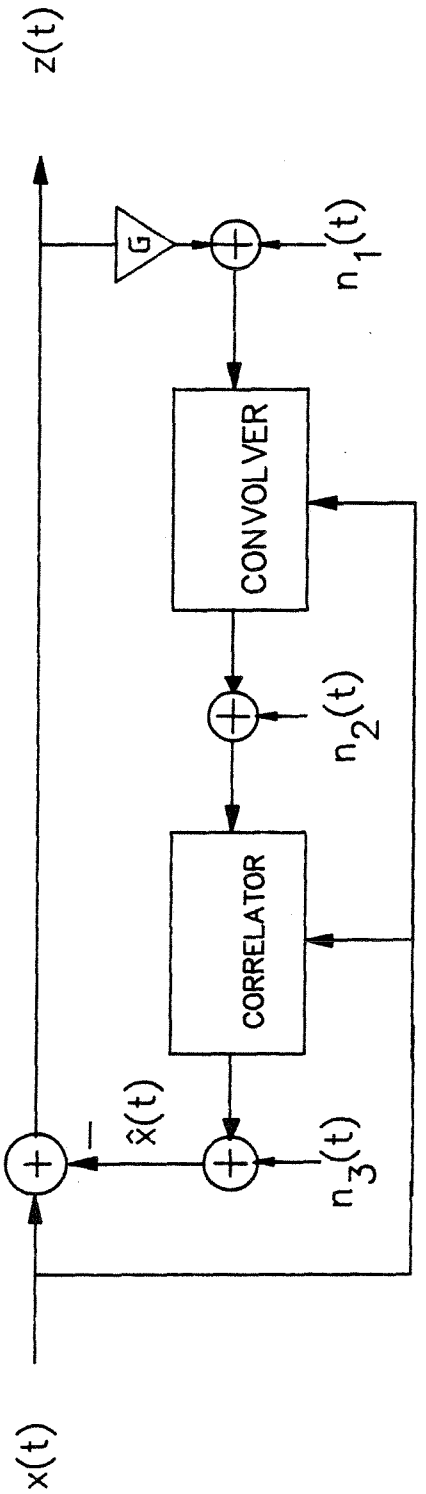

Fig. 3.20 System Noise Model

performs the integration in time. The sample products are the same as those in the space integrating version, but each product is integrated separately to produce each of the N output values. The integration time therefore becomes independent of the AOD parameters. Typically, durations exceeding milliseconds are achievable [4].

Although many different architectures have been developed to exploit the time-integrating concept to produce correlations, we review one specific implementation to discuss some performance issues common to conventional architectures. Shown in Fig. 3.22 is a coherent time-integrating correlator implemented with two AODs placed in a Mach Zender interferometer [11]. The collimated input light is split by BS1 into two paths with an AOD in each, and each AOD is angularly positioned to diffract the light into the positive Doppler-shift order. With the undiffracted beams removed by spatial filtering, the diffracted beams are combined by the beam splitter BS2 and imaged onto the linear CCD detector array, which integrates the intensity incident on each pixel and produces a serially scanned output. Mirror M2 can be rotated slightly so that the two combined diffracted beams do not propagate collinearly, producing on the detector an intensity grating pattern modulated by the product of the two counter-propagating signals from the AODs. If the AODs are driven by the signals $s_1(t) = Re\{\mathrm{a}_1(t)exp(j2\pi f_0 t)\}$ and $s_2(t) = Re\{\mathrm{a}_2(t)exp(j2\pi f_0 t)\}$, then the intensity distribution at the detector plane can be shown to be

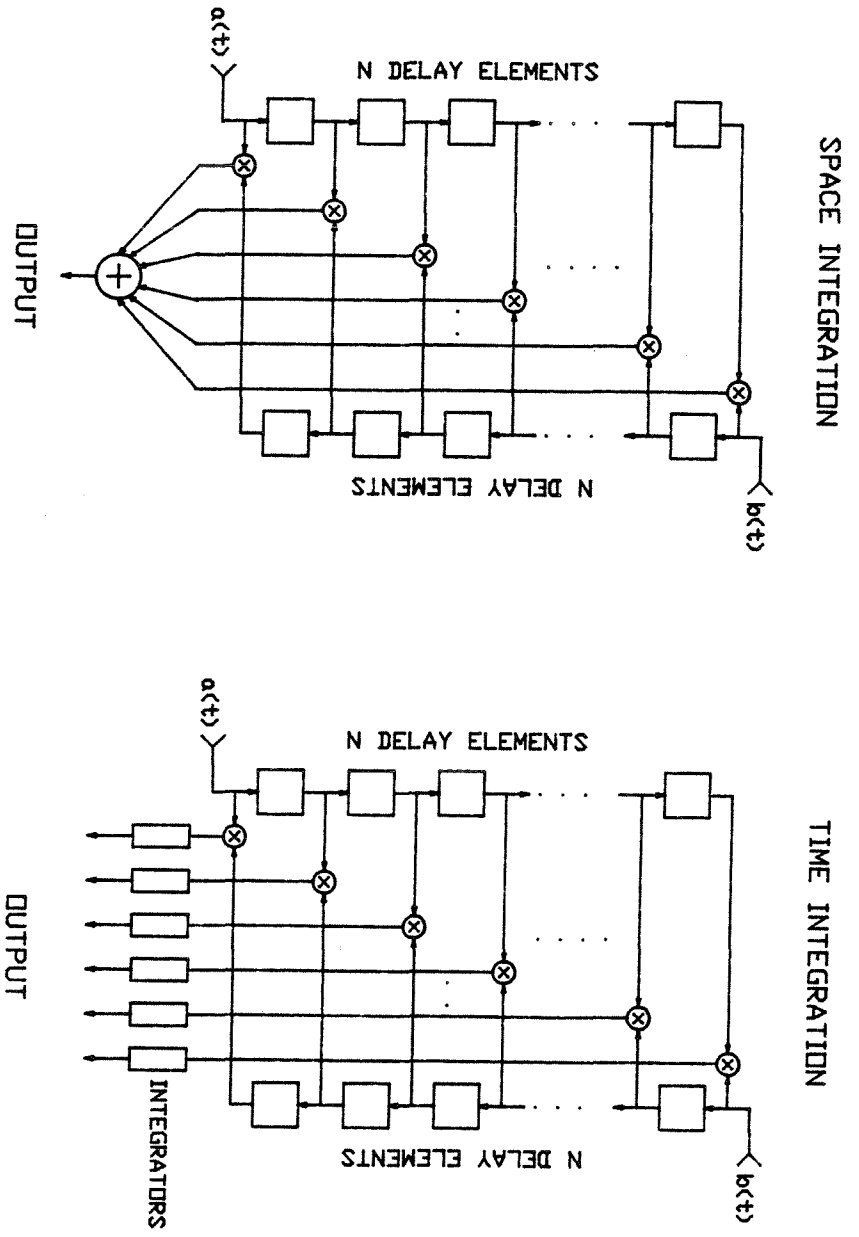

Fig. 3.21 Tapped Delay Line Correlators a)space-integration b)time-integration

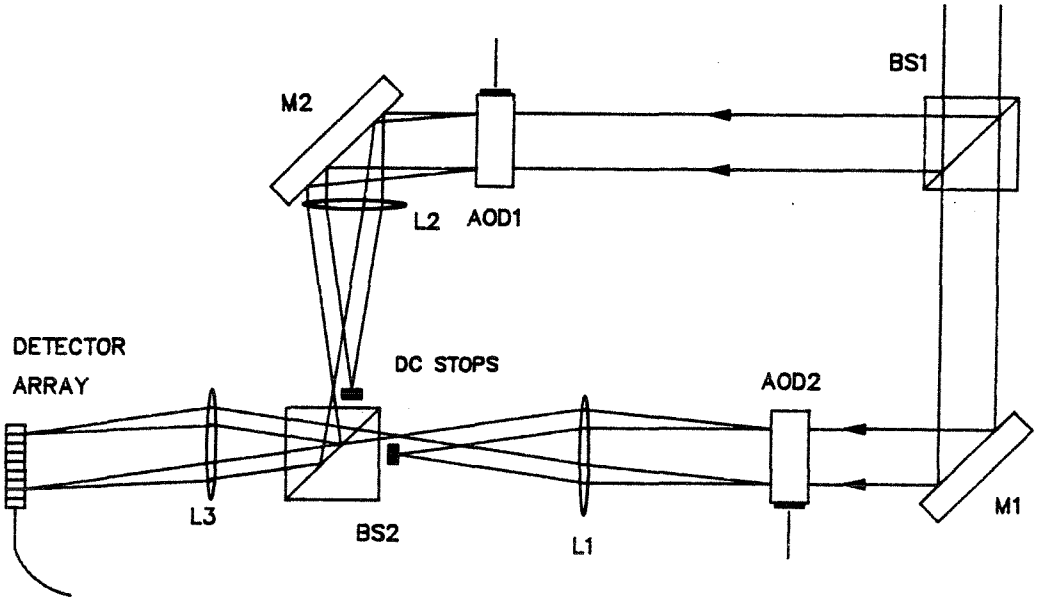

Fig. 3.22 Coherent Time-Integrating Correlator

$$I(x,t) = |\mathbf{a}_1(t - x/v - T/2) + \mathbf{a}_2(t + x/v - T/2)exp(j2\pi sin\theta x/\lambda)|^2$$

$$= |\mathbf{a}_1(t - x/v - t/2)|^2 + |\mathbf{a}_2(t + x/v - T/2)|^2$$

$$+ 2Re\{\mathbf{a}_1^*(t - x/v - T/2)\mathbf{a}_2(t + x/v - T/2)exp(j2\pi sin\theta x/\lambda)\}, \tag{3.23}$$

where the first two terms are bias values with slow spatial variations and the third term is the correlation product placed on a spatial carrier. The intensity distribution is spatially sampled by the detector elements, and the resulting photogenerated charges are accumulated over a duration τ to yield the correlation result

$$c(x_n) = \int_0^\tau I(x,t)dt$$

$$= \tau(a_1^2 + a_2^2) + 2Re\{exp(j2\pi sin\theta x_n/\lambda) \tag{3.24}$$

$$\int_0^\tau \mathbf{a}_1^*(t - x/v - T/2)\mathbf{a}_2(t + x/v - T/2)dt\},$$

where the moduli of the signals have been assumed to be constant values a_1 and a_2, and x_n indicates the n^{th} sampled position. These sampled correlation values are then loaded onto an analog shift register, which is read out serially, converting the spatial carrier into a temporal one. The bias is then removed by electronically high pass filtering the signal.

The concept is demonstrated by the experimental results shown in Figs. 3.23-3.26. Flint glass AODs with 10 $\mu sec.$ time apertures were used along with a 512-element Reticon CCD photodiode array operated at an integration time of about 4 msecs. For all three cases, a single signal drove both AODs with equal amplitudes

so that the maximum modulation depth was achieved (i.e., $a_1(t) = a_2(t) = a(t)$). When the signal is an unmodulated carrier, then the output is an unmodulated spatial carrier on a bias as illustrated by Fig. 3.23, where the slight modulation is due to non-uniformities in the AODs. The autocorrelation of a linear FM signal with a bandwidth of 100 kHz and a duration of 80 msecs. is shown in Fig. 3.24, where the output displays the main lobe and portions of the first sidelobes of the expected result. Compression of the autocorrelation peak due to an increase of the chirp bandwidth to 3 MHz is shown in Fig. 3.25. Fig. 3.26 is the autocorrelation result for a squarewave modulation at $f_s = 240$ kHz, showing the expected triangle wave modulation.

A major drawback of time-integrating systems such as the one just described is the bias that builds up along with the signal. Indeed, the experimental results shown were under the ideal condition of equal amplitude signals that led to full modulation depths. In general, however, a mismatch in the signal levels leads to outputs with less than ideal modulation depths and to a decrease in the overall dynamic range of the system. If DR is the dynamic range of the output detector, then the effective dynamic range at the output becomes $DR' = DR[SBR/(1 + SBR)]$, where SBR is the signal-to-bias ratio of the intensity distribution at the detector plane [5]. Although a dynamic range of 1000:1 is readily available (e.g., Reticon with τ= 4 msecs. [6]), DR' is at best half that of the detector and is typically much smaller because of uneven signal levels in the two AODs. The electronic filtration of the

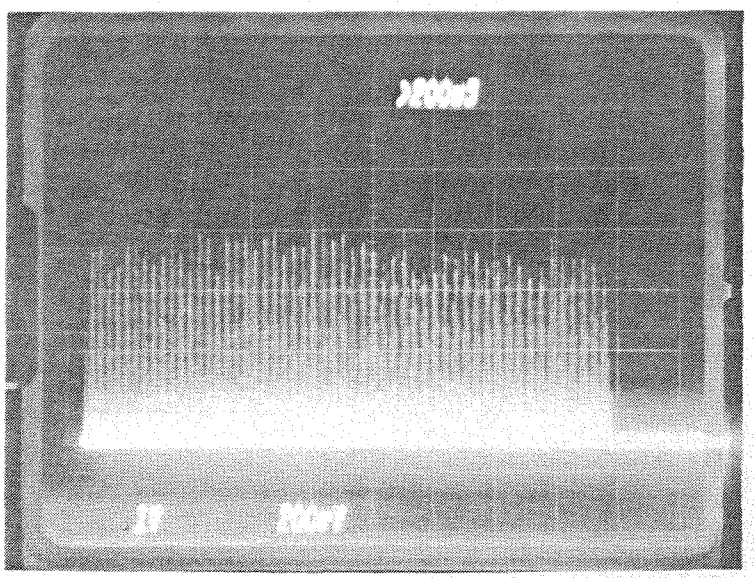

Fig. 3.23 Standard Time-Integrating Correlator Output for DC Inputs Showing the Spatial Carrier

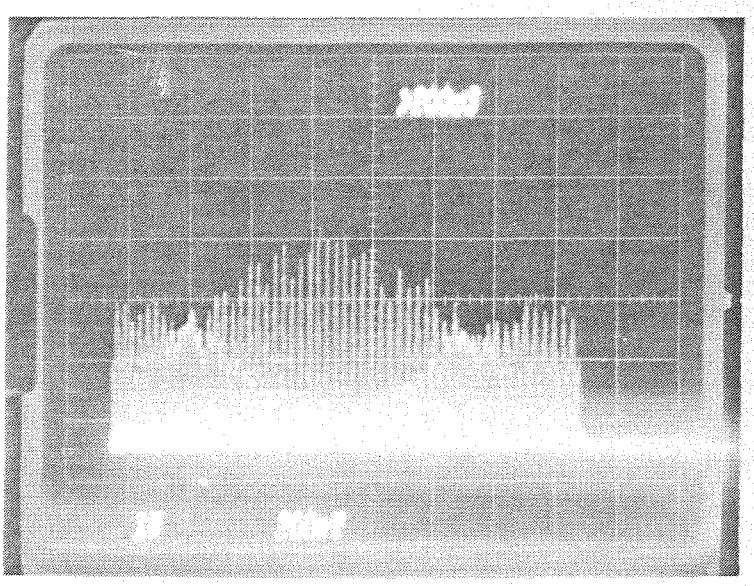

Fig. 3.24 Autocorrelation of 100 KHz Chirp (duration=80msec.)

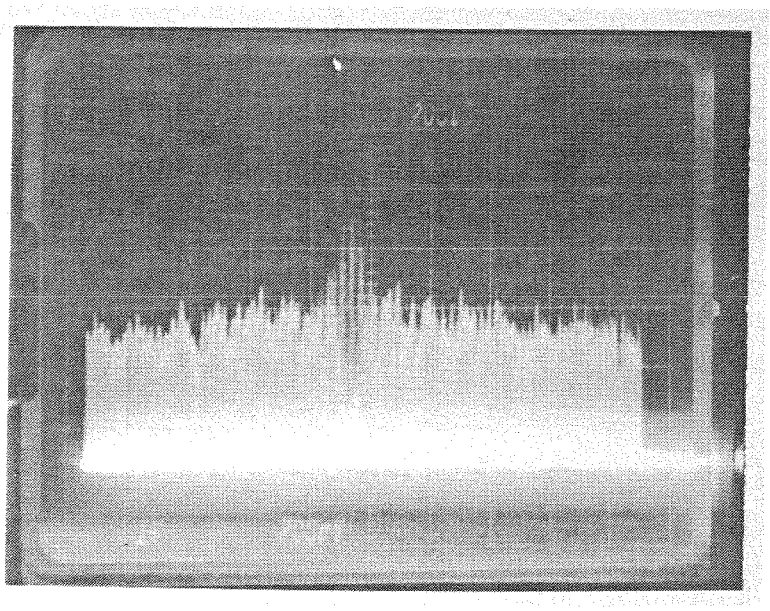

Fig. 3.25 Autocorrelation of 3 MHz Chirp (duration=50msec.)

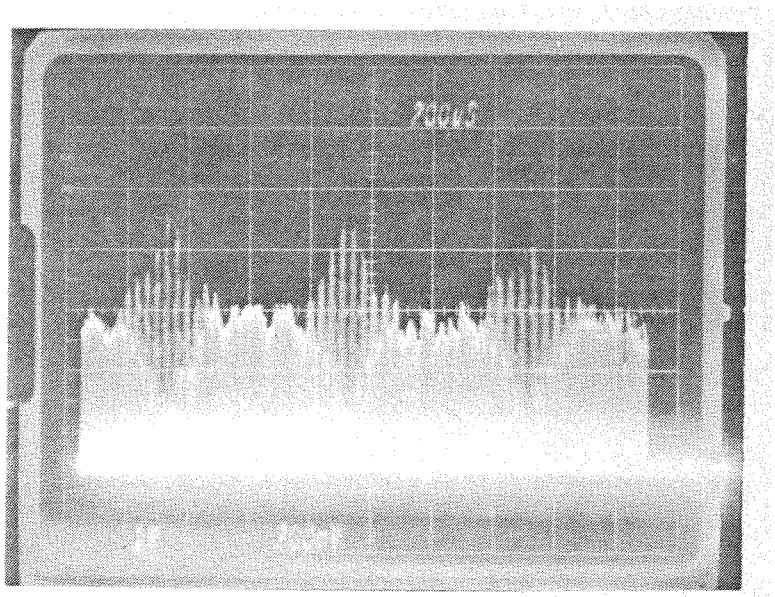

Fig. 3.26 Autocorrelation of 240 KHz Square Wave

scanned output does not alleviate the dynamic range problem since this procedure is performed after the detection of the signal. As stated before, the frequency of the spatial carrier must be sufficiently low as to avoid undersampling by the detector array. Because of this, a constraint is placed on the space bandwidth product of the system.

3.2.2 Time-integration using a photorefractive crystal

A new method of time-integration is here examined whereby the dynamic range along with the bandwidth constraints is eased through a novel use of a photorefractive crystal (BSO:$Bi_{12}SiO_{20}$) as the time-integrating detector. Here, the correlation is formed as a modulated index grating in the crystal and read out with an auxiliary read beam. Spatially constant bias terms which adversely affect conventional correlators do not form index gratings so that the read out amplitude is bias-free, although the diffraction efficiency of the crystal is reduced as a result of the bias. The resolution of the crystals is typically much better than that achievable with CCD arrays, allowing very high bandwidth (up to that acceptable by the AODs) signals to be processed. Because the correlation output appears as an optical field *amplitude*, such a system is easily incorporated into a coherent processor. We first review the basic concepts involved in the photorefractive effect, emphasizing its time-integrating properties, and then proceed to the discussion of its use in a

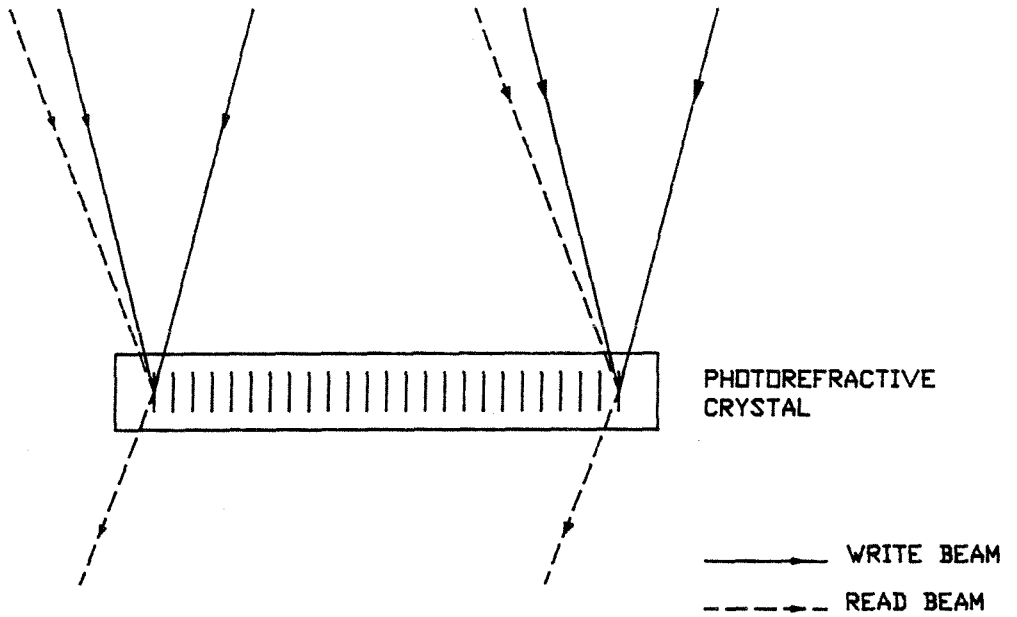

Fig. 3.27 The Photorefractive Effect

time-integrating correlator, which is to be incorporated into an adaptive filtering system.

The photorefractive effect can be understood in the following way. As shown in Fig. 3.27, two writing beams of light intersect in the crystal to form an intensity grating that is partially absorbed to excite charge carriers from traps into the conduction band. Because of the spatially varying intensity pattern, the photogenerated charges in the crystal redistribute themselves into a space-charge grating, driven by drift and diffusion processes. The electric field associated with the space charge distribution accordingly modulates the refractive index of the crystal through the electro-optic effect, and as a result, a holographic index grating is produced. The

grating can then be addressed non-destructively by a third beam, whose wavelength is chosen for negligible absorption by the crystal.

The photorefractive effect has been studied and modeled rather extensively [10]. Here, we review some dynamical aspects to show its time-integrating property. If the two writing beams of Fig. 3.27 are modulated both spatially and temporally and turned on abruptly at $t = 0$, then the general expression for the intensity distribution within the crystal is given by

$$I(x,t) = \begin{cases} I_0 + Re\{I_1(x,t)exp(jkx)\} & \text{if } t > 0; \\ 0 & \text{otherwise.} \end{cases} \tag{3.25}$$

Assuming that nonlinear effects such as self-diffraction are negligible and that the spatial variations of $I_1(x,t)$ are slow compared to the grating frequency, the space charge field that is formed in the crystal can be shown to be [7]

$$\begin{aligned} E_{sc}(x,t) &= \frac{K_1}{I_0} exp(jkx) \int_0^t exp[(t'-t)/\tau] I_1(x,t')dt', \\ \tau &= \frac{K_2}{I_0}, \end{aligned} \tag{3.26}$$

where K_1 and K_2 are complex constants that depend on material parameters, the grating frequency, and the externally applied electric field. The response is that of a leaky integrator and can be approximated as

$$E_{sc}(x,t) \approx \frac{K_1}{I_0} exp(jkx) \int_t^{t+\tau} I_1(x,t')dt'. \tag{3.27}$$

The space charge field modulates the index of refraction via the electro-optic effect to create an index perturbation which is nondestructively read out with an auxiliary

plane wave at a non-absorbing wavelength. The amplitude of the diffracted reading beam is proportional to $E_{sc}(x,t)$ given by Eq. 3.27 and is therefore the original write beam modulation, I_1, integrated in time without any bias.

A correlator that exploits the effects just described was set up using 2 flint glass AODs as the input devices and a BSO crystal (< 110 > cut, 15x15x2 mm) with an external electric field of 7 kv applied in the < 001 > direction as the time-integrating element. The basic architecture shown in Fig. 3.28 places the AODs in a collinear geometry. Here the light diffracted (positive Doppler shift) from AOD1 passes through AOD2 to be imaged onto the crystal. The DC beam from AOD1 is also diffracted into the positive Doppler shift order by AOD2 and imaged onto the crystal with a demagnification factor of two, since the BSO crystal is smaller than the AODs by roughly that factor.

Any undiffracted light is removed by spatial filtering in the Fourier plane of L3 and the two diffracted beams are incident on the crystal at twice the Bragg angle with respect to each other. With $\mathrm{a}_1 exp(j2\pi f_0 t)$ and $\mathrm{a}_2 exp(j2\pi f_0 t)$ driving AOD1 and AOD2 respectively, the intensity incident on the crystal can be described by

$$I(x,t) = |\mathrm{a}_1(t - x/v - T/2)|^2 + |\mathrm{a}_2(t + x/v - T/2)|^2 + 2Re\{\mathrm{a}_1^*(t - x/v - T/2)\mathrm{a}_2(t + x/v - T/2)exp(j2\pi sin\theta_B x/\lambda)\}. \tag{3.28}$$

The direction of the read beam is adjusted for maximum diffraction efficiency from the photorefractive grating. Using Eqs. 3.27 and 3.28, the amplitude of the read-out wave diffracted by the crystal is determined to be proportional to the following

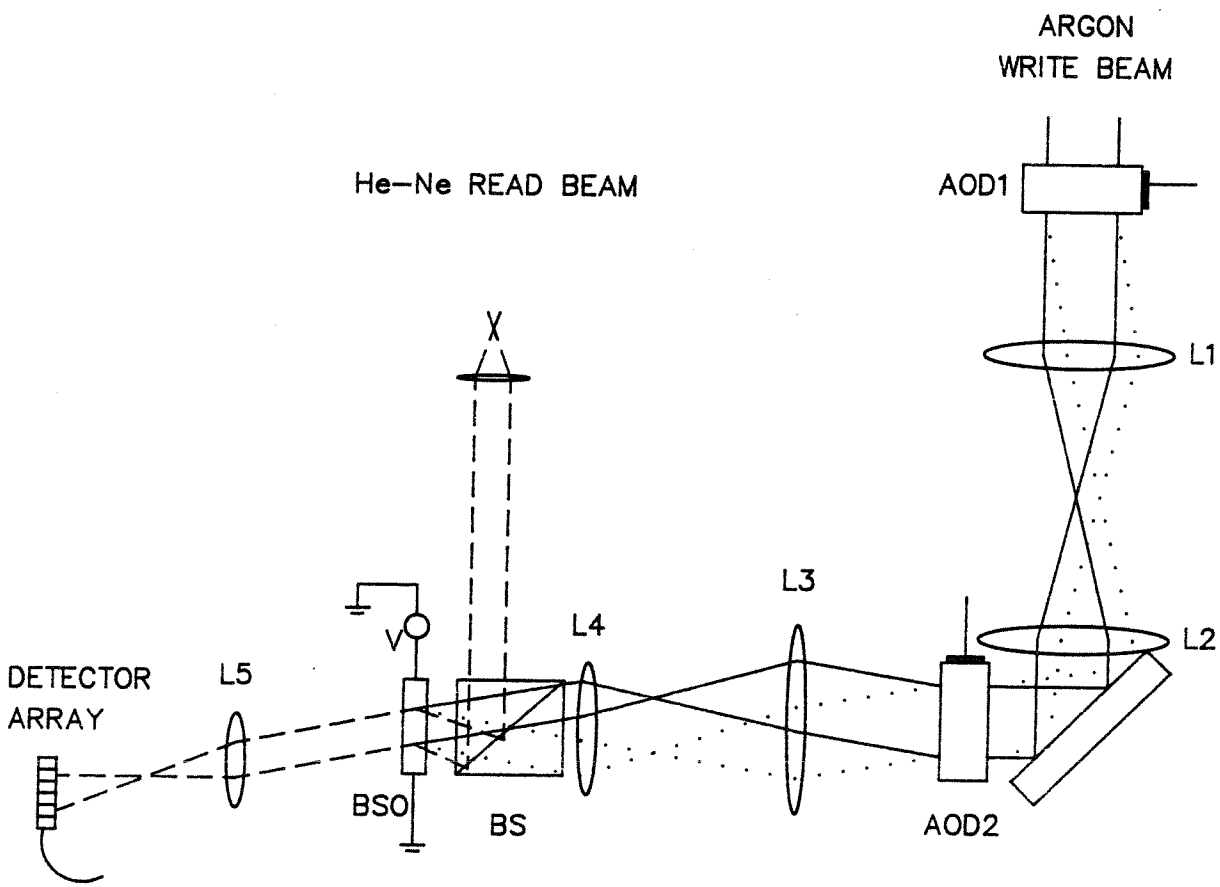

Fig. 3.28 Photorefractive Time-Integrating Correlator

integral:

$$E_{diff}(x,t) \propto \int_{t}^{t+\tau} \mathrm{a}_1^*(t' - x/v - T/2)\mathrm{a}_2(t' + x/v - T/2)dt'. \qquad (3.29)$$

This is the desired correlation.

Both AODs were driven with a symmetric linear chirp with a bandwidth of 5 MHz centered at 70 MHz and accessed with argon laser light (λ = 514nm) to provide the two writing beams. Cylindrical lenses (not shown in the figure) were used to expand these beams to illuminate the full aperture of the crystal, and the average intensity of the writing beams was equal to 1 $\mu W/cm^2$. The correlation was read out using He-Ne (λ = 633nm) laser light, which is negligibly absorbed by the crystal, and the light diffracted by the crystal was imaged horizontally and focused verticaly onto a linear CCD detector array.

Fig. 3.29 shows the correlation obtained when both AODs are equally driven with the same signal. Since the intensity is detected by the CCD array, the results shown in Figs. 3.29-3.33 are the modulus squares of the correlation functions. It is true that an increase in the writing intensity bias due to unequal signal levels in the AODs or the addition of noise would appear directly on the output of a standard time-integrating correlator. On the other hand, the overall diffraction efficiency and therefore the output signal from the photorefractive crystal is reduced according to Eq. 3.29, while the bias is completely blocked from appearing at the output by the holographic writing/reading process. As the SNR is continually decreased, the

diffraction efficiency deteriorates until the output is overcome by scattering noise and thermal and shot noise within the crystal. Since Eq. 3.27 shows that the strength of the photorefractive grating is essentially proportional to the modulation depth of the writing intensity distribution, we can define the dynamic range to be $DR_{BSO} = m_{min}^{-1}$, where m_{min} is the minimum modulation depth of the writing intensity distribution to which the crystal will respond. The modulation depth can easily be controlled by varying the signal levels in the AODs. The dynamic range was measured to be equal to 23 dB. We expect that through careful design (crystal polishing, anti-reflection coating, etc), this figure can be substantially increased.

Additional results were obtained using TeO_2, which has longer time apertures (> 60 $\mu secs.$), allowing a wider correlation viewing window. Shown in Fig. 3.30 is the autocorrelation of a 20 % duty cycle square wave of frequency f_s =73.5 kHz. Because of nonuniformities in the BSO and the nonuniform reading beam, the output was apodized by a bell-shaped distribution. Fig. 3.31 shows the result for the square wave with a higher frequency (f_s =147 kHz) where the result shows the apodization more clearly. Fig. 3.32 is the autocorrelation of a chirped signal with a bandwidth of 16.7 kHz and duration of 7.8 msecs. And finally, noise in the form of a 50 MHz sinusoid was introduced additively in one of the AODs to reduce the SNR to -17dB for the 147 kHz square wave input. The bias free result is shown in Fig. 3.33. Here again, the background DC bias is due entirely to dark currents in the detector.

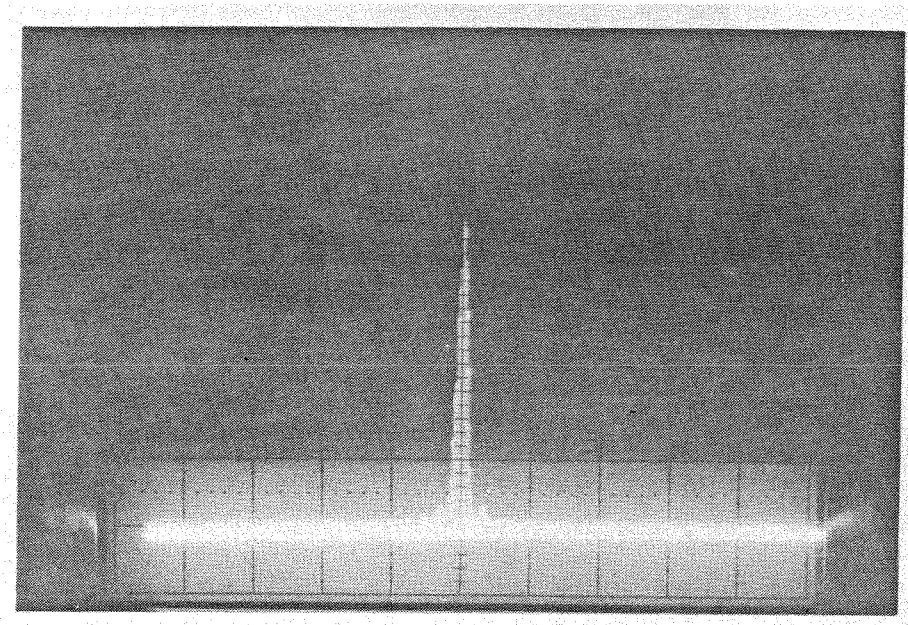

Fig. 3.29 Autocorrelation of 5 MHz Bandwidth Chirp Centered at 7 MHz Using the Photorefractive Correlator

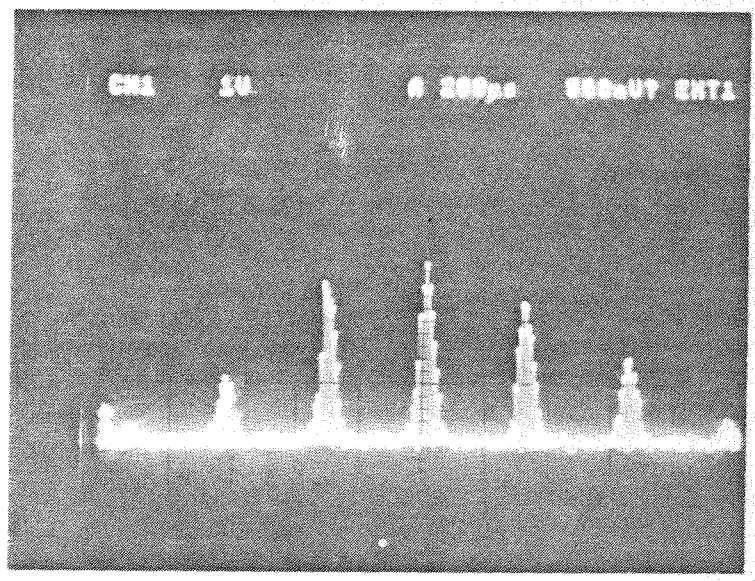

Fig. 3.30 Autocorrelation of 73.5 KHz Square Wave (20 % duty cycle) Using the Photorefractive Correlator with TeO_2 AODs

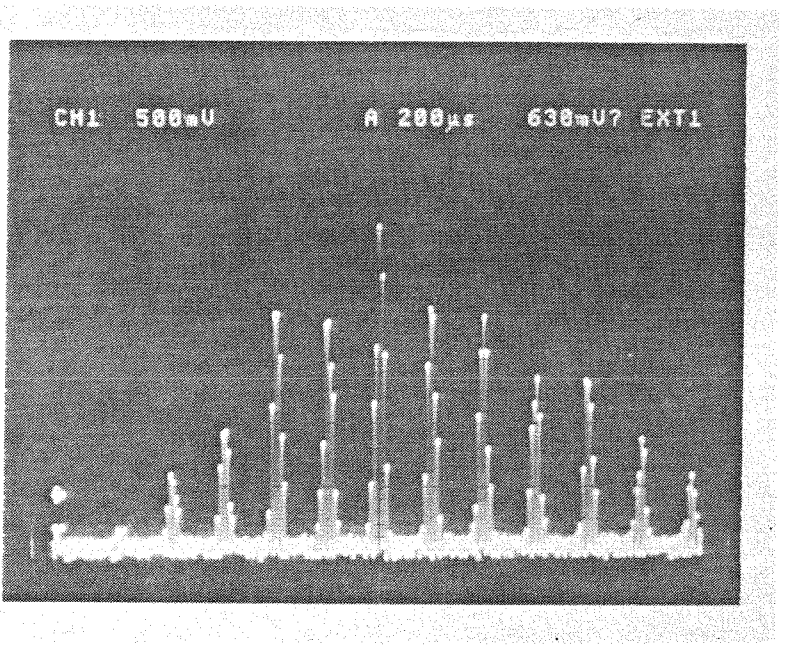

Fig. 3.31 Autocorrelation of 147 KHz Square Wave (20 % duty cycle) Using the Photorefractive Correlator with TeO_2 AODs

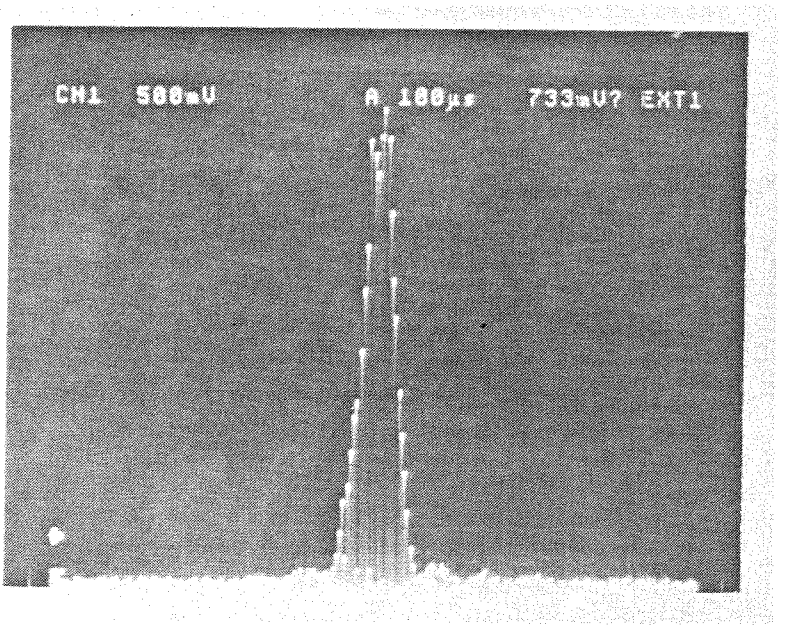

Fig. 3.32 Autocorrelation of 16.7 KHz Bandwidth Chirp (duration= 7.8 msec.) Using the Photorefractive Correlator with TeO_2 AODs

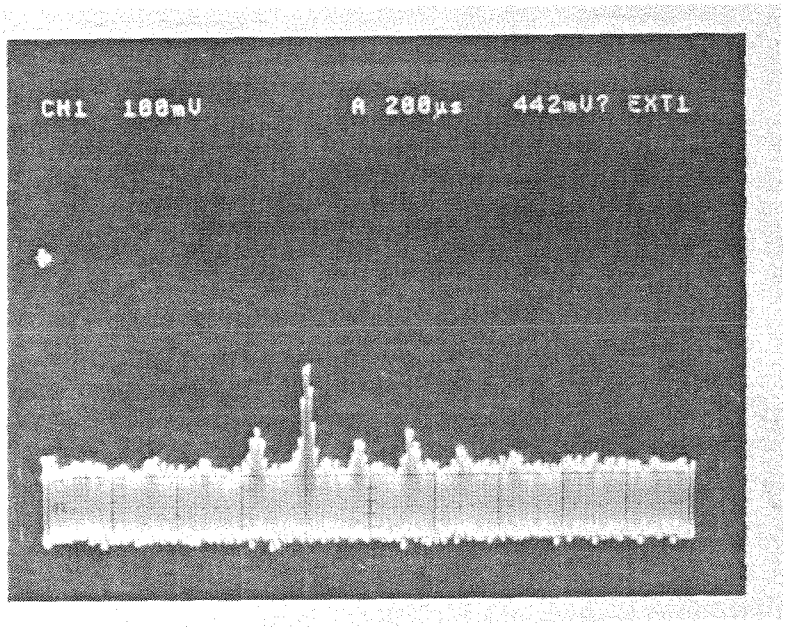

Fig. 3.33 Cross Correlation of 147 KHz (20% duty cycle) Square Wave with Same Signal Corrupted by 50 MHz Sinusoid at SNR = -17 dB

3.2.3 Space-time-integrating optical processor

In the space-integrating (SI) adaptive implementations, the desired correlation is formed by a SI correlator and read out with a SI convolver. Alternative approaches where integration in both time and space are used have been described by Rhodes [8] and Penn *et al.*[9]. In such systems, the correlation integral is computed on a time-integrating spatial modulator and read out with a SI convolver. We now consider such an implementation using the photorefractive time-integrating correlator described in the previous section. The advantages of this implementation over the previous ones [8,9] which used the Hughes liquid crystal light valve and a phos-

phor screen, respectively, as the time-integrating SLMs are: 1)the system response speed is easily controllable since the response time of the photorefractive effect depends on the exposure level; 2)a coherent implementation is possible; 3)higher resolution is exhibited by the photorefractive devices; 4)since the crystal does not respond to DC or bias levels, the implementation will not suffer from bias build up problems common among time-integrating systems; 5)the photorefractive devices are simpler since they require only the crystal and a voltage source to supply the external electric field required for some crystals.

A SI convolver compatible with the BSO system is required in order to implement the passive processor (adaptive estimator) using the photorefractive correlator. A coherent realization is shown in Fig.3.34 where the He-Ne beam path that was used to read out the correlation written on the BSO now includes an additional AOD with some demagnifying optics. The output and input signals ($z(t)$ and $x(t)$, respectively) constitute the inputs to the correlator AODs (AOD1 and AOD2). AOD3 is also driven by the input signal $x(t)$ and diffracts a portion of the He-Ne read beam to pass through the BSO unaffected by the grating in the crystal because of Bragg mismatch. The DC beam from AOD3, however, is Bragg matched to the index grating in the crystal and reads out the correlation function. If all of the AODs are driven at the same center frequency, then the beam diffracted by the BSO crystal and that diffracted by AOD3 are collinear and interefere temporally at frequency f_0, the Doppler frequency introduced by AOD3. The two diffracted

waves are Fourier transformed by lens L5, and the resulting intensity is detected by the photodetector. The output current is the convolution of the input $x(t)$ and the correlation formed within the crystal, and it becomes the feedback signal $\hat{x}(t)$, which is then subtracted from the input to produce the output signal. The resulting input-output equation is

$$z(t) \approx x(t) - G \int_{-T/8}^{T/8} \int_{t-\tau}^{t} x^*(t' - 2\alpha - T/2) \, x(t - 4\alpha - T/2) z(t' + 2\alpha - T/2) dt' d\alpha, \tag{3.30}$$

which is similar to that of the SI system (Eq. 3.12) except for the presence of both space and time integrals.

One underlying assumption behind Eq. 3.29 and hence 3.30 is that the crystal is thin enough to put the read out process into the Raman-Nath regime [1]. This is not usually the case, however, and the coupling between the writing beams must be taken into account. Coupled wave theory predicts that the phase of the index grating will be a function of the two write beam intensities [10]. To verify this effect, all of the AODs were driven by a common sinusoid of frequency f_0=70 MHz, and the phase of the output from the photodetector was compared to that of the input sinusoid for various writing beam intensity ratios which were controlled by varying the signal levels that drive AOD1 and AOD2. The results are shown in Fig. 3.35 where the upper trace of each picture shows the reference signal that drives the AODs and the bottom portion shows the reconstructed sinusoid from the photodetector. The intensity of one of the two writing beams was fixed at 12

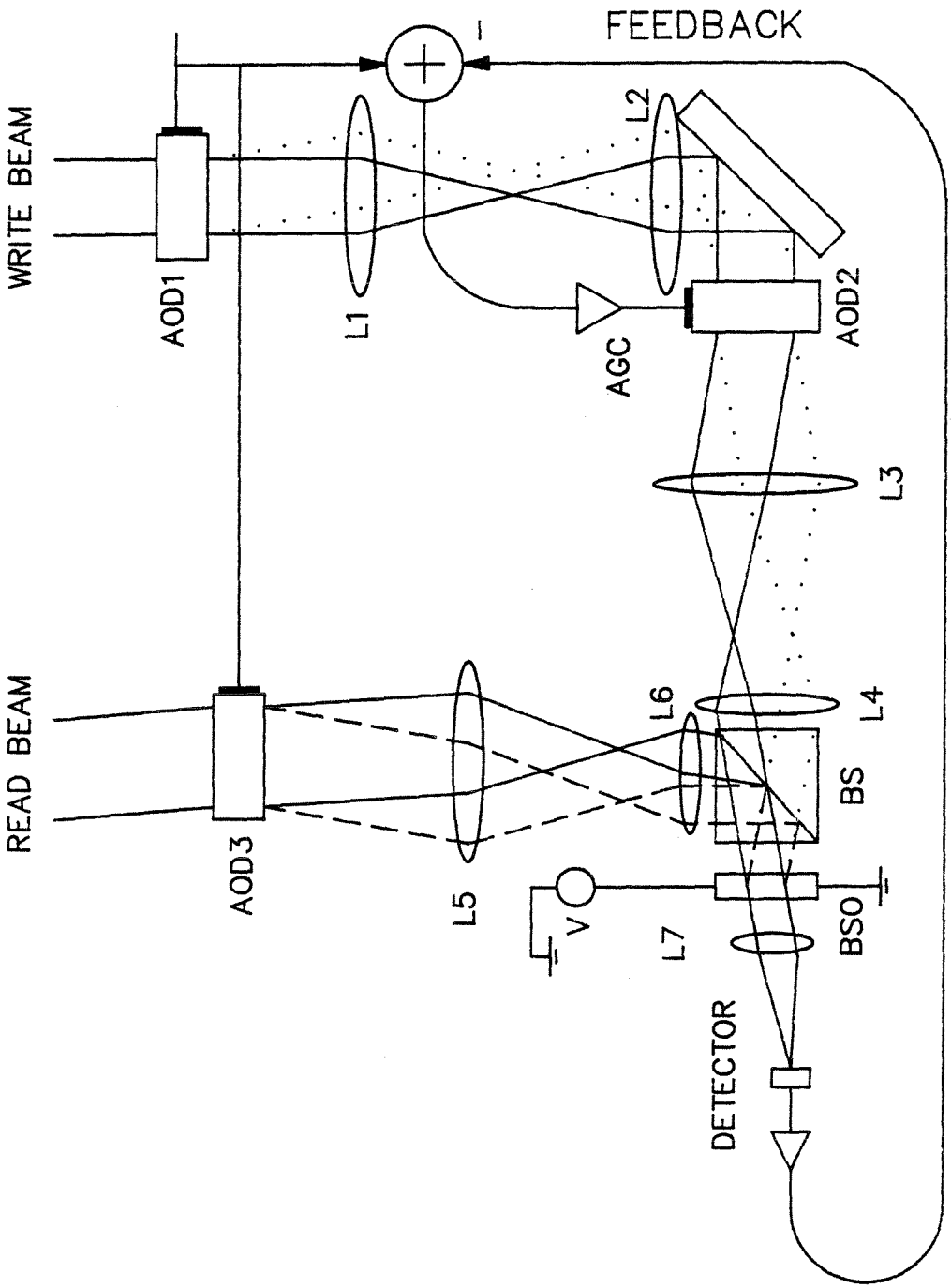

Fig. 3.34 Space-Time-Integrating Adaptive Filter Using the Photorefractive Correlator

$\mu W/cm^2$, while the other assumed values of 12, 5.8, 3, and 1 $\mu W/cm^2$. The phase of the reconstruction changes by as much as 25 degrees as the intensity ratio is varied. This introduces a complication in the present system because, as soon as the processor begins to suppress an incoming jammer, the output, $z(t)$, begins to decrease in amplitude. This causes the ratio of the intensities of the two write beams that emerge from AOD1 and AOD2 to diminish. This translates to a phase change in the feedback signal, causing instability. A remedy, however, is effected by placing an automatic gain control (AGC) amplifier at the input to AOD2. As adaptation proceeds and $z(t)$ begins to decrease, the AGC tracks the drop in amplitude to keep the input of AOD2 at a fixed value. The speed of the AGC must be much faster than that of the BSO response, which was on the order of hundreds of milliseconds.

The system just described has been set up in the laboratory for preliminary study using an Avantek RF (5-100 MHz) AGC amplifier whose response time is about 25 $\mu secs$. Fig. 3.36 shows the spectrum of the input signal, a jammer at 70 MHz, and that of the processor output. The scales of both pictures are the same. The observed suppression of the jammer was about 15 dB. Better suppression can be expected as AGC amplifiers with higher dynamic range are used.

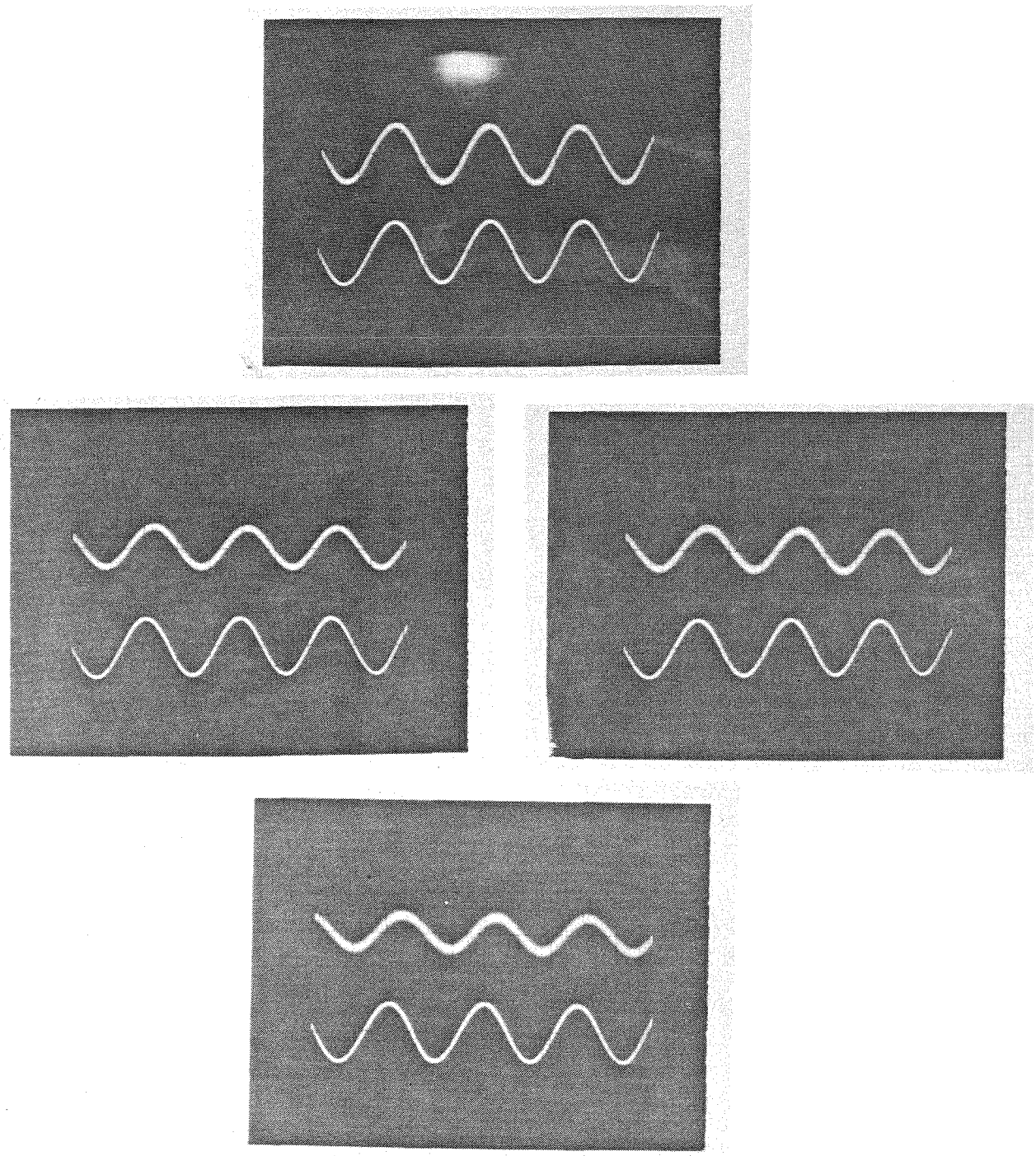

Fig. 3.35 Dependence of the Phase of the Reconstructed Signal on the Writing Beam Intensity Ratio (the intensity of one beam was fixed at $I_0 = 12\ \mu\mathrm{W/cm^2}$ while the intensity of the other beam was varied): **a)** $I_1 = 12\ \mu\mathrm{W/cm^2}$, **b)** $I_1 = 5.8\ \mu\mathrm{W/cm^2}$, **c)** $I_1 = 3\ \mu\mathrm{W/cm^2}$, **d)** $I_1 = 1\ \mu\mathrm{W/cm^2}$.

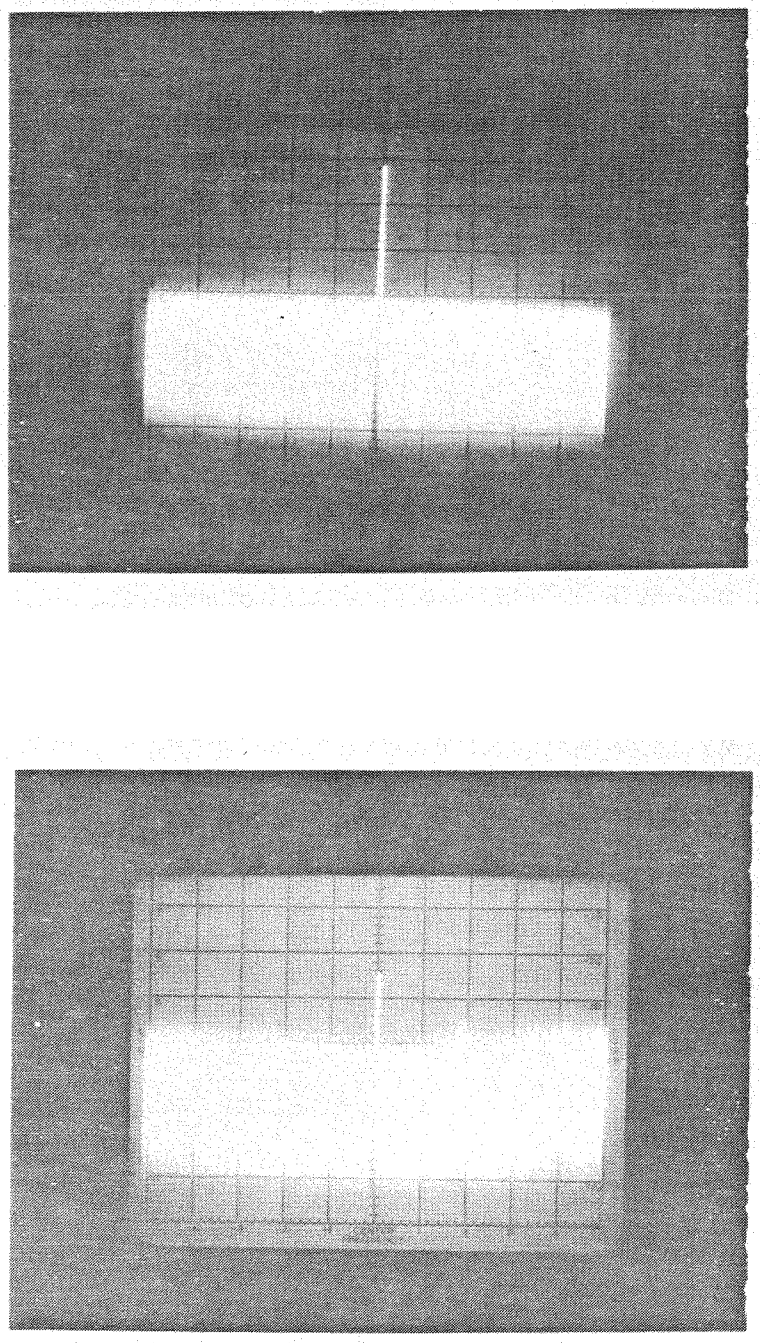

Fig. 3.36 Jammer Nulling Result a)input spectrum b)output spectrum (the two pictures are at the same dB scale)

References for Chapter 3

[1] A. Korpel, "Acousto-optics," in *Applied Solid State Science: Advances in Materials and Device Research,* R. Wolfe, Ed., Academic Press, New York, (1972).

[2] Instructional Manual: Model AOD-70 Acousto-optic light deflector, IntraAction Corp., Bellwood, IL.

[3] R. Arens, "Complex processes for envelopes of normal noise," *IRE Trans. Info. Theory*, **IT-32**, 204 (Sept. 1957).

[4] R. A. Sprague and C. L. Koliopoulos, "Time-integrating acousto-optic correlator," *Appl. Opt.*, **15**, 89 (1976).

[5] D. Psaltis, "Incoherent electro-optic image correlator," *Optical Engineering,*, **23**, 12 (1984).

[6] EG&G Reticon: Image Sensing Products Catalog, p.1-3, 1986.

[7] M. Cronin-Golomb, "Large Nonlinearities in Four-Wave Mixing in Photorefractive Crystals and Applications in Passive Optical Phase Conjugation," PhD. Thesis, California Institute of Technology (Mar. 1983).

[8] J. F. Rhodes, "Adaptive filter with a time-domain implementation using correlation cancellation loops," *Appl. Opt.*, **22**, 282 (1983).

[9] W. A. Penn *et al.*, "Acousto-optic adaptive processing," *Final Draft*, **RADC-TR-83-156**, Phase Report,(Dec. 1983).

[10] N. V. Kukhtarev *et al.*, "Holographic storage in electro-optic crystals, Parts I and II," *Ferroelectrics*, **22**, 949 (1979).

[11] W. T. Rhodes, "Acousto-optic signal processing: convolution and correlation," *Proc. IEEE*, **69**, 65 (1981).

Chapter 4. Extension to 2-Dimensional Signal Processing

4.1 Narrowband Processors in Broadband Environments

The extension of adaptive filtering techniques to the space-time domain is applicable for sonar and radar signal processing where the outputs from an array of sensors must be weighted and summed to optimally estimate a signal in the presence of noise [1-3]. When the array processor encounters only narrowband signals centered at a common carrier frequency, f_0, the filter structure shown in Fig. 4.1 is identical to that of the temporal filter except that the input samples are the outputs of the sensors instead of a tapped delay line. In such applications, only spatial discrimination of signals is required, and the jammer nulling capabilities of such systems are quite good as long as the jammers are narrowband. The output can be described by the following equation

$$z(t) = \sum_{n=1}^{N} h_n u_n(t), \tag{4.1}$$

where N is the number of elements in the array and h_n is the adaptively controlled weight for the n_{th} sensor output $u_n(t)$.

After suppressing the temporal carrier term $exp\{j2\pi f_0 t\}$, the signal received by the n_{th} element due to a narrowband signal arriving at an angle θ from boresight can be expressed as

$$u_n(t) = a(t)exp\{-j2\pi f_0 sin\theta nd/c\}, \tag{4.2}$$

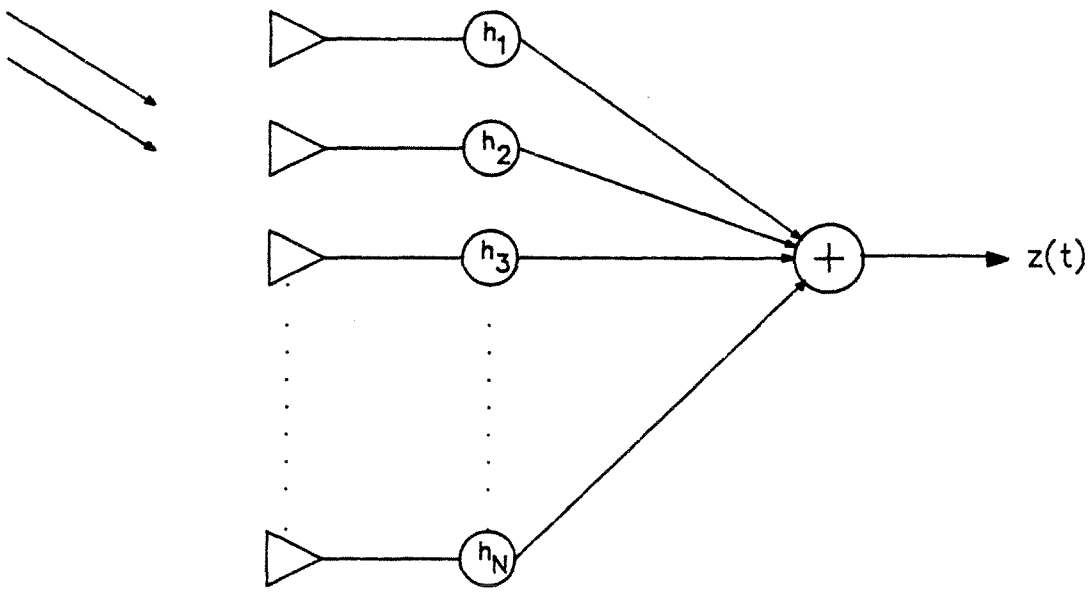

Fig. 4.1 Narrowband Array Processor

where c is the speed of light, $a(t)$ is the slowly varying envelope of the signal, and d is the spacing between the array elements. The goal of the adaptation is the minimization of the mean squared error between the actual output of the processor and a desired signal. The scenario with which we will be concerned is the one where the desired signal is known to be on boresight, and interference from directions other than this must be suppressed. This is sometimes known as *sidelobe cancellation* [4]. An example of narrowband nulling is shown in Fig. 4.2, where the array gain pattern for a uniformly weighted array and the minimum mean-squared error gain pattern for receiving a signal on boresight and rejecting a jammer of the same frequency at a sidelobe angle are plotted.

Although the jammer is received at a sidelobe angle and is attenuated relative to the signal, the power of the jamming interferences is typically much larger than that of the signal, and so the summed output of the uniformly weighted processor will be dominated by the interference. In this case, the optimum pattern to which the adaptive processor converges places a perfect null precisely at the direction of the interference.

Given the size of the array (N = the number of receiving elements), an upper bound on the number of spatial jammers of the same frequency f_0 that the array is able to reject can be established. The m_{th} jammer from a set of M jammers can be represented by an N-element vector $\underline{u}^{(m)}$ whose n_{th} element is given by

$$u_n^{(m)} = exp\{-j2\pi f_0 sin\theta_m nd/c\}. \tag{4.3}$$

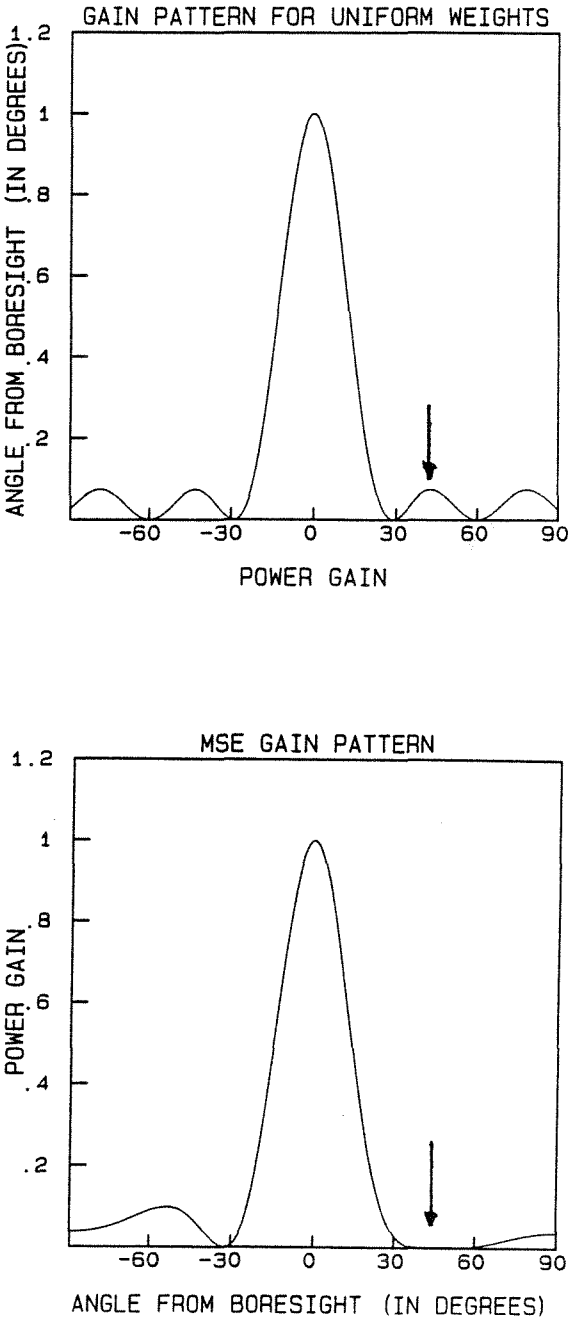

Fig. 4.2 Narrowband Sidelobe Cancellation (arrow indicates the angular position of the jammer): a)uniformly weighted array gain pattern; b)minimum mean squared error array gain pattern (jammer incidence angle is 50°)

Simultaneous nulling of all of the M jammers leads to the system of equations

$$\begin{pmatrix} u_1^{(1)} & u_2^{(1)} & \cdots & u_N^{(1)} \\ \vdots & \vdots & \ddots & \vdots \\ u_1^{(M)} & u_2^{(M)} & \cdots & u_N^{(M)} \\ s_1 & s_2 & \cdots & s_N \end{pmatrix} \begin{pmatrix} h_1 \\ h_2 \\ \vdots \\ h_N \end{pmatrix} = \begin{pmatrix} 0 \\ \vdots \\ 0 \\ 1 \end{pmatrix}, \tag{4.4}$$

where $\underline{s}$ represents the signal vector, and the last equation of the system arises from the constraint that the signal be accepted. If the jammers are distributed spatially such that the vectors $\{\underline{u}^{(m)}\}_{m=1}^{M}$ and $\underline{s}$ are linearly independent, then in order for a solution $\underline{h}$ to exist, there can be at most N equations in the system, yielding the upper bound of $M \leq N - 1$. The linear independence condition is akin to that of general position in pattern recognition [9] and assures that the jammers are irregularly distributed in space.

Since the narrowband arrays assign only one weight per sensor, no consideration of the temporal content of the received signal is taken. The spatial distinction of a signal is judged based on the observed differences in the phase of the signal as received by each element. If a particular jammer contains many frequencies spread over a significant bandwidth, each component will result in a unique relative phase difference from element to element and hence will look like a multiplicity of jammers directed at different angles. Thus, if a narrowband processor encounters a sufficiently wideband interference in some direction, it will use up all of its degrees of freedom (the adjustable weights) to null this single directional noise.

Two examples are shown in Figs. 4.3 and 4.4, where the minimum mean-squared error array patterns are plotted for a boresight desired signal and a multi-

frequency jammer incident at $\theta = 60°$. The element spacing in each case is $\frac{c}{2f_0}$. The jamming frequencies are f_0, $.85f_0$, and $.7f_0$, with the signal power and the power in each jamming frequency being equal. For each case (Fig. 4.3, Fig. 4.4), a gain pattern for each jamming frequency is plotted, since the array response is frequency dependent. Fig. 4.3 depicts the response of a 2 element array, and it is clear that only the frequency $.85f_0$ is nulled perfectly, while Fig. 4.4, which corresponds to a 4 element array, shows perfect nulling for all three frequencies.

4.2 Optimum Broadband Systems

In narrowband applications, bandpass filters are used to assure a narrowband signal and noise environment as shown in Fig. 4.1, but where signals with large bandwidths must be processed, such filters cannot be used. Even in broadband noise environments, we would like the N element array to be capable of cancelling $N-1$ jammers in general, regardless of their respective bandwidths. This requires that more degrees of freedom be available for the output of each sensor than the single weight that the narrowband processor provides. Shown in Fig. 4.5 is an N element array processor that satisfies the requirements for operation in broadband environments by passing the output of each sensor through a linear time-invariant filter, or equivalently, a tapped delay line [5-7]. While spatial discrimination is still made possible by the spatial sampling done by the array of sensors, the additional capability of making distinctions based on the temporal content of the received

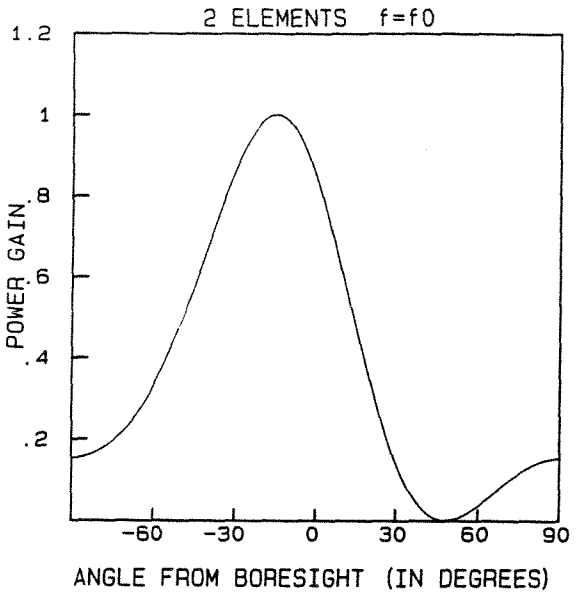

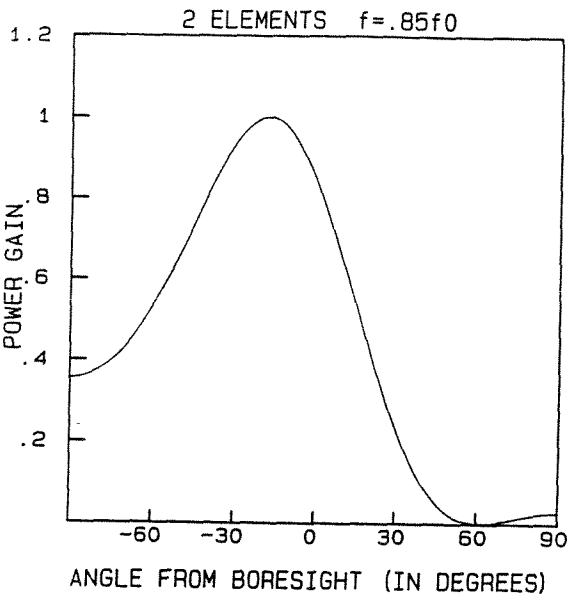

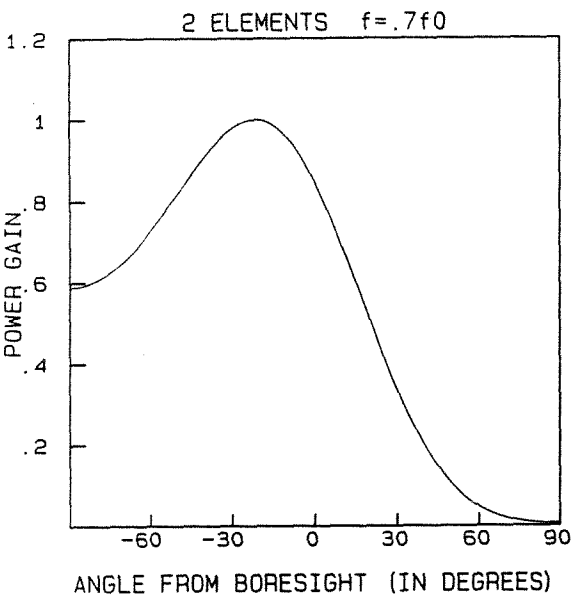

Fig. 4.3 Minimum Mean Squared Error Gain Patterns for a Multiple Frequency Jammer ($f = f_0, .85f_0, .7f_0$) Incident at 60° from Boresight (2 element array, element spacing is $c/2f_0$): a)response for f_0; b)response for $.85f_0$; c)response for $.7f_0$

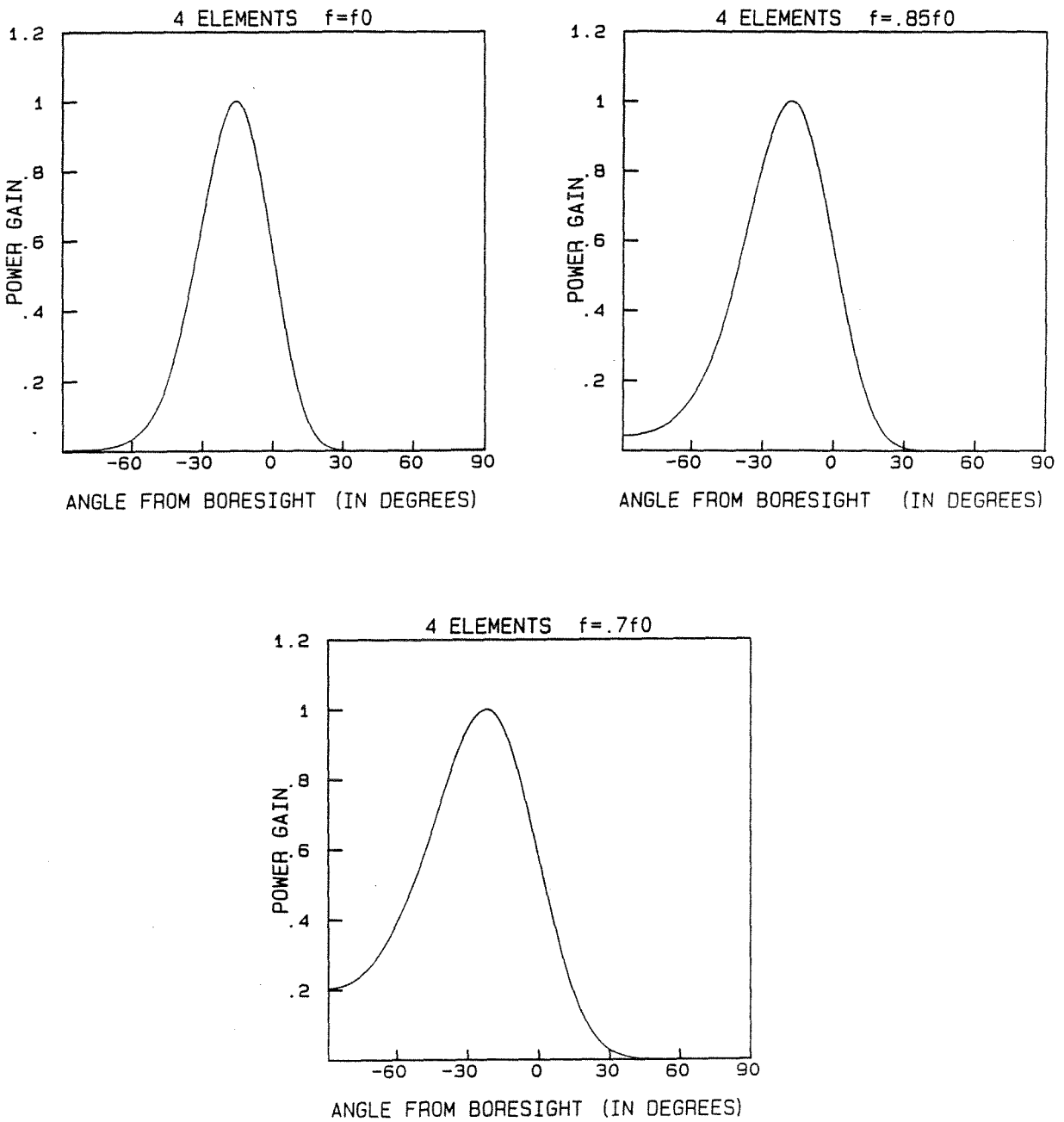

Fig. 4.4 Minimum Mean Squared Error Gain Patterns for a Multiple Frequency Jammer ($f = f_0, .85f_0, .7f_0$) Incident at 60° from Boresight (4 element array, element spacing is $c/2f_0$): a)response for f_0, b)response for $.85f_0$, c)response for $.7f_0$

signals is offered by the array of filters.

An optimum choice of the linear filters based on the mean squared error criterion can be made in the present scenario of a desired signal incident on boresight and broadband jammers from other directions. Let $s(t)$ represent the desired signal which is assumed to derive from a stationary random process with zero mean and autocorrelation function given by $R(\tau) = E[s(t+\tau)s^*(t)]$. Since the desired portion of the received signal arrives on boresight, there is no dispersion, and each element receives an identical desired signal $\alpha s(t)$. The interference that arrives from different directions will induce signals in each element with different delays.

Let $v_n(t)$ be the interference component received by the n_{th} element, assumed also to derive from a zero mean stationary random process with covariance function given by $\gamma_{mn}(\tau) = E\left[v_m(t+\tau)v_n^*(t)\right]$. The total signal received by the n_{th} element is therefore given by $u_n(t) = \alpha s(t) + v_n(t)$. The output of the array processor is given by

$$z(t) = \sum_{n=1}^{N} \int_{-\infty}^{\infty} h_n(\tau) u_n(t-\tau) d\tau. \tag{4.5}$$

The problem is to minimize the mean-squared error

$$\epsilon[h_n(\tau)] = E[|z(t) - s(t)|^2], \tag{4.6}$$

by varying the filter kernels $h_n(\tau)$. By using simple variational arguments, it is shown in Appendix B that the minimizing solution for $h_n(\tau)$ must satisfy the system

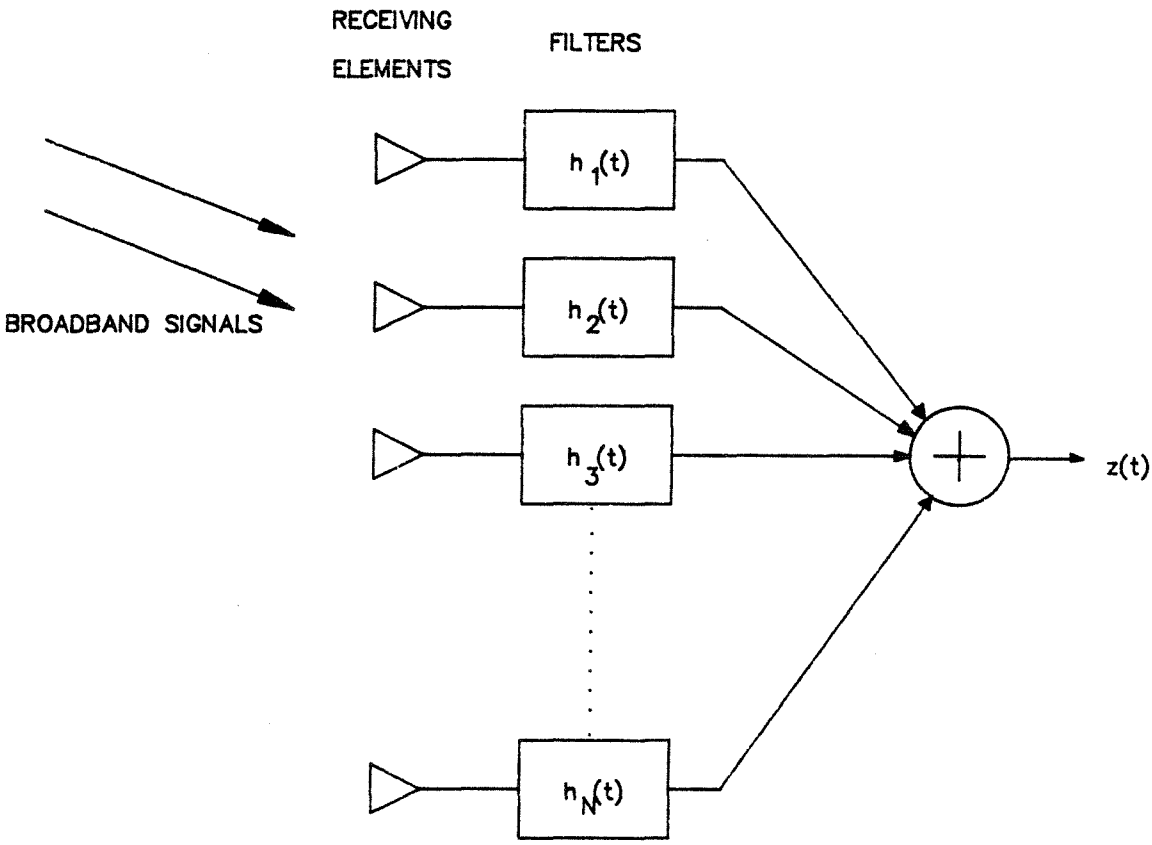

Fig. 4.5 Frost's Broadband Array Processor

of linear integral equations

$$\sum_{m=1}^{N} \int_{-\infty}^{\infty} h_m(\tau) \left[\alpha R(t-\tau) + \gamma_{mn}(t-\tau)\right] d\tau = R(t), \tag{4.7}$$

where $n = 1, 2, \ldots, N$. Transformation of the above system to the frequency domain yields

$$\sum_{m=1}^{N} H_m(f) \left[\alpha S(f) + \Gamma_{mn}(f)\right] = S(f). \tag{4.8a}$$

Here $S(f)$ is the spectral density function of the signal and $\Gamma_{mn}(f)$ is the cross-spectral density matrix of the interference, given by the Fourier transforms of the corresponding covariance functions, and $H_m(f)$ is the frequency response of the m_{th} filter of the array. For comparison, the corresponding equation for a narrowband processor with a single complex weight w_m for the m_{th} receiving element is

$$\sum_{m=1}^{N} w_m \left[\alpha + C_{mn}\right] = 1, \quad for\ n = 1, 2, ..., N, \tag{4.8b}$$

where α is the amplitude of the received signal component on boresight and $C_{mn} = E[v_m v_n^*]$, the covariance matrix of the noise components. A comparison of Eqs. 4.8a and 4.8b shows that the optimal broadband strategy is to simply provide an optimum narrowband weight for each frequency f. Thus, the optimum broadband system reduces to a channelized system of optimum narrowband sub-systems.

If we now assume that the signal spectrum is approximately white (e.g., spread spectrum codes) with spectral density S_0 and the received signal component is small compared to the noise so that $\alpha S_0 \ll 1$, then Eq. 4.8 can be approximated by

$$\sum_{m=1}^{N} H_m(f) \Gamma_{mn}(f) \approx S_0. \tag{4.9}$$

The frequency-dependent response of the individual filters can now be varied to compensate for the spectral characteristics of the environment, whereas the narrowband processor offered no such flexibility with its single, frequency-independent weight for each sensor.

4.3 Directional Cancellation of a Single Broadband Interference[2,4-6]

The example of a cancellation of a multi-frequency interference given in Fig. 4.4 shows that a narrowband array processor suppresses a broadband jammer by placing the null over a wide region near the interference direction. This is true in general for any narrowband array processor with a number of elements sufficiently large to null a broadband interference. A large number is needed because the array pattern shifts with frequency. By solving Eq. 4.9 explicitly for the case of a single broadband interference incident at an angle θ_i with respect to boresight, we will show analytically that the broadband system suppresses the interference with a null that does not shift with frequency, placed precisely at θ_i.

Let $\alpha(t)$ be the broadband interference waveform incident at an angle θ_i with respect to boresight, so that the n_{th} element receives the relatively delayed version $\alpha(t - n\Delta)$, where $\Delta = dsin\theta_i/c$. Assume that the interference waveform is derived from a zero mean stationary random process with the autocorrelation function given by $\gamma(\tau) = E[\alpha(t+\tau)\alpha^*(t)]$, the covariance between the interference received by the

n_{th} and m_{th} elements is given by

$$\begin{aligned}\gamma_{mn}(\tau) &= E\left[\alpha(t+\tau-m\Delta)\alpha^*(t-n\Delta)\right] \\ &= \gamma(\tau+(n-m)\Delta).\end{aligned} \tag{4.10}$$

The inclusion of sensor or receiver noise that is uncorrelated for each element and assumed to be white with spectral density σ_0^2 yields

$$\gamma_{mn}(\tau) = \gamma(\tau+(n-m)\Delta) + \delta_{mn}\delta(\tau)\sigma_0^2 \tag{4.11}$$

as the covariance of the total noise present in the m_{th} and n_{th} elements. The noise cross spectral density matrix, required for the optimal solution, is the Fourier transform of the above expression. It is given by

$$\Gamma_{mn}(f) = exp\{j2\pi f(n-m)\Delta\}S_\alpha(f) + \delta_{mn}\sigma_0^2. \tag{4.12}$$

The particularly simple form assumed by the noise cross spectral density matrix enables the inversion of Eq. 4.9 to be carried out explicitly. It can be shown that the solution of Eq. 4.9, which gives the optimum form for each filter, is given by

$$\begin{aligned}H_n(f) = (S_0/\sigma_0^2)\{1 - exp\{-j\pi f\Delta(N+1-2n)\} \\ \frac{sin(\pi fN\Delta)}{sin(\pi f\Delta)}S_v(f)/(\sigma_0^2+NS_v(f))\}.\end{aligned} \tag{4.13}$$

The gain pattern that results from this choice of filters can be determined by computing the array response to a monochromatic plane wave signal at various frequencies and incidence angles. Specifically, if we let θ represent the incidence angle of this probe beam, the gain pattern as a function of the probe frequency and angle

is given by

$$g(f,\theta) = (exp\{-j\pi f(N+1)\Delta'\}S_0/\sigma_0^2)\Big\{\frac{sin(\pi fN\Delta')}{sin(\pi f\Delta')} - exp\{-j\pi f(\Delta'-\Delta)(N+1)\}\frac{sin(\pi fN\Delta)}{sin(\pi f\Delta)} \frac{sin(\pi fN(\Delta'-\Delta))}{sin(\pi f(\Delta'-\Delta))}\frac{S_v(f)}{(\sigma_0^2+NS_v(f))}\Big\}, \tag{4.14}$$

where $\Delta' = dsin\theta/c$. At incidence angles other than that of the interference, θ_i, the second term is small since $\Delta \neq \Delta'$ so that

$$g(f,\theta \neq \theta_i) \approx (S_0/\sigma_0^2)exp\{-j\pi f(N+1)\Delta'\}\frac{sin(\pi fN\Delta')}{sin(\pi f\Delta')}, \tag{4.15}$$

which is simply the array pattern with uniform weighting.

When we probe near the interference, however, so that $\theta \approx \theta_i$, then the second term becomes appreciably large and the gain becomes

$$g(f,\theta \approx \theta_i) \approx (S_0/\sigma_0^2)exp\{-j\pi f(N+1)\Delta\}\frac{sin(\pi fN\Delta)}{sin(\pi f\Delta)} \{1 - NS_v(f)/(\sigma_0^2+NS_v(f))\}. \tag{4.16}$$

With the assumption that the interference power is large compared to that of the detector noise so that $NS_v(f) >> \sigma_0^2$, the gain becomes zero near the interference direction. Note also that this null in the array pattern remains fixed for all frequencies where there is sufficient interference power to overcome the detector noise.

4.4 Adaptive Array Processor

As in the strictly temporal case, the adaptive broadband sidelobe canceller also utilizes convolvers and correlators to accomplish the desired task. However, because of the multi-dimensional nature of the signals (spatial and temporal), arrays of correlators and convolvers must be employed. The basic system is shown in Fig. 4.6.

The output of the processor is simply the sum of all of the signals from the array elements and a feedback signal, which is derived from a cascade of multi-channel correlation and convolution operations performed on the output and input signals. The output is fed back to the first block, which calculates the correlation between the output signal and the N input signals from the array elements. Each of the resulting correlation functions, given by $(u_n(t) \star z(t))$, $n = 1, 2, \ldots, N$, is then convolved with its corresponding input. The N convolved results are summed to give

$$\hat{u} = G \sum_{n=1}^{N} u_n(t) * (u_n(t) \star z(t)) \tag{4.17}$$

as the feedback signal, where G is the feedback gain.

To show that the adaptive processor approximates the optimum response, however, the output must first be expressed in the form of Eq. 4.5, where the impulse response for each array filter is explicitly shown. We will show that the equation describing the filter impulse response functions, $h_n(t)$, $n = 1, 2, \ldots, N$, of the adaptive processor is approximately equivalent to that of the minimum mean-squared

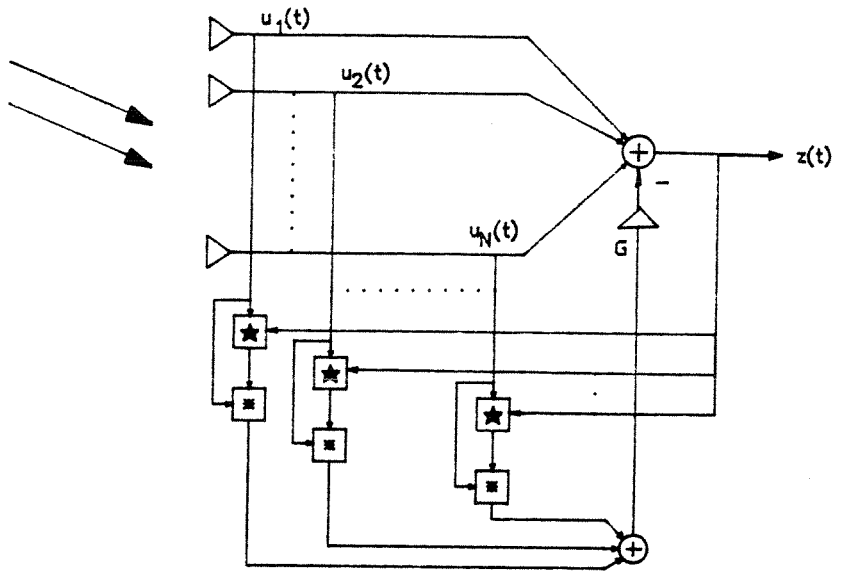

a)

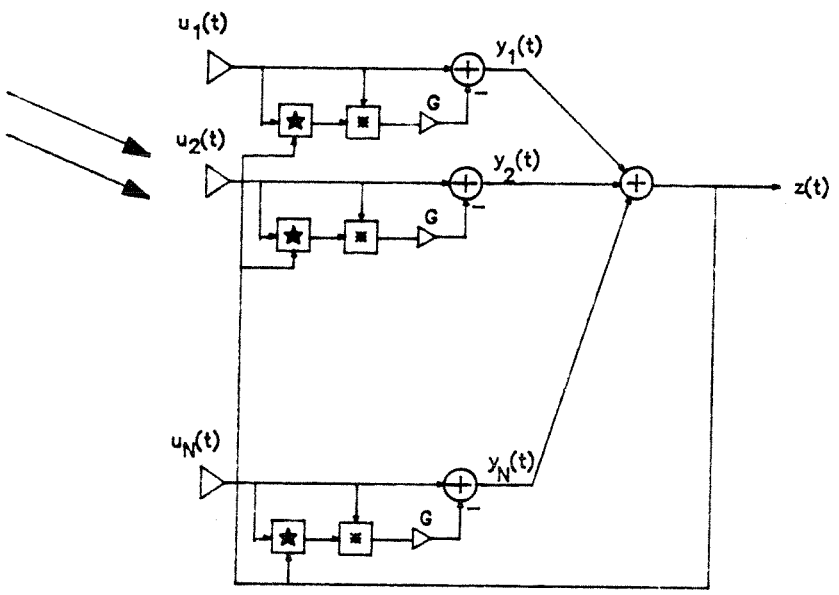

b)

Fig. 4.6 Broadband Adaptive Sidelobe Canceller a) and b) are identical systems

error processor given by Eq. 4.9.

In order to clarify the analysis to follow, we redraw the schematic of Fig. 4.6a as shown in Fig. 4.6b so that as in the Frost architecture (Fig. 4.5), the output from individual filters can be identified and described. Here, the output of the n_{th} filter is given by

$$y_n(t) = \int_{-\infty}^{\infty} h_n(t-\tau)u_n(\tau)d\tau,$$

or equivalently, $Y_n(f) = H_n(f)U_n(f)$ where $Y_n(f)$ is the Fourier transform of $y_n(t)$. The overall output is then given by $z(t) = \sum_n y_n(t)$. Inspection of Fig. 4.6b yields

$$\begin{aligned} x_n(t) =& u_n(t) - G\big[u_n(t) \star z(t)\big] * u_n(t) \\ =& \Big[\delta(t) - G\big[u_n(t) \star z(t)\big]\Big] * u_n(t), \end{aligned} \tag{4.18}$$

where $\delta(t)$ is the Dirac delta function. Since $x_n(t) = h_n(t) * u_n(t)$, the impulse response of the n_{th} filter is described by

$$\begin{aligned} h_n(t) =& \delta(t) - Gu_n(t) \star z(t) \\ =& \delta(t) - Gu_n(t) \star \sum_{m=1}^{N} u_m(t) * h_m(t). \end{aligned} \tag{4.19}$$

Taking the Fourier transform of the above equation and rearranging yields

$$\sum_m \left[\delta_{nm} + GU_n^*(f)U_m(f)\right] H_m(f) = 1, \tag{4.20}$$

where $U_n(f)$ is the Fourier Transform of $u_n(t)$. If the feedback gain G is sufficiently large so as to leave the first term of Eq. 4.19 negligible compared to the second, then Eq. 4.20 becomes

$$G\sum_m U_n^*(f)U_m(f)H_m(f) \approx 1. \tag{4.21}$$

This is of the same form as the optimum equation, Eq. 4.9, provided that the input SNR is sufficiently low so that we can identify $u_n^*(f)u_m(f)$ as the estimate of the noise cross spectral density matrix $\Gamma_{mn}(f)$. The particularly simple form of Eq. 4.20 can be inverted, however, to give a closed form solution for the adapted filtering functions. The derivation is analogous to that leading up to Eq. 4.13 and yields

$$H_n(f) = 1 - \frac{U_n^*(f)\sum_{m=1}^N U_m(f)}{1 + G\sum_{m=1}^N |U_m(f)|^2}, \quad n = 1, 2, .., N. \tag{4.22}$$

Suppose that the total signal received by the array consists of a weak probe signal on boresight represented by $p(t)$ whose Fourier transform is $P(f)$ and strong interference signals incident in other directions, the noise received by the n_{th} element represented by $v_n(t)$ whose Fourier transform is $V_n(f)$. Thus, the total input is given by $u_n(t) = p(t) + v_n(t)$. The probe is sufficiently weak as to only negligibly affect the determination of the filtering functions $H_n(f)$ so that approximately,

$$H_n(f) \approx 1 - \frac{V_n^*(f)\sum_{m=1}^N V_m(f)}{1 + G\sum_{m=1}^N |V_m(f)|^2}, \quad n = 1, 2, .., N. \tag{4.23}$$

The output is described by

$$\begin{aligned} Z(f) &= \sum_{n=1}^N H_n(f)U_n(f) \\ &= \sum_{n=1}^N \left[1 - \frac{V_n^*(f)\sum_{m=1}^N V_m(f)}{1 + G\sum_{m=1}^N |V_m(f)|^2}\right]\left[P(f) + V_n(f)\right]. \end{aligned} \tag{4.24}$$

Further expansion yields

$$Z(f) \approx \left[N - \frac{|\sum_{m=1}^{N} V_m(f)|^2}{1 + G\sum_{m=1}^{N} |V_m(f)|^2}\right] P(f) + \sum_{n=1}^{N} V_n(f) \left[1 - \frac{\sum_{m=1}^{N} |V_m(f)|^2}{1 + G\sum_{m=1}^{N} |V_m(f)|^2}\right]. \tag{4.25}$$

As expected, the second term is effectively suppressed if the feedback gain can be made large.

4.5 Optical Implementation

The optical implementation of the adaptive sidelobe canceller is a fairly straightforward extension of the optical techniques used for the temporal systems described in Chapter 3. The extension is made simply by using arrays of convolvers and correlators to handle the N input signals from the antenna array sensors. The input spatial light modulators to be used are multi-channel and single channel acousto-optic devices that offer large dynamic range and can operate on broadband signals. We concentrate first on a space-time integrating system that involves the use of a photorefractive crystal to perform the time integration. A strictly space integrating array processor is described in Section 4.6.

The basic task of the processor is to form the feedback signal given by Eq. 4.17. Note, however, that since correlation can be expressed as $u_n(t) \star z(t) = u_n^*(-t) * z(t)$,

and convolution is both an associative and commutative operation, the feedback signal can be expressed equivalently as

$$\hat{u}(t) = Gz(t) * \sum_{n=1}^{N} u_n(t) * u_n^*(-t). \tag{4.26}$$

This rearrangement suggests that we can modify the system architecture somewhat by first computing an autocorrelation function of each input signal, adding the autocorrelations and convolving the summed result with the output, $z(t)$, to form the feedback signal as illustrated in Fig. 4.7.

For the purpose of discussion, however, we adhere to the strict interpretation of Eq. 4.17 as discussed in 4.4. As shown in Fig. 4.6a, the output is first correlated against each of the N input waveforms, and each resulting correlation is then convolved with its corresponding input. The N convolution-correlation signals thus produced are summed to form the feedback signal. The multi-channel correlations are performed using time integration and the convolution with the output signal is achieved with space integration.

Shown in Fig. 4.8 is the multi-channel correlator, where the output autocorrelations are written as modulations of an index grating formed on the crystal by the photorefractive effect. More specifically, AOD1 and AOD2 are arranged to operate in a coherent, additive architecture. The single channel AOD1 diffracts a portion of its input light. This passes through AOD2 without being affected because of Bragg mismatch and is imaged onto the crystal to yield the amplitude $z(t+x/v-T/2)exp\{j2\pi f_0(t+x/v)\}$ in the crystal plane. The multi-channel AOD2

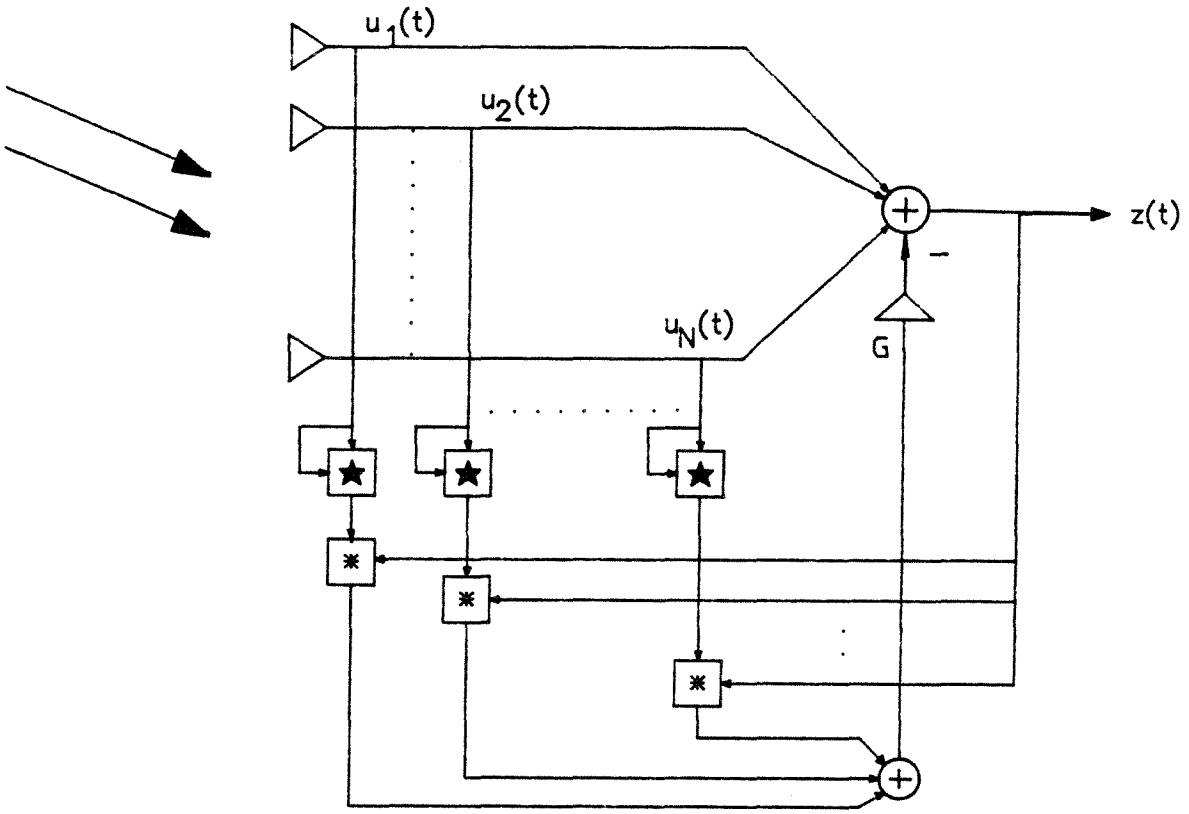

Fig. 4.7 Variant of the Broadband Adaptive Array Processor

diffracts the undiffracted beam from AOD1, which is aligned to be well matched to its acoustic gratings to yield the optical amplitude

$$\sum_n u_n(t - x/v - T/2) r_n(y) exp\{j2\pi f_0(t - x/v)\},$$

also imaged onto the crystal. Here $r_n(y)$ characterizes the vertical confinement of the acoustic beam in each channel of the multi-channel AOD and can be approximated by

$$r_n(y) = (\frac{1}{N\delta y}) rect\left[\frac{y - (n - \frac{N+1}{2})y_0]}{\delta y}\right], \quad n = 1, 2, .., N, \tag{4.27}$$

δy being the acoustic beam width and y_0 the separation between neighboring channels, where N is assumed to be odd.

These two amplitudes are incident at an angle with respect to each other. Since both have the same Doppler-shift in frequency, an intensity grating is seen by the crystal. In fact, an array of one-dimensional modulated index gratings, each confined vertically by $r_n(y)$, is formed within the crystal. It can be shown that the modulation functions are proportional to the desired correlation functions, and specifically, the diffracted light due to the n_{th} grating when the crystal is illuminated by a plane wave is given by [8] $E_n(x, y)exp\{-j2\pi f_0(2x/v)\}$. Here

$$\begin{aligned} E_n(x, y) &\propto r_n(y) \int_0^t exp[(t' - t)/\tau] u_n(t' - x/v - T/2) z^*(t' + x/v - T/2) dt' \\ &\propto r_n(y) \int_{t-x/v-T/2-\tau}^{t-x/v-T/2} u_n(t') z^*(t' + 2x/v) dt'. \end{aligned} \tag{4.28}$$

In this equation, the exponentially decaying window function has been approximated by a rectangular window of temporal duration τ. The resulting integral is

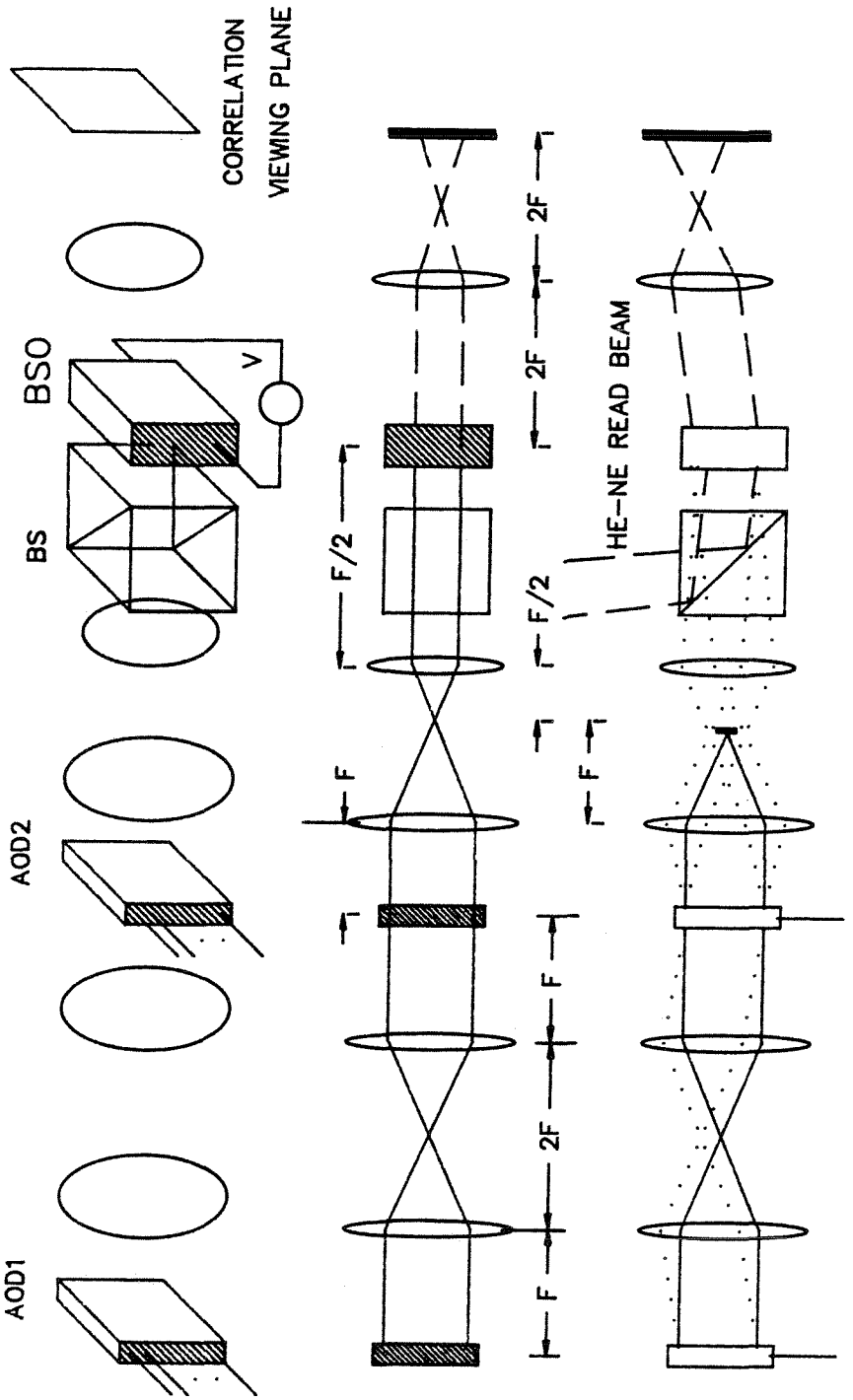

Fig. 4.8 Multi-Channel Photorefractive Correlator

proportional to the correlation function of $u_n(t)$ and $z(t)$ with $2x/v$ as the shift variable.

To complete the task of forming the feedback signal, we combine the previously described correlators with a space integrating convolver, resulting in the system shown in Fig. 4.9. The added portions are the multi-channel AOD (AOD3) which is driven by the system output $z(t)$, some imaging optics, and a single photodetector. Since the autocorrelations are available at a compressed horizontal spatial scale, $2x/v$, a combination of cylindrical and spherical lenses C1,L5,L6 is used to anamorphically image AOD3 onto the crystal. This anamorphic imaging provides a 2:1 demagnification ratio in the horizontal direction and 1:1 in the vertical.

A portion of the He-Ne read beam is diffracted by AOD3 and passes through the crystal unaffected since its propagation direction is not properly Bragg-matched to the correlation gratings in the crystal. The DC beam from AOD3, however, is arranged to be Bragg matched to the gratings and reads out the correlation functions. If the acoustic velocity in AOD3 is v, the same as that of AOD1 and AOD2, and all of the AODs are driven at the same frequency, f_0, then the read beam diffracted by the crystal and that diffracted by AOD3 are collinear and interfere temporally at f_0 because of the Doppler shift induced by AOD3. The diffracted light amplitude just behind the crystal due to the crystal gratings is proportional to $\sum_n E_n(x,y)exp\{j2\pi f_0(-2x/v)\}$, and the diffracted light from AOD3 evaluated at the same plane is $\sum_n exp[j2\pi f_0(t-2x/v)]u_n(t-2x/v-T/2)r_n(y)$.

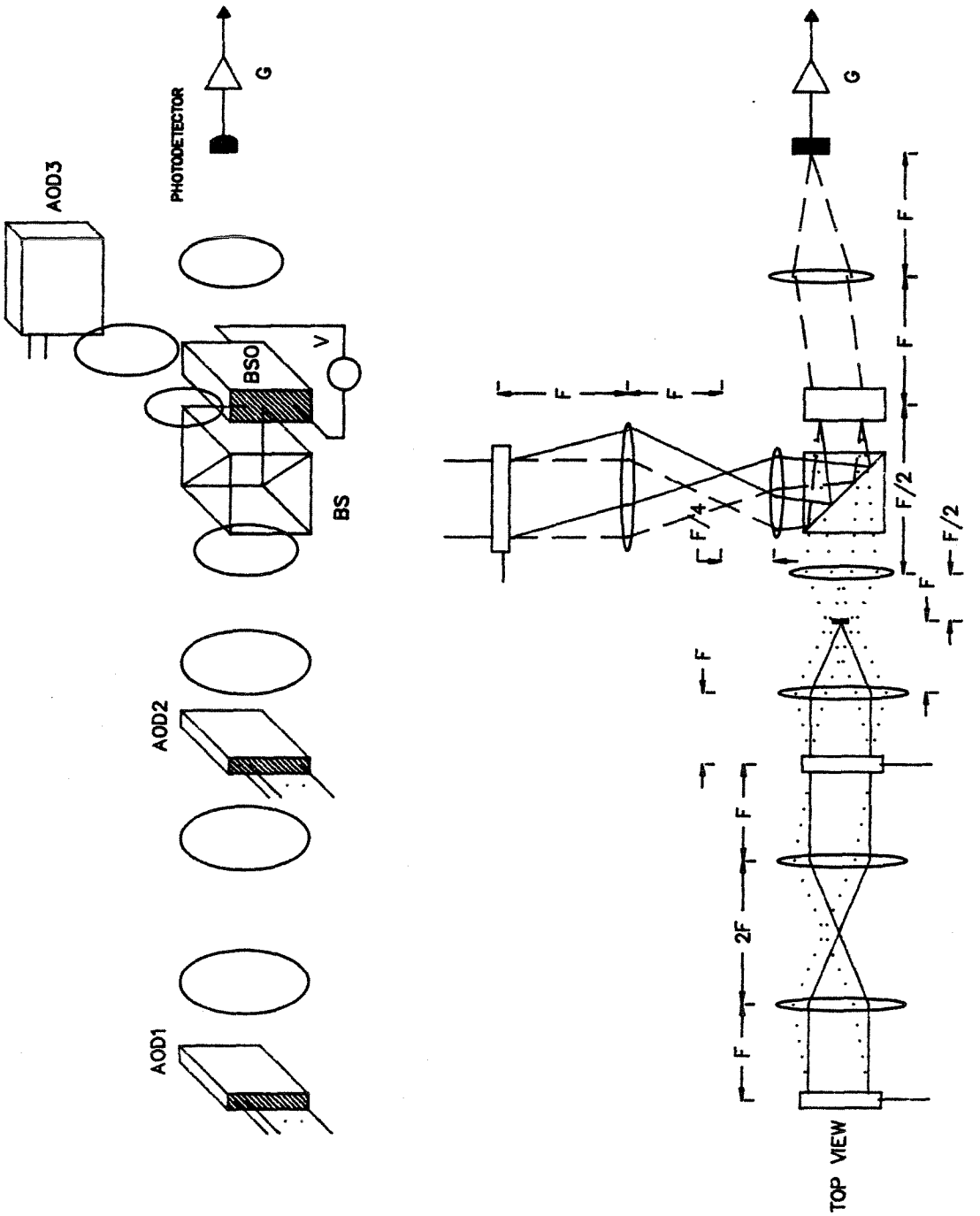

Fig. 4.9 Photorefractive Adaptive Array Sidelobe Canceller

The sum of the above two amplitudes are Fourier transformed by lens L7, and the resulting intensity distribution is integrated across the Fourier plane by a sufficiently large photodetector. If w is the width of each AOD, the result is the output photocurrent

$$\begin{aligned} i(t) &\propto Re\left\{ exp\{j2\pi f_0 t\} \sum_n \int_{-w/4}^{w/4} \int_{-\infty}^{\infty} E_n^*(x,y) u_n(t - 2x/v - T/2) dy dx \right\} \\ &\quad + DC terms \\ &\propto Re\Big\{ exp\{j2\pi f_0 t\} \sum_n \int_{-w/4}^{w/4} \int_{-\infty}^{\infty} \int_{t-x/v-T/2-\tau}^{t-x/v-T/2} r_n(y) u_n^*(t') z(t' + 2x/v) \\ &\quad u_n(t - 2x/v - T/2) dt' dy dx \Big\} + DC terms \\ &\propto Re\Big\{ exp\{j2\pi f_0 t\} \sum_n \int_{-T/4}^{T/4} \int_{t-x/v-T/2-\tau}^{t-x/v-T/2} u_n^*(t') z(t' + 2x/v) \\ &\quad u_n(t - 2x/v - T/2) dt' dx \Big\} + DC terms. \end{aligned} \tag{4.29}$$

The high frequency term centered at f_0 is approximately equal to the desired feedback signal given by Eq. 4.17. The output of the system $z(t)$ is then formed by subtracting the feedback signal from the sum of the input signals $\sum_n u_n(t)$ to yield

$$\begin{aligned} z(t) = \sum_n \Big\{ u_n(t) - (\frac{G}{T\tau}) \int_{-T/4}^{T/4} \int_{-\tau}^{0} u_n^*(t' + t - \beta - T/2) z(t' + t + \beta - T/2) \\ u_n(t - 2\beta - T/2) dt' d\beta \Big\}, \end{aligned} \tag{4.30}$$

where $\beta = x/v$, $T = w/v$, and G is the feedback gain. Here we have assumed that the signals received by the array are all centered at f_0 and that they drive the AODs directly after being amplified.

By defining an equivalent impulse response, $h_n(\alpha)$, for the system such that

$z(t) = \sum_n \int_{-\infty}^{\infty} h_n(\alpha) u_n(t-\alpha) d\alpha$, Eq. 4.30 can be expanded further to give

$$z(t) = \sum_n \Big\{ u_n(t) - (\frac{G}{T\tau}) \sum_n \int_{-T/4}^{T/4} \int_{-\tau}^{0} \int_{-\infty}^{\infty} u_n^*(t'+t-\beta-T/2) h_m(\alpha) \\ u_m(t'+t+\beta-T/2-\alpha) u_n(t-2\beta-T/2) d\alpha dt' d\beta \Big\}. \tag{4.31}$$

An equation that describes the impulse response can then be derived by noting that the output appearing on the left side of the above equation can be expressed, using the impulse response. With the assumption that the integration time, τ, is long enough to warrant the approximation $sinc[f\tau] \approx \delta(f)$, the resulting impulse response equation is given by

$$h_n(\beta) \approx \delta(\beta) - (\frac{G}{T}) rect[\frac{\beta - T/2}{T}] \sum_m \int \int_{-\infty}^{\infty} exp\{j2\pi f'(\beta - \alpha - T/2)\} \\ h_n(\alpha) U_n^*(f') U_m(f') df' d\alpha, \tag{4.32}$$

where $U_n(f)$ is the Fourier transform of the n_{th} input signal $u_n(t)$. Taking the Fourier transform of the above equation gives

$$H_n(f) = 1 - G \sum_m \int_{-\infty}^{\infty} exp\{j\pi(f'-f)T\} sinc[(f'-f)T] H_m(f') U_n^*(f') U_m(f') df'. \tag{4.33}$$

This is very similar to the optimal equation discussed in 4.2 if we identify the product $U_n^*(f)U_m(f)$ as an approximation of the required cross spectral density matrix. In particular, the effect of the finite convolution time is to distort the spectral properties of the input noise field. Thus, the optical implementation is expected to place a spectrally broader null in comparison with the interference bandwidth, but the spatial characteristics remain similar to the optimal case.

4.6 Adaptive Array Processor with Variable Look Direction

The array processor described thus far is a sidelobe-cancelling system where the maximum sensitivity (the "look direction") is always constrained to be in the direction of boresight.* In this section, an acousto-optic processor is presented which is an extension of the temporal active processor described in Chapter 3 to the space-time domain. The optical architecture considered uses space integration as opposed to the photorefractive implementation considered in the previous section. The optimizing criterion used is that of maximizing the output SNR (signal detection) and the signal need not arrive on boresight.

The scenario considered is that where a signal waveform $s(t)$ is incident on the array at a known angle θ with respect to boresight, and noise (possibly broadband) from directional sources corrupt the received signal waveform. Let $s_n(t) = s(t - n(d/c)cos\theta)$ be the signal waveform received by the n_{th} element. The total signal received by the n_{th} element is then given by $u_n(t) = s_n(t) + v_n(t)$, where $v_n(t)$ is the sum of all noise terms. Here d is the array element spacing, and c is the speed of light.

The output of a general space-time filter can be expressed as

$$y(t) = \sum_{n=1}^{N} \int_{-\infty}^{\infty} u_n(\tau) h_n(t - \tau) d\tau, \tag{4.34}$$

* The look direction can be changed by introducing appropriate delays in the signals received by each element before they are processed.

where $u_n(t)$ is the complex envelope of the total rf signal (centered at f_0) received by the n_{th} array element, and $h_n(t)$ is the filtering function for each channel. A similar expression is obtained for the optically implemented space-time filter using two multi-channel AODs shown in Fig. 4.10. This is completely analogous to the single channel AO convolver of Section 3.1.1. This system is coherent, and the output can be shown to be given by

$$y(t) = \frac{2c_1}{T} \sum_{n=1}^{N} \int_0^{T/2} u_n(t - \tau - T/2) h_n(t + \tau) d\tau, \tag{4.35}$$

where the filtering function $h_n(t)$ is used to drive the second AOD, and c_1 is a constant that depends on laser power, AOD diffraction efficiencies, and the quantum efficiencies of the detectors. The only differences from the general filter (Eq. 4.34) are limited accumulation time and the time compression of the output. This is of little consequence since signal detection rather than estimation is considered here. The noise $v_n(t)$ present in the received signal is modeled by a zero-mean random process with a covariance matrix given by

$$\gamma_{mn}(t) \equiv E[v_m(t) v_n^*(t - \tau)]. \tag{4.36}$$

It can be shown through variational arguments that the choice of $h_n(t)$, for which the SNR of the AO space-time filter is maximum at a specified time t_0, must satisfy the following system of integral equations:

$$\sum_{m=1}^{N} \int_{-\infty}^{\infty} \gamma_{mn}(\tau - \beta) h_m(\beta) d\beta = \lambda s_n^*(t_0 - \tau), \quad n = 1, 2, .., N. \tag{4.37}$$

The details of this derivation are given in Appendix B.

For adaptivity, we need to calculate and continuously update the filter function to drive the output to the optimum result. As with the temporal active processor, the output must be correlated with the input to produce the appropriate filter function. Since the array processor has N inputs and one output, this requires that we correlate N signals with a common one. This can be achieved with the arrangement shown in Fig. 4.11. That figure shows the use of a multi-channel AOD driven by the N antenna element outputs in conjunction with a single channel AOD driven by the processor output signal.

This architecture is identical to that of the one-dimensional correlator of Fig. 3.6, except that the first AOD has been replaced by a multi-channel AOD, and the output is detected not by a single detector but by an array of N detectors. Specifically, the complex envelope of the output of the n_{th} detector element is given by

$$r_n(t) = \frac{4c_2}{T} \int_{-T/4}^{0} y(t+\tau) u_n^*(t+2\tau - T/2) d\tau, \tag{4.38}$$

where c_2 is a constant that depends on the laser power, AOD diffraction efficiencies, and the quantum efficiency of the detector. For proper correlation to appear at each output, the signal driving the single channel AOD must be time-compressed by a factor of two. This is indeed the case for the system described. Thus, the AOD implemented space-time filter and the N channel correlator with a single reference are compatible.

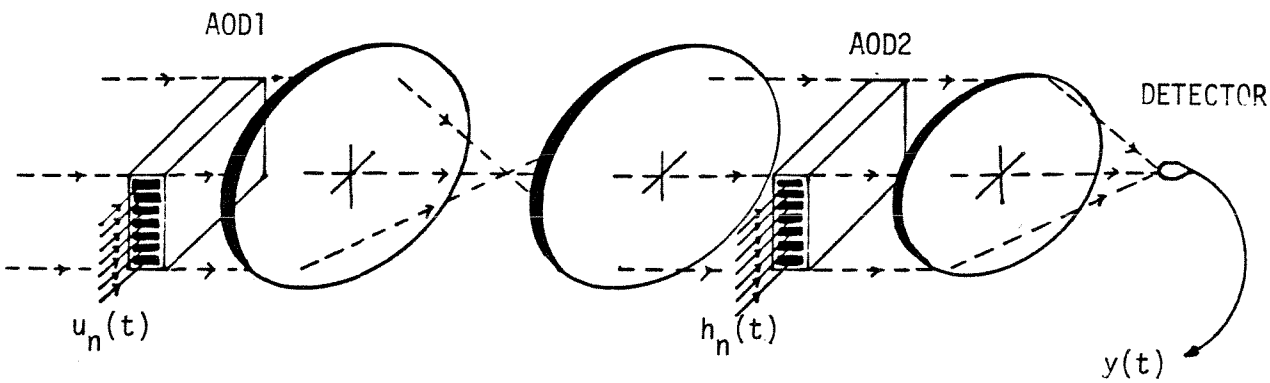

Fig. 4.10 Multi-Channel Acousto-Optic Space Integrating Convolver

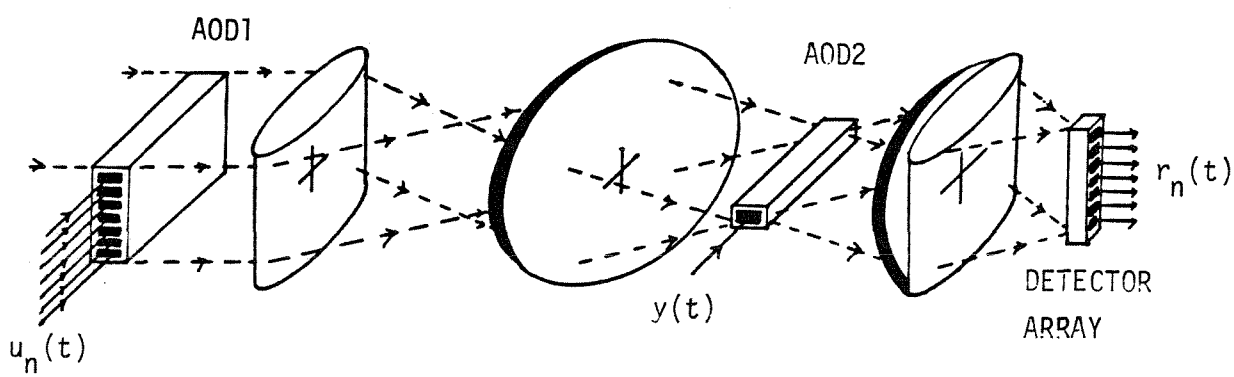

Fig. 4.11 Multi-Channel Acousto-Optic Space Integrating Correlator with a Single Reference

Shown in Fig. 4.12 is the array processor block diagram that shows the interconnections required; it is a direct extension of the temporal active processor to two dimensions. The output from each antenna element is correlated with the processor output to produce the filter function for that element. The "steering vector" $s_i^*(-t)$ determines the look direction of the array and also is the temporal reference signal used for the detection of the desired signal $s(t)$.

Fig. 4.13 shows the optically implemented adaptive array processor with the AOD implemented space-time filter in the upper branch and the N channel correlator in the lower one. By combining Eqs. 4.35 and 4.38, the equation that determines the filter function $h_n(t)$ is seen to be

$$h_n(t) = s_n^*(-t+t_0) - G\frac{8c_1c_2}{T^2}\sum_m \int_0^{T/2}\int_{-T/4}^{0} u_n^*(t+2/beta-T/2) \\ u_m(t+\beta-\tau-T/2)h_m(t+\beta+\tau)d\beta d\tau, \tag{4.39}$$

where G is the feedback gain. Under conditions of low input SNR and large feedback gain, Eq. 4.39 can be transformed to the frequency domain to yield

$$exp(-j2\pi f_0 t_0)S_n^*(f) \approx Gc_1c_2\sum_{m=1}^{N} H_m(f)\int_{-\infty}^{\infty} U_n^*(f')U_m(f') \\ exp[j\pi(f-f')T/4]sinc[(f-f')T/4]sinc[(f-f')T/2]df', \tag{4.40}$$

where $S_n(f)$ is the Fourier transform of $s_n(t)$.

For comparison, consider the Fourier transform of Eq. 4.36; the optimum filter equation is given by

$$\sum_m \Gamma_{mn}(f)H_m(f) = \lambda exp(-j2\pi f t_0)S_n^*(f), \tag{4.41}$$

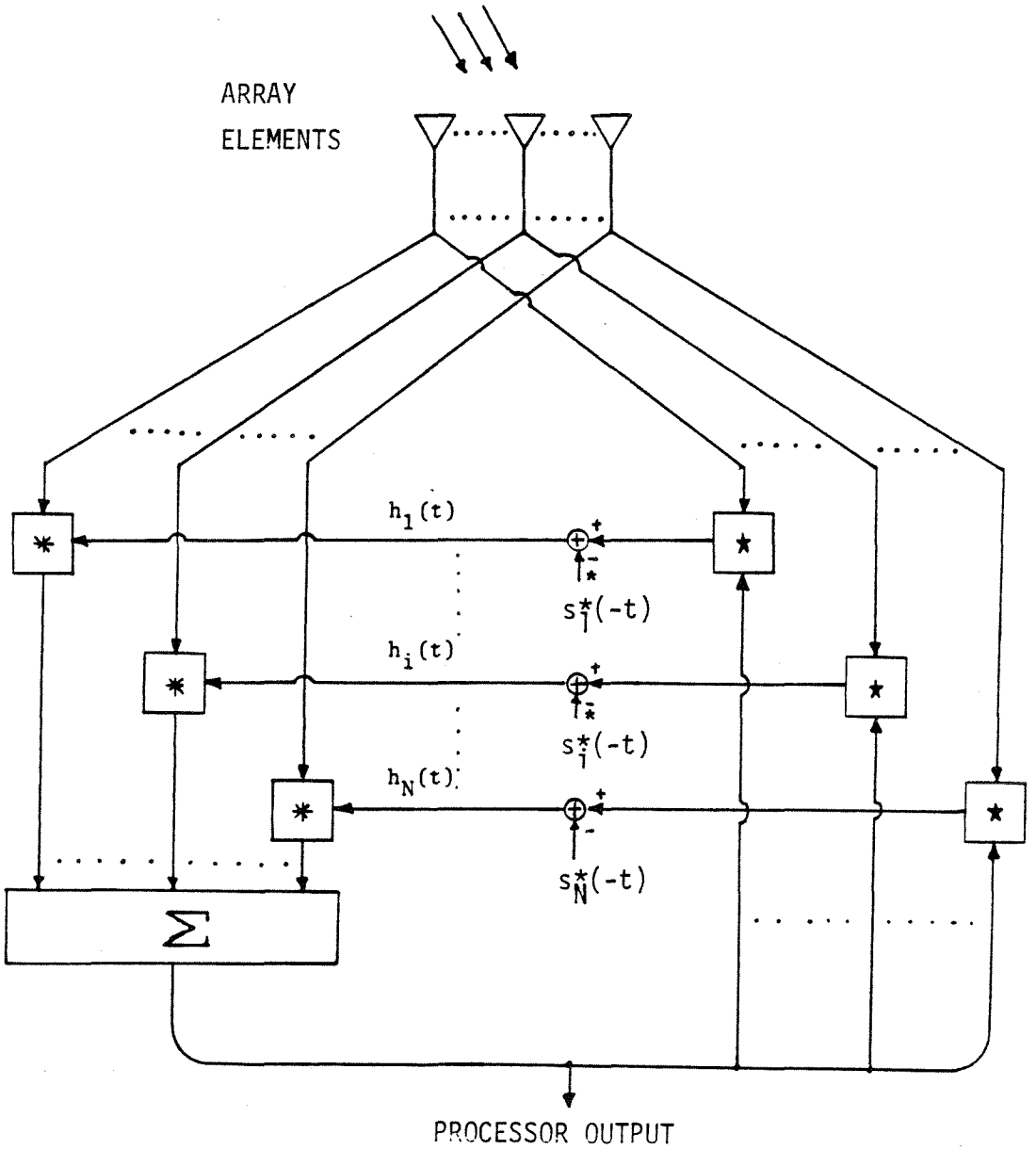

Fig. 4.12 Broadband Adaptive Array Processor to Maximize the Output SNR

where $\Gamma_{mn}(f)$ is the spectral density matrix. Identifying the integral in Eq. 4.40 as the smoothed estimate of the cross spectral density matrix of the input noise vector, Eq. 4.40 is approximately equivalent to Eq. 4.41. However, the effect of the finite time integration window is seen in the smoothing of the noise spectrum.

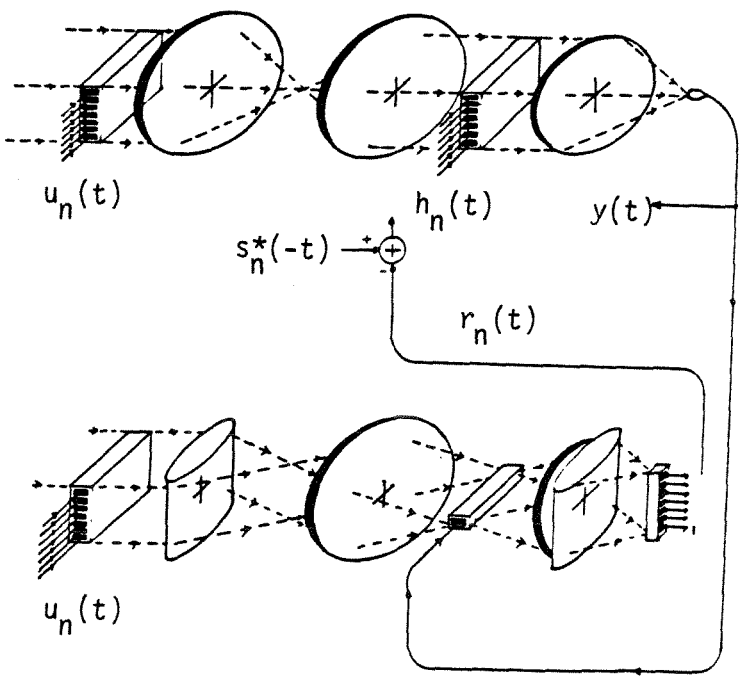

Fig. 4.13 Acousto-Optic Adaptive Array Processor to Maximize the Output SNR

References for Chapter 4

[1] A. P. Appelbaum, "Adaptive arrays," *IEEE Trans. Antennas. Prop.*, **AP-24**, 585 (1976).

[2] B. Widrow, P. E. Mantey, L. J. Griffiths, and B. B. Goode, "Adaptive antenna systems," *Proc.IEEE*, **55**, 2143 (1976).

[3] W. F. Gabriel, "Adaptive arrays - an introduction ," *Proc.IEEE*, **64**, 2 239 (Feb. 1976).

[4] R. A. Monzingo and T. W. Miller, *Introduction to Adaptive Arrays*, John Wiley and Sons, New York, 1980.

[5] O. L. Frost. III, "An algorithm for linearly constrained adaptive array processing," *Proc. IEEE*, **60**, no.8, 925 (Aug. 1972).

[6] J. H. Chang and F. B. Tuteur, "A new class of adaptive array processors," *J. Acoust. Soc. Am.*, **49**, no.3, 639 (Mar. 1971).

[7] W. E. Rodgers and R. T. Compton, Jr., "Adaptive array bandwidth with tapped delay-line processing," *IEEE Trans. Aero. Elec. Sys.*, **AES-15**, no.1, 21 (Jan. 1979).

[8] N. V. Kukhtarev, V. B. Markov, S. G. Odulov, and M. S. Soskin, "Holographic storage in crystals I: steady state," *Ferroelectrics*, **22**, 949 (1979).

[9] R. O. Duda and P. E. Hart, *Pattern Classification and Scene Analysis*, John Wiley and Sons, New York, 1973.

Chapter 5. Associative Memory Models

5.1 Introduction

Without regard to implementation details, an associative memory is characterized operationally by two key features. First, it is programmed to store input-output pairs of data so that when a certain input is recognized as one of the stored items, the output associated with it is retrieved. Secondly, it is capable of error correction, allowing input items that are distorted versions of any of the stored data to be recognized and mapped to the correct association. These characteristics are illustrated in Fig. 5.1, where the memory is used to associatively store pictures with their respective names so that the presentation of one of the stored pictures causes its name to appear as the output in response. Also illustrated is the notion of error correction. Although the input picture differs slightly from one of the stored pictures, the correct response is invoked. An associative memory can therefore be described as a system that can be programmed to perform many-to-one mappings of input $\underline{f}_m + \delta\underline{f}$ to outputs $\underline{g}_m$ for $m = 1, 2, \ldots, M$, where the input error $\delta\underline{f}$ is small in some sense.

Shown in Fig. 5.2 is a schematic diagram of a neural network where the circles represent the computing elements or "neurons" (which can be threshold gates), and the interconnecting lines represent the weights that couple the "neurons" to each other. See Refs. [1,4,5,8] for further detail on this type of neural network model.

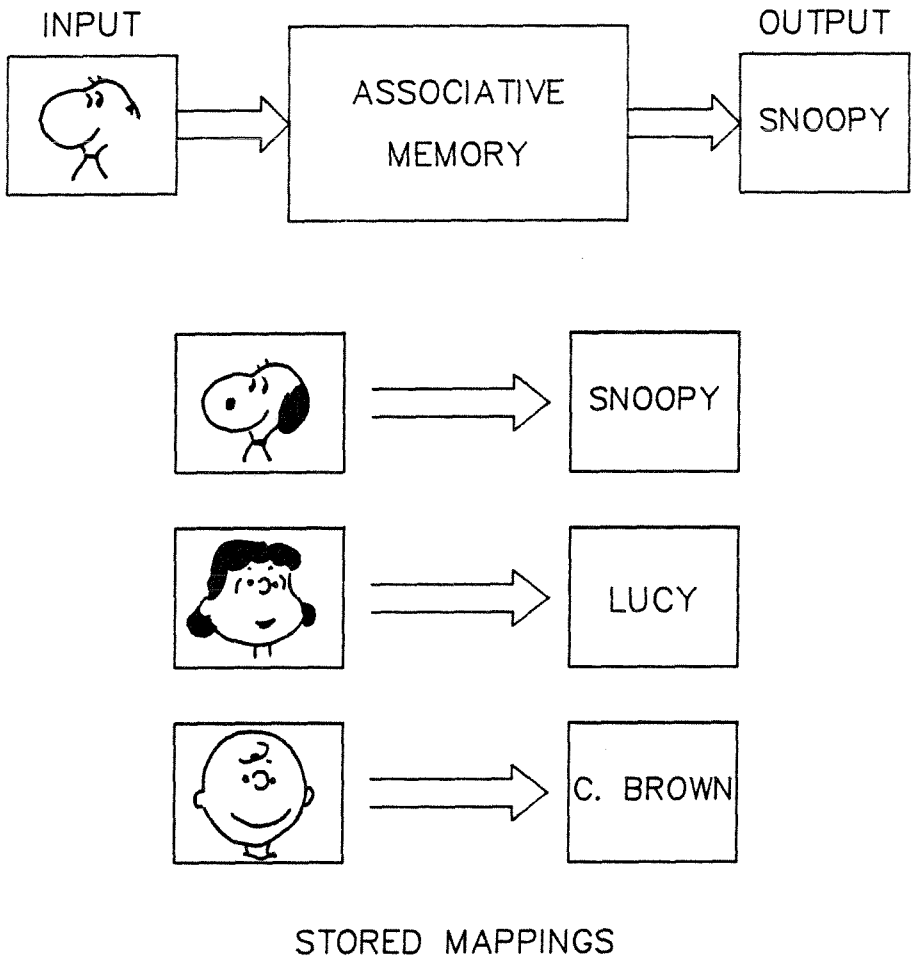

Fig. 5.1 Associative Memory (this is an example of heteroassociative memory where the three pictures are stored in association with their respective names)

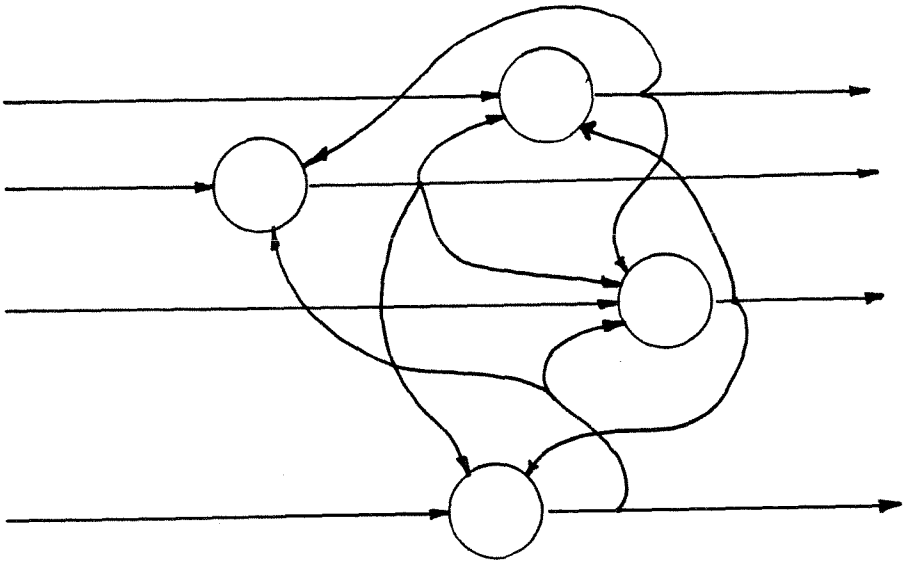

Fig. 5.2 A 4 Element Network

Each "neuron" has one output which, in this example, is connected to the input of every other neuron. The associative memory paradigm can be implemented in such a system by specifying the interconnection weight values such that a recognized input pattern elicits the desired output pattern through the cooperative action of the interconnected network. Data storage is therefore accomplished in a distributed way. It has been shown that associative recall is achieved even when some of the interconnections are corrupted by noise or damage [1].

In this chapter, we review some methods of specifying the interconnection weights for associative storage and recall of data and the issue of storage capacity. An optical system that implements the memory paradigms is then described.

5.2 Linearly Interconnected Memories

5.2.1 The Hopfield model [1]

The associative memory described in the previous section can also be thought of as an array of discriminant functions as shown in Fig. 5.3, if the output vector is binary valued [2]. In this case, each bit of the output vector is the result of a binary decision based on the input vector. A discriminant function can be any arbitrary function that maps the N dimensional input vector $\underline{f}$ to either "1" or "0." A linear discriminant function (LDF) is a specific case in which the decision rule is given by

$$\sum_{i=1}^{N} w(i)f(i) - \theta \gtrless 0, \tag{5.1}$$

where $w(i)$ are the weight values and θ is the threshold level. An associative memory that can store inputs $\underline{f}_m$ paired with outputs $\underline{g}_m$ can be constructed by configuring an array of N such LDF decision machines and appropriately selecting the required weight values. The number of dichotomies that can be performed by one LDF is limited to N where N is the number of elements of the weight vector. From this, it follows that an associative memory implemented by an array of N LDFs can store at most N associations. This provides an upper bound on the capacity of linearly interconnected memories [2].

There exist several methods for specifying the linear transformation (array of LDFs) for associative memory applications. To simplify the discussions to follow, we shall henceforth focus attention on the problem of *auto-association* in which the

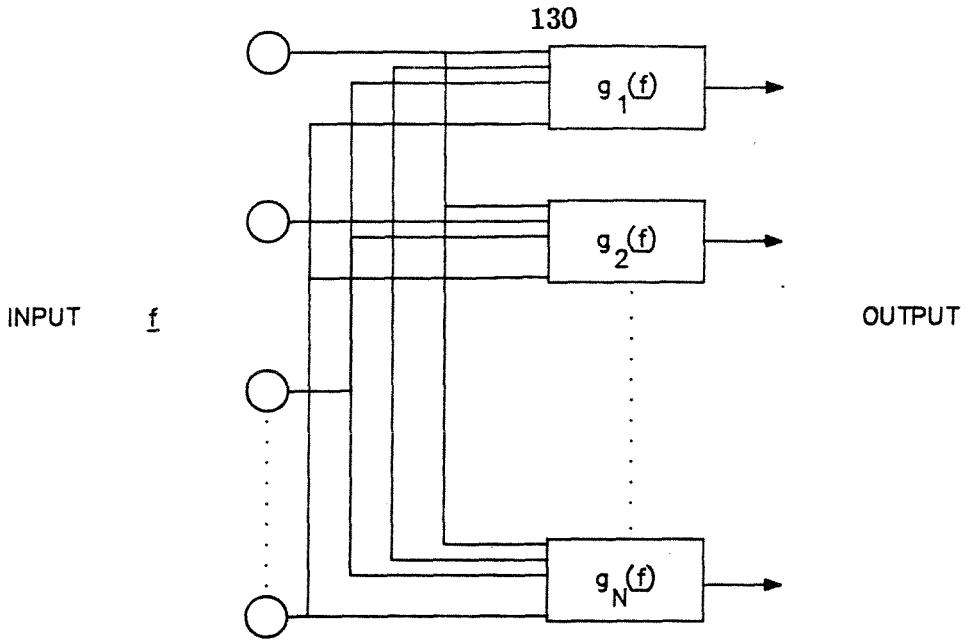

Fig. 5.3 Associative Memory as an Array of Discriminant Functions

linear transformation is chosen to store M N-bit binary, bipolar (i.e., each bit is ± 1) vectors $\underline{f}_m$ such that for each m, $\underline{f}_m$ is the memory output for an input $\underline{f}_m + \delta\underline{f}$. Related to a neural network-learning algorithm known as *Hebb's Hypothesis*, the outer product method offers a particularly simple prescription of the weight matrix [1,3]. Specifically, the weight matrix is given by the sum of outer products of the memory vectors:

$$w(i,j) = \begin{cases} \sum_{m=1}^{M} f_m(i) f_m(j), & \text{if } i \neq j; \\ 0, & \text{if } i = j. \end{cases} \tag{5.2}$$

When interrogated by one of the memory vectors, say $\underline{f}_1$, this yields the following product to be thresholded:

$$\begin{aligned} \hat{f}(i) &= \sum_{j \neq i} w(i,j) f_1(j) = \sum_{m=1}^{M} \Big[\sum_{j \neq 1} f_m(j) f_1(j) \Big] f_m(i) \\ &= (N-1) f_1(i) + \sum_{m=2}^{M} \Big[\sum_{j \neq 1} f_m(j) f_1(j) \Big] f_m(i) \end{aligned} \tag{5.3}$$

The response to an input $\underline{f}_1$ is a weighted sum of the stored vectors, the weights being the inner products between the stored vectors and the input. The sum is dominated by the desired response $f_1(i)$, which we call the *signal.* The output thresholded vector is given by

$$f(i) = sgn[\hat{f}(i)] = \begin{cases} 1 & \text{if } \hat{f}(i) \geq 0; \\ -1 & \text{if } \hat{f}(i) < 0. \end{cases} \tag{5.4}$$

If we assume that the memory vectors $f_m(i)$ are chosen randomly so that each bit is statistically independent with equal probabilities of being 1 or -1, the signal-to-noise ratio of the retrieved product can be computed to yield

$$\text{SNR} = \sqrt{(N-1)/(M-1)} \approx \sqrt{\frac{N}{M}}. \tag{5.5}$$

The *Hopfield model* incorporates feedback in which the *thresholded* output is used as the next input and the system is allowed to iterate until a fixed point is reached. If the SNR given by Eq. 5.4 is sufficiently high, then the prescribed memory vectors will indeed be stable fixed points of the system. Based on the SNR given by Eq. 5.4, a statistical bound on the total number of vectors that can be stored as stable fixed points has been found [4,5] to be $M < N/(2lnN)$.

Hopfield [1] has analyzed the dynamics of the associative memory network by defining an energy function for the network given by

$$H = -\frac{1}{2}\sum\sum_{i \neq j} f(i)w(i,j)f(j), \tag{5.6}$$

where $f(i)$ represents the output state of the memory at a particular time. If we allow only one randomly chosen bit to be changed at each iteration, the resulting

energy change is given by

$$\Delta H = -[\sum_{j \neq i} w(i,j) f(j)] \Delta f(i), \tag{5.7}$$

where only the i_{th} bit has been allowed to change according to the rule given by Eq. 5.4. This relation is true in general for any interconnection matrix $w(i,j)$ that is symmetric and has diagonal terms equal to zero. Clearly, for non-zero change, the output product $\sum_{j \neq i} w(i,j) f(j)$ and the change $\Delta f(i)$ have the same sign so that the energy is a non-increasing function of time. Thus, the Hopfield memory is guranteed to decrease the energy in closed loop operation until a local minimum in energy is reached. Since the stored vectors on the average preside at positions of locally minimum energy, the system will usually iterate until one of the M stored vectors is accessed.

The iterative operation of the system is illustrated by the computer simulation described by Fig. 5.4 where the matrix shown is the outer product weight matrix computed for the 4 20-bit binary, bipolar vectors shown next to it. The 4 vectors were first verified to be fixed points of the system. When probed by an input vector which is different from the first vector by 6 bits as shown, the system first corrected 5 bits as indicated and converged to the correct result by the third iteration.

The overall performance of the memory does not degrade noticeably when the interconnection matrix is "clipped" [1] in the following way.

$$w'(i,j) = \begin{cases} 1 & \text{if } w(i,j) \geq 0 \text{ and } i \neq j; \\ -1 & \text{if } w(i,j) < 0 \text{ and } i \neq j; \\ 0 & \text{if } i = j, \end{cases} \tag{5.8}$$

```
  memory vectors are (unipolar versions)
#1      0  1  0  0  0  0  1  1  1  1  0  1  0  1  0  0  0  1  0  1
#2      1  1  0  1  1  0  1  0  1  0  1  0  0  1  1  0  0  1  1  1
#3      0  1  1  0  1  0  0  0  1  1  0  1  0  1  1  0  1  0  1  1
#4      0  0  1  0  0  1  1  0  0  1  0  1  0  1  0  1  1  0  0  0


  The outer product interconnection matrix:

  0   0  -2   4   2   0   0   0   0  -4   4  -4   2  -2   2   0  -2   2   2   0
  0   0  -2   0   2  -4   0   0   4   0   0   0  -2   2   2  -4  -2   2   2   4
 -2  -2   0  -2   0   2  -2  -2  -2   2  -2   2   0   0   0   2   4  -4   0  -2
  4   0  -2   0   2   0   0   0   0  -4   4  -4   2  -2   2   0  -2   2   2   0
  2   2   0   2   0  -2  -2  -2   2  -2   2  -2   0   0   4  -2   0   0   4   2
  0  -4   2   0  -2   0   0   0  -4   0   0   0   2  -2  -2   4   2  -2  -2  -4
  0   0  -2   0  -2   0   0   0   0   0   0   0  -2   2  -2   0  -2   2  -2   0
  0   0  -2   0  -2   0   0   0   0   0   0   0   2  -2  -2   0  -2   2  -2   0
  0   4  -2   0   2  -4   0   0   0   0   0   0  -2   2   2  -4  -2   2   2   4
 -4   0   2  -4  -2   0   0   0   0   0  -4   4  -2   2  -2   0   2  -2  -2   0
  4   0  -2   4   2   0   0   0   0  -4   0  -4   2  -2   2   0  -2   2   2   0
 -4   0   2  -4  -2   0   0   0   0   4  -4   0  -2   2  -2   0   2  -2  -2   0
  2  -2   0   2   0   2  -2   2  -2  -2   2  -2   0  -4   0   2   0   0   0  -2
 -2   2   0  -2   0  -2   2  -2   2   2  -2   2  -4   0   0  -2   0   0   0   2
  2   2   0   2   4  -2  -2  -2   2  -2   2  -2   0   0   0  -2   0   0   4   2
  0  -4   2   0  -2   4   0   0  -4   0   0   0   2  -2  -2   0   2  -2  -2  -4
 -2  -2   4  -2   0   2  -2  -2  -2   2  -2   2   0   0   0   2   0  -4   0  -2
  2   2  -4   2   0  -2   2   2   2  -2   2  -2   0   0   0  -2  -4   0   0   2
  2   2   0   2   4  -2  -2  -2   2  -2   2  -2   0   0   4  -2   0   0   0   2
  0   4  -2   0   2  -4   0   0   4   0   0   0  -2   2   2  -4  -2   2   2   0


  ****************************************
  input memory number and # of errors  4  7
  1   1   0   1   1   0   0   0   0   1   0   1   0   1   0   1   1   0   0   0


  iteration #1 (analog output/ thresholded output/ correct memory vector)
-16  -8  16 -16  -8   8   4  -4   0   8  -8   8  -4   4   0   0   8  -8   0   0
  0   0   1   0   0   1   1   0   1   1   0   1   0   1   1   1   1   0   1   1
  0   0   1   0   0   1   1   0   0   1   0   1   0   1   0   1   1   0   0   0

  iteration #2 (analog output/ thresholded output/ correct memory vector)
-24   0  20 -24  -4   0  -4 -12  -8  24 -24  24 -16  16 -12   0  20 -20 -12  -8
  0   1   1   0   0   1   0   0   0   1   0   1   0   1   0   1   1   0   0   0
  0   0   1   0   0   1   1   0   0   1   0   1   0   1   0   1   1   0   0   0

  iteration #3 (analog output/ thresholded output/ correct memory vector)
-32 -24  28 -32 -20  16   4  -4 -16  32 -32  32  -8   8 -20  16  28 -28 -20 -16
  0   0   1   0   0   1   1   0   0   1   0   1   0   1   0   1   1   0   0   0
  0   0   1   0   0   1   1   0   0   1   0   1   0   1   0   1   1   0   0   0

  iteration #4 (analog output/ thresholded output/ correct memory vector)
-32 -24  28 -32 -28  24   4  -4 -24  32 -32  32  -8   8 -28  24  28 -28 -28 -24
  0   0   1   0   0   1   1   0   0   1   0   1   0   1   0   1   1   0   0   0
  0   0   1   0   0   1   1   0   0   1   0   1   0   1   0   1   1   0   0   0
```

Fig. 5.4 Computer Simulation Example of the Hopfield Memory Model (N=20, M=4): a)the interconnection matrix elements for the memory vectors shown in (b)(note the zero diagonal); b)the stored memory vectors; c)operation of the memory(the first line is the initial input vector, which is the fourth memory vector with 6 bits of error in the positions indicated). The second line gives the analog output vector, whose threshold binary version is given by the third line. The subsequent lines show how the memory behaves as the output from one iteration is used as the input for the next.

where $w(i,j)$ is the outer product matrix given by Eq. 5.2. This somewhat surprising result can be shown by computing the SNR of the recall process. The output product before being thresholded is given by

$$\hat{f}(i) = \sum_{j \neq i} sgn\Big[\sum_{m=1}^{M} f_m(i) f_m(j)\Big] f_1(j), \tag{5.9}$$

where $f_1(i)$ was used as the input. Unlike the original outer product case, a signal term cannot be identified from an additive noise term in this case. In the limit of large N, however, the mean of $\hat{f}(i)$ can be shown to be given by

$$E[\hat{f}(i)] \approx \sqrt{\frac{2}{\pi M}} N f_1(i), \tag{5.10}$$

which is the desired output diminished by a constant factor. The noise of the recall is then given by the variance of $\hat{f}(i)$, which can be verified to be

$$E[(\hat{f}(i) - E[\hat{f}(i)])^2] \approx N. \tag{5.11}$$

Thus, as a result of clipping the weight matrix, the overall SNR is diminished by the factor $\sqrt{2/\pi} \approx .798$ and equivalently, the storage capacity is reduced to

$$M \approx \frac{N}{\pi ln N}. \tag{5.12}$$

Clipping is of considerable interest when actual implementations of the memory is pondered, since interconnective weights that do not require grey levels can be achieved much more easily.

Computer simulations were performed to illustrate the functional dependence of the storage capacity on N, the size of the network. Both the outer product

and the clipped matrices were simulated for $N = 32, 64, 100, 128, 150, 180, 200$. The binary, bipolar vectors were chosen randomly for each matrix, and the maximum number of memory vectors such that they were *all* fixed points of the memory was determined for each memory size N. This procedure was done 7 times for each matrix, using independent vectors for each case. Shown in Fig. 5.5 are the results of the simulations along with the plots of the asymptotic capacity bounds given by $M = N/(4lnN)$ for the outer product matrix and $M = N/(2\pi lnN)$ for the clipped matrix. As the bounds indicate, the increase in capacity per increase in memory size diminishes as N increases.

5.2.2 The spectral scheme [4]

We now consider the so-called *spectral scheme* [4] for specifying the weight matrix. When probed by one of the stored vectors, the outer product memory yielded an output (before thresholding), which is *approximately* equal to the desired vector. In contrast, the spectral scheme prescribes the vectors to be stored as eigenvectors of the interconnection matrix, so that when probed by one of the M stored vectors, the spectral system yields the exact, desired vector to within a constant positive factor. The matrix is given by

$$\underline{\underline{w}}_s = \underline{\underline{FDF}}^{-1}, \tag{5.13}$$

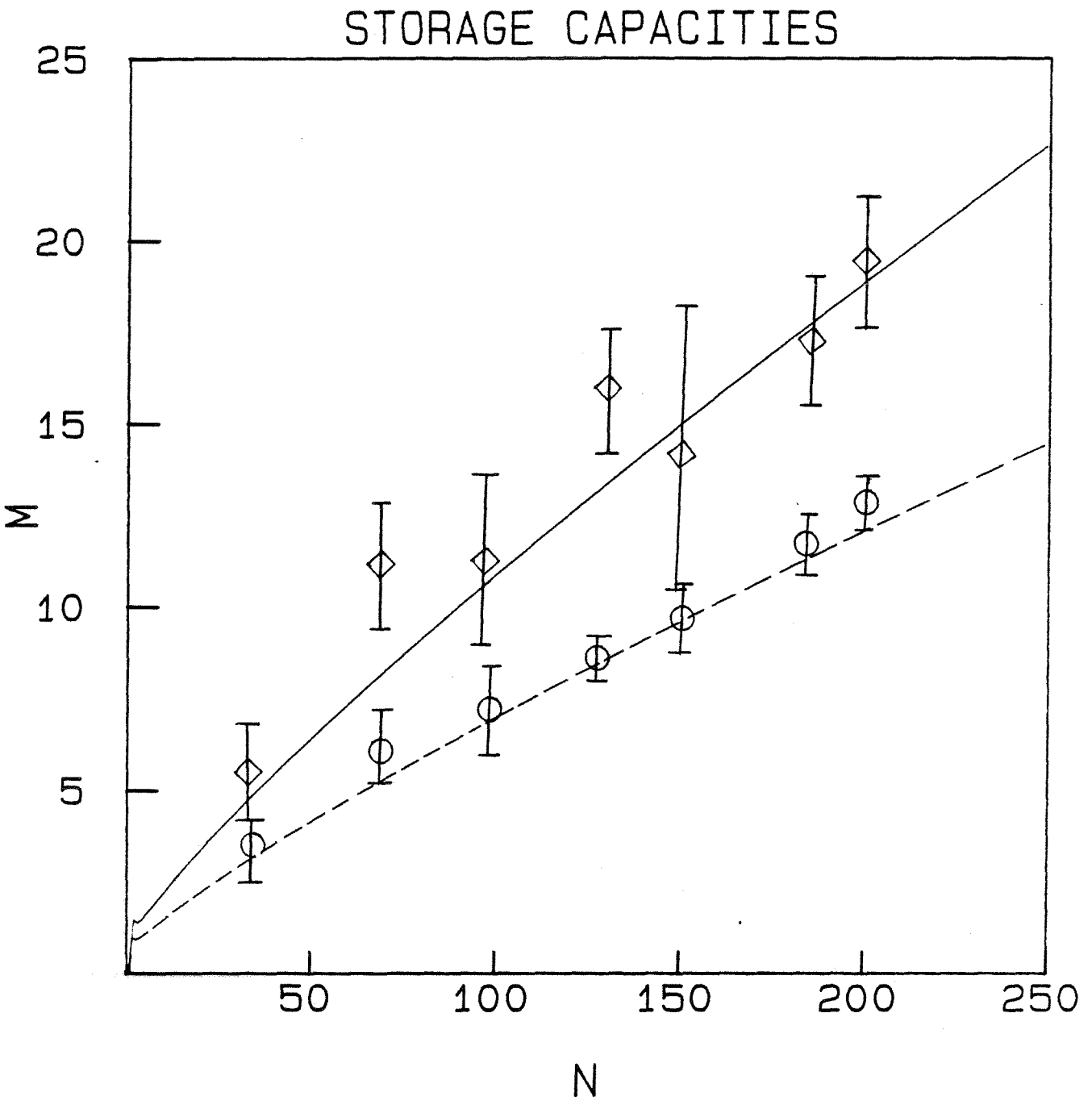

Fig. 5.5 Hopfield Memory Storage Capacity: the solid curve is the theoretical capacity of the Hopfield Memory and the dashed curve is the capacity of the clipped matrix memory. The capacities determined from computer simulations are indicated by the diamond (for the normal Hopfield model) and the circle (for the clipped matrix memory).

where

$$\underline{\underline{F}} = [\underline{f}_1, \underline{f}_2, \ldots, \underline{f}_M, \underline{z}_{M+1}, \underline{z}_{M+2}, \ldots, \underline{z}_N],$$

$$\underline{\underline{D}} = \begin{pmatrix} \lambda_1 & 0 & & \cdots & \cdots & 0 \\ 0 & \lambda_1 & & & & \\ & & \ddots & \ddots & & \vdots \\ \vdots & & \ddots & \lambda_M & \ddots & \\ \vdots & & & \ddots & 0 & \\ & & & & \ddots & 0 \\ 0 & & \cdots & \cdots & 0 & 0 \end{pmatrix}. \tag{5.14}$$

The $\underline{f}_m$ for $m = 1, 2, \ldots, M < N$ comprise the memory and are eigenvectors of $\underline{\underline{w}}_s$, each with eigenvalue $\lambda_m = \lambda$. The vectors $\underline{z}_m$ for $m = M+1, M+2, \ldots, N$ form the basis of the subspace orthogonal to that spanned by the memory vectors. Since the corresponding elements of the diagonal matrix are zero, the set $\{\underline{z}_m\}_{m=M+1}^{N}$ spans the null space of $\underline{\underline{w}}_s$. An arbitrary vector $\underline{f}$ can be written as a linear combination of the memory vectors and the null space vectors

$$\underline{f} = \sum_{m=1}^{M} \alpha(m)\underline{f}_m + \sum_{m=M+1}^{N} \alpha(m)\underline{z}_m. \tag{5.15}$$

The product of this arbitrary input vector with $\underline{\underline{w}}_s$ yields

$$\hat{\underline{f}} = \underline{\underline{w}}_s \underline{f} = \lambda \sum_{m=1}^{M} \alpha(m)\underline{f}_m, \tag{5.16}$$

which is a linear combination of the stored memory vectors. In particular, if the input $\underline{f}$ is one of the memory vectors, then the output consists solely of the same vector scaled by a constant. In general, if the input and one of the stored memories are close in Hamming distance, the corresponding expansion coefficient $\alpha(m)$ is large, so that the stored vector that most closely matches the input dominates the

output. Venkatesh and Psaltis [4] have shown that the capacity of such a memory grows linearly with N, making the spectral scheme more efficient than the outer product. Since the spectral matrix is symmetric, the energy theorem of Hopfield applies. In addition, the energy of each stored memory vector can be shown to be globally minimum as opposed to the locally minimum property of the outer product vectors. In the event that the matrix $\underline{\underline{F}}$ is ill-conditioned or singular, techniques involving the pseudo inverse may be used in place of Eq. 5.14. However, the spectral matrix is not as simple as the outer product matrix and requires, in general, more grey levels for implementation [4].

5.3 An Acousto-Optic Implementation of the Hopfield Model

5.3.1 Optical linear transformations

The associative memory models considered thus far are characterized by the requirement of global interconnectivity among the individual thresholding elements. Because of the robustness property of such networks, the interconnections need not be accurate. Optical techniques offer the capability of large-scale global connectivity, but the connections cannot be specified with great accuracy. Thus, optics seems to be well matched to the associative memory paradigm when actual implementations are considered.

Here, we consider an optical realization of the Hopfield-style networks described in the previous sections. At the heart of the system is an optical vector-matrix

multiplier [6] shown in Fig. 5.6. A one-dimensional array of light sources whose individual intensities represent the values of the input vector elements illuminates a computer-generated, two-dimensional transparency, which contains the interconnection matrix in such a way that each light source illuminates the corresponding column of the matrix. The light is then collected on a vertically oriented detector array so that the light from each row of the matrix is collected onto the corresponding detector. In this way, the desired matrix vector product is produced:

$$\hat{f}(k) = \sum_{l=1}^{N} w(k,l) f(l), \tag{5.17}$$

where $f(l)$ is the intensity of the l_{th} source and $\hat{f}(k)$ is the intensity sensed by the k_{th} detector. Using an array of LEDs as light sources and a photodiode array for detection, Farhat, Psaltis, Paek, and Prata [7]have realized a Hopfield memory of size $N = 32$. The basic system, which includes an array of 32 thresholding amplifiers for parallel feedback, is illustrated in Fig. 5.7. An input vector drives the LEDs, and the detected matrix-vector product is appropriately thresholded and fed back in parallel to drive the LEDs for the second iteration. The iterations proceed until an output vector that is a fixed point of the system is detected when the system stabilizes. One of the motivations for considering optical associative memories is the size of the networks that can be realized. If the number of elements becomes large, however, then the electronic portion of the LED system becomes burdensome, requiring a large number of thresholding amplifiers.

The system that we now describe [8] circumvents this problem by using a

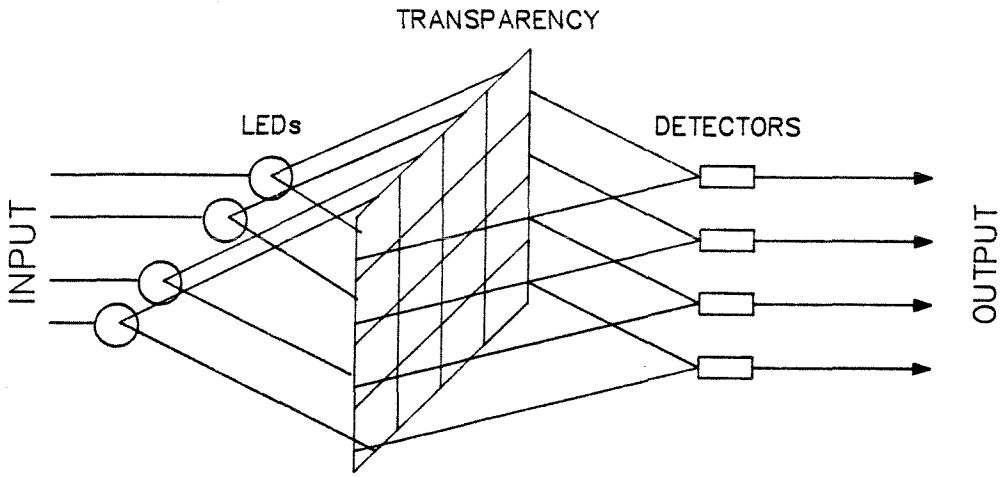

Fig. 5.6 Optical Matrix Vector Multiplier

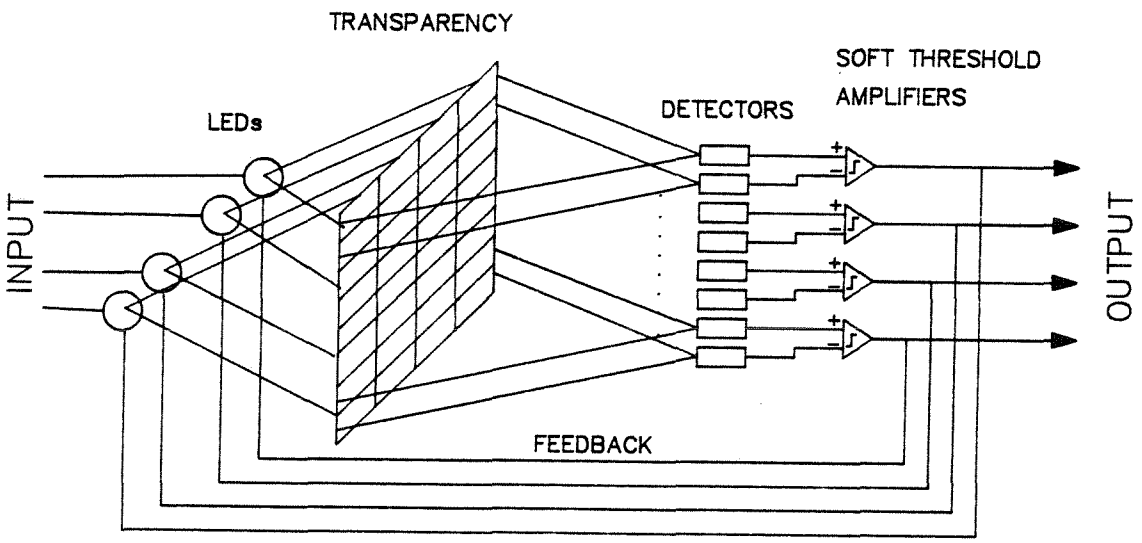

Fig. 5.7 LED Implementation of the Hopfield Model [7]

CCD detector array to obtain a scanned serial output, which is thresholded by one amplifier and fed back through one wire. Moreover, the array of LEDs is replaced by an acousto-optic device (AOD) used in conjunction with a pulsed laser diode. The effective number of pixels in the AOD is given by its space-bandwidth product, which typically range from hundreds to thousands. Moreover, CCD detector arrays with large numbers of detecting elements are currently available. Thus, the acousto-optic implementation can be easily expanded to accommodate large scale network models.

Before the system can be described, the question of how bipolar numbers can be represented in the optical realization must be answered. The Hopfield networks described in Section 5.2 require bipolar interconnection weights, and the state of each neuron itself is also bipolar (± 1). Since the acousto-optic implementation is essentially incoherent, the data must be represented in terms of intensities which cannot be negative. However, a bias can be added onto the weights so that each element becomes nonnegative.

In addition, the bipolar state of each neuron (± 1) are then replaced by (1,0). With $f(i)$ as the bipolar state of the i_{th} neuron at a particular time and $w(i,j)$ the bipolar interconnection matrix, the next state of the neuron is determined by the rule

$$f'(i) = sgn[\hat{f}(i)] = sgn[\sum_j w(i,j)f(j)]. \tag{5.18}$$

The unipolar representations of the state and matrix of weights are given by

$$\begin{aligned} v(i) &= (f(i)+1)/2, \\ u(i,j) &= w(i,j) + w_0\,(1-\delta(i,j))\,, \\ w_0 &= max_{i,j}[-w(i,j)], \end{aligned} \tag{5.19}$$

where $\delta(i,j)$ is the Kronecker delta. The diagonal terms of $w(i,j)$ are zero and need not be raised by a bias value. If we multiply the unipolar state vector and weight matrix, we get

$$\begin{aligned} \hat{v}(i) &= \sum_j u(i,j)v(j) \\ &= \sum_j \left[w(i,j) + w_0(1-\delta(i,j))\right]\left[f(i)+1\right] \\ &= \frac{1}{2}\{\sum_j w(i,j)f(j) + w_0 \sum_{j\neq i} v(j) + \sum_j w(i,j)\}. \end{aligned} \tag{5.20}$$

The third term, which is a row sum of the interconnection matrix, can be assumed to be zero if the memory data are chosen randomly.

The second term is approximately equal to the number of ones in the input state vector $v(i)$ and can be easily calculated for each iteration to be used as the threshold bias value against which $\hat{v}(i)$ is compared. The threshold rule

$$\hat{v}(i) = \begin{cases} 1 & \text{if } \hat{v}(i) \geq w_0 \sum_{j\neq i} v(i); \\ 0 & \text{if } \hat{v}(i) < w_0 \sum_{j\neq i} v(i) \end{cases} \tag{5.21}$$

is then equivalent to that dictated by Eq. 5.18. Therefore, an adaptive bias value, which is essentially proportional to the number of ones present in the input, can be used to completely overcome the difficulty of implementing memories that require bipolar representations, using an incoherent system.

5.3.2 Acousto-optic system description

The system, a 32 bit network, is shown schematically in Fig. 5.8, and its laboratory realization is shown in Fig. 5.9. An input vector set by an array of switches is first loaded into the input shift register whose serial output, properly mixed up to the rf center frequency (TeO_2 AOD: time aperture = 64 $\mu secs.$, bandwidth=40 MHz, center frequency f_0=50 MHz), drives the AOD. The register is read out at a rate of f= 1MHz so that the entire 32 bit sequence is 32 $\mu secs.$ long, occupying one-half the AOD aperture. At the moment when the sequence is centered within the AOD, the laser diode illuminates the AOD with a 50 $\mu sec.$ pulse of light, effectively freezing the motion of the data stream in the AOD. The light diffracted by the AOD is collimated vertically and imaged horizontally onto the interconnection matrix transparency.

A practical difficulty caused by the rather low sensitivity of the detector is overcome by increasing the integration time of the detector and repeatedly driving the AOD with the same input vector, thereby accumulating many identical products on the CCD array. The integration time of the detector was set to approximately 10 msecs., and since a product is formed once every 64 $\mu secs.$, about 156 samples are accumulated on the detector. The system therefore completes one iteration in 10 msecs. A timing diagram that illustrates the sequence of events is shown in Fig. 5.10. The accumulated matrix vector product is thresholded electronically by a comparator whose comparison value is proportional to the number of ones present

in the input shift register.

The digital result feeds a shift register clocked in synchronism with the CCD to sample appropriately the 32 output bits. The output data in the register are latched and displayed on an array of 32 LEDs. The latched data are also loaded onto another shift register whose serial output drives the AOD through the multiplexer, which has been now set to select the feedback data as its input for iterative operation.

For the experiments, two types of matrix transparencies were prepared: 1) the clipped outer product and 2) the spectral scheme (with grey levels). For each memory data set, the bipolar weight values were computed and biased for nonnegativity. Each resulting transparency contains a 32X32 array of square cells, and the total transparent area of each cell is the intensity transmittance of the cell representing the corresponding interconnection strength. The clipped matrix is particularly easy to prepare since each cell is either completely opaque or clear. An example of each transparency is shown in Fig. 5.11 and Fig. 5.15.

5.3.3 Experimental results

The system operation was demonstrated and evaluated, using first the clipped matrix scheme and then the spectral scheme. The results of the experiments are summarized in the data shown in Figs. 5.11-5.15, where computer simulations are included for comparison.

Fig. 5.11 summarizes the evaluation of the clipped matrix memory. A matrix

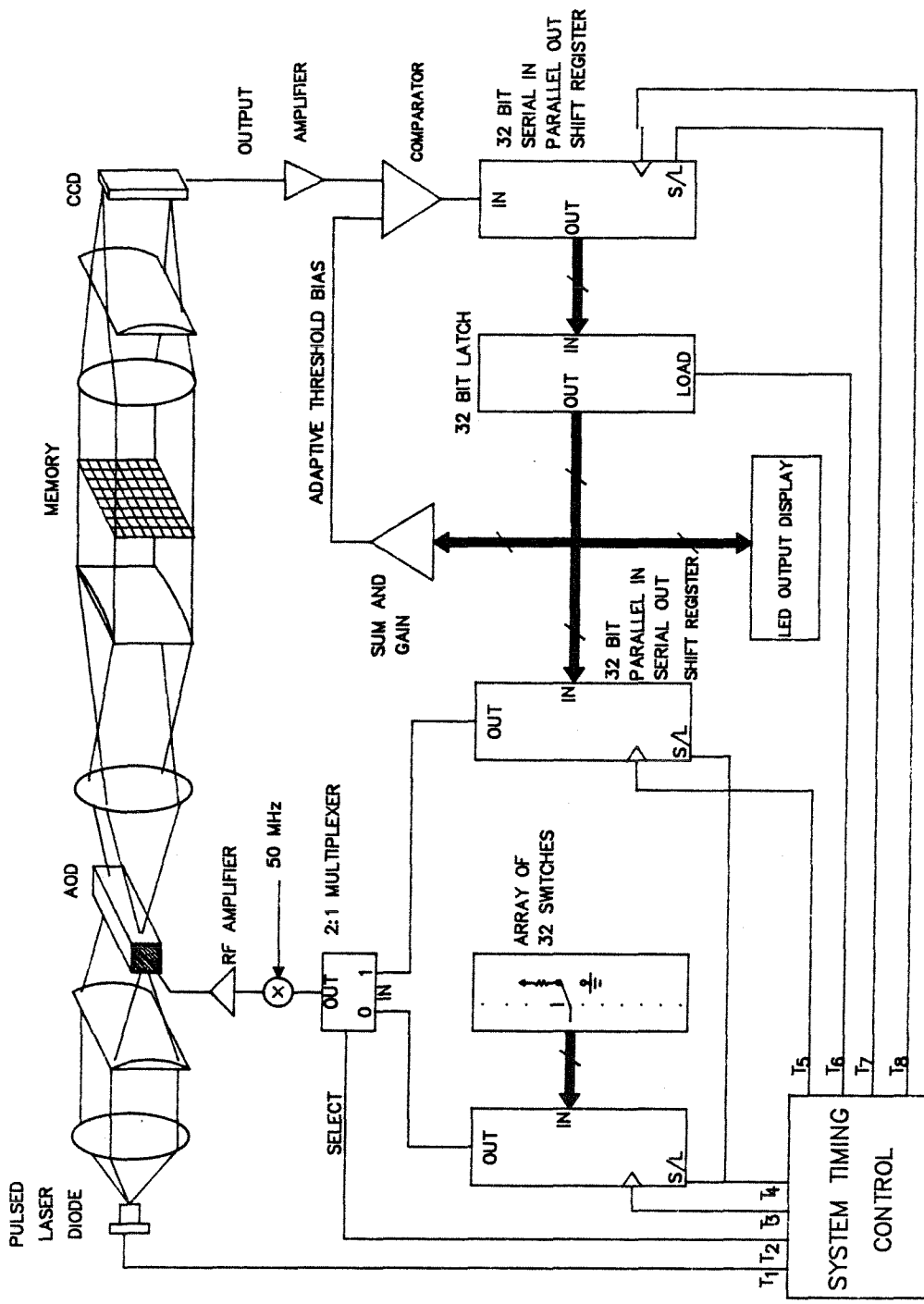

Fig. 5.8 32 Bit Acousto-Optic Implementation of the Hopfield Model

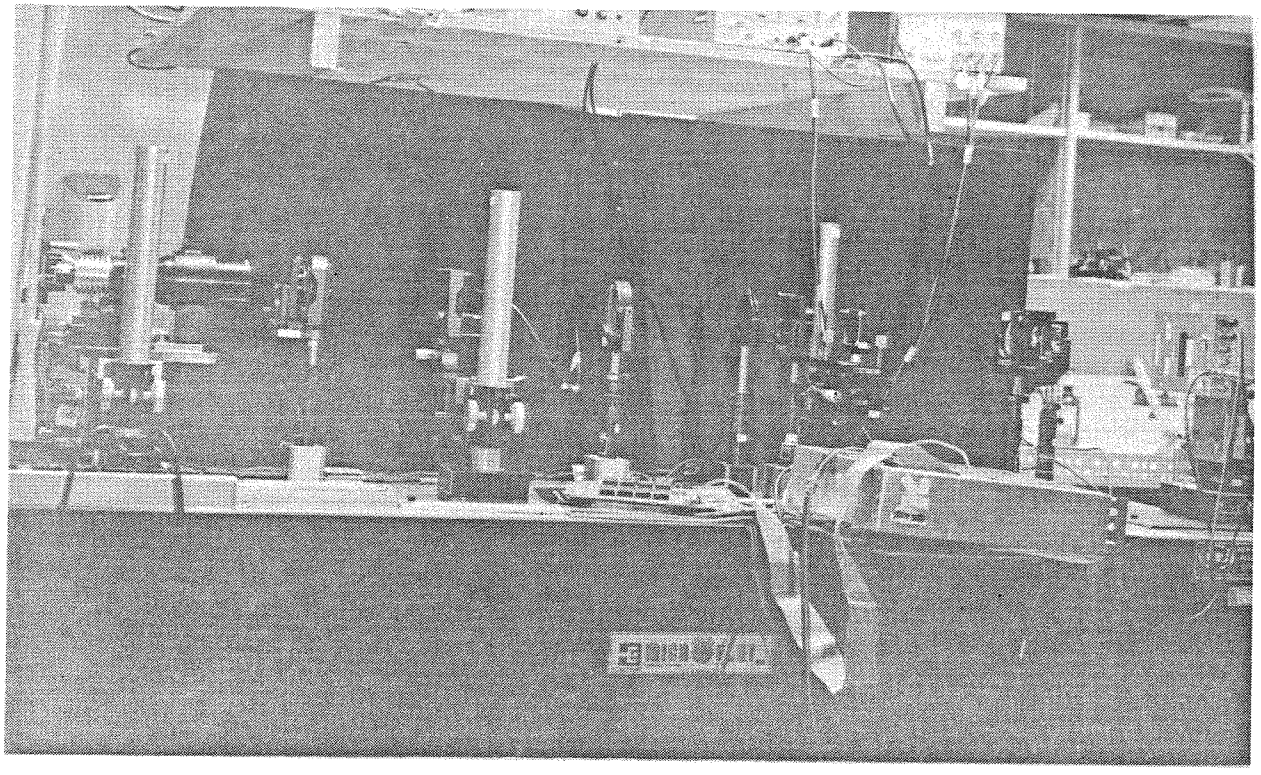

Fig. 5.9 Laboratory Realization of the System of Fig. 5.8

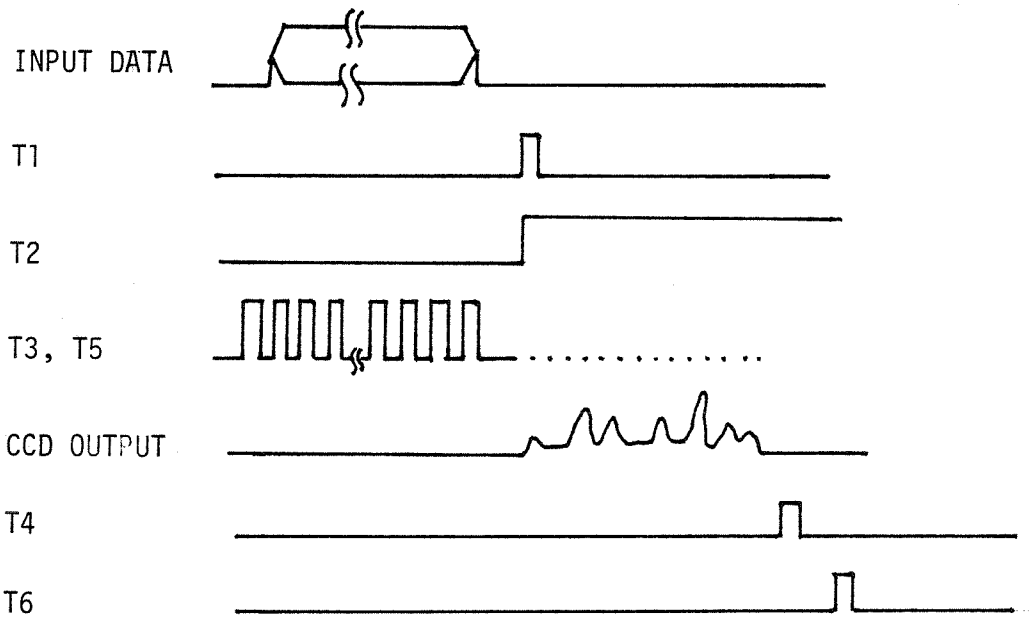

Fig. 5.10 Timing Diagram for Acousto-Optic Associative Memory

for a 32 bit network storing the three binary vectors shown was computed and a transparency prepared. By setting the array of input switches of the system, the stored vectors were first verified to be fixed points of the memory. If an error-laden version of a memory is used as the input, the system was able to converge to the correct memory as long as the error (in Hamming distance) was not too large. As shown, the error correction capability matches the simulated results well. Several examples of the system operation showing error correction are given in Fig. 5.12.

Because the present system operates synchronously where every bit is allowed to change all at once, the energy theorem of Hopfield [1] does not apply. As shown in Fig. 5.13, the system can be induced to break off into chaotic oscillations by using inputs sufficiently different from the memories. A solution to this problem is discussed in the next section. There, a technique involving a two-dimensional CCD detector in conjunction with analog shift registers and a thresholding amplifier with a wider linear region is used to implement a relaxational model for which an energy theorem guaranteeing stability exists [9].

The comparator used in the present system has a finite linear region over which its output does not assume TTL (Transistor to Transistor Logic: i.e., 0 and 5 volts) values. The effect of this on the system operation is shown in Fig. 5.14, where the outputs due to an error laden memory input are sketched for open-loop and closed-loop conditions. Shown also are the corresponding analog vectors, which are compared to the displayed DC level to be thresholded by the comparator.

Stored Binary Vectors

1)	1110	0001	0101	1101	1011	1101	1000	0010
2)	0110	0000	0010	0101	0100	1111	0101	1010
3)	1011	0011	1111	1110	0010	1100	0011	0000

Hamming Distances Between Vectors

	1	2	3
1	0	15	14
2	15	0	19
3	14	19	0

The Clipped Interconnection Matrix
(black=1, white=0)

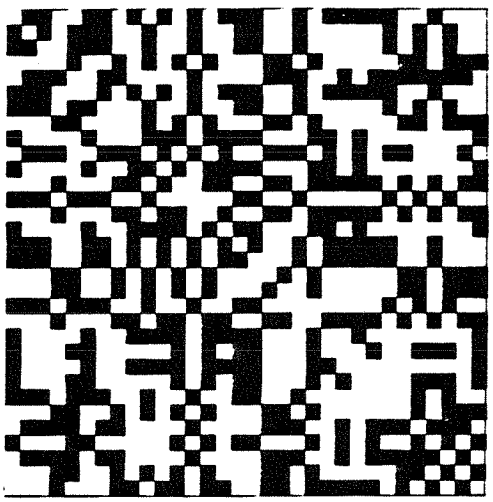

Max. No. of Correctable Input Errors

input	1	2	3
digital	11	8	12
optical	11	6	15

Fig. 5.11 Summary of Results for the Clipped Outer Product Matrix Memory

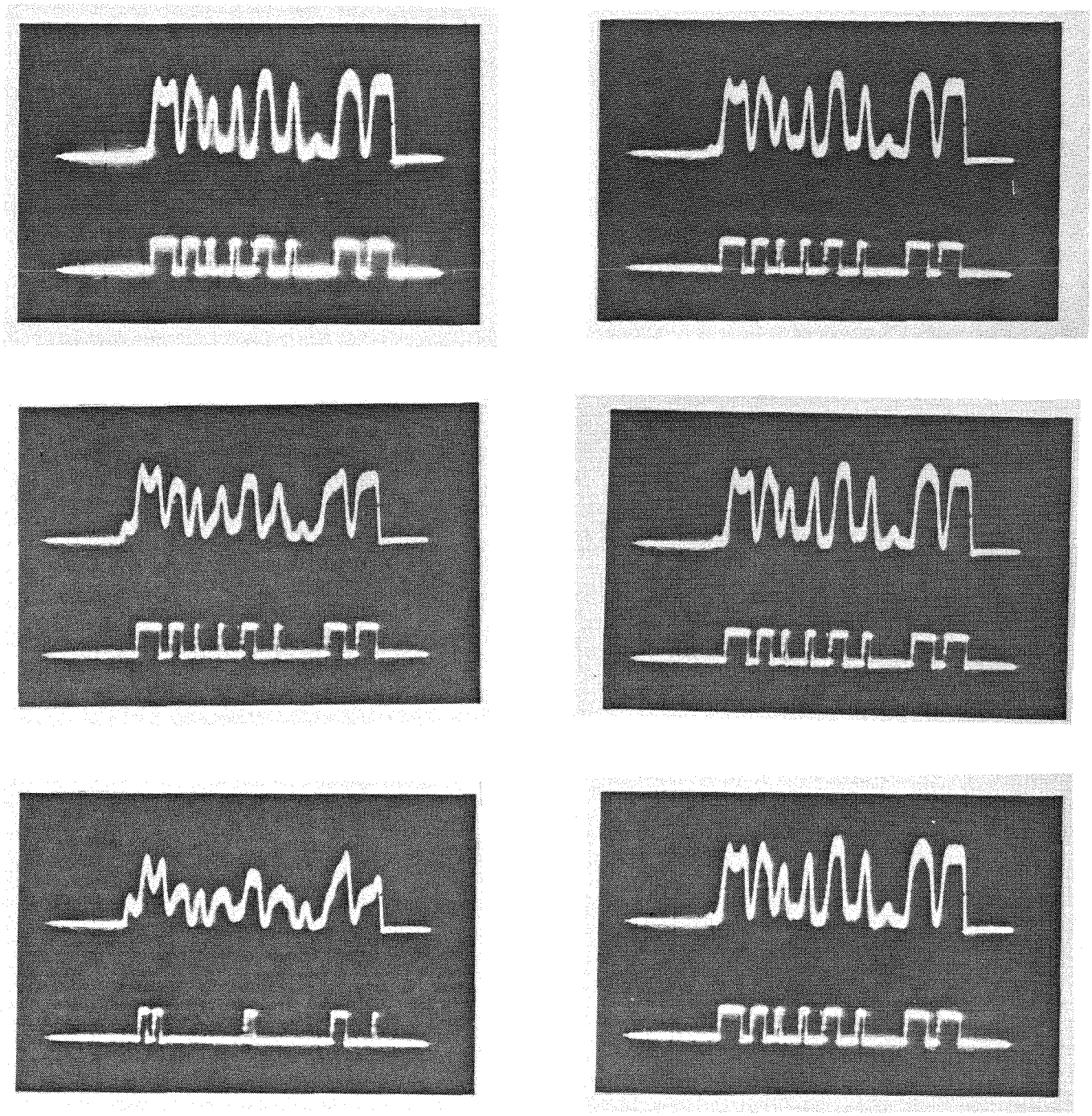

Fig. 5.12 Examples from the Operation of the AO Memory (analog/binary outputs: open-loop and closed-loop responses): **a**)outputs for input with no error, **b**)outputs for input with 4 bits in error, **c**)outputs for input with 8 bits in error.

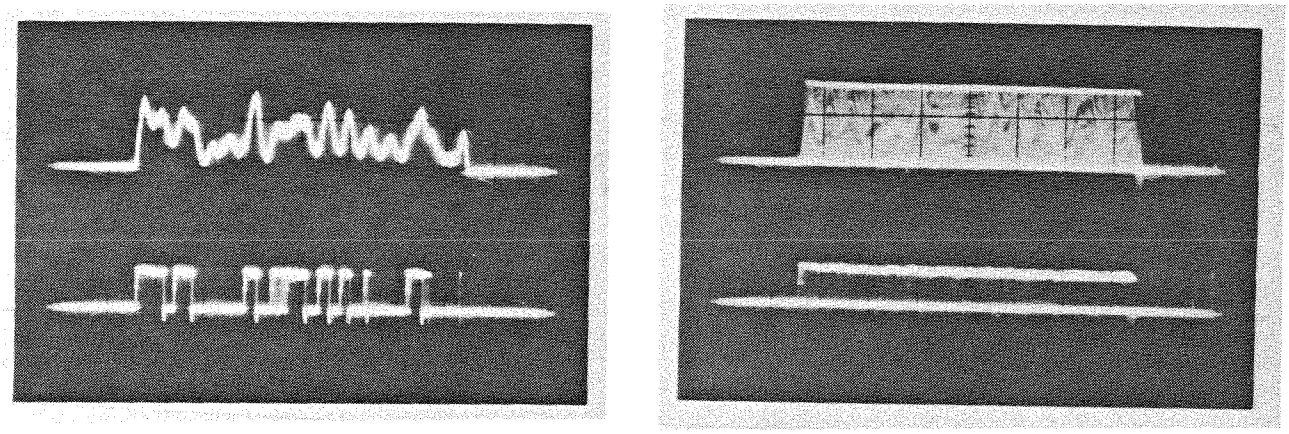

Fig. 5.13 Example of Chaotic Oscillation (see text): **a**)open-loop, **b**)closed-loop

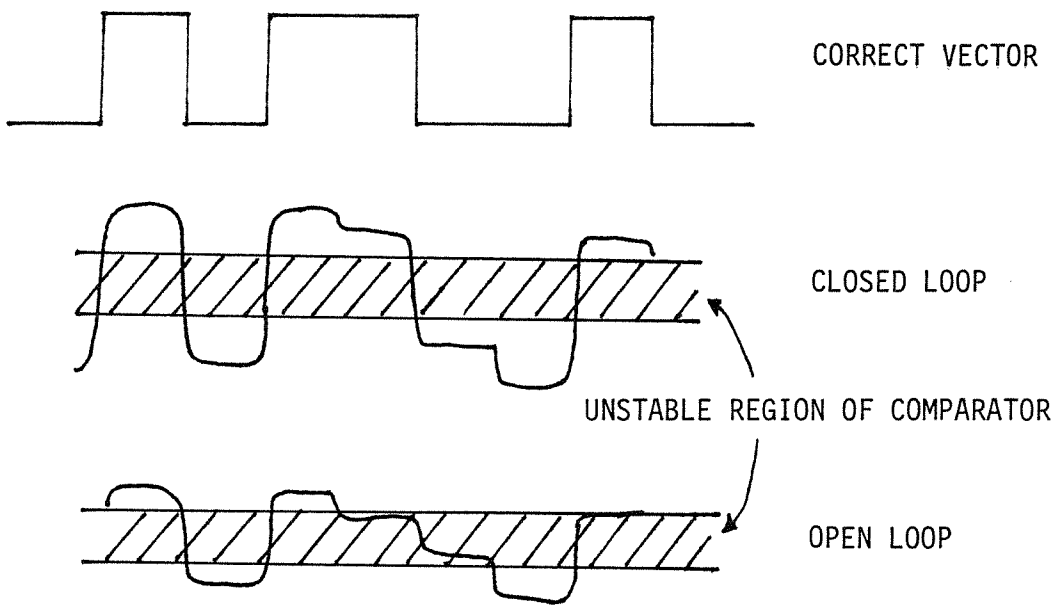

Fig. 5.14 Output Stability Under Open-Loop and Closed-Loop Operations (see text)

Stored Binary Vectors

1)	1100	1000	0110	0100	0111	1011	1111	0000
2)	1110	1101	1011	0011	0011	0000	0110	1000
3)	1100	0100	0001	1101	1010	1010	1011	1001
4)	0011	0010	1010	0011	0001	1101	1010	1011
5)	1010	0111	1010	0010	1011	0101	1101	0000

Hamming Distances Between Vectors

	1	2	3	4	5
1	0	16	14	20	16
2	16	0	16	16	12
3	14	16	0	20	20
4	20	16	20	0	14
5	16	12	20	14	0

The Spectral Interconnection Matrix
(black=1, white=0)

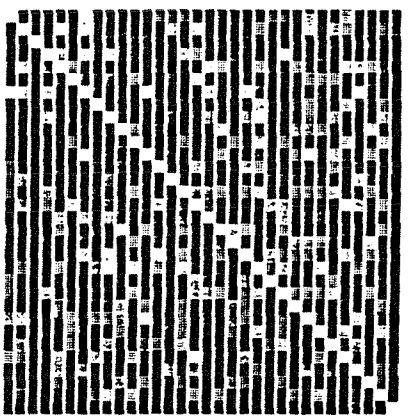

Max. No. of Correctable Input Errors

input	1	2	3	4	5
digital	11	7	10	6	13
optical	3	8	3	3	12

Fig. 5.15 Summary of Results for the Spectral Scheme Memory

The open-loop vector has values very close to the threshold bias. Hence, many of its elements are within the unstable region of the comparator, resulting in some metastable bits in the thresholded result. The closed-loop operation, however, iteratively corrects the errors until a fixed point is reached. The analog product shown in Fig. 5.14 corresponds to one of the prescribed memories. Note here that the values are well separated from the threshold bias. Hence, the corresponding binary output is stable as shown.

The storage capacity of the spectral scheme is somewhat larger. Results demonstrating the spectral scheme memory for 5 memory vectors are summarized in Fig. 5.15. The increased capacity is gained at the expense of requiring grey levels on the transparency. Because of the fine spatial structure within each cell used to provide grey levels, certain diffraction losses were incurred in the optical system. This, in addition to the fact that the matrix values themselves had to be quantized to a reasonable number of levels, accounts for the poor error-correcting capability of the optically implemented memory. All of the five memories were at any rate verified to be fixed points of the system.

5.3.4 Modifications for stability: relaxational operation

Linearly interconnected neural networks whose states are updated synchronously are susceptible to oscillatory behavior as seen in both the acousto-optic implementation and the computer simulations shown in Fig. 5.16. When the states

are updated asynchronously, restricting the state of only one neuron to change at any one time, the energy function defined by Eq. 5.6 was shown by Hopfield [1] to decrease or remain constant with each update. As evidenced by the examples in Fig. 5.16, the energy can actually increase in synchronously updated systems.

Hopfield [9] has considered the hard threshold decision given by the $sgn(.)$ function being replaced by an analog sigmoidal function incorporating time integrative delays into the system so as to more realistically model neurons. The resulting memory is guaranteed to be stable in the sense that its dynamics will always decrease an energy function analogous to Eq. 5.6. The fixed points of the analog system approach those of the binary system as the transition region of the sigmoidal function becomes narrower. The somewhat artificial asynchronism is not required by an analog, integrative system, in which the *analog* states of the neurons are allowed to change all at once. The dynamics of this analog network are governed by the equation

$$\tau \dot{f}_i(t) + f_i(t) = g\left(\sum_j w(i,j) f_j(t)\right), i = 1, 2, \ldots, N, \tag{5.22}$$

where $f_i(t)$ represents the analog state of the i_{th} neuron at time t, and $g(.)$ is a monotonically increasing sigmoidal function such as that shown in Fig. 5.17. The LED Hopfield implementation [7] actually operated in this way. The time constant of the individual thresholding amplifiers was about 60 msecs., and the transfer characteristics of each amplifier was sigmoidal. In consequence, the system displayed stable dynamics.

This relaxational mode of operation can be incorporated into the acousto-optic system by replacing the one-dimensional CCD with a two-dimensional one used in the time-delay-integrate (TDI[10]) mode, widening the linear region of the comparator, and replacing the digital shift registers with analog ones as shown schematically in Fig. 5.18. As before, with the proper mask in place and the input vector loaded in the AOD, the laser diode is pulsed. The lenses between the mask and the detector plane are perturbed so as to focus to a vertical line at the slit plane and vertically image the pixels of the mask onto the CCD detector. The matrix-vector product is therefore spread horizontally across the CCD (width of the spread is K pixels). Representing the p_{th} input vector by $v_j(p)$, the charge that is generated by the p_{th} exposure in the ik_{th} CCD pixel is given by

$$Q_{ik}(p) = \begin{cases} \sum_{j=1}^{N} u(i,j)v_j(p) & \text{if } 1 \leq k \leq K; \\ 0 & \text{otherwise.} \end{cases} \tag{5.23}$$

With reference to Fig. 5.19, the TDI mode operation shifts the previous charge distribution due to previous exposures horizontally by one pixel and the currently generated charge $Q_{ik}(p)$ is added to this. Shifting and adding charges for each exposure results in the following total charge to form on the ik_{th} CCD pixel:

$$\overline{Q}_{ik}(p) = \begin{cases} \sum_j u(i,j) \sum_{l=0}^{K-k} v_j(p-l) & \text{if } 1 \leq k \leq K; \\ 0 & \text{otherwise.} \end{cases} \tag{5.24}$$

The output taken from the $k = 1$ column of the CCD is

$$\hat{f}_i(p) = \sum_j u(i,j) \sum_{l=0}^{K-1} v_j(p-l). \tag{5.25}$$

This is processed by the soft-threshold comparator whose output is latched by the analog shift registers and fed back to the AOD for further iterations.

The output given by Eq. 5.25 along with the soft threshold function shown in Fig. 5.18 is an approximation of the integrative update rule given by Eq. 5.22. The important elements are: 1)the update decision is based not just on the immediate past state but on a sum of past states, and 2) the hard threshold is replaced by a sigmoidal transfer characteristic. Computer simulations illustrate the effectiveness of this approach. Shown in Fig. 5.20 is a comparison made between the operation of a synchronous memory (N=20) with hard threshold rule and that of the TDI system, which incorporates a sigmoidal threshold rule with an integrative decision based on the past K (K=5) states. Note that the energy of the binary system increased with iterations for certain cases, while the analog system reached the correct fixed points in the simulations by decreasing the energy.

```
          memory vectors are (unipolar versions):
#1        0  1  0  0  0  0  1  1  1  1  0  1  0  1  0  0  0  1  0  1
#2        1  1  0  1  1  0  1  0  1  0  1  0  0  1  1  0  0  1  1  1
#3        0  1  1  0  1  0  0  0  1  1  0  1  0  1  1  0  1  0  1  1
          ********************************************************

input     0  0  1  0  0  1  0  1  0  0  1  0  0  1  1  0  0  1  1  1

1)out     1  1  0  1  1  0  1  0  1  1  0  1  1  0  1  1  0  1  1  0
mem.#2    1  1  0  1  1  0  1  0  1  0  1  0  0  1  1  0  0  1  1  1
          energy=  26

2)out     1  1  1  1  0  0  0  1  1  0  1  0  0  1  0  0  1  0  0  1
mem.#2    1  1  0  1  1  0  1  0  1  0  1  0  0  1  1  0  0  1  1  1
          energy=  104

3)out     0  0  0  0  1  1  1  0  0  1  0  1  1  0  1  1  0  1  1  0
mem.#2    1  1  0  1  1  0  1  0  1  0  1  0  0  1  1  0  0  1  1  1
          energy=  104

4)out     1  1  1  1  0  0  0  1  1  0  1  0  0  1  0  0  1  0  0  1
mem.#2    1  1  0  1  1  0  1  0  1  0  1  0  0  1  1  0  0  1  1  1
          energy=  104

5)out     0  0  0  0  1  1  1  0  0  1  0  1  1  0  1  1  0  1  1  0
mem.#2    1  1  0  1  1  0  1  0  1  0  1  0  0  1  1  0  0  1  1  1
          energy=  104



input     1  0  1  1  1  1  0  0  0  0  0  1  0  1  0  0  0  1  0  1

1)out     0  1  0  0  1  0  1  0  1  1  1  0  1  0  1  1  0  1  1  0
mem.#1    0  1  0  0  0  0  1  1  1  1  0  1  0  1  0  0  0  1  0  1
          energy=  26

2)out     1  1  1  1  0  0  0  1  1  0  1  0  0  1  0  0  1  0  0  1
mem.#1    0  1  0  0  0  0  1  1  1  1  0  1  0  1  0  0  0  1  0  1
          energy=  104

3)out     0  0  0  0  1  1  1  0  0  1  0  1  1  0  1  1  0  1  1  0
mem.#1    0  1  0  0  0  0  1  1  1  1  0  1  0  1  0  0  0  1  0  1
          energy=  104

4)out     1  1  1  1  0  0  0  1  1  0  1  0  0  1  0  0  1  0  0  1
mem.#1    0  1  0  0  0  0  1  1  1  1  0  1  0  1  0  0  0  1  0  1
          energy=  104

5)out     0  0  0  0  1  1  1  0  0  1  0  1  1  0  1  1  0  1  1  0
mem.#1    0  1  0  0  0  0  1  1  1  1  0  1  0  1  0  0  0  1  0  1
          energy=  104
```

Fig. 5.16 Computer Simulations Showing Oscillations Due to Synchronous Updating (N=20, M=3, clipped matrix)

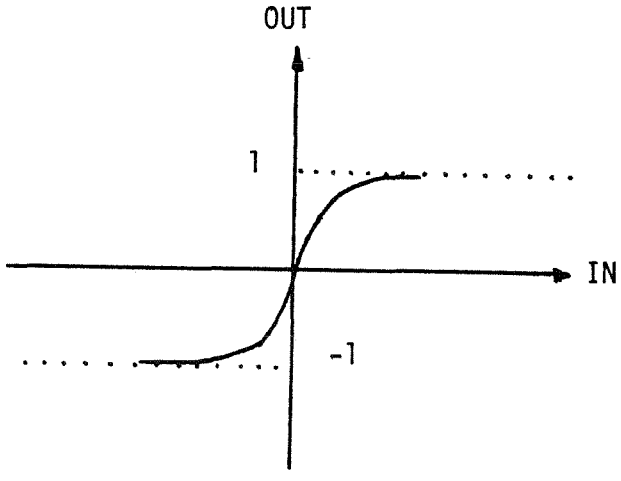

Fig. 5.17 Sigmoidal (soft) Threshold Function

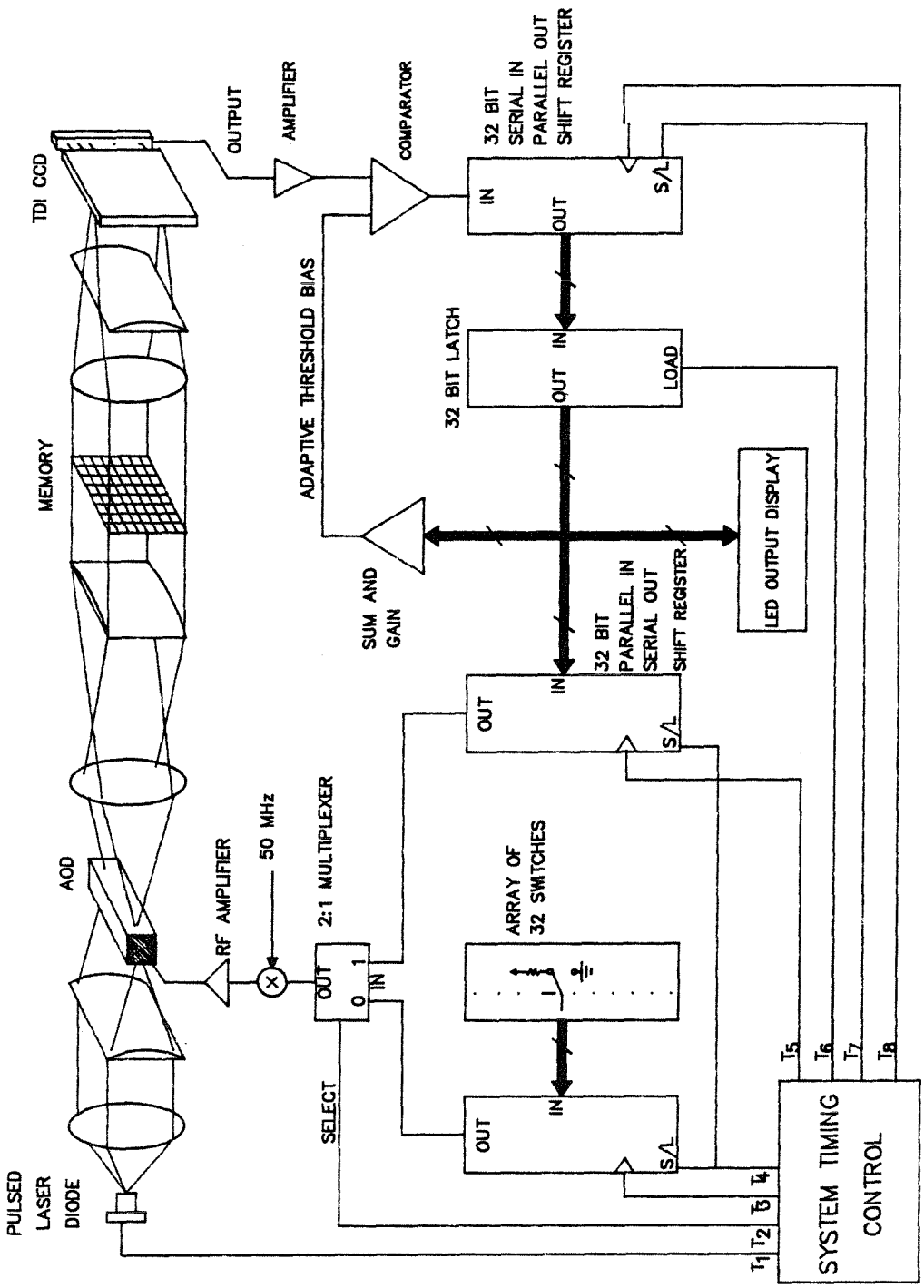

Fig. 5.18 Relaxational System Employing a TDI (time delay and integrate)-Mode CCD Detector

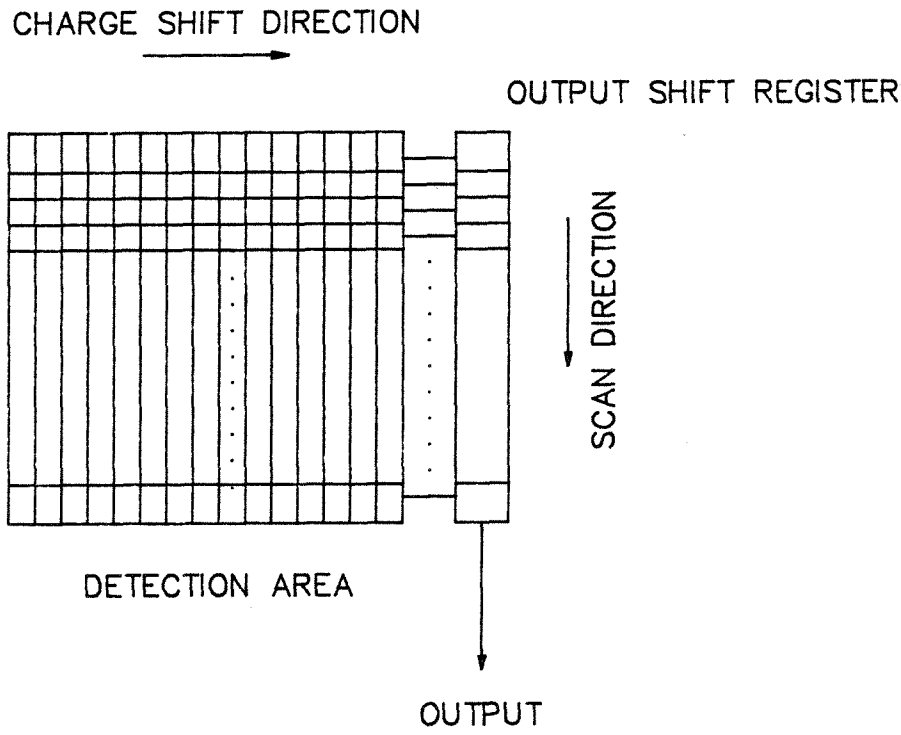

Fig. 5.19 TDI CCD Operation: the photogenerated charges are shifted to the right by one cell after each laser diode pulse with the newly generated charges being added onto the previously generated charges.

Fig. 5.20 Comparison Between Two Algorithms: a)hard threshold with synchronous updating; b)soft threshold with integrative updating

References for Chapter 5

[1] J. J. Hopfield, "Neural networks and physical systems with emergent collective computational abilities," *Proc. Natl. Acad. Sci. U.S.A.*, **79**, 2554 (1982).

[2] D. Psaltis and C. H. Park, "Nonlinear discriminant functions and associative memories," *APS Snowbird Conf. on Associative Memory*, **1**, (Snowbird, UT 1986).

[3] D. O. Hebb, *The Organization of Behavior*, Wiley, New York, 1949.

[4] S. Venkatesh and D. Psaltis, "Linear and logarithmic capacities in associative neural networks," *submitted for publication IEEE Trans. Info. Theory*, , ().

[5] R. J. McElice, E. C. Posner, E. R. Rodemich, and S. Venkatesh, "The capacity of the Hopfield Associative Memory," *to appear in IEEE Trans. Info. Theory*, **IT-33**, (June 1987).

[6] J. Goodman, A. R. Dias, and L. M. Woody, "Fully parallel, high-speed incoherent optical method for performing discrete fourier transforms," *Opt. Lett.*, **2**, 1 (1978).

[7] N. Farhat, D. Psaltis, E. Paek, and A. Prata, "Optical implementation of the Hopfield Model," *App. Opt.*, **24**, 1469 (1985).

[8] D. Psaltis, E. Paek, and J. Hong, "Acousto-optic implementation of the Hopfield Model," *JOSA*, **2**, no.13, 48 (Dec. 1985).

[8] J. J. Hopfield, "Neurons with graded response have collective computational properties like those of two-state neurons," *Proc. Natl. Acad. Sci. U.S.A.*, **81**, 3088 (1984).

Chapter 6. Storage Capacity of Holographic Memories

6.1 Introduction

The analogy between associative memories and holography was first pointed out by Van Heerden [1,2] and also by Gabor [3]. Consider the holographic recording and reconstruction processes illustrated in Fig. 6.1. The hologram records the interference pattern between two waves, one of which is normally referred to as the *reference wave* and the other as the *signal.* When the hologram is illuminated with the reference wave, the diffraction due to the stored interference pattern results in the reconstruction of the signal. The labels "reference" and "signal" are arbitrary, and it is possible to obtain the reconstruction of the reference wave by illuminating the holgram with the signal beam as well. Gabor [3] analyzed in some detail the performance of Fresnel holograms used as associative memories.

Whereas Gabor presented the holographic technique for only one association, recent publications have discussed the possibility of storing many associations on a single hologram [4-12]. It is therefore important to quantify the storage capacity of holographic associative memories, defined to be the maximum number of associations that can be stored and recalled with high fidelity. In this chapter, we present a discussion based on the degrees-of-freedom argument forwarded by Abu-Mostafa and Psaltis [13] to demonstrate the fundamental importance of the space-bandwidth product (SBP) of the hologram in determining the storage capacity. Specifically,

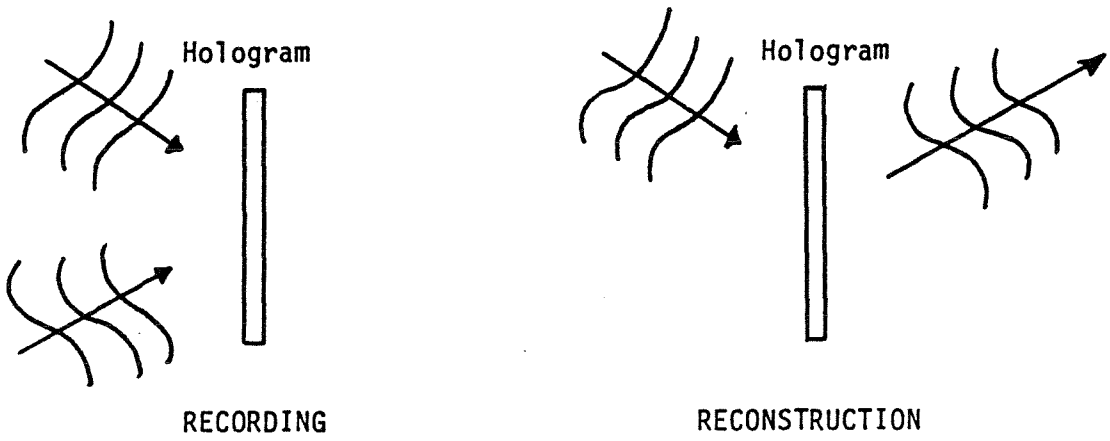

Fig. 6.1 Holography as an Associative System

we show that the total number of samples or bits that can be stored is equal to the SBP. This implies that the storage capacity of holographic associative memories is limited to one association if we wish to store images, each with a high SBP equal to that of the hologram. This result is then confirmed by deriving an expression of the signal-to-noise ratio (SNR) that is obtained when the hologram is reconstructed.

6.2 Degrees-of-Freedom Considerations

In a conventional hologram, two patterns are associated with one another by recording their mutual interference. More generally, a hologram can be thought of as an optical transparency whose complex transmittance can be controlled arbitrarily. Information is stored in the hologram such that when it is placed in the appropriate optical system and the system is illuminated by one of the specified inputs, the correct, associated output is produced.

A model that is sufficiently general to encompass all of the specific holographic memories is shown in Fig. 6.2. We will use this model to derive bounds on the capacity, which are generally applicable without requiring further knowledge of the implementation details. The information content of a hologram is characterized primarily by its SBP. Therefore, the system spatial coordinate is quantized by assigning $N_2 =$ SBP discrete pixels to the hologram. Similarly, the input and output planes are composed of N_1 and N_3 pixels, respectively. The input, output, and hologram planes have been identified in Fig. 6.2. To be general, arbitrary but

fixed, linear transformations $Q(j,i)$ and $R(k,j)$, $j = 1,2,..,N_2$; $i = 1,2,..,N_1$; $k = 1,2,..,N_3$, relate the input and output planes to the hologram plane.

This system associates or stores N_1-element vectors from a set of M "inputs" $f_m(i)$, where m is the memory index, pairwise with N_3-element vectors from the set of M "outputs" $g_m(k)$, such that the reconstruction of the vector $g_{m_0}(k)$ is obtained when its associated vector $f_{m_0}(i)$ is present at the input plane. The reconstruction process will be studied in detail to determine the maximum number of associations, M, given the freedom to write the hologram in any way we choose.

In reference to Fig. 6.2, the input-ouput relation that must be satisfied for selective recall can be described by the following set of equations:

$$g_m(k) = \sum_{j=1}^{N_2} \sum_{i=1}^{N_1} R(k,j) t_H(j) Q(j,i) f_m(i) \quad for \quad k = 1,2,..,N_2 \quad and \quad m = 1,2,..,M, \tag{6.1}$$

where $t_H(j)$, $j = 1,2,..,N_2$, are the pixel values that describe the hologram's transmittance. Since Eqs. 6.1 is a system of MN_3 equations in the N_2 unknowns $t_H(j)$, a solution $t_H(j)$ is guaranteed only if $MN_3 \leq N_2$. This provides an upper bound for the capacity of the holographic memory: $M \leq N_2/N_3$, where M is the number of associations and N_3 is the size of each output. Thus, there is a tradeoff in the memory capacity, and the fundamental limit is indeed set by the SBP of the hologram.

The equality constraints placed by Eq. 6.1 may appear to be severe, and one might wonder whether the storage capacity will increase substantially if we require

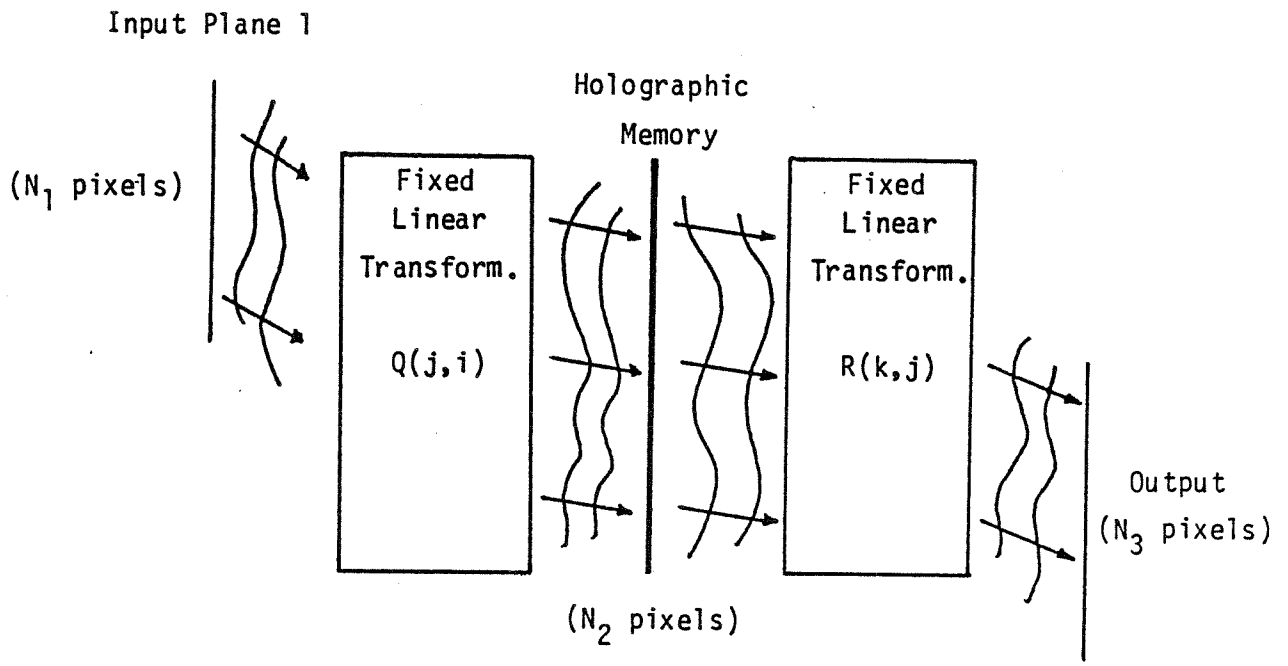

FIG.2 GENERAL HOLOGRAPHIC MODEL

Fig. 6.2 General Holographic Model

only approximate reconstruction. For instance, if we require only that the output of the holographic memory have the correct sign rather than the exact analog value, we can use Cover's result [14] for the capacity of linear discriminant functions to conclude that the capacity does not increase at all. We believe that this conclusion is not specific to this particular type of inaccuracy. In what follows, we analyze another approximate method of constructing optical associative memories, which also confirms this conclusion.

6.3 Holographic Associative Memories

6.3.1 Capacity derived from SNR considerations

A heuristic method of assigning values to $t_H(j)$ so as to satisfy approximately the constraints of Eq. 6.1 is found in optical holography [1-3]. Conventional holograms are prepared by recording on a photographic plate or any other suitable recording medium the mutual interference pattern between a pair of impinging waves that arise from the diffraction of optical field amplitudes at some defined input planes. This is shown in Fig. 6.3. For generality, we consider *fixed, linear* transformations to relate both input planes to the hologram plane. One wave is then reconstructed by illuminating the developed plate with the other. Pairs of data sets are stored by multiply exposing the hologram, resulting in a holographic plate transmittance function, which is a superposition of the interference patterns of the stored waves. If one particular wave is used as the input for the reconstruction,

the output will consist of the wave associated with that input but distorted by a cross-correlation noise term composed of the other stored waves. A good performance criterion is then the signal-to-noise ratio (SNR), defined as the ratio of the correct output signal amplitude to the standard deviation of the cross-correlation noise term.

We consider this holographic paradigm in which $t_H(j)$ is a superposition of products of linearly transformed vectors. In reference to Fig. 6.3, the transmittance of the hologram is described by

$$t_H(j) = \sum_{m=1}^{M} \{\sum_{l=1}^{N_1} Q^*(j,l) f_m^*(l)\} \{\sum_{n=1}^{N_3} S(j,n) g_m(n)\}, \quad j = 1,2,..,N_2, \tag{6.2}$$

where we have omitted inconsequential terms such as bias, which also appears in the holographic recording process. The response due to a particular input $f_{m_0}(i)$ is

$$g(k) = \sum_{j=1}^{N_2} R(k,j) t_H(j) \sum_{i=1}^{N_1} Q(j,i) f_{m_0}(i), \quad k = 1,2,..,N_3, \tag{6.3}$$

which when expanded gives

$$\begin{aligned} g(k) &= \sum_{i=1}^{N_1}\sum_{l=1}^{N_1}\sum_{j=1}^{N_2}\sum_{n=1}^{N_3} R(k,j) S(j,n) Q^*(j,l) Q(j,i) f_{m_0}^*(l) f_{m_0}(i) g_{m_0}(n) + \alpha(k), \\ \alpha(k) &= \sum_{m \neq m_0}^{M}\sum_{i=1}^{N_1}\sum_{l=1}^{N_1}\sum_{j=1}^{N_2}\sum_{n=1}^{N_3} R(k,j) S(j,n) Q^*(j,l) Q(j,i) f_m^*(l) f_{m_0}(i) g_m(n), \end{aligned} \tag{6.4}$$

Here the expression for $g(k)$ has been resolved into a signal term and a cross-correlation noise term, $\alpha(k)$.

If we assume that the elements of the vectors $f_m(i)$ and $g_m(n)$ take the values +1 or -1 with equal probability and each element is statistically independent from all the others, then the expected value of the output is

$$E[g(k)] = \sum_{n=1}^{N_3} \sum_{j=1}^{N_2} R(k,j)S(j,n) \sum_{i=1}^{N_1} |Q(j,i)|^2 g_{m_0}(n), \tag{6.5}$$

where we have used the fact that $E[f_{m_0}(l)f_{m_0}(i)] = \delta(l,i)$, the Kronecker delta. If we choose the set of possible transformations $Q(j,i)$ such that the row sums $\sum_{i=1}^{N_1} |Q(j,i)|^2 = 1$ for all j, then Eq. 6.5 further simplifies to

$$E[g(k)] = \sum_{n=1}^{N_3} \sum_{j=1}^{N_2} R(k,j)S(j,n)g_{m_0}(n). \tag{6.6}$$

For $E[g(k)]$ to be proportional to the correct recall term, $g_{m_0}(k)$, we see that $R(k,j)$ and $S(j,n)$ must satisfy the condition

$$\sum_{j=1}^{N_2} R(k,j)S(j,n) = c\delta(k,n), \tag{6.7}$$

where c is a constant.

The requirement $\sum_{i=1}^{N_1} |Q(j,i)|^2 = 1$ that was invoked to derive the above result is not overly restrictive, as it is applicable to most transformations of interest. Specifically, this condition describes transformations which distribute the input energy uniformly over the hologram plane, making efficient use of the space on the hologram. That is, a uniform, incoherent intensity distribution at the input plane 1 of Fig. 6.2 is mapped to a uniform intensity at the hologram plane. Some examples are Fresnel, Fourier, and diffuse transformations.

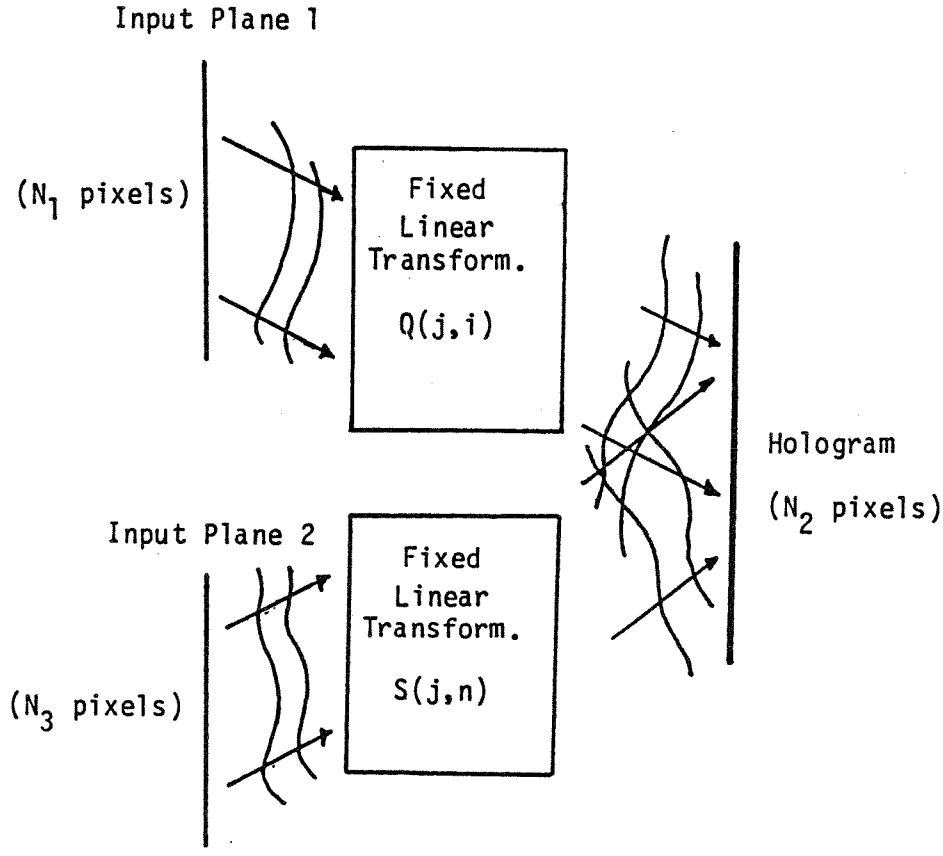

Fig. 6.3 Holographic Recording

Satisfying Eq. 6.7 guarantees that the expected value of the output will be proportional to the correct stored pattern. In order to obtain an estimate for the variance of the reconstruction, we need to specify the transformations $R(k,j)$ and $S(j,n)$ more precisely. We make the reasonable requirement that the energy dissipated by the transformation $S(j,n)$ does not depend on the specific vectors $g_m(n)$ being stored. Again, transformations of interest such as Fourier, Fresnel, and diffuse transformations satisfy this condition. Mathematically, this leads to the requirement that $S(j,n)$ have orthogonal columns:

$$\sum_{j=1}^{N_2} S^*(j,k)S(j,n) \;\propto\; \delta(k,n). \tag{6.8}$$

To satisfy both Eqs. 6.7 and 6.8, we require that

$$S(j,n) = R^*(n,j) \quad \text{and} \quad \sum_{j=1}^{N_2} R(k,j)R^*(n,j) = c\delta(k,n). \tag{6.9}$$

Having concluded that $E[g(k)] = cg_{m_0}(k)$ when Eq. 6.7 holds, we now calculate the noise variance $\sigma^2(k)$:

$$\begin{aligned}\sigma^2(k) &= E[|\alpha(k)|^2] \\ &= (M-1)\sum_{i=1}^{N_1}\sum_{l=1}^{N_1}\sum_{j_1=1}^{N_2}\sum_{j_2=1}^{N_2}\sum_{n=1}^{N_3} R(k,j_1)R^*(k,j_2)R^*(n,j_1)R(n,j_2) \\ &\qquad Q^*(j_1,l)Q(j_1,i)Q(j_2,l)Q^*(j_2,i).\end{aligned} \tag{6.10}$$

The index k is kept to show the possible dependence of the variance on the output bit position. To arrive at a more uniform measure of the noise, we calculate the

variance averaged over the N_3 output bits to be

$$\begin{aligned}\sigma^2 &= (1/N_3)\sum_{k=1}^{N_3}\sigma^2(k) \\ &= (M-1)/N_3 \sum_{j_1=1}^{N_2}\sum_{j_2=1}^{N_2}\Big|\sum_{k=1}^{N_3} R(k,j_1)R^*(k,j_2)\Big|^2\Big|\sum_{i=1}^{N_1} Q(j_1,i)Q^*(j_2,i)\Big|^2.\end{aligned} \tag{6.11}$$

A lower bound on the noise variance can be derived by first noting that

$$\sigma^2 \geq \left[(M-1)/N_3\right]\sum_{j=1}^{N_2}\Big\{\Big|\sum_{k=1}^{N_3}|R(k,j)|^2\Big|^2\Big|\sum_{i=1}^{N_1}|Q(j,i)|^2\Big|^2\Big\}. \tag{6.12}$$

But since we have restricted the $Q(i,j)$'s such that $\sum_{i=1}^{N_1}|Q(j,i)|^2 = 1$ and also $\sum_{k=1}^{N_3}\sum_{j=1}^{N_2}|R(k,j)|^2 = cN_3$ from Eq. 6.9, we get

$$\begin{aligned}\sigma^2 &\geq \left[(M-1)/N_3\right]\sum_{j=1}^{N_2}\Big|\sum_{k=1}^{N_3}|R(k,j)|^2\Big|^2 \\ &\geq \left[(M-1)/(N_2N_3)\right]\Big|\sum_{j=1}^{N_2}\sum_{k=1}^{N_3}|R(k,j)|^2\Big|^2 \;=\; (M-1)c^2N_3/N_2,\end{aligned} \tag{6.13}$$

where the inequality $N_2\sum_{j=1}^{N_2}|a(j)|^2 \geq \left|\sum_{j=1}^{N_2}a(j)\right|^2$ was used. Using the above lower bound and noting from Eqs. 6.6 and 6.7 that the output signal amplitude is c, the SNR can be bounded from above as

$$\begin{aligned}\text{SNR} &\equiv (\textit{signal amplitude})/\sigma \\ &\leq \sqrt{N_2/(M-1)N_3}.\end{aligned} \tag{6.14}$$

The output SNR must be sufficiently large for effective operation of the memory. If we require that SNR ≥ 1, then we get the capacity bound of

$$(M-1) \leq N_2/N_3, \tag{6.15}$$

which is recognized, for $M \gg 1$, to be the bound derived earlier, using the degrees-of-freedom arguments.

6.3.2 An example

A simple example is in order here to show that the upper bound SNR of Eq. 6.14 can be achieved. Suppose that binary, bipolar vectors $f_m(i)$, $i = 1, 2, .., N_2$ ($N_1 = N_2$) are to be associated with the vectors $g_m(n)$, $n = 1, 2, .., N_3$, by using the recording and reconstruction schemes shown in Figs. 6.3a, 6.3b. The vectors $f_m(i)$ are imaged onto the hologram via the identity transformation $Q(j, i) = \delta(j, i)$, $i = 1, 2, .., N_2$, while the transformation $R(k, j) = \delta(k, j \ mod \ N_3)$, $k = 1, 2, .., N_3$ generates multiple images (N_2/N_3 of them) of the $g_m(n)$'s on the hologram. With this arrangement,

$$\sum_{j=1}^{N_2} R(k, j) R^*(n, j) = (N_2/N_3)\delta(k, n), \tag{6.16}$$

and the noise variance given by Eq. 6.11 evaluates to

$$\sigma^2 = (M - 1)N_2/N_3. \tag{6.17}$$

The resulting output SNR is thus

$$\text{SNR} = \sqrt{N_2/(M - 1)N_3}, \tag{6.18}$$

which is the maximum achievable SNR. The redundancy that results from the multiple image storage leads to the enhancement of the SNR by the factor $\sqrt{N_2/N_3}$, and increasing redundancy leads to an increasing SNR.

6.4 Conclusion

The storage capacity of holographic associative memories using planar holograms was estimated. An argument based on the available degrees of freedom showed that the number of patterns that can be stored is limited by the space-bandwidth product of the hologram divided by the number of pixels in each pattern. A statistical calculation showed that if we attempt to store associations by multiply exposing the hologram, the cross-talk among the stored items severely degrades the output fidelity, thus confirming the storage capacity predicted by the degrees-of-freedom argument.

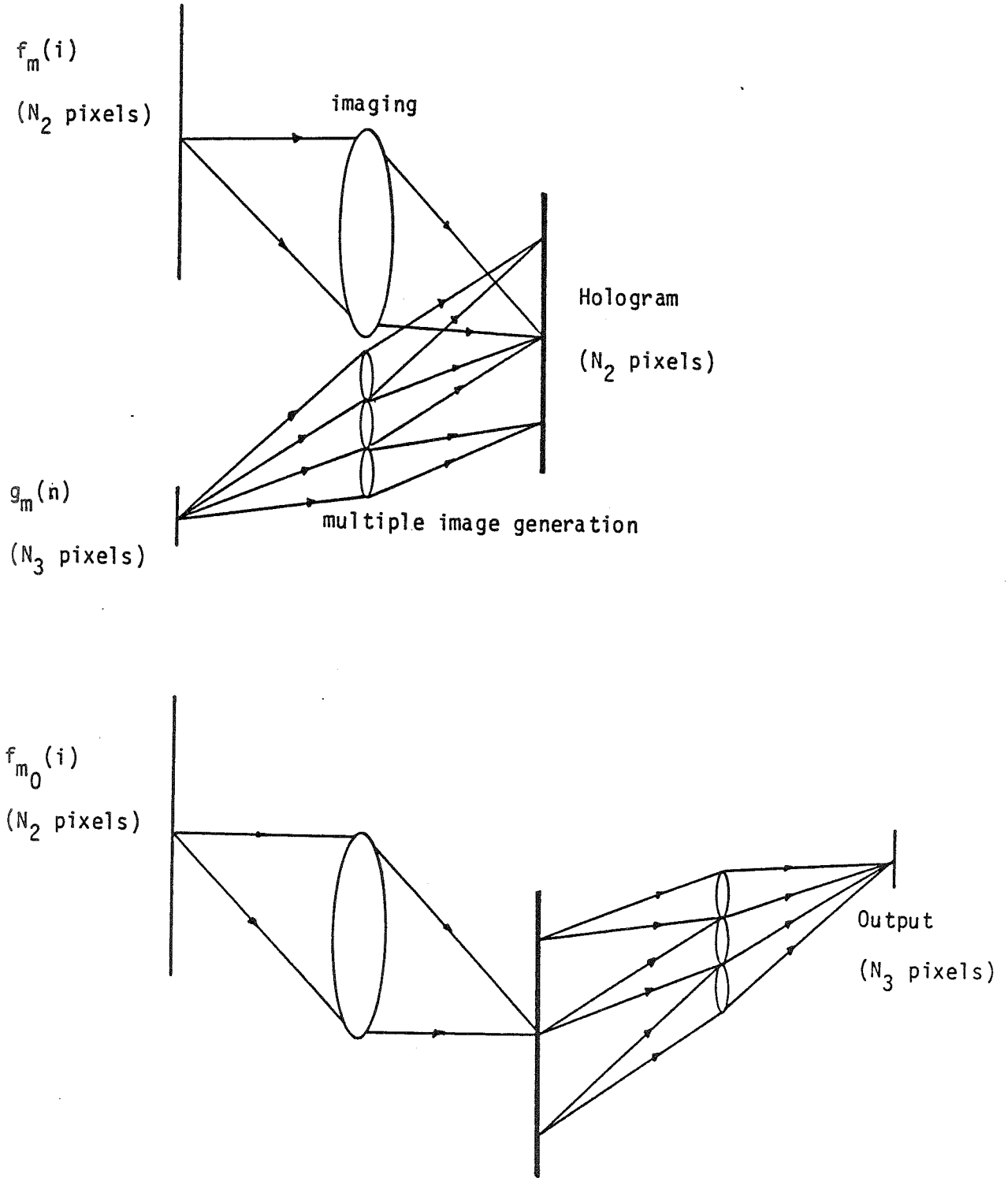

Fig. 6.4 Example System

References for Chapter 6

[1] P. J. Van Heerden, "A new optical method of storing and retrieving information," *Appl. Opt.*, **2**, 387 (1963).

[2] P. J. Van Heerden, "Theory of optical information storage in solids," *Appl. Opt.*, **2**, 393 (1963).

[3] D. Gabor, "Associative holographic memories ," *IBM J. Res. Devel.*, **13**, 156 (1969).

[4] H. J. Mager, O. Weiss, and W. Waidelich, "Sequential associative information storage and reconstruction in a holographic circuit," *Opt. Commun.*, **9**, 156 (1973).

[5] D. Psaltis and N. Farhat, "New approach to optical information processing based on the Hopfield Model," *Proc. Int. Comm. of Optics*, **ICO-13**, 24, Sapporo, Japan (Aug. 1984).

[6] D. Psaltis and N. Farhat, "Optical information processing based on an associative memory model of neural nets with thresholding and feedback," *Opt. Lett.*, **10**, 98 (1985).

[7] H. Mada, "Architecture for optical computing using holographic associative memories," *Appl. Opt.*, **24**, 2063 (1985).

[8] H. J. Caulfield, "Associative mappings by optical holography," *Opt. Commun.*, **55**, 80 (1985).

[9] B. Soffer, G. J. Dunning, Y. Owechko, and E. Marom, "Associative holographic memory with feedback using phase conjugating mirrors," *Opt. Lett.*, **11**, 118 (1986).

[10] D. Anderson, "Coherent eigenstate memory," *Opt. Lett.*, **11**, 56 (1986).

[11] M. Cohen, "Self-organization, association, and categorization in a phase conjugating resonator," *Proc. Soc. Photo-Opt. Instrum. Eng.*, **625**, 30 (1986).

[12] A. Yariv, S. Kwong, and K. Kyuma, "Optical associative memories based on photorefractive oscillations," *Proc. Soc. Photo-Opt. Instrum. Eng.*, **613**, 1 (1986).

[13] Y. S. Abu-Mostafa and D. Psaltis, "Computation power of parallelism in optical architectures," *IEEE Computer Soc. Workshop on Computer Architecture for Pattern Analysis and Image Database Management*, , Miami Beach, Fla. 42 (Nov. 1985).

[14] T. Cover, "Geometrical and statistical properties of systems of linear inequalities with applications in pattern recognition," *IEEE Trans. Elec. Comp.*, **EC-14**, 326 (1965).

Chapter 7. Shift-invariant Associative Memories

7.1 Introduction

Because of the important role that it plays in pattern recognition, the simple decision machine discussed in Chapter 2 in the context of learning (see Fig. 2.2) has been analyzed in detail with respect to its pattern-dichotomizing capabilities [1,2]. The linear structure of the machine, however, proves to be too simple to extend its recognition capabilities to be invariant with respect to certain transformations of the input pattern such as changes in scale, position, and changes in the angular orientation of the pattern [3] if the input field is extended to two dimensions. In this chapter, we discuss shift invariance in the context of associative memories and show that the linearly interconnected memory, which is basically an array of linear recognition machines, cannot exhibit shift-invariant operation. Following this, two systems (along with their optical realizations), which do exhibit shift-invariance, are described in detail, with attention given to the analysis of storage capacities.

Among the various rules for choosing the interconnection strengths in linear memories, the outer product rule is particularly simple and, as will be shown, extendable to apply to nonlinearly interconnected machines [6,8]. The weight values $w(i,j)$ for auto-associatively storing N-bit binary, bipolar vectors $\underline{f}_m$ is the sum of

the outer products of the vectors:

$$w(i,j) = \sum_{m=1}^{M} f_m(i) f_m(j). \tag{7.1}$$

The optical system [4,5] that directly implements this idea was discussed earlier in Chapter 5 and is shown schematically in Fig. 7.1. The signal produced at each detector just before the threshold gates in Fig. 7.1 is the product

$$g(i) = \sum_{j=1}^{N} w(i,j) f_{m_0}(j) = \sum_{m=1}^{M} [\sum_{j=1}^{N} f_m(j) f_{m_0}(j)] f_m(i). \tag{7.2}$$

The response to an input $\underline{f}_{m_0}$ is seen to be a weighted sum of the stored vectors, the weights being the inner products between the stored vectors and the input. As inner products can be easily computed optically, Eq. 7.2 suggests implementations different from that shown in Fig. 7.1. Shown in Fig. 7.2 is one such implementation.

The first part of the system is a one-dimensional multi-channel correlator. The slit samples the correlation functions at the zero-shift position to obtain the inner products. A mask containing the same vectors is placed in the second portion of the system. The vectors are written vertically and stacked horizontally such that a corresponding inner product produced by the front part of the system illuminates the appropriate vector. The light from each vertical position is collected horizontally onto a single detector to obtain the sum over m in Eq. 7.2. While the output threshold gates are the only nonlinearities found in the outer product scheme, the expanded system of Fig. 7.2 allows the possibility of placing nonlinearities also in

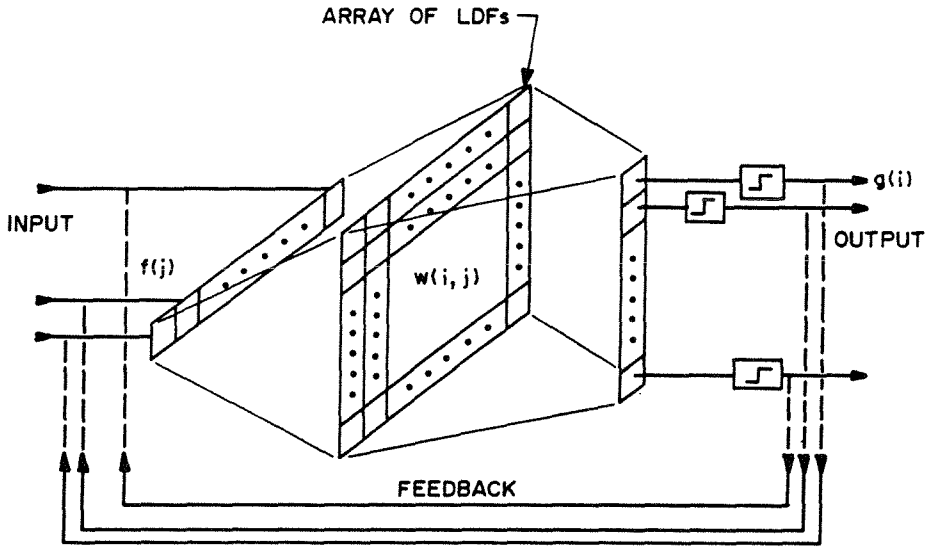

Fig. 7.1 Optical Associative Memory

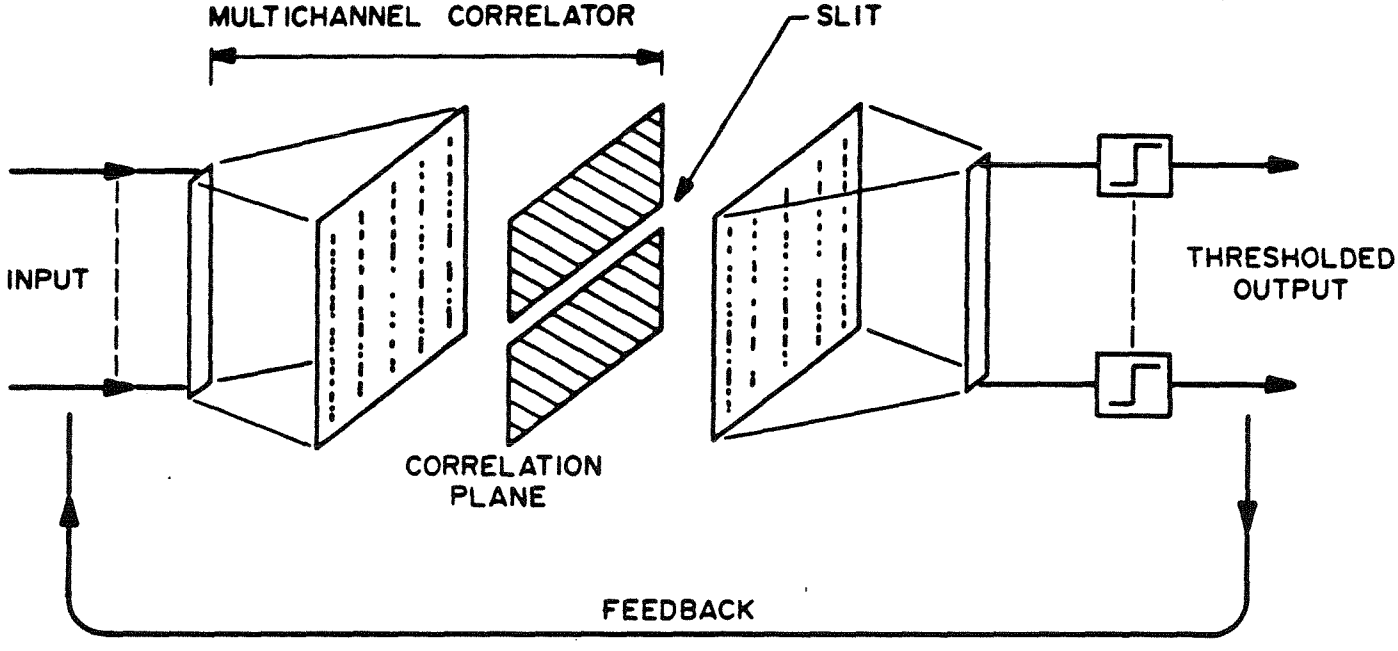

Fig. 7.2 Alternate Optical Implementation of the Linearly Interconnected Memory

the correlation plane [6-8]. It will be shown in later sections that this is indeed necessary if shift-invariant (SI) operation is required.

7.2 Shift-Invariance and Linear Memories

In relation to associative memories, two types of shift-invariance can be considered, as illustrated in Fig. 7.3. The goal in both cases is to store a set of signals and retrieve them in response to any shifted version of those signals. The first type is the usual notion of invariance, where the response to a shifted input is also to be shifted by a proportionate amount. The output of the second type always remains centered regardless of the shift occurring at the input. Note that in both cases, error correction is illustrated.

We immediately recognize a potential problem with incorporating shift-invariance in the associative memories described in the previous section. If each shifted version of the M N-bit vectors is treated as a separate entity and shifts of up to N-bits are allowed at the input, then such a system must be capable of storing on the order of MN items, where M is the number of distinct vectors to be stored. The LDF memory described earlier, which uses linear interconnections to store information, has a maximum storage capacity of N vectors, and hence, such a system can store only 1 item with full shift-invariance.

That the storage capacity is 1 for both types of shift-invariance can be shown with the following simple but fundamental arguments. Let $h(x, x')$ be the impulse

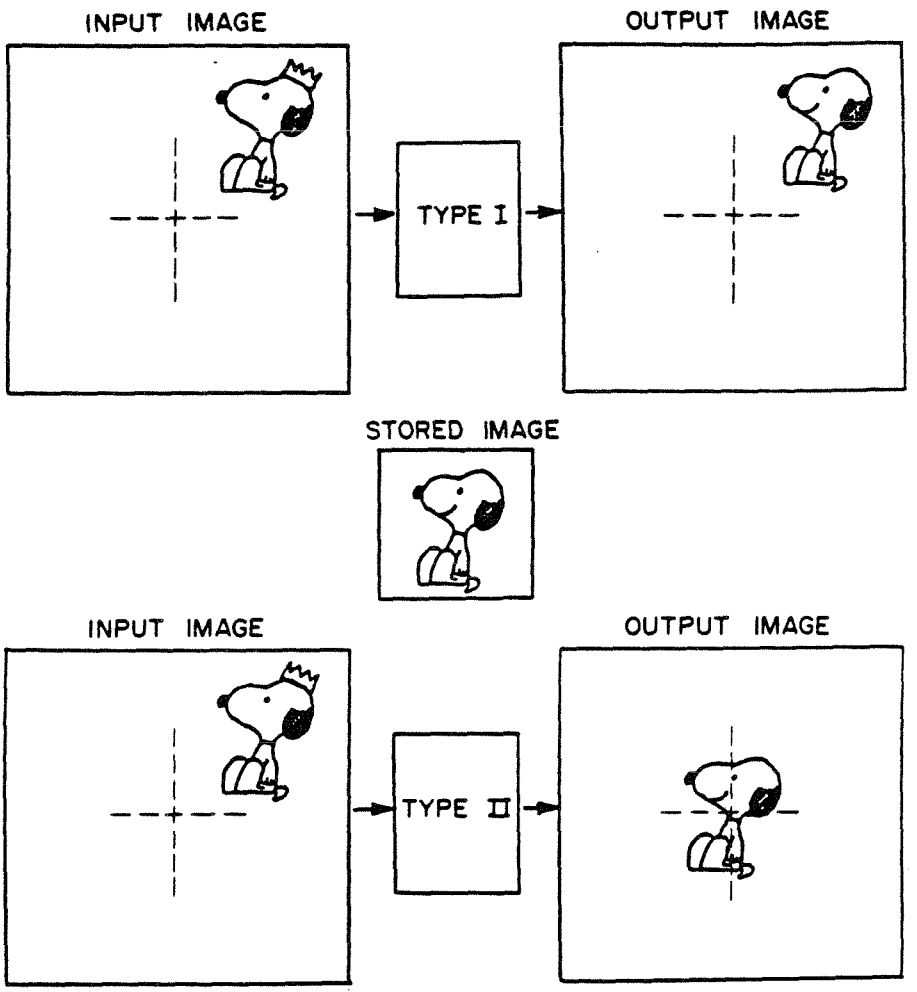

Fig. 7.3 Shift-Invariance

response of a linear optical system that is used to store associations (such as the systems in Figs. 7.1 and 7.2), and let $\{f_m(x),\ g_m(x)\}$ be the pairs of data to be stored with each function having a space-bandwidth product equal to N. For perfect recall the kernel must then satisfy the following set of M integral equations:

$$g_m(x) = \int h(x,x')f_m(x')dx', \quad m = 1,2,..,M. \tag{7.3}$$

If shift-invariance of type I is required, then the kernel must be a function only of the difference between its two arguments. With this, Eq. 7.3 reduces to a set of convolution integrals, which can be written in the Fourier domain as follows:

$$G_m(\omega) = H(\omega)F_m(\omega), \quad m = 1,2,..,M, \tag{7.4}$$

where $G_m(\omega)$, $H(\omega)$, and $F_m(\omega)$ are the Fourier transforms of $g_m(x)$, $h(x)$, and $f_m(x)$, respectively. For arbitrary pairs $\{g_m(x),\ f_m(x)\}$, $H(\omega)$ is completely determined by one pair of data, so that storage is limited to one association. Shift-invariance of type II requires that the output $g_m(x)$ be the same for $f_m(x-\alpha)$, for all possible shifts α. Using Eq. 7.3, this condition leads to:

$$\int h(x,x')f_m(x'-\alpha)dx' = \int h(x,x')f_m(x')dx'. \tag{7.5}$$

For arbitrary $f_m(x)$, $h(x,x'+\alpha) = h(x,x')$ for all α, which can be true only if $h(x,x') = h(x)$. The kernel $h(x)$ is completely determined by one pair of data, again resulting in a storage capacity of one association.

7.3 Optical Systems with Linear Interconnections

It is interesting to see how the degradation in performance occurs in an optical implementation if we attempt to incorporate shift-invariance. Specifically, we estimate here the fidelity of the reconstruction in a holographic associative memory, using signal-to-noise ratio (SNR) as the measure. Holography was the first optical implementation of associative memory based on the fact that a hologram stores an object wave in relation to a reference by recording their mutual interference. Either wave can be approximately reconstructed in response to the other [9,10]. If we use Fourier transform holograms, the overall system can be made SI (Shift-Invariant), as illustrated in Fig. 7.4.

It is possible to record multiple associations on the same hologram by repeated exposures. The issue is then, how many such associations can be stored? The complex amplitude transmittance of the hologram is proportional to $\sum_{m=1}^{M} F_m^*(\vec{x}')G_m(\vec{x}')$, where $F_m(\vec{x}')$ and $G_m(\vec{x}')$ are the Fourier transforms of $f(\vec{x})$ and $g(\vec{x})$, respectively. We find it convenient to treat the problem with a discrete analysis. Therefore, we represent the input, output, and hologram planes each by N pixels, where N is the SBP of the hologram. When one of the stored images $f_{m_0}(i)$ is used as the input, the resulting output is described by the following sum of convolutions of the stored

output vectors with the correlations of $f_{m_0}(i)$ with the references $f_m(i)$:

$$\begin{aligned} g(k) &= \sum_{m=1}^{M} \sum_{j=-N}^{N} R_m(j) g_m(k-j) \\ &= R_{m_0}(0) g_{m_0}(k) + \alpha(k) = N g_{m_0}(k) + \alpha(k), \qquad (7.6) \\ \alpha(k) &= \sum_{j \neq 0} R_{m_0}(j) g_{m_0}(k-j) + \sum_{m \neq m_0} \sum_{j=-N}^{N} R_m(j) g_m(k-j), \end{aligned}$$

with $R_m(j) = \sum_{i=1}^{N} f_m(i) f_{m_0}(j+i)$. Since the overall operation is a cascade of a correlation with a convolution, the system is SI. From Eq. 7.6, the output is seen to contain the correct recall term but with cross correlation noise. This is similar to the situation in Eq. 7.2, except that the interference term is now a double summation including all of the shifted versions of each stored memory.

If all of the stored vectors are binary, bipolar with pixel values that are statistically independent, the signal-to-noise ratio (SNR), defined as the ratio of the signal term to the standard deviation of $\alpha(k)$, is calculated to be

$$\text{SNR} = \sqrt{N / E[\alpha^2(k)]} \approx \sqrt{1/2M}. \qquad (7.7)$$

From the above equation, even if $M = 1$, the SNR=1/2, which implies that the reconstruction of even a single, stored association is noisy. This has been confirmed experimentally by Paek and Psaltis [11,12].

A SI system can also be implemented with the scheme shown in Fig. 7.2. When the input shifts vertically in the system of Fig. 7.2, the peak in the correlation plane also shifts and is blocked by the slit. As a result, a reconstruction is not obtained

and the system is not SI. This system can be easily made SI by removing the slit in the correlation plane. If in its place, however, a larger aperture is placed so as to transmit correlation peaks that are displaced from the center zero-shift position by L bits in each direction, the convolution sum of Eq. 7.6 becomes limited to include only the central $2L + 1$ bits of the correlation function, improving the SNR of Eq. 7.7 to

$$\text{SNR} = \sqrt{N/[(2L+1)M]}. \tag{7.8}$$

If $L = N$, this system becomes strictly equivalent to that of Fig. 7.4. At the other extreme, the SNR for $L = 0$ corresponds to the situation in which no shifts are allowed at the input and is equal to that of the outer product memory; this system has been optically implemented by Paek and Psaltis [11,12]. The low SNR derives from the fact that the number of degrees of freedom available in the hologram is insufficient to store the memory vectors along with all of their shifted versions, which are treated by these systems merely as additional items to be stored. It was shown in the previous chapter that the SBP of the hologram must be multiplexed in some way among the associations to be stored for such systems to be effective.

7.4 Optical Memory with Distributed Nonlinearities

7.4.1 Nonlinear correlation plane

The fact that the number of vectors that can be categorized by LDFs is limited to be less than N contradicts the requirement for SI in a memory comprised of

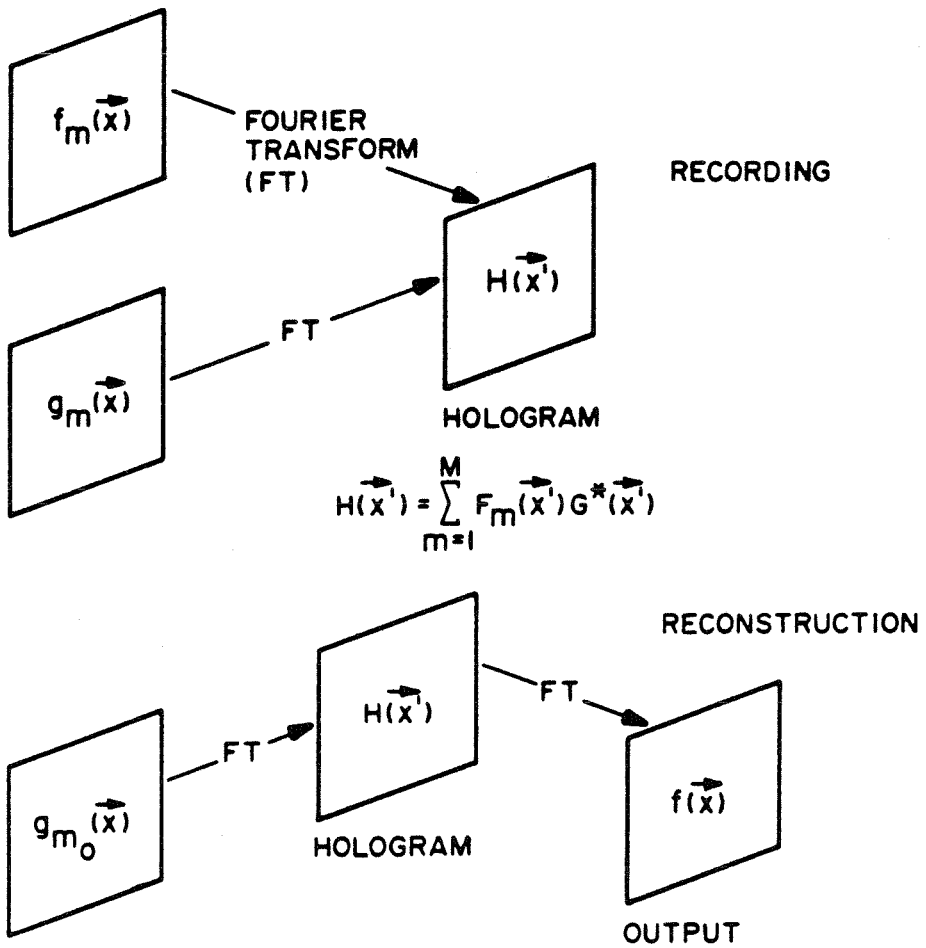

Fig. 7.4 Shift-Invariant Optical Associative Memory

an array of LDF's since all of the shifted versions of a single item exhaust the capacity of the memory. Thus, we are led to consider memories that use nonlinear discriminant functions [6,7]. Shown in Fig. 7.5 is an architecture designed to implement a particular nonlinear discriminant function. This system is arrived at by replacing the slit in the system of Fig. 7.2 by a nonlinear operation over the entire correlation plane. Specifically, the input vector is correlated with all of the stored memories $\{f_m(i)\}$, $m = 1, 2, .., M$. The resulting correlation functions are then mapped, using point nonlinearities. The next stage convolves the processed correlation functions with the associated memory signals, and the resulting outputs are summed and thresholded.

Since the overall operation is a composition of correlations and convolutions with uniform point nonlinearities, the system is SI and can be described by:

$$f_{out}(x) = \sum_{m=1}^{M} \text{N.L.}[f_m(x) \star f_{m_0}(x)] \ * \ f_m(x), \tag{7.9}$$

where $N.L.[\ ]$ indicates the nonlinear operation, and $\star$ and $*$ denote the correlation and convolution operations, respectively. The input $f_{m_0}(x)$ is one of the stored items. The purpose of the nonlinearities is to enhance the processing gain that is present at the correlation plane by increasing the strength of the peaks relative to the sidelobes.

7.4.2 Shift-invariant optical memory

We consider two such nonlinearities as shown in Fig. 7.6. If a threshold function is used [13], then for proper operation of the system, the threshold level must be adjusted to always pick out only the maximum peak among the various correlations. If such a threshold level can be found, the output threshold gates along with the feedback become unnecessary, as only one of the stored memories would be read out. If, however, the threshold level were fixed and several peaks exceeded that level, the output signal term would be an equally weighted sum of several memory signals, resulting in a completely ambiguous recall. We therefore consider softer nonlinearities that retain enough information about the specific input beyond the correlation plane. Thus, the decision is distributed between the output threshold operation on the individual bits and on the correlation plane.

The square law is of special interest, since it is easily realized optically. If M N-bit binary, bipolar signals $f_m(k)$ are stored and the input window allows $2N$ shifts (N bits in each direction), then the input-output equation can be written as:

$$f(k) = \sum_{m=1}^{M} \sum_{j=-N}^{N} R^2_{mm_0}(j) f_m(k-j), \tag{7.10}$$

where $R_{mm_0}(j) = \sum_{i=1}^{N} f_m(i) f_{m_0}(i+j)$ is the correlation function of the m_{th} stored memory vector and the input vector $f_{m_0}(i)$. A more general situation, where the degree of shift-invariance can be controlled to allow L shifts in each direction with $0 \leq L \leq N$, is achieved by limiting the convolution summation interval to $[-L, L]$

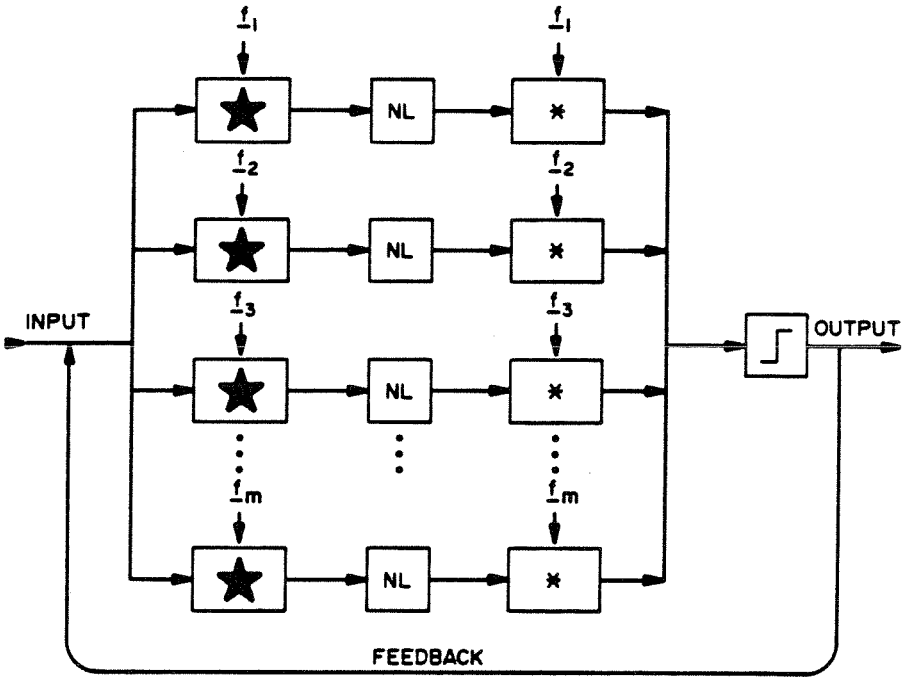

Fig. 7.5 Distributed Nonlinearity System

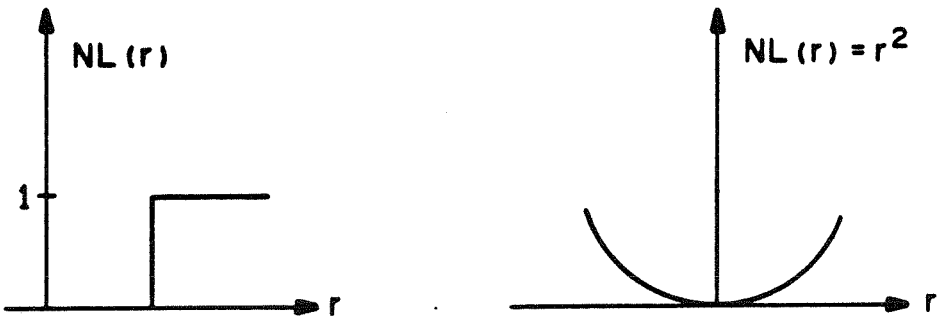

Fig. 7.6 Nonlinearities: (left) threshold, and (right) square law

as follows:

$$f(k) = \sum_{m=1}^{M} \sum_{j=-L}^{L} R^2_{mm_0}(j) f_m(k-j). \tag{7.11}$$

For the optical implementation of Fig. 7.2, this corresponds to the placement of an aperture followed by a spatial light modulator to perform the squaring operation in the correlation plane. Eq. 7.11 can be expanded to yield:

$$\begin{aligned} f(k) &= R^2_{m_0m_0}(0) f_{m_0}(k) + \alpha(k) \\ &= N^2 f_{m_0}(k) + \alpha(k), \\ \alpha(k) &= \sum_{j \neq 0} R^2_{m_0m_0}(j) f_{m_0}(k-j) + \sum_{m \neq m_0} \sum_{j=-L}^{L} R^2_{mm_0}(j) f_m(k-j). \end{aligned} \tag{7.12}$$

The output SNR can then be computed to yield the result

$$\text{SNR} = N^2 / \sqrt{E[\alpha^2(k)]} \approx \frac{N}{\sqrt{3M(2L+1)}}. \tag{7.13}$$

For comparison, the SNR of the outer product memory, which is not SI, is SNR $= \sqrt{N/M'}$, where the maximum value that M', the number of stored vectors, can take is approximately $.15N$ [2].

We obtain an estimate for the maximum number of vectors M that can be memorized by the nonlinear SI system (allowing L-bit SI in each direction) by requiring that it produce the same SNR as the outer product memory:

$$M_{max} \approx N M'_{max} / [3(2L+1)] \approx .15N^2 / [3(2L+1)], \tag{7.14}$$

which demonstrates the tradeoff that exists between the storage capacity and the degree of shift-invariance. Whereas the linearly connected machine described in

the previous section does not have sufficient degrees of freedom to store and recall even one vector with shift-invariance, the present system possesses a useful capacity described by Eq. 7.14 because of the squaring operation performed in the correlation plane.

The SI memory that we are describing is related to the quadratic associative memories discussed by Psaltis and Park [6]:

$$f(i) = \sum_{j=1}^{N} \sum_{k=1}^{N} w(i,j,k) f_{m_0}(j) f_{m_0}(k). \tag{7.15}$$

In this quadratic memory, a 3-dimensional tensor, $w(i,j,k)$, is used to store the information. The recall is accomplished by first forming the outer product of the input vector with itself and multiplying the resulting matrix with $w(i,j,k)$. To realize a SI quadratic memory, the weights must be selected as follows:

$$w(i,j,k) = \sum_{m=1}^{M} \sum_{l=-L}^{L} f_m(i-l) f_m(j+l) f_m(k+l). \tag{7.16}$$

It can easily be shown that if in Eq. 7.15 the tensor $w(i,j,k)$ is formed according to Eq. 7.16, then a shift in the input vector results in an equal shift in the output. Substitution of Eq. 7.16 into Eq. 7.15 then yields

$$\begin{aligned} f(i) &= \sum_{m=1}^{M} \sum_{l=-L}^{L} \sum_{j=1}^{N} \sum_{k=1}^{N} f_m(i-l) f_m(j+l) f_m(k+l) f_{m_0}(j) f_{m_0}(k) \\ &= \sum_{m=1}^{M} \sum_{l=-L}^{L} f_m(i-l) \Big| \sum_{j=1}^{N} f_m(j+l) f_{m_0}(j) \Big|^2. \end{aligned} \tag{7.17}$$

The above equation is identical to Eq. 7.11, which demonstrates the equivalence of the SI quadratic memory and the square law system of Fig. 7.5. The significance of

this result is that it is possible to implement an SI quadratic memory without the need to realize optically a 3-dimensional tensor of weights which would require a total of N^3 connections. By implementing the same memory by using a square law in the correlation plane, we need to specify only MN weights where the maximum value of M is given in Eq. 7.14. If $L = N$, the total number of connections that need to be specified holographically reduces to $.15N^2/6$, corresponding to a total of $.15N/6$ separate images.

The system was simulated for the case $L = N$ and the results are shown in Figs. 7.7a-7.7f. Two 32 bit, binary, bipolar vectors shown in the marked regions of Figs. 7.7a and 7.7b were programmed into the memory. The first line in each figure constitutes the particular input used, and the subsequent lines contain the thresholded output vectors after each iteration; "+" indicates a +1 and "−" indicates a −1. Because of the inherent three valuedness of the data representation, namely, +1, −1, and 0, a threshold with a "dead zone" was fixed in the simulations, as shown in Fig. 7.8.

Figs. 7.7a and 7.7b show that the two programmed vectors are indeed fixed points of the system, and in particular, Fig. 7.7b demonstrates the memory's shift-invariance. Figs. 7.7c-7.7f serve to illustrate the error-correcting capability of the system. In each case, the system converges to the correct result within 3 iterations. With a small decrease in performance (capacity and/or error correction), the system can be implemented with a strictly 2-level threshold with no dead zone

by configuring the memory with a combination of unipolar and bipolar signals and using unipolar inputs.

7.5 Two-Dimensional SI for One-Dimensional Data

We now discuss a novel method of storing and recalling 1-dimensional data with SI in both dimensions. This method utilizes the SI properties resulting from Fourier transform holograms but does not require nonlinear discriminant functions. Shown in Fig. 7.9 is the basic system. For illustration, the storage and recall of only one item is shown. The mask whose complex amplitude transmittance function is given by the outer product $T(\omega_x, \omega_y) = F^*(\omega_x)F^*(\omega_y)$ is placed in the Fourier transform plane with respect to both input and output planes of the memory vector, where $F(\omega_x)$ is the Fourier transform of $f(x)$. There is an analogy between this and Eq. 7.1, the only difference being that the outer product of the Fourier transforms is recorded rather than the outer products of the vectors themselves.

The memory is reconstructed by placing at the input plane in Fig. 7.9 a transmittance function given by $f(x - \Delta_x)\delta(y - \Delta_y)$, which is Fourier-transformed by lens L1. This transform is multiplied by $T(\omega_x, \omega_y)$ to give:

$$\tilde{F}(\omega_x, \omega_y) = F^*(\omega_y)|F(\omega_x)|^2 e^{-j(\omega_x \Delta_x + \omega_y \Delta_y)}. \tag{7.18}$$

The resultant product $\tilde{F}(.)$ is then Fourier-transformed again by L2 to give at the

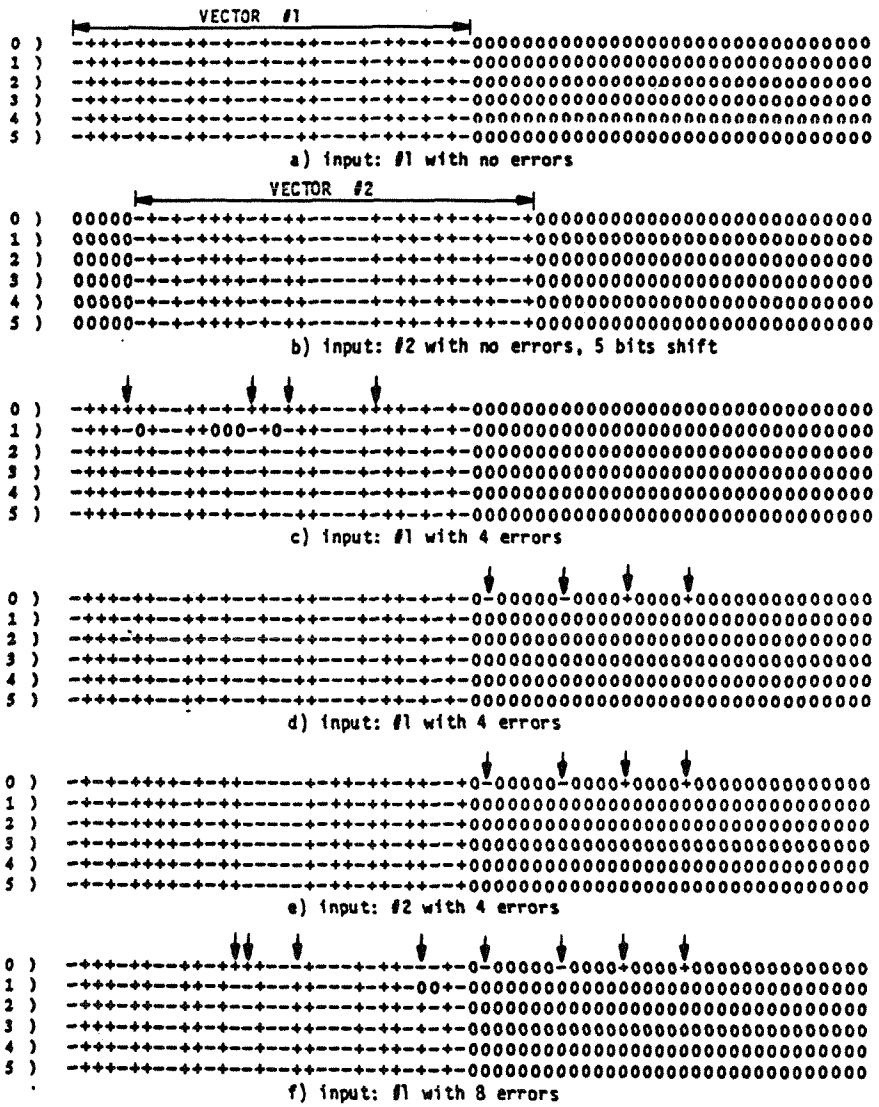

Fig. 7.7 Computer Simulation Results for Square Law System: Input errors are marked by arrows. a)input:2 with no errors; b)input: 2 with no errors, 5 bits of shift; c)input: 1 with 4 errors; d)input: 1 with 4 errors; e)input: 2 with 4 errors; f)input: 1 with 8 errors

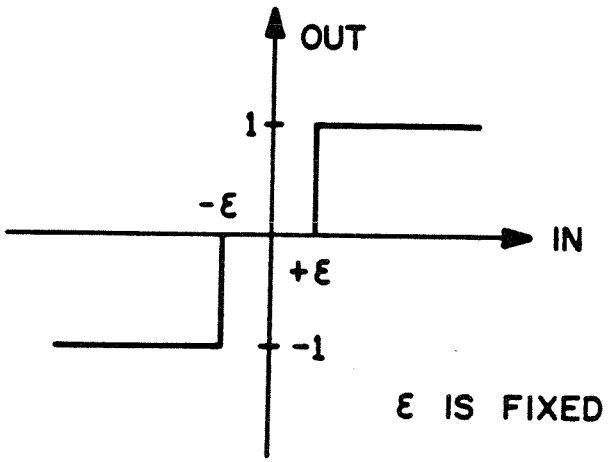

Fig. 7.8 Threshold with Fixed Dead Zone

output plane

$$f_{out}(x,y) = R(x+\Delta_x)f(y+\Delta_y),$$
$$R(x) = \int f(\alpha)f(\alpha - x)d\alpha. \tag{7.19}$$

Here $R(x)$ is the autocorrelation function of $f(x)$. This is thresholded and the resulting 2-dimensional binary signal is fed back into the system by reflection. Since the amplitude transmittance function of the mask is symmetric with respect to an interchange of its two arguments, the feedback operation places the reflected signal centered at the position where the original vector appeared as illustrated in Fig. 7.9. In the forward operation, the x-shift is encoded into a horizontal shift of the autocorrelation function, while the y-shift appears as a vertical shift in the reconstructed signal. Because the shifts have been encoded in this way, many such

associations can be made by simply adding the corresponding terms to the mask function $T(\omega_x, \omega_y)$, which becomes

$$T(\omega_x, \omega_y) = \sum_{m=1}^{M} F_m^*(\omega_x) F_m^*(\omega_y). \tag{7.20}$$

If the system is interrogated with an input $f_{m_0}(x - \Delta_x)\delta(y - \Delta_y)$, then the output can be written as a sum of the correct recall term with the proper shifts and a cross-correlation noise term as follows:

$$\begin{aligned} f_{out}(x, y) &= R_{m_0}(x + \Delta_x) f_{m_0}(y + \Delta_y) + \sum_{m=1}^{M} R_m(x + \Delta_x) f_m(y + \Delta_y), \\ R_m(x) &= \int f_m(\alpha) f_{m_0}(\alpha + x) d\alpha. \end{aligned} \tag{7.21}$$

This equation is similar to Eq. 7.6, except that the interference term does not have a double summation. In this case, the energy is spread over a 2-dimensional plane allowing the 1-dimensional vector to be observed with higher fidelity. This allows us to implement a SI memory that can store multiple 1-dimensional vectors.

Specifically, considering a system that stores M N-bit, binary, bipolar vectors whose individual bits are statistically independent, the output SNR can be calculated to be:

$$\text{SNR} \approx N/\sqrt{NM + (M-1)^2} \approx \sqrt{N/M}, \tag{7.22}$$

where the last approximation is valid for large N. Eq. 7.22 shows that the capacity approaches that of the conventional outer product scheme while maintaining SI. The increased capacity is gained at the cost of requiring a 2-dimensional array of threshold gates at the output plane.

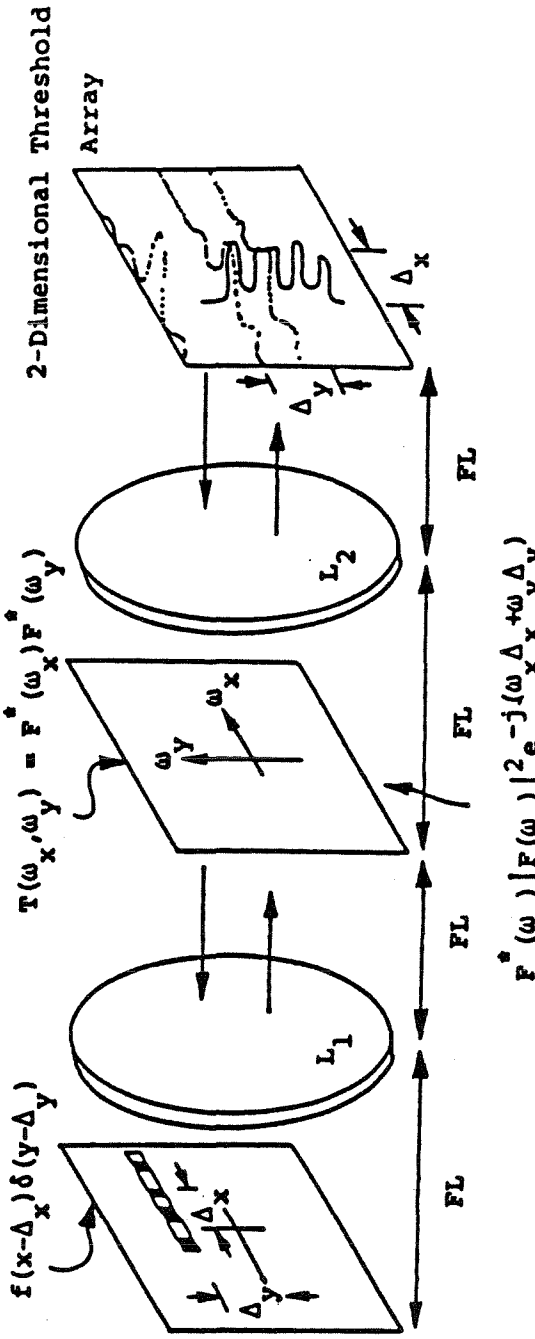

Fig. 7.9 One-Dimensional Data Storage with Two-Dimensional Shift-Invariance

References for Chapter 7

[1] Cover, T., "Geometrical and statistical properties of systems of linear inequalities with applications in pattern recognition," *IEEE Trans. Elec. Comp.*, **EC-14**, 326 (1965).

[2] Nilsson, N. J., *Learning Machines*, Mc Graw Hill, New York, 1965.

[3] Minsky, M. and S. Pappert, *Perceptrons*, MIT Press, Cambridge, MA, 1969.

[4] Farhat, N., D. Psaltis, A. Prata, and E. Paek, "Optical implementation of the Hopfield Model," *App. Opt.*, **24**, 1469 (1985).

[5] Psaltis, D., E. Paek, and J. Hong, "Acoustooptic implementation of the Hopfield Model," *JOSA*, **2**, no.13, 48 (Dec. 1985).

[6] Psaltis, D. and C. H. Park, "Nonlinear discriminant functions and associative memories," *APS Snowbird Conf. on Associative Memory*, **1**, (Snowbird, UT 1986).

[7] Psaltis, D., J. Hong, and S. Venkatesh, "Shift-invariance in optical associative memories," *Optical Computing, J. A. Neff, ed., Proc. SPIE*, **625**, 189 (1986).

[8] Lee, Y. C., G. Doolen, H. H. Chen, G. Z. Sun, T. Maxwell, H. Y. Lee, and L. Giles, "Machine learning using a higher order correlation network," *APS Snowbird Conf. on Associative Memory*, **1**, (Snowbird, UT 1986).

[9] Van Heerden, P. J., "A new optical method of storing and retrieving information," *Appl. Opt.*, **2**, 387 (1963).

[10] Gabor, D., " Associative holographic memories ," *IBM J. Res. Devel.*, **13**, 156 (1969).

[11] Paek, E. and D. Psaltis, "Holographic implementation of a neural network," *OSA Annual Meeting*, , (Seattle, Wash. 1986).

[12] Paek, E. and D. Psaltis, "Optical associative memory using Fourier transform holograms," *Optical Engineering*, **26**, no.5, 428 (May 1987).

[13] Athale, R. A., C. B. Friedlander, and B. G. Kushner, "Attentive associative architectures and their implications to optical computing," *Optical Computing, J. A. Neff, ed., Proc. SPIE*, **625**, 179 (1986).

Chapter 8. Conclusions

8.1 Summary of the Thesis

Optical implementations of various computing structures derived from neural network models have been considered. First, an algorithm by which such networks can learn to do computation tasks such as pattern recognition was used to perform adaptive filtration of signals in the presence of additive noise whose properties are not well known *a priori*. Optical implementations of the adaptive systems were demonstrated, which use readily available devices such as the acousto-optic device. Along with the description and demonstration of the systems, performance issues such as stability and maximum noise nulling capability were addressed theoretically and verified experimentally. The adaptive filters were then generalized to the space-time domain of phased array antenna signal processing where optical implementations requiring the use of multi-channel acousto-optic devices were presented.

The techniques of recognition that were described during the discussion of adaptive systems were then extended to tackle the problem of associative memory with optical implementations in mind. The parallelism and global interconnective capabilities that are possible with optical techniques make it possible to implement very large-scale, associative memory systems. First, an acousto-optical system that implemented various linearly interconnected associative memory models (such as the *Hopfield* model) was demonstrated and its various parameters such as the memory

storage capacity and the attraction radius of each memorized item were characterized.

Secondly, holographic associative memories in which planar holograms are used to record interferometrically the associations between various items were considered and an upper bound was derived under very general conditions. The bound states that the important parameter is the space bandwidth product (SBP) of the hologram, which is essentially the number of independent pixels on the hologram, the variable parameters, and in summary, any such holographic memory can at most store and retrieve on the order of N_2/N_3 images, each with N_3 pixels where N_2 is the SBP of the hologram.

Associative memories whose performance is invariant with respect to shifts in the input pattern position were then considered, and in particular, memory systems that employ strictly linear interconnections were shown to be ineffective. A network that used nonlinear interconnections was shown to exhibit useful storage capacity while maintaining a shift-invariant operation. Finally, a novel encoding scheme was presented that stores one-dimensional data and retrieves data invariantly with respect to position shifts of the input data stream on the input plane.

8.2 Directions for Future Research

With respect to adaptive systems and their optical implementations, actual laboratory operation of adaptive broadband phased array processors have yet to be

demonstrated. The high complexity presented by the array-processing task is well matched to the capabilities of multi-channel acousto-optic devices that are currently available and may well be out of reach of reasonable electronic implementations.

Learning was discussed solely in the context of adaptive filtering. It is an issue also for associative memories, and simple methods by which machines can be programmed to store and retrieve data should be considered. The holographic paradigm offers one such method. The capacity result derived for planar holograms should be generalized so as to cover the case of volume holograms.

Invariance with respect to only one transformation of the input pattern, namely, that of position of the pattern was considered for associative memory. Other forms of invariance, such as rotation invariance and scale invariance should now be considered.

Appendix A

Effects of System Noise on the Passive Processor

In this appendix, the deterioration of the jammer cancelling capability of the passive processor (Chapter 3) caused by noise in the system is considered. By inspection of the system diagram (Fig. 2.6a), the system equation can be manipulated to yield an equation governing the feedback signal $\hat{x}(t)$. Using Eqs. 3.8, we get

$$\hat{x}_0(t) = \frac{8c_1c_2}{T^2}\int_{-T/4}^{0}\int_{0}^{T/2} x^*(t+2\beta-T/2)x(t+\beta+\tau-T/2)z_0(t+\beta-\tau)d\tau d\beta,$$
$$z_0(t) = x(t) - \hat{x}_0(t). \tag{A1}$$

The above equations neglect the system noise entirely and are used to derive the ideal response $\hat{x}_0(t)$. For a jammer input $x(t) = Aexp(j2\pi f_0 t)$, the above equations combine to yield:

$$\hat{x}_0(t) = \frac{8c_1c_2}{T^2}A^2\int_{-T/4}^{0}\int_{0}^{T/2} exp[j2\pi f_0(\tau-\beta)] \{Aexp[j2\pi f_0(t+\beta-\tau)] - \hat{x}_0(t+\beta-\tau)\}\, d\tau d\beta. \tag{A2}$$

This integral equation is solved, using Fourier techniques, to yield the steady-state solution:

$$\hat{x}_0(t) = \frac{Gc_1c_2A^3}{1+Gc_1c_2A^2}exp(j2\pi f_0 t), \tag{A3}$$

where we assume that the gain has been adjusted for stability as discussed in the text. In the present analysis, it is possible to involver more rigorously the apodization

functions that are required to provide deep stable nulls, but to provide a more compact discussion, we neglect this apodization.

To analyze the effects due to noise, the following statistics are assumed for the noise contributions from the detectors and amplifiers: $\sigma n_i(t)$ are independent, stationary, complex Gaussian processes, each with zero mean and variance σ^2. The autocorrelation and spectral density function for each $n_i(t)$ are denoted by $R_i(t)$ and $S_i(f)$, respectively. By inspection of the noise model of Fig. 3.20, the feedback signal contaminated by the noise can be shown to be described by

$$\begin{aligned}\hat{x}(t) = {} & \sigma n_3(t) + \sigma\frac{4c_2}{T}\int_{-T/4}^{0} x^*(t+2\beta-T/2)n_2(t+\beta-T/2)d\beta \\ & + \sigma\frac{8c_1c_2}{T^2}\int_{-T/4}^{0}\int_{0}^{T/2} x^*(t+2\beta-T/2)x(t+\beta+\tau-T/2)n_1(t+\beta-\tau)d\beta d\tau \\ & + G\frac{8c_1c_2}{T^2}\int_{-T/4}^{0}\int_{0}^{T/2} x^*(t+2\beta-T/2)x(t+\beta+\tau-T/2)x(t+\beta-\tau)d\beta d\tau \\ & - G\frac{8c_1c_2}{T^2}\int_{-T/4}^{0}\int_{0}^{T/2} x^*(t+2\beta-T/2)x(t+\beta+\tau-T/2)\hat{x}(t+\beta-\tau)d\beta d\tau. \end{aligned} \tag{A4}$$

If we make the substitution $\hat{x}(t) = \hat{x}_0(t) + \sigma\hat{x}_1(t)$ in Eq. A4, using also the noiseless response given by Eq. A1, we get

$$\begin{aligned}\hat{x}_1(t) = {} & n_3(t) + \frac{4c_2}{T}\int_{-T/4}^{0} x^*(t+2\beta-T/2)n_2(t+\beta-T/2)d\beta \\ & + \frac{8c_1c_2}{T^2}\int_{-T/4}^{0}\int_{0}^{T/2} x^*(t+2\beta-T/2)x(t+\beta+\tau-T/2)n_1(t+\beta-\tau)d\beta d\tau \\ & - G\frac{8c_1c_2}{T^2}\int_{-T/4}^{0}\int_{0}^{T/2} x^*(t+2\beta-T/2)x(t+\beta+\tau-T/2)\hat{x}_1(t+\beta-\tau)d\beta d\tau. \end{aligned} \tag{A5}$$

The above equation can be specialized for the jammer input $x(t) = exp(j2\pi f_0 t)$ to yield

$$\hat{x}_1(t) = \{n_3(t) + \frac{4c_2}{T} A exp[-j2\pi f_0(t - T/2)] \int_{-T/4}^{0} exp(-j4\pi f_0 \beta) n_2(t + \beta - T/2) d\beta$$
$$+ \frac{8c_1c_2}{T^2} A^2 \int_{-T/4}^{0} \int_{0}^{T/2} exp[j2\pi f_0(\tau - \beta)] n_1(t + \beta - \tau) d\beta d\tau\}$$
$$- \frac{8c_1c_2}{T^2} A^2 G \int_{-T/4}^{0} \int_{0}^{T/2} exp[j2\pi f_0(\tau - \beta)] \hat{x}_1(t + \beta - \tau) d\beta d\tau. \quad (A6)$$

The terms in braces in Eq. A6 can then be considered to comprise a stochastic input $\hat{n}(t)$ to the system described by:

$$\hat{x}_1(t) = \hat{n}(t) - \frac{8c_1c_2}{T^2} A^2 G \int_{-T/4}^{0} \int_{0}^{T/2} exp[j2\pi f_0(\tau - \beta)] \hat{x}_1(t + \beta - \tau) d\beta d\tau, \quad (A7)$$

where $\hat{x}_1(t)$ is the output and $\hat{n}(t)$ is the random excitation. If $\hat{n}(t)$ is wide-sense stationary, the spectral density of the output, $\hat{x}_1(t)$ can be shown to be

$$S(f) = \frac{S_n(f)}{1 + GA^2c_1c_2 exp[-j3\pi(f - f_0)T/4] sinc[(f - f_0)T/2] sinc[(f - f_0)T/4]}, \quad (A8)$$

where $S_n(f)$ is the spectral density function for the random noise process $\hat{n}(t)$. Since the noise sources $n_i(t)$ in the system are independent, zero mean, and stationary, the

composite process $\hat{n}(t)$ is wide-sense stationary with autocorrelation function given by

$$R_n(\alpha) = R_3(\alpha) + \frac{16c_2^2A^2}{T^2} exp(-j2\pi f_0\alpha) \int \int_{-T/4}^{0} exp[-j4\pi f_0(\beta - \beta')] R_2(\alpha + \beta - \beta')d\beta d\beta'$$
$$+ \frac{64c_1^2c_2^2A^4}{T^4} \int \int_{-T/4}^{0} \int \int_{0}^{T/2} exp[-j2\pi f_0(\beta - \beta')]exp[j2\pi f_0(\tau - \tau')] R_1(\alpha + \beta - \beta' - \tau + \tau')d\tau d\tau' d\beta d\beta'. \quad (A9)$$

Fourier transformation with respect to α yields the spectral density function:

$$S_n(f) = S_3(f) + c_2^2A^2 sinc^2[(f - f_0)T/4]S_2(f + f_0) + c_1^2c_2^2A^4 sinc^2[(f - f_0)T/4]sinc^2[(f - f_0)T/2]S_1(f). \quad (A10)$$

The above equation in conjunction with Eq. A8 is the main result of the present analysis. The noise contribution to the output given by Eq. A8 shows that the contribution from the source $n_3(t)$ will be dominant, since the others are filtered by the convolver and correlator to contribute a narrowband process centered at the jammer frequency. These narrowband processes are further suppressed by the system. The total noise power at the output is therefore approximately σ^2.

Appendix B

Optimum Broadband Array Processors

The optimum broadband array-processing systems discussed in Chapter 4 are derived in this appendix. The two optimality criteria considered are the mean squared error and the maximum output SNR conditions. Simple variational arguments are used to derive the necessity conditions for these criteria. Since the costs to be minimized are quadratic functionals of the impulse responses that are varied, these necessity conditions are sufficient as well, and so describe the systems uniquely. Throughout this appendix, the noise received by the n_{th} array element is represented by $v_n(t)$ which is assumed to be a zero mean, stationary, random process with covariance $\gamma_{mn}(\tau) = E[v_m(t)v_n^*(t-\tau)]$.

Minimum Mean Squared Error Sidelobe Canceller

We model the desired signal by a zero-mean stationary random process $s(t)$ whose autocorrelation function is given by $R(\tau) = E[s(t)s^*(t-\tau)]$. Let the total signal (desired signal plus noise) received by the n_{th} element be represented by $u_n(t) = s(t) + v_n(t)$. Since the scenario of interest focuses on a signal arriving on boresight, each element receives the same desired signal without dispersion.

The form of the processor is shown in Fig. 4.5, where the parameters that must be optimized are the N impulse response functions. The output signal is given by

$$z(t) = \sum_{n=1}^{N} \int_{-\infty}^{\infty} h_n(\tau) u_n(t-\tau) d\tau, \tag{B1}$$

and the cost to be minimized is given by

$$\begin{aligned} C[h_n(t)] &= E[|z(t) - s(t)|^2] \\ &= \sum_m \sum_n \int \int_{-\infty}^{\infty} h_m^*(\beta) h_n(\tau) [R(\beta - \tau) + \gamma_{nm}(\beta - \tau)] d\tau d\beta \\ &\quad + R(0) - \{\sum_n \int_{-\infty}^{\infty} h_n(\tau) R(-\tau) d\tau + c.c.\}, \end{aligned} \tag{B2}$$

where we have assumed the noise and signal portions to be statistically independent. Let $\hat{h}_n(t)$ represent the optimum filter for the n_{th} element, and let $g_n(t)$ represent any other impulse response function. In order for $\hat{h}_n(t)$ to be the cost-minimizing solution, the perturbed cost function $C[\hat{h}_n(t) + \alpha g_n(t)]$ must have a minimum value at the point $\alpha = \alpha_R + j\alpha_I = 0$, where α_R and α_I are real. The two conditions that express this mathematically are

$$\begin{aligned} \frac{\partial}{\partial \alpha_R} C[\hat{h}_n(t) + \alpha g_n(t)]\Big|_{\alpha=0} &= 0, \\ \frac{\partial}{\partial \alpha_I} C[\hat{h}_n(t) + \alpha g_n(t)]\Big|_{\alpha=0} &= 0. \end{aligned} \tag{B3}$$

Carrying out the above calculations leads to two equations which combine to yield

$$\sum_n \int_{-\infty}^{\infty} g_n(\tau) \{\sum_m \int_{-\infty}^{\infty} h_m^*(\beta) [R(\beta - \tau) + \gamma_{nm}(\beta - \tau)] d\beta - R^*(\tau)\} d\tau = 0. \tag{B4}$$

Since $g_n(t)$ is an arbitrary function in Eq. B4, the terms within the braces must sum identically to zero. This gives the following condition that the optimum filter

must satisfy:

$$\sum_m \int_{-\infty}^{\infty} h_m^*(\beta)[R(\beta-\tau)+\gamma_{nm}(\beta-\tau)]d\beta - R^*(\tau) = 0, \qquad (B5)$$

which is both necessary and sufficient because the cost functional is quadratic. This is the generalization of Wiener's result to the space-time domain of broadband phased arrays.

Maximum Output SNR Array Processor

We now consider the task of signal detection, using the array processor of Fig. 4.5. The signal is a known waveform $s(t)$, which arrives at an angle θ with respect to boresight, and the noise field is the same as that discussed for the MMSE (Minimum Mean-Squared-Error) processor. The total signal received by the n_{th} element is therefore given by

$$u_n(t) = s_n(t) + v_n(t), \qquad (B6)$$

where $s_n(t) = s(t - ndcos\theta/c)$ is the signal waveform as seen by the n_{th} element.

The output is given by

$$e(t) = \sum_n \int_{-\infty}^{\infty} u_n(t-\tau)h_n(\tau)d\tau. \qquad (B7)$$

Since the processor is linear, the signal component can be readily identified from the noise at the output. The output signal and noise are described, respectively by

$$\begin{aligned} e_{signal}(t) &= \sum_n \int_{-\infty}^{\infty} s_n(t-\tau)h_n(\tau)d\tau, \\ e_{noise}(t) &= \sum_n \int_{-\infty}^{\infty} v_n(t-\tau)h_n(\tau)d\tau. \end{aligned} \qquad (B8)$$

The goal is to maximize the output SNR given by

$$SNR = \frac{|e_{signal}(t_0)|^2}{E[|e_{noise}(t_0)|^2]} \tag{B9}$$

at a prescribed time t_0.

An equivalent problem is to minimize the output noise power while constraining all admissible impulse responses to give the same output signal amplitude at t_0. In particular, the functional expressed by Eq. B9 can be maximized by minimizing the cost given by

$$\begin{aligned} Q[h_n(t)] &= E[|e_{noise}(t_0)|^2] - \lambda\{\sum_n \int_{-\infty}^{\infty} s_n(t_0-\tau)h_n(\tau)d\tau - c\} \\ &= \sum_n \sum_m \int \int_{-\infty}^{\infty} h_n(\tau)h_m^*(\beta)\gamma_{nm}(\beta-\tau)d\tau d\beta \\ &\quad - \lambda\{\sum_n \int_{-\infty}^{\infty} s_n(t_0-\tau)h_n(\tau)d\tau - c\}, \end{aligned} \tag{B10}$$

where the constraint $e_{signal}(t_0) = c$ has been included through the use of the Lagrangian multiplier λ.

Again, representing the optimum filter by $\hat{h}_n(t)$ and an arbitrary function by $g_n(t)$, we apply the conditions given by Eq. B3 to obtain

$$\sum_n \int_{-\infty}^{\infty} g_n(\tau)\{\sum_m \int_{-\infty}^{\infty} \gamma_{nm}(\beta-\tau)h_m^*(\beta)d\beta - \lambda s_n(t_0-\tau)\}d\tau = 0. \tag{B11}$$

Since $g_n(t)$ is an arbitrary function, the terms within the braces must sum identically to zero, yielding the condition

$$\sum_m \int_{-\infty}^{\infty} \gamma_{mn}(\tau-\beta)h_m(\beta)d\beta = \lambda^* s_n^*(t_0-\tau), \tag{B12}$$

which is the matched filter result generalized for phased-array processing. The Lagrangian multiplier λ is immaterial since it merely multiplies all N filters by a constant factor and has no effect on the output SNR. Therefore, Eq. B12 describes the optimum result to within a constant factor.